MASTER THESIS
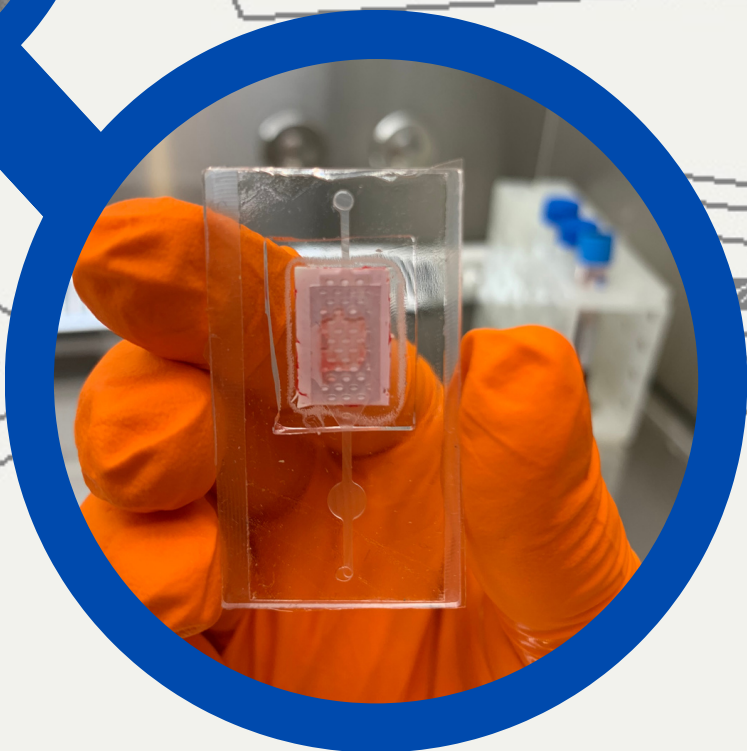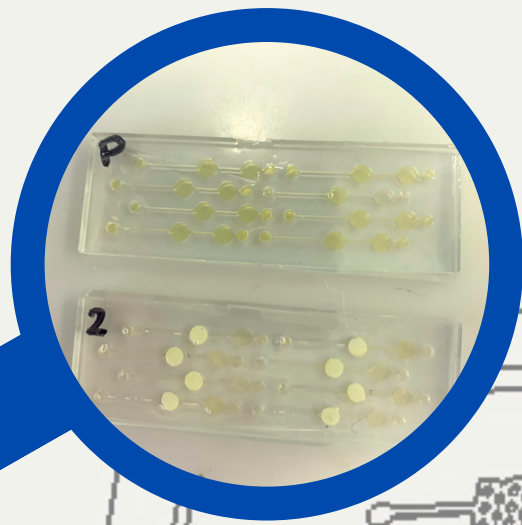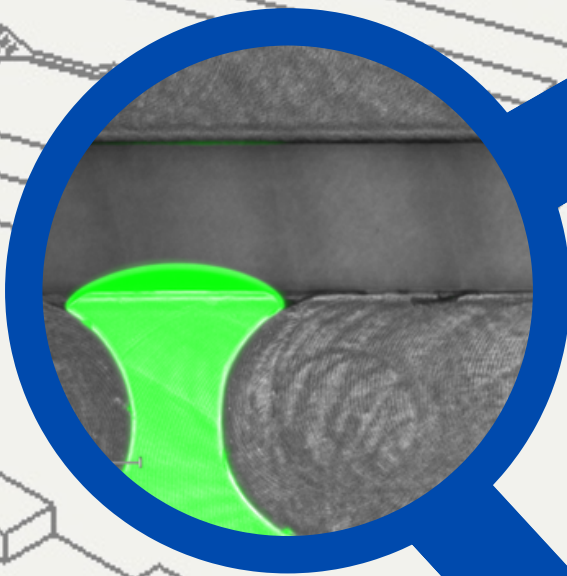
Kim Eline de Jager

Development of a microfluidic device for point-of-care testing of free thiol levels in plasma

A lab-on-a-chip for biomarker detection of oxidative stress in IBD patients

Kim Eline de Jager

k.e.dejager@student.utwente.nl

Biomedical Engineering

July 2023

Supervisors:

University of Twente:

Prof.dr.ir. L.I. Segerink
Dr.ir. J.T.W. Berendsen
Prof.dr.ir. D. Fernandez Rivas

University Medical Centre Groningen:

Dr. A.R. Bourgonje
Prof.dr. H. Van Goor
Dr. S.J. Gordijn
Dr. A.C. Muller Kobold

UNIVERSITY OF TWENTE. BIOS Lab on a Chip group umcg

Abstract

Measuring levels of biomarkers, radiology, histopathology and endoscopy are used for the diagnosis, prognosis, and monitoring of disease activity in IBD patients. The current golden standard for measuring disease activity in IBD patients is the fecal biomarker calprotectin. However, all current diagnostic tests are limited in the prediction of long-term outcomes, which emphasizes the need for new biomarkers. In patients with IBD, oxidative stress leads to damage of the mucosal layer and bacterial invasion, which enhances disease progression. The strong correlation between disease activity and reduced antioxidant free thiol levels in plasma is promising for early diagnosis and easy disease monitoring, which has high clinical relevance. The aim of this thesis was to develop a microfluidic device for POCT of free thiol levels in plasma. Also, the underlying goal was to design a LoC for biomarker detection of oxidative stress in IBD patients. The current assay is time-consuming and requires large patient blood samples. It was aimed to create a LoC that has a monolithic approach performing all steps of the current assay: plasma separation through centrifuging, plasma dilution with Tris buffer, a background measurement, diluted plasma mixing with DTNB, and absorbance measurement using the plate reader.

For the on-chip blood plasma separation an asymmetric membrane is used. A capillary pump was used to wick the plasma from the membrane, which led to plasma being obtained in 100% of the cases. After the addition of the Tris buffer, the plasma flowed through the microfluidic channels in 66.6% of the devices.
Different devices are made allowing the storage of two reagents on-chip, which had a high success rate of meniscus formation and reaching the read-out reservoir (up to 100%). A serpentine structure showed enhancement of the mixing process of these reagents throughout the channel and over time. More research is needed to create a control read-out on-chip for validation of the device. A Quake-valve could be used to prevent backflow and precise volume regulation, which needs 1500 mbar of pressure to be closed.
Lyophilization of the DTNB shows a linear relationship between the absorbance and concentration of L-Cysteine until a concentration of 250 μM is reached, after which the calibration curve saturates. No significant differences within the calibration curves obtained in the well plate and with liquid DTNB on-chip were found. Even though, there was a significant difference in the found absorbance between the two methods, no significant difference was found between the measured free thiol concentration in plasma. The intra-CV% of the free thiol concentration determined on-chip is 19.5% compared to the 3.94% of the currently used assay. The accuracy of the according calibration curve was 88.0% with an inter-CV of 9.00%. The LLOQ was 109.6 μM. In conclusion, the first steps toward a sample-in-answer-out microfluidic device for measuring oxidative stress, show promising results.
Finally, it was possible to create a calibration curve of L-Cysteine with a linear relationship ($R^2 = 0.98$) utilizing a portable spectrophotometer.

1

Samenvatting

Het meten van biomarkerniveaus, radiologie, histopathologie en endoscopie worden gebruikt voor de diagnose, prognose en monitoring van ziekteactiviteit bij IBD-patiënten. De huidige gouden standaard voor het meten van ziekteactiviteit bij IBD-patiënten is de fecale biomarker calprotectine. Alle huidige diagnostische testen zijn echter beperkt in het voorspellen van langetermijnresultaten, wat de behoefte aan nieuwe biomarkers benadrukt. Bij patiënten met IBD leidt oxidatieve stress tot beschadiging van de mucosale laag en bacteriële invasie, wat de ziekteprogressie versterkt. De sterke correlatie tussen ziekteactiviteit en verlaagde antioxidant vrije thiolspiegels in plasma is veelbelovend voor vroegtijdige diagnose en eenvoudige ziektebewaking, wat een hoge klinische relevantie heeft. Het doel van dit afstudeeronderzoek was het ontwikkelen van een microfluïdisch apparaat voor *point-of-care* testen van vrije thiolspiegels in plasma. Het onderliggende doel was ook om een *lab-on-a-chip* te ontwerpen voor biomarkerdetectie van oxidatieve stress in IBD-patiënten. De huidige test is tijdrovend en vereist grote bloedmonsters van patiënten. Het doel was om een *lab-on-a-chip* te maken met een monolithische benadering die alle stappen van de huidige assay uitvoert: scheiding van plasma door centrifugeren, verdunning van plasma met Tris-buffer, een achtergrondmeting, mengen van verdund plasma met DTNB en een absorptiemeting in een *plate reader*.

Voor de bloedplasmascheiding op de chip is een asymmetrisch membraan gebruikt. Een capillaire pomp werd gebruikt om het plasma van het membraan te verkrijgen, wat gelukt is in 100% van de geteste apparaten. Na toevoeging van de Tris-buffer stroomde het plasma in 66,6% van de apparaten door de microfluïdische kanalen.

Er zijn verschillende apparaten gemaakt voor de opslag van twee reagentia op de chip, die een hoge slagingskans hadden bij de meniscusvorming en het bereiken van het uitleesreservoir (tot 100%). Een serpentijnstructuur liet een verbetering zien van het mengproces door het hele kanaal en in de loop van de tijd. Er is meer onderzoek nodig om een controle-uitlezing op chip te maken om de resultaten te valideren. Een Quake-klep, welke met een druk van 1500 mbar kan worden gesloten, kan worden gebruikt om terugstroming te voorkomen en het volume nauwkeurig te regelen.

Lyofilisatie van DTNB laat een lineair verband zien tussen de extinctie en de concentratie L-Cysteïne tot een concentratie van 250 μM, waarna de ijkcurve verzadigt. Er werden geen significante verschillen gevonden in de ijklijnen die werden verkregen in de *well plate* en met vloeibare DTNB op de chip. Hoewel er een significant verschil was in de gevonden absorptie tussen de twee methoden, werd er geen significant verschil gevonden tussen de gemeten vrije thiolconcentratie in plasma (p=0.61). Het intra-CV% van de vrije thiolconcentratie in plasma bepaald op de chip is 19,5% vergeleken met de 3,94% van de momenteel gebruikte test. De nauwkeurigheid van de bijbehorende ijklijn was 88,0% met een inter-CV van 9,00%. De LLOQ was 109,6 μM. Concluderend kunnen we stellen dat de eerste stappen in de richting van een sample-in-answer-out microfluïdisch apparaat voor het meten van oxidatieve stress veelbelovende resultaten laten zien.

Ten slotte was het mogelijk om een ijkcurve van L-Cysteïne te maken met een lineair verband ($R^2 = 0,98$) met behulp van een draagbare spectrofotometer.

Contents

Nomenclature

Abbreviations

μ**PAD** Microfluidic Paper-based Analytical Device, page 105

ASCA Anti-Saccharomyces Cerevisiae Antibody, page 10

BPS Blood Plasma Separation, page 17

CAD Computer-Aided Design, page 22

CD Crohn's Disease, page 9

CRP C-Reactive Protein, page 10

CV Coefficient of Variation, page 15

DTNB Ellman's Reagent:5,5'-dithio-bis-[2-nitrobenzoic acid], page 109

eHealth Electronic Health, page 14

ELISA Enzyme Linked Immuno Sorbent Assay, page 14

IBD Inflammatory Bowel Disease, page 9

IFN-γ Interferon-gamma, page 10

IL Interleukin, page 10

IPAA Ileal-Pouch-Anal-Anastomosis, page 10

LoC Lab-on-a-chip, page 15

pANCA Perinuclear Antineutrophil Cytoplasmic Antibody, page 10

PCR Polymerase Chain Reaction, page 102

POCT Point-of-care testing, page 14

POC Point-of-care, page 14

RBC Red Blood Cell, page 91

ROS Reactive Oxidative Species, page 11

Th T-helper, page 10

TNF- Tumor Necroses factor-α, page 10

UC Ulcerative Colitis, page 9

WBC White Blood Cell, page 91

ID Inner Diameter, page 30

From equations

1 Introduction

In 2020, the prevalence of Inflammatory Bowel Disease (IBD) in the Netherlands is predicted by computer models to be at 691 per 100,000 citizens [1]. The latest population-based cohort study in the Netherlands was between 2004-2010 [2]. The prevalence increased by 53.7% in this time period to 432.1 cases per 100,000 inhabitants. Linschoten et al. found another increase of 12% in the prevalence over the following 10 years [1]. IBD is a collective term for Crohn's disease (CD) and Ulcerative Colitis (UC), characterized by a chronically inflamed gastrointestinal tract. In CD the inflammation is fragmented throughout the complete gastrointestinal tract, while in UC it is predominantly in the colon and rectum mucosa [3]. Strictures and fistulas can develop, causing abdominal pain and fatigue [4]. Additional symptoms of IBD are fevers, weight loss, and diarrhea: predominantly watery for CD patients and bloody for UC patients [5]. The mean time between symptoms and diagnosis is larger for CD than for UC, as the symptoms of UC are less heterogeneous. In 10-15% of the cases the symptoms are constantly present, while in most of the cases, the disease can be remission with unpredictable flare-up episodes [4]. The latest reported incidences in the Netherlands are 17.2 per 100,000 for CD and 10.5 per 100,000 for UC [6]. The highest incidence of the Netherlands is in South Limburg, and the Dutch CD incidence is the highest in Europe [7]. Additionally, for CD patients the peak incidence is seen in adolescence, meaning most CD patients are diagnosed during their adolescence [6]. The increasing incidence is presumably due to environmental risk factors such as diet, antibiotics, hygiene, microbial exposures, and pollution, especially under bearers of genetic risk factors [8]. Developing IBD is related to over 201 genetic mutations, and children of parents with IBD are five times more susceptible to developing IBD [5].

According to Lopes et al., lifestyle has a large influence on developing IBD [9]. Low modifiable lifestyle risk factors such as smoking, could have prevented the disease in 43.9%–51.2% and 20.6%–27.8% of the cases for CD and UC, respectively. A healthy lifestyle shows an even bigger possible prevention of 48.8%–60.4% in CD and 46.8%–56.3% in UC. Possible prevention in sometimes half of the cases shows the importance of early detection [9].

No individual's gut microbiota is identical, although the functions remain the same [3]. In patients with IBD, the gut microbiota are imbalanced, causing a reduced function of the intestines. Even though the actual cause of IBD remains unknown, it is shown that patients with IBD have reduced intestinal biodiversity and an increased variety of proteobacteria. There is no ideal measure for the diagnosis and distinction between CD and UC [10]. The diagnosis and monitoring of IBD is very complicated as there is no direct correlation between symptoms and disease progression in terms of strictures and fistula development [4]. Despite sedation, bowel preparation and a small risk of complications, accompanied by poor patient satisfaction, endoscopy is the golden standard for diagnosis [11].

Measuring levels of biomarkers, radiology, histopathology and endoscopy are used for the diagnosis, prognosis, and monitoring of disease activity in IBD patients [10, 12, 13]. Currently, the most commonly tested biomarkers are the fecal markers calprotectin and lactoferrin [13]. Calprotectin is stable for a week when stored at room temperature and

is an indirect marker for the neutrophil concentration in the bowel mucosa [5]. Using a threshold value of 100 μg/g for the identification of IBD, the sensitivity is 98% and the specificity is 91% [12]. There is no ideal cutoff value for calprotectin above which IBD can be diagnosed with a high level of certainty [12], although above 250 μg/g inflammation is indicated [5]. The high accuracy of the biomarker reduced the use of radiology and endoscopy. Another bowel inflammation biomarker is the protein lactoferrin, which is secreted by mucosal membranes and has a sensitivity of 80% and specificity of 82% [12]. Most studies show similar clinical value for calprotectin and lactoferrin [13]. Still, the utilization of calprotectin "is currently considered to be the best discriminating biomarker for endoscopically proven inflammatory disease activity" [11].

Blood-based biomarkers are preferred to biomarkers taken from the feces [13]. From the patient's perspective stool biomarkers cause embarrassment in sample collection, a dirty feeling, and difficulties in transportation of the sample [14]. These reasons lead to a reduced acceptability of stool biomarkers.

C-reactive protein (CRP) is used as a blood-based biomarker since the serum levels increase for 100% of CD patients and 50% of UC patients compared to healthy individuals [13]. CRP is also used for the distinction between active and quiescent IBD. The combination of increased CRP levels and clinical symptoms can identify active mucosal disease. However, CRP is less sensitive and its connection to mucosal inflammation is lower compared to calprotectin and lactoferrin [12]. Other examples of biomarkers from the blood used to distinguish between CD and UC are perinuclear antineutrophil cytoplasmic antibodies (pANCAs) and anti-Saccharomyces cerevisiae antibodies (ASCAs). Increased ASCAs levels are associated with CD, and higher levels of pANCAs with UC, respectively [5, 13].

Although IBD does not have a cure, there are several treatment options for IBD, which each have their own limitations [4, 10]. Even if the disease is quiescent for long periods, the symptoms can recur. There are different medical and surgical treatment options, yet the focus in treating IBD is on mucosal healing since this reduces hospitalization in the most cases [15]. The majority of patients with UC have a restorative procto-colectomy with ileal-pouch-anal-anastomosis (IPAA), meaning the removal of the ileum and rectum while preserving the anal sphincter [10]. However, this is not recommended for CD patients. In up to 90% of the cases of CD patients with IPAA, patients develop fistula or other complications [10]. Additionally, after restorative surgery CD patients frequently need a stoma.

The main characteristic of IBD's pathology is inflammation. In CD the inflammatory disease has elevated T-helper (Th) 1 and Th17 levels, while in UC the Th2 levels are increased [5]. The type of involved T-cells is also linked to the natural killer genotype, which is KIR2DL3/HLA-C1 in CD patients and KIR2DL5/2DS in UC patients [16]. In both cases this results in the secretion of proinflammatory cytokines. In CD the most abundant cytokines are interleukin (IL)-17, interferon-gamma (IFN-γ), and tumor necrosis factor-alpha (TNF-α), and in UC IL-5 and IL-13 are secreted. The pathways can be found in Figure 1 (A for CD and B for UC). The excessive production of the inflammatory cytokines produced by neutrophils and other leukocytes at the location of inflammation is the main pathophysiological process of IBD [5]. In CD types of natural killer cells produce IL-22 and IL-23-activated IFN-γ. These cytokines expand the CD4 T-cells and

then secrete TNF-α, IFN-γ, and IL-17 [16]. In UC natural killer-like T-cells secrete IL-13, which induces damage to the cells. Other types of natural killer cells stimulate Th1 secretion, causing a Th1/Th2 imbalance. This imbalance and the excessive IL-13 secretion cannot be controlled by the natural killer cells maintaining the TNF-α/IFN-γ response.

Additionally, inflammation is strongly connected to the production of reactive oxidative species (ROS) [17]. Commonly known ROS are superoxide anions (O_2^-), hydrogen peroxides (O_2H_2) and hydroxyl radicals ($\cdot OH$) [18]. Besides involvement in inflammation, ROS are active in cell signaling, -differentiation, -death, and growth regulation [17]. ROS are mainly produced in the mitochondria via electron transport. If ROS are not detoxified, they can disrupt normal cell functioning by damaging DNA and affecting gene regulation [19]. Additionally, excessive ROS can damage proteins and lipids, and negatively influence ion transport, intermediary metabolism, and mitochondrial function.
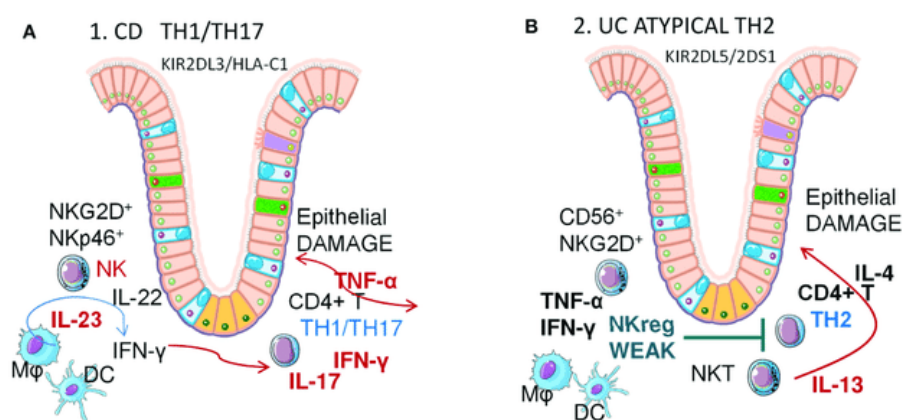
Figure 1: The pathway of CD (a) and UC (b), with Mϕ, macrophages; DC, dendritic cells; NK, natural killer cells; NKT, natural killer-like T cells (reprinted from [16]).

Oxidative stress is a phenomenon of an imbalance between the oxidants and antioxidants in a patient's cells and tissue, leading to imbalanced detoxification of ROS. Oxidative stress is related to aging and many diseases such as cardiovascular diseases and diabetes mellitus [18]. The production of ROS is a normal process in aerobic organisms and in a healthy situation should lead to homeostasis instead of creating oxidative stress. In patients with IBD, oxidative stress leads to damage of the mucosal layer and bacterial invasion, which enhances disease progression [17]. This phenomenon does not only occur in the inflamed cells, it is also present in the deeper layers of the intestinal wall [19]. Moreover, oxidative stress is also found in peripheral blood leukocytes of IBD patients [17]. ROS production by neutrophils and other immune cells occurs before the infiltration in the mucosal layer, which confirms the association of ROS production with disease development [17, 20]. Specifically for CD patients, the serum advanced oxidation protein concentration is higher compared to the healthy control group (5.02–15.15 and 0.75–2.70 μmol/g respectively) [21]. As the ROS/antioxidant imbalance explains pathophysiological aspects of IBD [20], it is a valuable biomarker.

1.1 Free thiol concentration as a biomarker

In healthcare, there is a growing focus on precision medicine. For IBD this means, besides better classification between UC and CD and determination of the optimal clinical pathway, there is an increased interest in finding effective and reliable biomarkers [22]. Biomarkers tests should be "non-invasive, sensitive, disease-specific, easy to perform, and cost-effective" [22]. Additionally, for ideal usage, biomarker assays should have rapid test outcomes, be standardizable and widely available, and have a high shelf-life [23]. Biomarkers are obtained from different body samples, yet blood biomarkers are not commonly used even though they are non-invasive, easy to obtain and relatively hard to contaminate [22]. Biomarkers are relevant in many different stages of the disease; early disease detection, diagnosis, classification, monitoring, and prediction of therapy progress.

According to the World Health Organization, a biomarker is "any substance, structure or process that can be measured in the body or its products and influence or predict the incidence of outcome or disease" [24]. Judging by this description, all oxidants and antioxidants and indirectly related species could be biomarkers for oxidative stress. However, measuring elements associated with oxidative stress is challenging. ROS have a short half-life time, and currently, the specificity and sensitivity of measuring techniques are relatively low [19]. As ROS are involved in many processes, they produce diverse by-products, which could function as biomarkers [25]. The downside is that these indirect measurements of by-products are not specific, meaning that for example cell membrane breakdown products could be caused by other biological processes. The direct measurement of antioxidants simulates the capacity to detoxify ROS, and are therefore promising biomarkers.

Cysteine thiols (R-SH), also called redox switches, are popular targets for ROS [19]. Redox switches have a crucial buffer effect on the homeostasis of oxidants and antioxidants. Free thiols are readily oxidized by ROS by forming disulfide linkages (R-S-S-R'). Albumin and other blood proteins take up 75% of the total amount of thiols [11]. The other 25% are low-molecular-weight thiols, such as cysteine. Healthy patients will have higher concentrations of free thiols. The serum levels of albumin-adjusted free thiols in CD and UC patients are 19.4 ± 3.1 and 17.8 ± 3.4 μmol/g, respectively, which are reduced as compared to the levels of healthy patients (21.1 ± 1.9 μmol/g) [11]. There are many studies that show the reduced free thiol levels for IBD patients [11, 20, 26].

In studies on other diseases related to oxidative stress, like cardiovascular disease, serum free thiols have been investigated as a possible biomarker [20]. In recent years, free thiols are thoroughly investigated as potential biomarkers and have shown strong results [11, 17, 19, 20, 21, 26]. A study by Bourgonje et al. specifically on the functioning of free thiols as a biomarker for IBD claims that quantifying the redox status is superior to the standard calprotectin biomarker [11]. In their study they concluded that compared to fecal calprotectin, serum free thiols better discriminate between mild disease activity and moderate or severe disease activity based on the Simplified Endoscopic Score for Crohn's disease for CD and the Mayo endoscopic subscore for UC (AUC 0.76 vs. 0.87, P < 0.05) [11]. Luceri et al. name several advantages of using serum free thiols as a biomarker for IBD, including ease of collection, scalability and low costs [21]. Furthermore, using

the free thiol concentration as a biomarker could contribute to better disease monitoring as oxidative stress is, among other things, connected to the development of fistulas. Neubauer et al. state that the reduced antioxidant capacity, thiol stress, also contributes to negative results of corticosteroids therapy [26]. Additionally, they agree with the possibility of plasma free thiol measurements to assess mucosal healing. The strong correlation between disease activity and reduced plasma/serum free thiols is promising for early diagnosis and easy disease monitoring, which has high clinical relevance [21].

1.2 Clinical relevance

Unfortunately, there are currently no disease-specific biomarkers for IBD, only general inflammation biomarkers [12]. Specific biomarkers may aid in new understandings of the pathophysiology of IBD and in providing patient-centered therapy. The current golden standard for measuring disease activity in IBD patients is the fecal biomarker calprotectin. However, all current diagnostic tests are limited in the prediction of long-term outcomes, which emphasizes the need for new biomarkers.

The goal of IBD treatment is to better the long-term quality of life for IBD patients while also examining the course of the disease [15]. Therapy looks into treating symptoms as well as mucosal healing. Sustained remission and reduced hospital admissions result from early IBD detection and a focus on mucosal healing. In addition to patient-centered care, a systematic literature review shows multiple studies on remote monitoring and telemedicine in IBD patients [15]. A study from California shows increased quality of life and reduced hospitalizations [27]. In this treat-to-target approach, the patients play a large role. A German study found that remote monitoring improves the patient's capacity for self-management [28]. Related to this, myIBDcoach, a self-management program, was created in the Netherlands [29]. With the help of this software outpatient visits and hospital admissions were reduced, nonetheless, emergency visits and quality of life remained unchanged.

Monitoring of disease activity and progression leans more towards the "treat-to-target" approach. CD has three stages in the disease progression [30]. Firstly, the penetration of the fecal contents into the intestinal wall. Disease progression will lead to a weak inflammatory response since the immune cells are impaired or diminished. In the last stage, an adaptive immune response including T-cells will try to take over the macrophages and neutrophils. By frequently monitoring and evaluating the disease progress, more specific therapy can be proposed, and increased intestinal damage and hospital admissions can be prevented [31]. As stated before, the treat-to-target standard is currently utilized by frequent endoscopic assessments [11, 32]. Next to the high costs and productivity loss, this procedure has a high patient burden since it is invasive and requires bowel preparation. Patient preferences are important to take into consideration when designing a clinical pathway, especially in monitoring the disease as IBD patients undergo many diagnostic tests.

If no healing of the mucosal layers is seen, the disease progression is worse [13]. For these patients, non-invasive biomarkers in addition to calprotectin are of high clinical value. Calprotectin can assess mucosal healing, yet has several disadvantages. In combi-

nation with other biomarkers it will be more specific and could assess whether invasive investigation is required.

Due to the known aspecific biomarkers for IBD, there has been a shift from single biomarkers for diagnosis and monitoring to the so-called biomarker panel approach [23]. In this approach, the aim was to combine different biomarkers to find biomarkers that are collectively specific for IBD. The shown relation between the reduced free thiol levels in IBD patients and disease activity has high clinical relevance since better monitoring of disease flare-ups could lead to better precision medicine.

1.3   Point-of-care testing

More advantages would arise if the measurement of redox switches could be point-of-care (POC) tested [33]. The costs are rising with the earlier stated increasing incidence of IBD patients in the Netherlands [7]. More patients lead to more hospitalizations, check-ups and therefore costs.

Point-of-care testing (POCT) is the performance of medical examinations near the bedside, which reduce waiting time and allow for faster responses [33]. Tests are more often performed and analyzed outside the laboratory by nurses. Best-known examples of POCT data encompass measurements such as body temperature, blood pressure, -saturation levels, and glucose concentrations in blood or urine. Additional instances consist of techniques like venipuncture, fingerpricks or urine samples. POCT improves the quality of healthcare, eliminates the need for patients to visit hospitals, and alleviates the burden on specialists responsible for conducting the tests.

The current biomarkers in assessing IBD are stool (calprotectin) and serum (CRP) markers, which are not tested POC. However, the topic of POCT of IBD biomarkers has been increasingly researched [34]. There are home kits available for fecal calprotectin, which are sent through mailing and assessed at the lab. The functioning of the Bühlmann home test kit, IB*Doc*®, is compared to the Bühlmann laboratory assay, and is proven to be a suitable alternative, which could provide more rapid responses to relapses [35]. Fingerprick dried blood spots of CRP are not yet on the market, but they show promising results for POCT of IBD [34]. Currently, the intestinal ultrasound is tested POC [34]. For POCT only a low-frequency abdominal for identification of the pathology and a high-frequency probe for better spatial resolution are required. A standard procedure is performed for assessment of the complete colon. The focus is on the identification of transmural inflammation by measuring the bowel wall thickness. The ultrasound predicts the UC Mayo score for active disease 85% and 94% sensitivity and specificity, respectively [34].

On top of these developments, electronic health (eHealth) has developed quickly over the last few years, in which digital technologies and communication tools are utilized in order to support and enhance healthcare delivery, patient care, and health management [34]. These developments add to the possibility of remote monitoring. Combining intestinal ultrasounds, eHealth and POCT of serum and stool biomarkers could improve treatment outcomes.

Lastly, POCT for IBD patients also includes drug monitoring. The anti-TNF therapy infliximab is currently monitored using enzyme linked immuno sorbent assay (ELISA), yet the POC rapid tests show similar evidence in infliximab serum concentration mea-

surements [36].

The interest in Lab-on-a-Chip (LoC) devices for the use of POCT has rapidly grown [37]. Microfluidic devices allow for the integration of miniaturization, portability and automation of multiple assays into one chip. Ideally, LoC devices have a sample-in-results-out principle. However, it is challenging to implement all assay steps into one single device. Other challenges lie in increasing the sensitivity, specificity and scalability of the device. Preferably the LoC is independently utilized by non-experts, requiring minimal user intervention besides extracting the body fluid of interest.

1.4   Research aim

The aim of this thesis was to develop a microfluidic device for POCT of free thiol levels in plasma. Also, the underlying goal was to design a LoC for biomarker detection of oxidative stress in IBD patients.

Already, the first steps were taken toward the design and fabrication of this microfluidic device [38]. Esmay Hammink concluded that absorbance measurements of plasma free thiols are most feasible [38]. The five steps of free thiol detection in the lab include plasma separation through centrifuging, plasma dilution with Tris buffer, a background measurement, mixing with DTNB, and absorbance measurement using the plate reader (Figure 2). Until now, there has been a focus on developing the last two steps on a chip. The plasma volumes of the current protocol utilizing DTNB for free thiol detection are lowered to 6 μL having an inter-coefficient of variation (CV) of 10.5%, to be suitable for microfluidic testing.

Trigger valves, having a height difference of 1100 or 1500 μm, were added to the design to enable flow stoppage and subsequent liquid release using capillary pressure, which had a 100% success rate of stopping the narrow channel liquid's flow for 10 minutes. With a path length of 2 mm the absorbance measurements still showed good results, so the height of the measuring reservoirs was set to this height.

In this thesis, optimizing the already taken steps in creating a microfluidic device for the detection of free thiols in plasma will be the focus. Additionally, it is aimed to incorporate the plasma separation from the fingerprick blood and plasma dilution to the device, to create a sample-in-answer-out LoC to enable at-home monitoring of IBD progression. For at-home absorbance measurements a portable spectrophotometer will be needed as well. Additional challenges will be in storing the different reagents on-chip and mixing them with the plasma, especially in the specific ratios. Classic microfluidic challenges are optimizing the capillary flow and pressure, and the functioning of the valves.

This study focused on patients with IBD. However, in the future, the developed microfluidic device could also be utilized for patients with cardiovascular disease, placental ischemia, or preeclampsia as these diseases are also related to oxidative stress [18, 39]. Additionally, multiple biomarkers could be implemented into the device to more accurately determine the disease dynamics of IBD as one biomarker is unable to show the complete reduction-oxidation status.
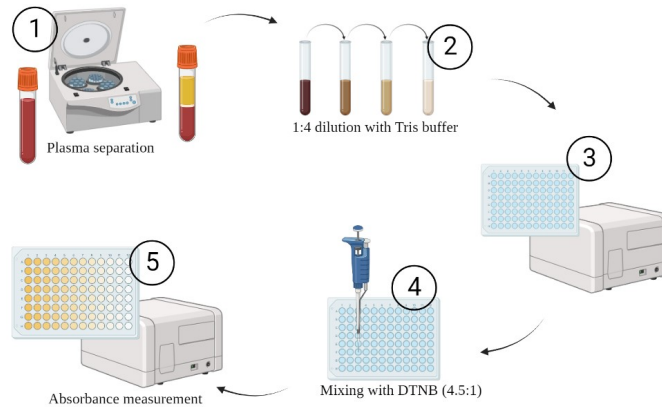
Figure 2: The five steps of free thiol detection in the lab: 1. plasma separation from whole blood using a centrifuge, 2. plasma dilution with 0.1 M Tris buffer, pH 8.2 (1:4 ratio), 3. a background absorbance measurement, 4. mixing diluted plasma with 1.9 mM DTNB (4.5:1 ratio) and 5. an absorbance measurement using a plate reader [created with BioRender].

1.5 Device requirements

All microfluidic devices should meet several requirements since they should be suitable and safe for clinical practice situations. After studying the theory of microfluidics and flow dynamics (Appendix A), a specification sheet is made with all the technical aspects the device should include. From extensive literature research (Appendix B), it is decided what should be included to create a sample-in-answer-out device. The development steps to obtain this device are listed. Thereafter, the additional requirements for the clinical practice are summed up.

1.5.1 Specification sheet

Based on the written theory overview (Appendix A), a specification sheet is made for the microfluidic necessities in the device (Figure 3). The microfluidic device that is aimed to develop, will mainly have laminar flow, and a low Reynolds number. The capillary pressure is dependent on the size of the microfluidic channel and the hydrophobic/hydrophilic characteristics of the used materials, and is estimated to be between -500 and 195 Pa [40]. It is expected to use trigger valves in the design to control the flow of the reagents. From previous work it is known that trigger valves work with a height difference of 1500 μm [38]. A capillary pump can be useful in the design to wick fluids into a certain direction. A passive capillary pump will be used to help wick the plasma sample. It is expected that in the testing phase active syringe pumps or pipetting will be used for injecting the reagents into the chip. Lastly, due to the laminar flow, the mixing process in the chip will need to be improved. The efficiency of the serpentine structure, with and without side wells, and the herringbone structure will be investigated.
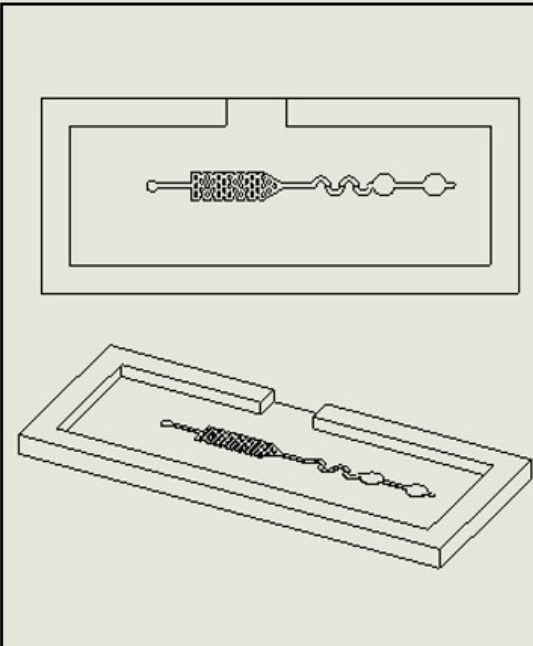
	Type	Specification
Capillary flow	Laminar flow	*Flow rate 0.01-1 mL/min*
Capillary pressure	Straight channel geometry	*ΔP = -500 – 195 Pa*
Microfluidic valve	Trigger valves	*Height difference 1500 μm*
Capillary pump	Passive capillary pump	*For BPS (Pipetting for buffer)*
Mixing technique	Passive mixing technique	*Serpentine (+ side wells) Herringbone*

Figure 3: Specification sheet of the microfluidic device that is aimed to develop.

1.5.2 Development steps

Based on the literature research it is concluded that the following steps need to be investigated and included into a microfluidic device (Appendix B):

1. **Sample collection**
A fingerprick will be performed using a lancet. Afterward, the Minivette® will be used to collect the blood sample from the finger and transfer the accurate volume to the LoC.

2. **Blood plasma separation**
To make a sample-in-answer-out microfluidic device it is preferred to add the fingerprick whole blood to the chip and acquire the blood plasma separation (BPS) on-chip. The passive separation method microdfiltration is chosen. Challenges will lie in the low obtained yield and difficulties in reproducibility. Still, this method is preferred over the centrifuge as this is a bulky, expensive machine, which is not suitable for POCT. The used membrane will be the Pall Vivid™ Plasma Separation Membrane type GR since this type has the largest recommended whole blood sample volume per squared centimeter.

3. **Addition of Tris buffer**
For the storage of the Tris buffer on-chip the preferred option is the use of blister pouches. They have a clear button-like mechanism and the direction of the flow after actuation is clear. Additionally, blister pouches have a low reagent loss and are commercially available. The pouches will be manually actuated and used to add the Tris buffer to the plasma to obtain the dilution.

17

4. **Optimization of the mixing process** ⟳

   After the addition of the Tris buffer to the plasma sample, the two liquids need to be mixed. Since diffusion in microfluidic devices with mainly laminar flow takes a long time, structures are added to the channel geometry to enhance mixing. Different structures can enhance mixing to reduce the reaction time from up to 12 hours to seconds [41]. The literature states many different options for the enhancement of turbulent flow in microfluidic devices. The herringbone structure and the serpentine structures with and without side wells will be compared in terms of the obtained mixing efficiency. Based on the comparison, the best suitable mixing structure will be added to the device.

5. **A control read-out** ☑

   In the standard protocol utilized by the UMCG, the absorbance of the plasma sample is measured before and after the addition of DTNB. The addition of a control read-out is important as in this way the test can also be considered invalid if the control measurement shows questionable results. An example is when a hemolytic or lipemic plasma sample is obtained which influences the absorbance measurement. The experimental absorbance measurement after the DTNB addition can with use of a control read-out be corrected for the deviation, or the test can be considered invalid after above a certain control read-out absorbnce value.

6. **Volume control** ⬭

   For the detection of the free thiols in plasma, it is essential that the standard assay ratios are very precise. The exact 1:4 dilution of plasma is important since the concentration is calculated based on this ratio. However, it is hypothesized that the ratio of the diluted plasma and DTNB is less important. It will be investigated whether an excess of DTNB will be sufficient to perform the experiment. Mechanically or pneumatically activated valves are interesting to control the flow. Different types of valves will be tested to find a suitable solution for the fixed volumes in the assay. Additionally, backflow or diffusion of DTNB to the control read-out reservoir should be prevented.

7. **Lyophilization of DTNB** ❄

   As concluded from the literature research, lyophilization of reagents on-chip is a very suitable manner to storage reagents as it increases stability and ease of transportation. Additionally, it allows for a sample-in-answer-out device since no reagents preparation or pipetting is required. DTNB is suited for lyophilization as it is not temperature sensitive and is also delivered in powdered form. Since the use of paper-based microfluidics has many advantages, including storing lyophilized reagents, the integration of filter paper in the device will be assessed.

8. **A portable spectrophotometer** ⬛

   There have been many studies on the use of smartphone for colorimetric assessments of color-change related assays. The possibility of a paper-based microfluidic device with a colorimetric assay will be investigated. Additionally, a portable spectrophotometer is aimed to develop and compare to the standard plate reader. Both the use of a smartphone camera and a LED will be investigated for the measurements as the portability of the device optimizes the use for POCT.

A schematic overview of the 8 different steps can be seen in Figure 4. These steps will first be developed separately for optimization. All development steps will preferably be integrated into a single device to obtain a sample-in-answer-out lab-on-a-chip. The focus will be on the optimization of the different steps, before starting the integration phase.
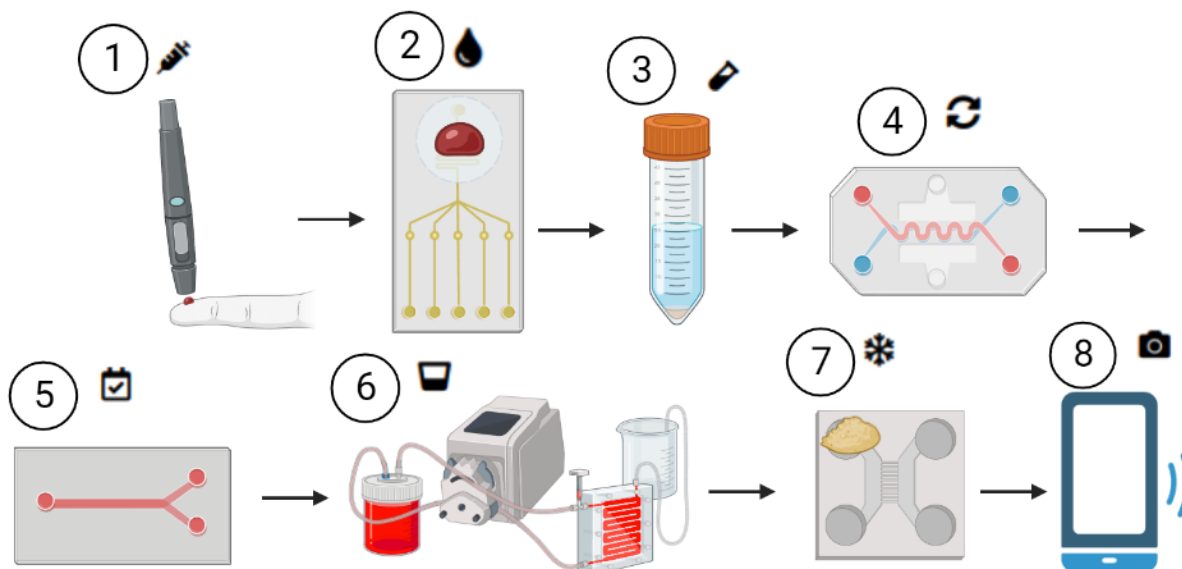
Figure 4: A schematic overview of the 8 different steps of the to-be-developed assay on chip: 1. sample collection, 2. plasma separation, 3. the addition of the Tris buffer, 4. mixing of the sample and buffer, 5. the control read-out, 6. fixed volumes of the involved liquids, 7. lyophilization of the reagent DTNB, and 8. an at-home absorbance read-out device.

1.5.3 Practical requirements

The to-be-developed device should meet several requirements for utilization in the practical setting. Since it will be used by for POCT by either a medical specialist or layman performing a self-test. Safety issues should also be taken into consideration.

1. The device can measure the free thiol concentration in the physiological range of 100-500 μM.

2. The device should have a monolithic approach.

3. The device should have a lower limit of quantification of 50 μ.

4. The absorbance measurements should only detect free thiols in plasma samples and have no interference from other substances for high specificity.

5. The device can obtain plasma from fingerprick whole blood samples with a purity of >99%.

6. The accuracy of the test should be >95%

7. The test should have a high precision (CV <5%)

8. The device should have a control read-out to check validity of the test.

9. The complete test time does not exceed 30 minutes.

10. The measurement accuracy and uncertainty should be clear and not affect clinical applications [2].

11. It should be a robust device having a whole blood sample input and only making use of buttons for clear instruction.

12. The device should be made of only low-cost materials.

13. The test should be user-friendly, so the patient or caregiver should be able to prepare the reagents, collect the sample, perform the test, and read out the results with simple included instructions [42].

14. The results should be quantitative and presented in a manner that they are easily understood [42].

15. Since the test is designed for disease monitoring it should be communicated and clear that action based on the test results or changes in treatment should always be in consultation with clinicians [42].

16. Due to hygienic reasons, it should be a single-use device.

17. The packaging of the device should be sterile, which should be clearly indicated on the packaging including sterilization method, and month and year of fabrication [42].

18. The clinical relevance study performance by laymen and in relevance settings should be in compliance with the ISO 15189:2022 for POCT [2].

1.6 Reader's guide

This thesis features many different aspects. To understand the fundamentals of microfluidic devices, the theory of capillary flow and pressure, microfluidic valves, mixers, and pumps has been investigated (Appendix A). From this overview follow the specification sheet for the developed microfluidic device (Figure 3). Several studies have investigated the use of LoC devices and to accurately implement the device requirements, literature research is performed (Appendix B). Based on this literature research, the development steps of the microfluidic device for POCT of free thiol levels in plasma have been established. The materials and methods of these different development steps can be read in the next Chapter, in order of action for the different steps (Chapter 2). The sample collection step is not covered. At the end of the chapter, the first step towards integration of the distinct steps can be read. In the same order, the results and discussion points can be read in Chapter 3. Based on the discussed findings a conclusion in drawn (Chapter 4), which is followed by the limitations of the study and future research recommendations (Chapter 5). The report is closed with the acknowledgments.

2 Materials and methodology

In order to create a sample-in-answer-out microfluidic device for the detection of plasma free thiols in IBD patients multiple steps are developed for the creation of the final design. In this chapter, the materials and methodology of the performed experiments are discussed. Through absorption measurements, the concentration of free thiols in diluted plasma is determined due to colorization by DTNB. The blood plasma separation is realized using a Pall plasma membrane. The Tris buffer is stored on-chip in a blister pouch, which can be opened via manual actuation. DTNB is lyophilized on the chip and the mixing with the diluted plasma is optimized using different structures. An experimental and control read-out reservoir are designed on a LoC. To prevent flow from the experimental read-out to the control read-out, both mechanical and pneumatic valves are tested. Lastly, a portable read-out device with a LED and photodiode is used to measure the absorbance of the free thiols.

2.1 Assumptions based on previously performed experiments

The results from previous work have been included in this study [38]. Experiments were performed on PBS spiked with L-Cysteine to investigate if lower sample volumes were possible. 4, 6 and 10 μL plasma samples were used, leading to 16, 24 or 40 μL total volume after dilution with 0.1M Tris buffer. 6 μL plasma samples showed the best results, and will be worked with in this thesis.
The path length, and thus height of the read out reservoirs, was calculated at 3.06 mm for the 6 μL samples. However, 2 mm high reservoirs also gave promising results (<5% Intra-CV). To miniaturize the dimensions of the chip, a 2 mm path length will be used. Based on the previous trigger valve characterization, height difference 1100 and 1500 μm had a 100% success rate. Only after reaching the filter paper in the outlet of the device, emptying of the inlet of the narrow channel occurred. Moreover, better mixing was obtained for lower pipetting velocities. Additionally, the micromilling failed for serpentine structure due to too small dimensions. So, larger bends will be designed to optimize mixing.

2.2 Materials

The materials used for the chip fabrication are PMMA (ERIKS kunststoffen, Ede) and PDMS (Sylgard 184, Dow Corning, Midland, Michigan). The biopsy puncher used to create the inlets and outlets are purchased from Harris Uni-core. The food dye used in the experiments (Jo-LA) was diluted 1:10 with water. The Tris buffer (Tris(hydroxymethyl) aminomethane) was purchased from Merck (KGaA, Darmstadt, Germany) and the L-Cysteine was purchased from Sigma-Aldrich ((R)-2-Amino-3-mercaptopropionic acid, 97%, GmbH, Steinheim, Germany). The materials for the phosphate buffer (K_2HPO_4 and KH_2PO_4, Merck, KGaA, Darmstadt, Germany) and DTNB (> 98%, Sigma-Aldrich, GmbH, Steinheim, Germany) were kindly gifted by the UMCG. The used 96 well plates are from Costar and the 384 well plates are from Nunc. The Experimental Centre of the Technical Medicine Centre (Univeristy of Twente) provided the human whole blood (3.2% sodium citrate, Vacuette, Greiner Bio-One). The blood collection procedure is

approved by METC Twente, and the volunteers gave informed consent (Declaration of Helsinki). The used machinery is mentioned in the specific sections of the methodology, as well as additional materials for specific purposes of the designed LoCs.

2.3 Chip Designs

Different chip designs are developed and tested in order to obtain a fully functional microfluidic device. The walkthrough of the different chip designs during the project can be found in Appendix C.

2.3.1 Mold fabrication

A computer-aided design (CAD) software is used for all different chip designs (SolidWorks, 2021). The add-on HSM Works is used to generate a toolpath in a .simpl file, which is compatible with the micromilling software (Datron Next,Mühltal, Germany). The toolpaths are loaded into the software and the micromilling machine mills the design (Datron NEO, Mühltal, Germany). The used material for micromilling is PMMA with 4 mm height (8 mm for the two read-out design, Section 2.8). The spindle speed is set to 20000 rpm and the tolerance to 0.001 mm. The more specific settings are shown in Appendix D. After micromilling, the designs are checked under the microscope (Leica DM 6000M, camera Leica DMC 2900).

2.3.2 Chip fabrication

The PDMS elastomer base and curing agent were mixed in a 10:1 ratio for 30 seconds at high speed. The mixture is degassed in the desiccator for at least 20 minutes. The mixture is poured on the created PMMA mold and placed in the oven for two hours at 60 °C. After curing the PDMS, the chips are peeled off the mold and the in- and outlets are punched with a 2.5 mm puncher (1 mm puncher for the volume control chips, Section 2.9). A small hole in the wall of the designs is made to remove the PDMS more easily from the mold. The PDMS chips are plasma bonded on a microscopic glass slide (CUTE, Femto Science, Besançon, France).

2.4 Plate reader-compatible chip holder

A 384 wells plate was used to create the holder for the chips. The partition between the wells of rows F until K and columns 5 until 21 were removed to precisely fit a microscopic glass slide. Additionally, well E5, E21, L5, and L21 were removed to be able to place the glass slide with tweezers.

An experiment comparing the developed chip holder to the original 384 wells plate is performed to validate the functioning of the developed chip holder. The plate reader (SpectraMax ID3, Molecular Devices, San Jose) is run at 412 and 630 nm for the chip holder only containing a microscopic glass slide, selecting the 384 wells plate settings. The mean absorbance value and the standard deviation of the removed wells is compared to the values of the same cells in an original 384 wells plate.

The developed plate reader-compatible chip holder is used for all further experiments. In the plate reader software (SoftMax Pro 7.0, Molecular Devices, San Jose) the 384 plate

reader with clear bottom settings are used, measuring the absorbance at 412 nm and 630 nm. The distance between the wells was measured to be 4.5 mm, so this distance was used in the Solidworks designs.

2.5   Blood plasma separation   🌢

At first, it was investigated whether both plasma and serum were usable samples. The anticoagulant citrate in the donor blood prevents the blood from coagulation and it was hypothesized that this blood will therefore easier flow through the microfluidic channels. To counteract the anticoagulation, a re-calcification buffer (HEPES + 63.2 mM $CaCl_2$ + 31.6 mM $MgCl_2$) was added to the blood, which led to coagulation of the blood (Figure 5(a)). Both types of samples, shown in Figure 5(a), were added to a microfluidic chip and the flow was investigated under a microscope (EVOS m5000, Invitrogen, Thermo Fisher Scientific, Massachusetts, USA). In all blood experiments the provided whole blood samples were used within 4 hours after being drawn and in the following experiments whole blood samples without re-calcification buffer were used.

The design of the blood plasma separation device was inspired by Emma Moonen [43]. The design has a capillary pump, on which the membrane is placed to help wick the plasma from the membrane (Figure 5(b)). Additionally, the design has a read-out reservoir that can be used to look at the obtained sample under the microscope. Different heights of the design are tested: 0.3 and 0.15 mm. At the end of the channel, an air vent is created by leaving a hole in the sealing tape. An inlet is created before the blood sample reservoir to pipette the Tris buffer into the channel and help flush the obtained plasma sample into the reservoir.

(a)   *(b)*
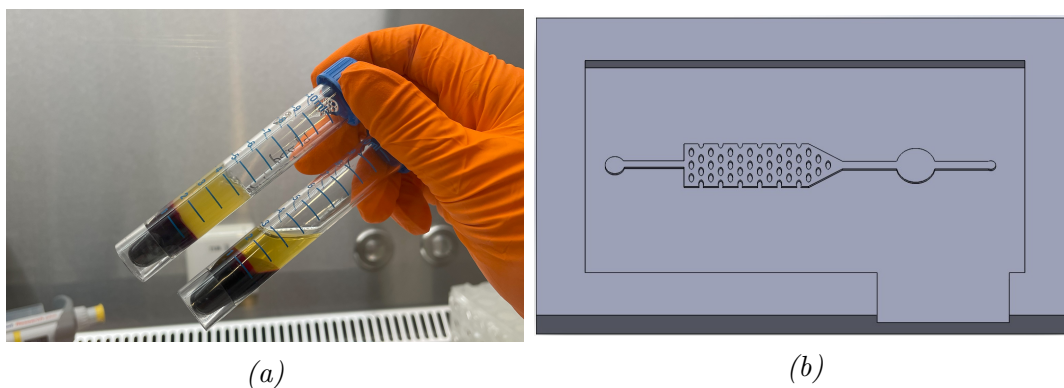
Figure 5: A test tube with anticoagulant citrate (bottom) and a test tube with the antagonist re-calcification buffer added (top) (a) and the Solidworks design of the BPS device (b).

The different materials and parts of the chip design can be seen in Figure 6(a). Initially, two different materials were used for the chip base; PMMA and PDMS. A positive shape is milled from the PMMA, for the chips with a PMMA base. Milling is done according to the steps in Section 2.3.1. For the other BPS chips, a mold of the negative shape is made of PMMA, and the positive shape is created by pouring PDMS over the mold (as in Section 2.3.2). In both cases, the base had to be sealed. Different types of sealing were

tested: PDMS bonding, adhesive tape (ARcare®), or PCR well plate sealing (Bio-rad, Hercules, USA)). Two varying dimensions of the opening for for the plasma passage in the seal were examined: 1.4x0.9 cm^2 and 1.2x0.7 cm^2. This opening and the in- and outlet were cut using the Cricut (Cricut, Inc., South Jordan).

The asymmetric membrane (Vivid^{TM} Plasma Separation Membrane GR, Pall, USA) was placed on top of the sealing with the dull side up (1.4x0.9 cm^2). A top well was sealed on top of the membrane with adhesive tape, to create a fluid-tight seal. The top well had the dimensions 2x1.5 cm^2 with a small indent of 0.2 mm high for the placement of the membrane and a 1x0.5 cm^2 hole at the top for adding the blood sample. The height of the blood sample inlet was 2 mm. The small air vent in the sealing was used as an outlet to be able to pipette the obtained plasma out of the device for validation. The completely assembled chip can be seen in Figure 6(b). 100 μL whole blood was pipetted into the top well, on top of the membrane. After 20 minutes, it was investigated whether blood plasma was obtained at the bottom of the chip. The pillars in the collecting reservoir are to increase capillary force and wick the plasma from the membrane.

The plasma purity was validated by investigating the obtained plasma under the microscope for cells in the read-out reservoir (EVOS m5000, Invitrogen, Thermo Fisher Scientific, Massachusetts, USA). Additionally, plasma was pipetted out of the chip and a cell counter was used to determine whether cells were still present in the plasma (LUNA, BioCat GmbH, Heidelberg, Germany). The cell count of control plasma samples, obtained through sedimentation, were used for comparison.

(a)   *(b)*
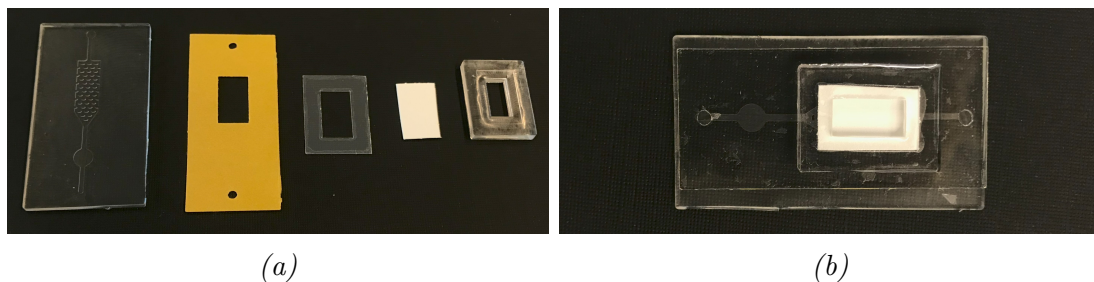
Figure 6: The separate parts of the blood plasma separation chip with from left to right: the PDMS base, PCR well plate sealing tape, adhesive tape, membrane, and top well (a) and the assembled chip (b).

2.6 On-chip reagent storage

To test the principle of the blister pouches eye lenses are used. The later discussed two read-out design is used for the test (Section 2.8). The chip is made according to standard protocol (Section 2.3.2). Additionally, a blunt needle is cut and glued into the inlet using ultraviolet curing (NOA 83H, Norland Products, Cranbury). It was made sure that the needle protruded 1 mm from the top of the chip. Blue food coloring was pipetted into the trigger valve. Afterward, an eye lens (-1.25 soft day lens, Kruidvat, Renswoude) was pushed onto the needle and it was investigated whether blue food coloring reached the read-out reservoir.

Figure 7: The set-up of the experiment using an eye lens to mimic the blister pouch with a blunt needle glued in the inlet.

2.6.1 Two reagents chips

The standard protocol includes two steps in which two reagents need to be mixed (Appendix E). Firstly, the plasma needs to be diluted 4 times with Tris buffer, thereafter the diluted plasma needs to be mixed 4.5:1 with DTNB. A design containing two reservoirs is made. These reservoirs can store the two reagents that need to be mixed. The focus was on the mixing of plasma and the Tris buffer since the goal was to lyophilize DTNB on-chip. Four variations of the two reagent chips are designed (Figure 8).

By placing the reservoirs directly opposite from each other, the capillary pressure balance was disrupted. By pipetting a small volume of activation fluid in the inlet, the two reservoirs were aimed to be emptied by breaking the meniscus of the reagents at the end of the reservoir. Since the pressure is higher at the side of the reservoirs, it was aimed to let the liquid easily flow to the read-out reservoir after actuation. The pressure barrier of the trigger valves is -168 Pa (Appendix F.1). The reservoirs were 2 mm high, so when diluted plasma was stored in the larger reservoir and DTNB in the smaller reservoir, the background measurement could be performed in the larger reservoir before actuation. The effect of the width of the channel immediately after the inlet was investigated by making a narrowing after the inlet for the designs in Figure 8(a),(b), and connecting the inlet to the channel in the designs in Figure 8(c),(d). The calculations of the retention burst valves of the reservoirs can be found in Appendix F.2. For space savings it was investigated whether a channel at an angle of 90° (Figure 8(b),(c)) gave the same results as a straight channel (Figure 8(a),(d)).

To quantify the functioning of the four different chip designs, their success rate is determined. 12 μL blue food coloring is pipetted into the smaller reservoir, and 36 μL yellow food coloring is pipetted into the bigger reservoir (Figure 8). The reservoirs are designed to fit 6 and 18 μL to mimic the protocol's plasma-to-Tris buffer ratio. In previous work, it was discovered that 6 μL plasma samples are large enough to perform absorbance measurements for accurate determination of the free thiol concentration. However, in this experiment double the volume was added to the reservoirs to increase the hydrostatic pressure. To activate the device 20 μL water was pipetted into the inlet. The test was considered successful if the two food colorings mixed creating a green color. The homogeneity of the obtained green was not measured since a separate experiment is performed for the optimization of the mixing process. Another requirement was the green food coloring reaching the read-out reservoir. The success rate of the meniscus forma-

tion before actuation and the success rate of green food coloring reaching the reservoir were assessed separately. The test was performed for all four designs (n=5). Additionally, the limitations were observed to take into consideration in further microfluidic chip development.
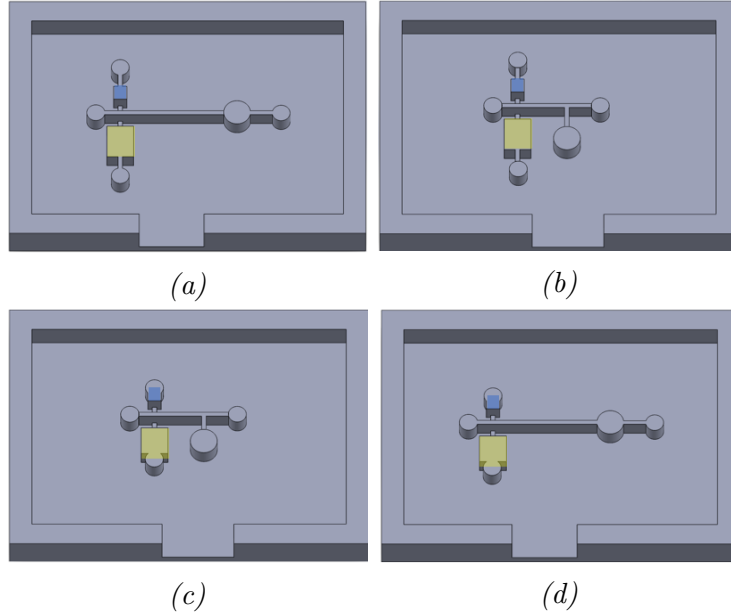
Figure 8: The four different designs for two reagents on-chip with differences in width after inlet: narrowing after the inlet (a+b) vs. inlet connected to channel (c+d), and differences in channel direction: straight (a+d) vs. at 90° (b+c)

2.7 Optimizing the mixing process

Different designs are made to increase the mixing efficiency. From the theory, it was concluded that a serpentine structure, especially with side wells, or a herringbone structure enhances turbulent flow and therefore mixing efficiency [41, 44]. A positive herringbone design is chosen for the best mixing efficiency [45]. The serpentine mixer with and without side wells and the herringbone structure are integrated into the best-performing two-reagent design (Figure 9). The details of the design can be found in Appendix C.4. A comparison of the mixing efficiency results of the three designs is made and, the results are also compared to the initial straight channel design (Figure 8(d)). For each chip, 30 μL blue food dye is pipetted into the larger reservoir and 12 μL water is pipetted into the smaller reservoir (n=3). To activate the device 25 μL water is pipetted into the inlet. Pictures are taken under the microscope at 5 time points (t=0, 5, 10, 15, and 20 min) (Olympus SZX10, camera Nikon DS-Fi3).
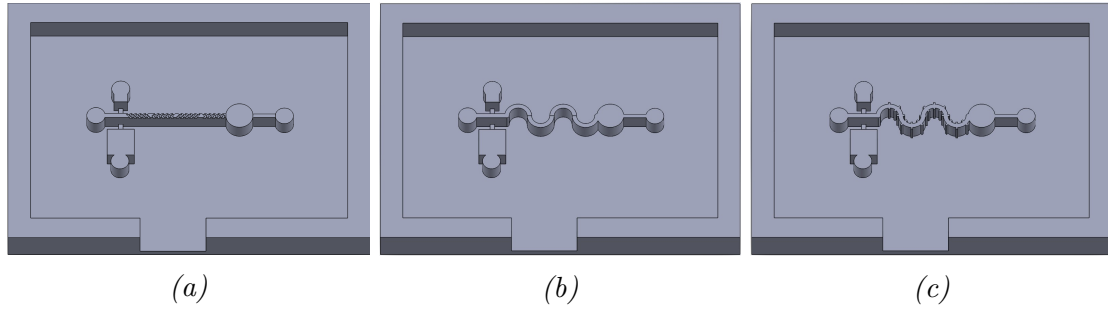
Figure 9: The three different designs for enhancing the mixing process: a herring-bone structure (a), a serpentine structure (b), and a serpentine structure with side wells (c).

2.7.1 Quantification mixing process

The cross-section of the channel is analyzed at three locations at t=0; right after the trigger valve, halfway, and right before the reservoir. It is hypothesized that at the start of the channel, the water and food dye will have laminar flow and do not mix. Therefore, the mixing concentration over the cross-section (80 pixels) is expected to look like a step function (Figure 10). It is hypothesized that over the length of the channel, the mixing will increase and the step function will transform into a horizontal line. The mean concentration at the different cross-sections along the channel is plotted over the distance of the cross-section. The intensity is related to the concentration and the concentration values are normalized using the intensity in the blue food dye reservoir as the highest possible concentration. The highest pixel intensity is set as the lowest concentration.
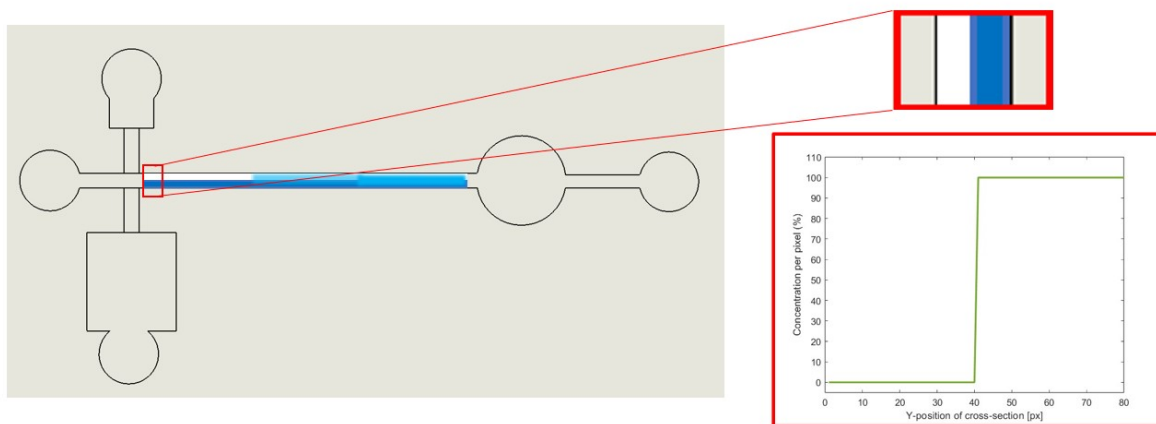
Figure 10

Next to the normalized values of the concentration based on the intensity of the image, the intensity of the pixels is also plotted over the distance. Both analyses are done in Matlab, by taking selecting the pixels, taking the gray values of the cross-sections, and plotting over the Y-position (Figure 11). The complete Matlab script can be found in Appendix G.1 and G.2.

27
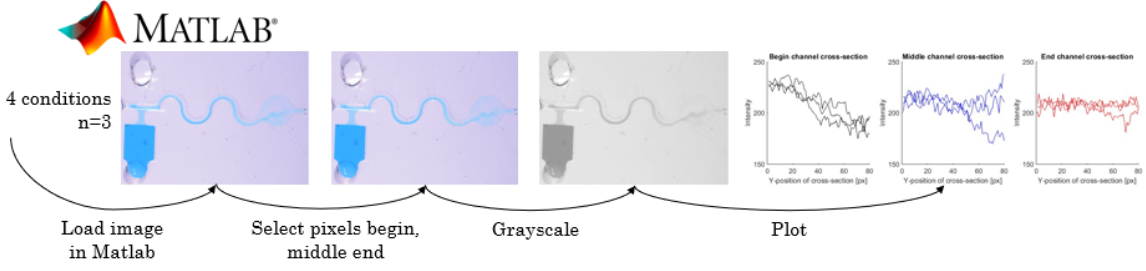
Figure 11: Schematic overview of the quantification of the mixing process method in Matlab

Additionally, mixing efficiency over time is analyzed. At the end of the channel, pixels are selected in all images of the different time points (t=0, 5, 10, 15, and 20 min) and a graph is created of the mixing efficiency over the different time points. To quantify the mixing efficiency, equation 1 is used [46, 47]:

$$\eta = \left(1 - \frac{\sigma_{mix}}{\sigma^0}\right) \cdot 100\% = \left(1 - \frac{\sqrt{\frac{1}{N}\sum_{i=1}^{N}(c_i - \bar{c})^2}}{\sqrt{\frac{1}{N}\sum_{i=1}^{N}(c_0 - \bar{c})^2}}\right) \cdot 100\% \tag{1}$$

where, σ_{mix} is the standard deviation, σ^0 represents 0% mixing, N is the number of measurement points, c_i the measured concentration across the channel, $\bar{c}$ is the average mixed concentration, c_0 is the concentration at t=0,. Instead of concentration, intensity is used. The Matlab scripts of the mixing efficiency over time can be found in Appendix G.3.

2.8 Two read-out design

A design has been made in which an additional read-out reservoir has been added (Figure 12(a)). In this control read-out reservoir the absorbance before the addition of DTNB can be measured. A trigger valve is designed to contain DTNB, which can be activated by the addition of the diluted plasma in the inlet. An outlet is created as air vent for the device, in which filter paper was added to empty the reservoir.

2.8.1 Flow characterization

An experiment is performed in which the flow of the DTNB is characterized. The diffusion time for the two read-out design is expected to be 1.33 hours (Appendix H). Additionally, in this design, the hydrostatic pressure in theory is -19.62 Pa, and the capillary pressure -222.8 Pa. The Reynolds number decreased with increasing injection time, so the water is pipetted in the inlet quickly. Still, in the microfluidic device the Reynolds number is relatively low. Due to the low Reynolds number, it is expected to have laminar flow in the microfluidic channels. To validate this assumption a fluorescent dye is used. Fluorescent dyes have been popular for characterization purposes for a long time [48]. Fluorescent dyes can also be utilized to characterize the liquid flow in microfluidic devices. The system's fluid dynamics can be determined without flow disturbance.

28

For the experiment FITC (fluorescein-5-isothiocyanate), which gives a green fluorescent signal, is used. Firstly, 1 mg FITC is dissolved in 2 mL di-sodium hydrogen phosphate solution. Afterwards, 8.6 μL of the solution is pipetted into the trigger valve (Figure 12(b)). Water simulating the diluted plasma is pipetted into the inlet of the main channel. The first 5 minutes after pipetting the flow is analyzed using a microscope (EVOS m5000, Invitrogen, Thermo Fisher Scientific, Massachusetts, USA).

FITC is used since it is similar to DTNB in term of size and weight. DTNB ($C_{14}H_8N_2O_8S_2$) has a molecular weight of 396.4 g/mole and an atomic mass of 395.972 Dalton [49]. FITC ($C_{21}H_{11}NO_5S$) has a molecular weight and an atomic mass of 389.4 g/mole and 389.036 Dalton, respectively [50].

(a)   (b)
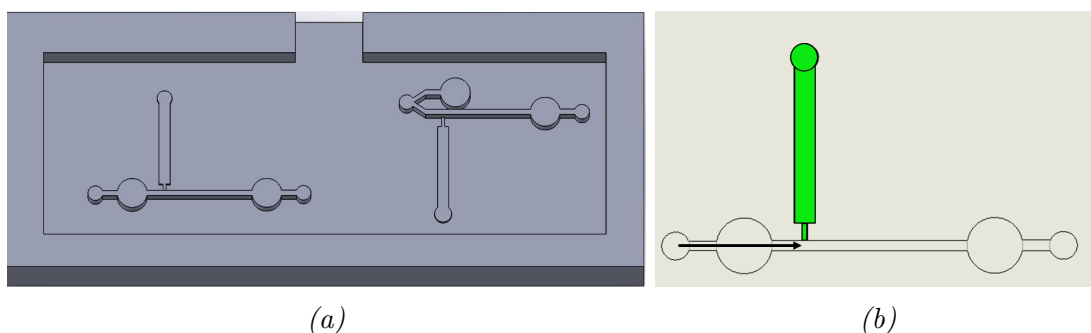
Figure 12: The SolidWorks design of the two read-out chip (a) and the direction of flow indicated by an arrow and the trigger valve labeled in green for the FITC (b).

2.9   Volume control

Precise volumes and volume control are important in microfluidic devices. In this study the 1:4 ratio of plasma and Tris buffer, and the prevention of backflow of DTNB, are aimed to be achieved using valves. A plastic mechanically operated valve was made, which fits the microfluidic device between the bottom and pressure pillar. By turning the cap, the pillar was lowered and pressure was applied to the microfluidic channel through the mechanical actuation. After pipetting blue food coloring into the inlet, it was visually determined whether the valve closed the microfluidic channel.
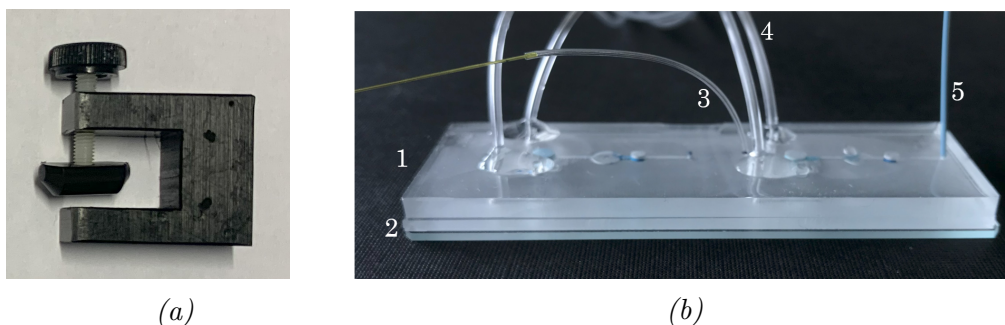
Figure 13: The design of the mechanically actuated G-clamp valve and the assembled Quake-valve design with 1. the top PDMS flow layer, 2. the bottom PDMS control layer, 3. the inlet tubing, 4. the connecting tubing to the pressure pump, 5. the tubing going to the waste vial.

After experimenting with different mechanically and pneumatically activated valves (Appendix C.5), a pneumatic valve adapted from Bossink et al. [47] was used to obtain the precise volumes for the plasma:Tris buffer ratio in the chip (Figure 13(b)). It is a double-layered PDMS chip with a bottom-up Quake-valve principle. The control layer is filled with air to create a pressure closing the perpendicular channel above. The reservoir near the inlet has the exact needed volume (18 μL) to mix with the 6 μL plasma samples. The two PDMS layers were plasma bonded (CUTE, Femto Science, Besançon, France) and the connection tubing is glued into the inlets using ultraviolet curing (NOA 83H, Norland Products, Cranbury).

2.9.1 Valve characterization

For the characterization of the pneumatic valve different set-ups are used (Figure 14). The different elements of the set-up are labeled with a number. For the first experiment, a 100 μL syringe (Microlab, Hamilton Company) containing blue food coloring is connected to the syringe pump (Nemesys S, Cetoni GmbH). The syringe is connected to capillary tubing (inner diameter (ID) 100 μm and outer diameter 360 μm), which is connected to tubing (ID 400 μm) inserted in the inlet of the chip (Figure 15, set-up 7a). The Nemesys software (neMESYS, Cetoni GmbH) is used to set the flow rate to 10 μL/min to check for leakage. After filling all the channels and reservoirs in the chip with food coloring, the flow rate was set to zero. Then, the pressure pump (Fluigent, Le Kremlin-Bicêtre) and the software (oxyGEN, Fluigent, Le Kremlin-Bicêtre) were used to increase the pressure of the control layer in steps of 100 mbar (0-1600 mbar). The microscope is used to visually assess whether the pneumatic valve closes the capillary flow channel above, and at which pressure (Nikon Eclipse TE2000-U, camera Nikon DS-Ri1).

The set-up with the flow sensor (Flow board and flow unit S, Fluigent, Le Kremlin-Bicêtre) is used to investigate with which pressure the valve opens again (Figure 15, set-up 7b). The pressure pump (Fluigent, Le Kremlin-Bicêtre) is connected to a vial containing blue food coloring. The vial has a short needle in which air is pumped by the pressure pump and a longer needle the dye flows into. The tubing is connected the flow unit, which is connected to a flow board that indicates the flow rate in the oxyGEN software. At first, the relation between the applied pressure difference and the obtained

flow rate is investigated. Afterward, two experiments are performed. In one experiment the pressure difference is set to 30 mbar, which gave a flow rate of 137 μL/min with a control layer pressure of 0 mbar. The applied pressure difference was set relatively high since it was calculated that the hydraulic resistance in the channel was also high (Appendix I). The positive pressure applied to the control layer is increased (500-1700 mbar) with steps of 100 mbar, and the flow rate is analyzed for each pressure.

In another experiment, the applied pressure to the control layer was set at 1500 mbar. The applied pressure difference between the inlet and outlet of the chip is increased by increasing the pressure of the pressure pump with steps of 2 mbar (0-40 mbar). The flow rate is analyzed for each applied pressure difference.
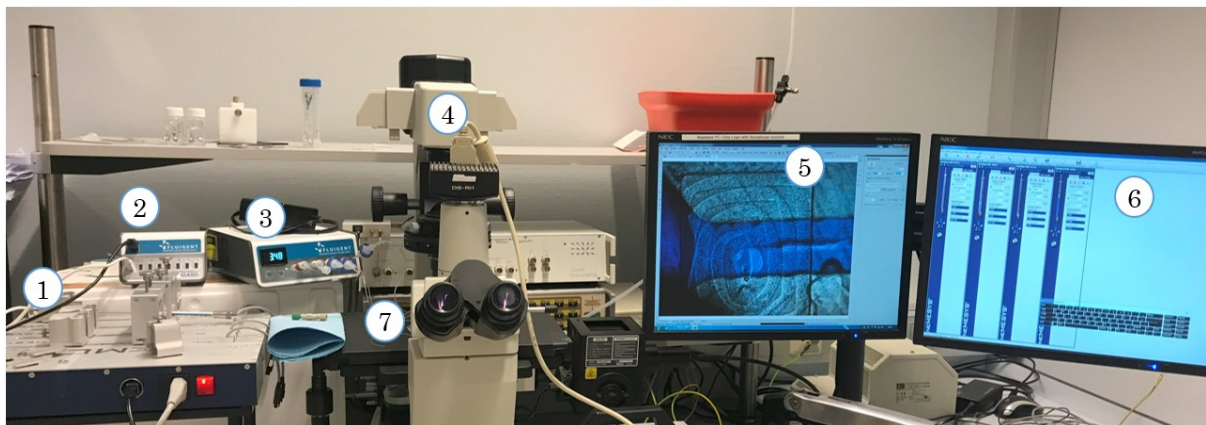
Figure 14: An overview of the set-up used for the pneumatic valve characterization, with a syringe pump (1), flow-rate sensor (2), pressure pump (3), microscope (4), microscope imaging software (5), Nemesys software (6), and testing area (7).
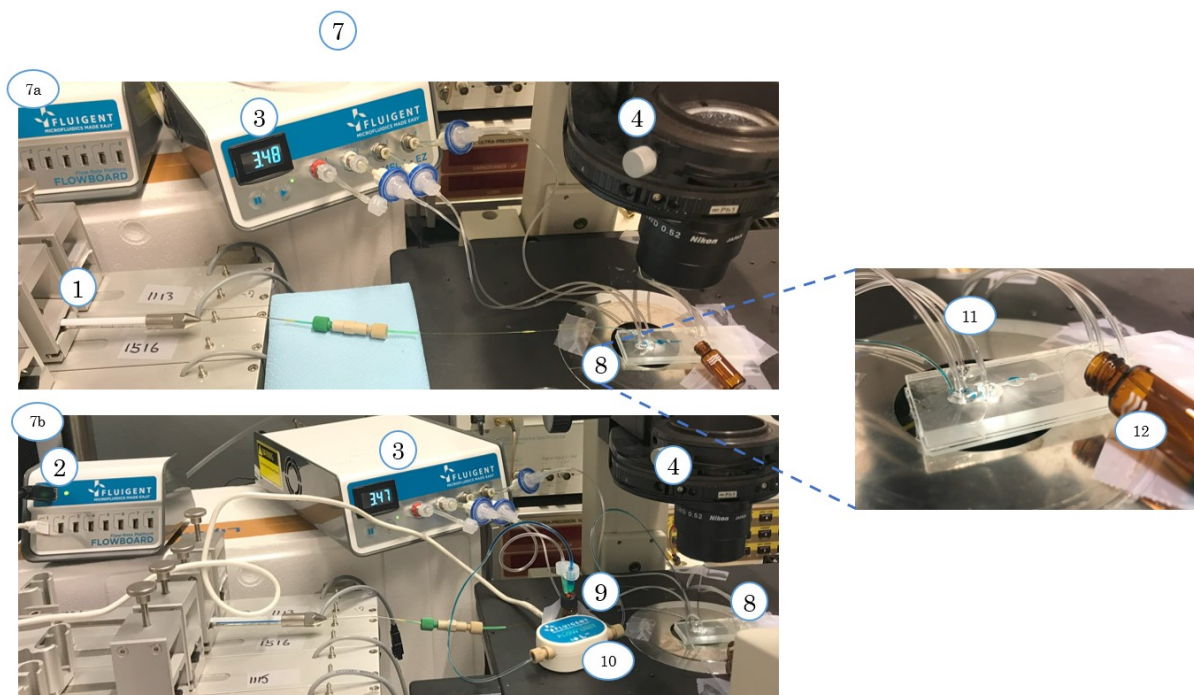
Figure 15: An zoomed overview of the testing area (7) of the set-up used for the pneumatic valve characterization, with a syringe pump (1), flow-rate sensor (2), pressure pump (3), microscope (4), the microfluidic device (8), vial containing food coloring (9), flow unit (10), the tubing connected to the pressure pump and inlet tubing (11), waste reservoir (12).

2.10   Calibration curve L-Cysteine on-chip

For POCT it is desired that the analysis of standards could be excluded from the test. Therefore, it is important that the calibration curve is very stable and can be used for the determination of the free thiol concentration in the plasma samples of patients. It is investigated whether the standards used to make a calibration curve show a linear relationship when tested on-chip, and the results are compared to the absorbance of the standards measured in a 96-well plate. In the well plate 90 μL of 15.625 to 1000 μM L-Cysteine in 0.1M Tris, pH8.2 is pipetted in triplo. The absorption is measured before and after the addition of 20 μL 1.9 mM DTNB, pH 7. On-chip, half the volumes are pipetted into the eight inlets (Figure 16). A small air vent was created in the read-out reservoir. A calibration curve is created for both situations.

To investigate the stability of the calibration curve, the standards are measured in three different situations. At t=0 and t=1, with 21 days in between, the measurements are performed according to the standard protocol with freshly prepared solutions. Additionally, the absorbance of the standards prepared at t=1 with the DTNB solution prepared at t=0 is analyzed. Lastly, the absorbance values are compared to the theoretically calculated absorbance values. The calculation of the theoretical absorbance values can be seen in Appendix J.
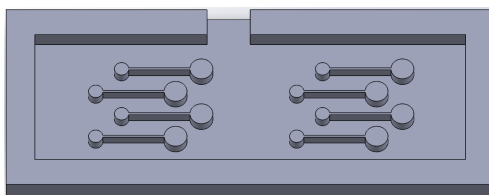
Figure 16: The chip design used for the measurement of the 8 standard concentrations (0-1000 μM).

2.11   Lyophilization of DTNB   ❄

To establish whether DTNB can be freeze-dried on-chip, an experiment is performed. The standards are prepared according to the free thiol ELISA protocol described in Appendix E. DTNB is lyophilized both in the microfluidic device and in an Eppendorf (n=10). The two read-outs microfluidic device was used (Section 2.8). 20 μL DTNB is pipetted into the Eppendorf or microfluidic device outlet. The DTNB in the Eppendorfs was frozen by putting the Eppendorfs in liquid nitrogen with the lid open. The DTNB in the devices was frozen by keeping the microfluidic device in a -80°C freezer overnight. Afterward, the Eppendorfs and devices were placed in a vacuum chamber overnight in the dark. The main drying program was run at -55 °C and 1 mbar.

 After the freeze-drying process, 90 μL 1 mM L-Cysteine in 0.1 M Tris (pH 8.2) was pipetted into the Eppendorfs and device. The mixture of the Eppendorfs was transferred to a 96 wells plate. Standards were prepared to conpare the results of the freeze-dried DTNB to the standard protocol utilizing liquid DTNB. Since no background measurements could be obtained in the microfluidic devices, the background measurements of the standard with the same concentration (1mM) L-Cysteine was used. See Appendix K for a detailed protocol of the lyophilization of DTNB on-chip and in Eppendorfs.

Table 1: The types of samples of which absorbance is measured in the lyophilization experiment including the volumes L-Cystein and DTNB.

Type of sample	Description
Control (well plate)	90 μL 1 mM L-Cysteine in Tris buffer + 20 μL 1.9 mM DTNB in PBS
Eppendorf	90 μL 1 mM L-Cysteine in Tris buffer + 20 μL freeze-dried 1.9 mM DTNB
Microfluidic device	90 μL 1 mM L-Cysteine in Tris buffer + 20 μL freeze-dried 1.9 mM DTNB

2.12   Excess of DTNB lyophilized on filter paper   ❄

It was investigated whether the concentration of the reactant DTNB influences the measured absorbance. It was hypothesized that an excess of the disulfide DTNB would cause the reaction to shift toward the products. If a lower concentration disulfide is present, the formed mixed disulfides could react with residual thiols. To investigate whether the reaction is an equilibrium reaction, different concentrations of 20 μL liquid DTNB (0.24-3.8 mM) are added to the different standards L-Cysteine (90 μL). The measurements are performed in triplo according to the standard protocol (Appendix E).

Afterward, an excess of two different concentrations of DTNB were pipetted onto pieces

of filter paper: 3.8 mM and 7.6 mM. The liquid DTNB was freeze-dried on the paper by putting it in liquid nitrogen and leaving it in a vacuum overnight. The lyophilization protocol of the control was used, except it was placed straight in the liquid nitrogen and vacuum chamber, not placed in Eppendorfs (Appendix K). A 3.5 mm puncher was used to punch circles out of the filter paper. These filter paper circles containing lyophilized DTNB precisely fit in the reservoirs of the renewed calibration curve microfluidic design (Figure 17). After the PDMS came out of the plasma oven, the punched circles were placed into the reservoir closest to the inlet using tweezers, after which the chip was quickly sealed with a microscopic glass slide. 90 μL of 15.625 to 1000 μM L-Cysteine in 0.1 M Tris, pH 8.2 is pipetted into the 8 inlets in triplo. A control was performed in a 96-well plate using a standard protocol (Appendix E), and an on-chip control using liquid DTNB was performed using half the volumes from the standard protocol: 45 μL and 10 μL for the standards and DTNB, respectively. No control read-out reservoirs were added to the devices with freeze-dried DTNB for the absorbance measurements before the addition of DTNB.

(a)

(b)
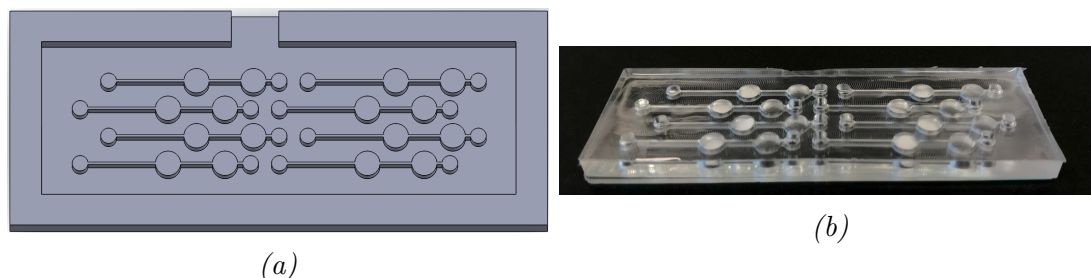
Figure 17: The chip design used for the measurement of the 8 standard concentrations (0-1000 μM) with the first reservoir for the placement of lyophilized DTNB on filter paper in Solidworks (a) and the assembled chip with filter paper (b).

2.12.1 Validation of the calibration curves

To investigate whether the obtained calibration curves meet the accuracy, precision, and sensitivity requirements, a validation study is conducted. The percentage of recovery, the coefficient of variation, the limit of detection, and the lower limit of quantification are determined. The accuracy is calculated with the following equation [51]:

$$Accuracy = 1 - \left[\left(\frac{(TheoreticalValue - ExperimentalValue)}{TheoreticalValue} \cdot 100\% \right) \right] \quad (2)$$

The precision is expressed in the coefficient of variation (CV) which shows the extent of variability in relation to the mean concentration. The used formula is:

$$CV = \frac{SD}{Mean} \cdot 100\% \quad (3)$$

In the equation SD is the standard deviation. The limit of detection (LOD) is the smallest concentration that can be distinguished from zero and the lower limit of quantification (LLOQ) is the smallest concentration of free thiols that can be determined with acceptable repeatability and accuracy. The following equations are used [51]:

$$LOD = \frac{3.3\sigma}{SD} \quad (4)$$

$$LLOQ = \frac{10\sigma}{SD} \tag{5}$$

In the equations is σ the slope of the calibration curve. A calibration curve of the concentration over the absorbance is made, based on the values between 0-250 μM. These calibration curves are used to calculate the concentrations based on the measured absorbance values. The calculated concentrations are utilized for the accuracy and precision determination. For the LOD and LLOQ the slopes of the calibration curves of the absorbance over the concentration are used. For these slopes, all tested values are included.

To validate the device an ANOVA test is conducted. Both the calibration curves and the measured plasma samples are investigated, and the different measurement methods (well plate and chip with liquid DTNB) are compared. First of all, a one-way ANOVA is conducted to examine the differences in absorption measured with the well plate across the different standard concentration levels. This is also done for the differences in absorption measured on-chip. A Q-Q plot and a plot of the residuals over the fitted values are obtained from the data.

2.13   Plasma measurements on-chip

The variance in measured plasma samples over time was assessed. By knowing the variance in plasma samples, in which the free thiol concentration is determined using the standard protocol, the acceptable variance of the assay on-chip can be established. Data from the 1000 IBD cohort study performed in Groningen was requested at the UMCG. Two control samples are added to each well plate in the study. These control samples of the different tested well plates and on the different test days are compared in terms of intra-CV.

Validation of the suitability of the chip for free thiol concentrations in plasma is performed. A blood sample is centrifuged for 10 minutes at 3500 rpm at 20 $°C$. Plasma is obtained and diluted 1:4 with Tris buffer. Three different conditions of the plasma measurements are investigated: in a well plate, on-chip with liquid DTNB, and on-chip with freeze-dried DTNB (n=8). For the on-chip measurements the design in Figure 17 is used. 90 μL diluted plasma is pipetted into the well or chip. For the well plate and liquid DTNB conditions, the control absorbance measurement is performed before the addition of 20 μL DTNB. To determine the concentration free thiols in the plasma sample, calibration curves are obtained for all conditions, as discussed in Section 2.12.

2.13.1   Validation

To determine whether the difference in the free thiol concentration in the plasma samples obtained through the ELISA with the well plate and the test on-chip is significant, a Welch Two Sample t-test is performed (R-Studio). Additionally, an ANOVA test was conducted on the data comparing plasma concentrations for the different methods, and a Bland-Altman plot was created. Lastly, a Q-Q plot and a plot of the residuals over the fitted values are obtained from the data. The used R-script can be found in Appendix L.1.

2.14   Portable spectrophotometer

Initially, a paper-based colorimetric assay was conducted. This involved cutting filter paper into small strips. A 96-well plate was used for making the calibration curve standard concentrations in triplo, according to the standard protocol (Appendix E). The filter paper strips were then placed in the wells to absorb the L-Cysteine concentrations. Microscopic images were captured using a Nikon Olympus SZX10 microscope (Nikon DS-Fi3 camera) and an iPhone X smartphone camera. RGB values were determined using Matlab software. The average RGB values of the three samples were utilized to create a color test strip, similar to a pH test strip and iPhone X.

Another investigated method was a colorimetric analysis of the L-Cysteine concentration determination without the use of filter paper. A set-up was created for measurements using a smartphone. The well plate with the samples was placed in a box to minimize light affecting the measurement (Figure 18(a)). A hole in the bottom of the box was cut allowing light to pass through the sample, and a blue paper was placed behind the sample since it is the complementary color to the yellow from the sample (Figure 18(b)). Both light blue and dark blue colored paper were tested. The RGB values of different concentrations of yellow food coloring were determined using the smartphone application "Colorimeter App" (Smyk Serhii). The food coloring concentrations were 0, 20, 40, 60, 80, 100% pure food coloring (Jo-La) and supplemented with water.

(a)   *(b)*
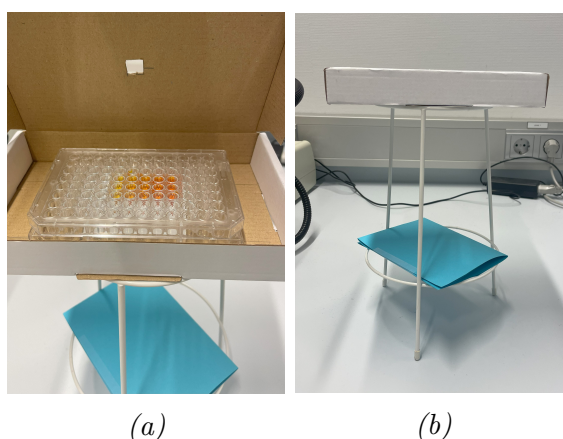
Figure 18: The set-up of the colorimetric analysis measurement using yellow food coloring in open (a) and closed (b) conditions.

It was hypothesized that a portable spectrophotometer using a LED and photodiode would give the most consistent results for the absorbance measurements. Micronit was approached for a collaboration on the use of their portable spectrophotometer for the determination of free thiol concentrations in plasma. During the COVID-19 pandemic, they developed a rapid test with the same principle as conventional PCR, yet with better scalability and lower costs [52]. They use loop-mediated isothermal amplification (LAMP) for DNA amplification and use reflection for the measurements. The portable spectrophotometer, called a "Mykee", has different colored LEDs and a sensor for the measurements (Figure 19(a)). The cartridge is white and covered with PCR sealing tape (RTS Scientific Co., Ontario, Canada), so they could be re-used. After pipetting a sample

into the inlet and pushing it to the read-out reservoirs by putting a cap on the inlet and using air to push the liquid through. The cartridge has six reservoirs, which are labeled A-F (Figure 19(b)).

The applicability of the Mykee for measuring the free thiol concentration in plasma was determined. Different concentrations of L-Cysteine in Tris buffer (0, 31.25, 250, 500, 1000 μM) were determined using both a white and blue LED. The most important settings are intensity, integration time, and gain. To find the optimal settings, different combinations of settings were tested. For both LEDs the integration time was set at the maximum of 255 ms and the gain at 8. The intensity of the white LED was set at 200 and of the blue LED at 128. The details on the settings of the Mykee can be found in Appendix M.1.

To find the influence of stray radiation on the measurements, the percentage of absorbance at 1 mM L-Cysteine was investigated. This was used to correct for it in the data analysis in Python. The absorbance was measured for samples of 1-6 mM L-Cysteine concentrations with steps of 1 mM at 412 and 630 nm in triplo, before and after the addition of 1.9 mM DTNB. Python was used for the data analysis of the absorbance measurement performed with the Mykee (Appendix M.2). Finally, the created calibration curves with the Mykee are compared to the theoretically obtained calibration curve, and the calibration curves obtained with the plate reader. The slope, offset, and R^2 values are compared to analyze the linear fit and suitability to measure the free thiol concentration.

(a)   (b)
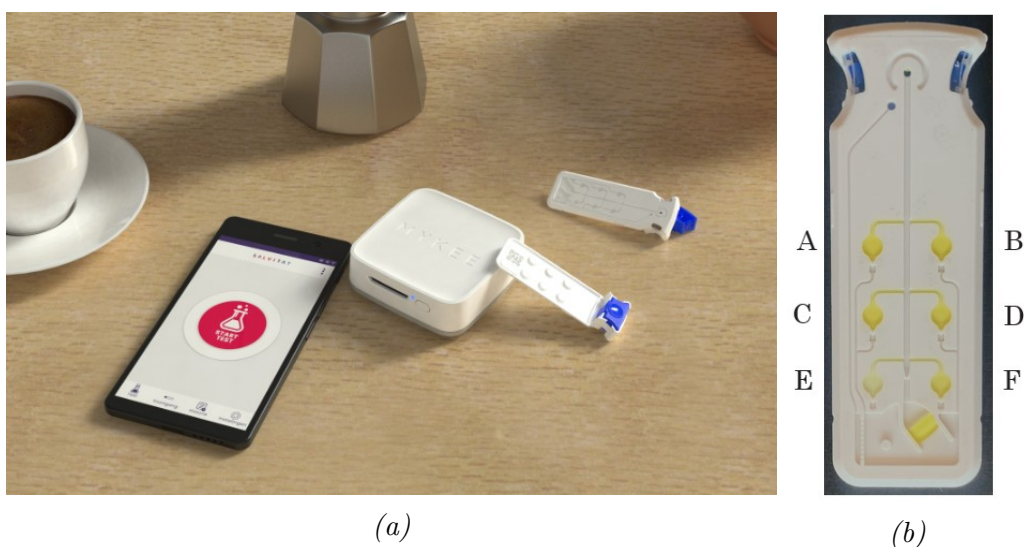
Figure 19: The design of the Mykee in white (a) and a close-up of the cartridge with corresponding labels of the reservoirs (b).

2.15 Integration of the different steps into one chip

The sample collection using the Minivette® was not tested. A pipette was used for the introduction of the blood sample to the device (63 μL). Integration of blood plasma separation, Tris buffer addition, enhanced mixing design, and freeze-drying of DTNB was created (Figure 20). No blister pouch was used for the addition of the Tris buffer, again a pipette was used (25 μL). The reservoir height was set to 0.15 mm as well as rest of

the device height. This lower reservoir height will have a signification influence on the measured absorbance due the Lambert-Beer law. However, the height was reduced as it was expected that with the small volume would already be difficult to reach the reservoir. It appears like two read-out reservoirs are included. However, the first circle reservoir is for the placement of the freeze-dried filter paper. An instruction video of the created integrated microfluidic device is made.

(a)

(b)
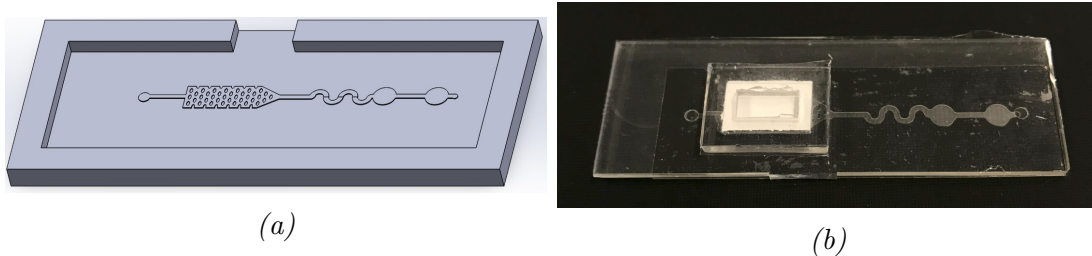
Figure 20: The integrated design in SolidWorks (a) and the assembled chip (b).

3 Results and Discussion

3.1 Plate reader-compatible chip holder

The chip holder was successfully milled (Figure 21). The glass slide could not be moved inside the holder and the holder fits the plate reader perfectly. However, due to the material properties of polystyrene, the bottom of the created chip holder was not completely transparent. The glass transition phase of polystyrene is reached around 100 °C. This temperature could be reached during the milling of the plate. The polystyrene melted around the milling tool, causing the bottom not to be as clear and transparent as before the milling. This is confirmed by the difference in absorbance of the chip holder compared to the standard 384 wells plate measured without any liquid (Appendix N). The baseline measurement showed higher absorbance at both measured wavelengths (412 and 630 nm) for the empty chip holder compared to the empty well plate with larger standard deviation as well (Table 2). Additionally, the chip holder showed a difference in absorbance between the two measured wavelengths, while the well plate had no difference in absorbance. A possible solution could be to completely remove the bottom of the chip holder except for the edges to rest the microscopic glass slide on. Due to the difficulties with milling the material, this was not attempted in this research.
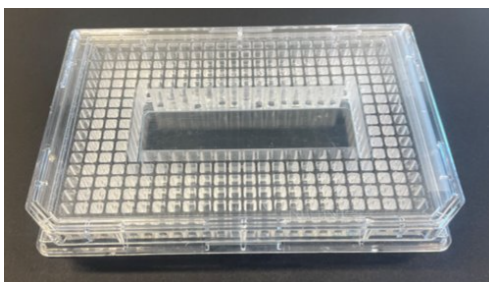
Figure 21: The design of the chip holder with well F5:K21 removed.

Table 2: The average absorbance value and standard deviation of the absorbance measurements for the 384 well plate and created chipholder for wells F5:K21 at wavelength 412 and 630.

	412 nm		630 nm	
	AVG	SD	AVG	SD
384 well plate	0.0397	0.0031	0.0397	0.0026
Chip holder	0.1960	0.0397	0.1537	0.0397

3.2 Blood Plasma Separation 💧

Plasma obtained by centrifuging whole blood samples did flow through the channels in the microfluidic device, also after the addition of an anticoagulant counteracting agent (Appendix O). After concluding this, the BPS using the designed chips was tested.
All microfluidic BPS devices were assembled successfully (Figure 22(a), 22(b)). Initially, in all assembled chips, there was no leakage of whole blood into the read-out channel

or underneath the PDMS sealing. In 55.6% of the microfluidic blood plasma separation devices with 100 μL whole blood added to the top well, plasma was visible in the capillary reservoir underneath the membrane (Figure 22(c)). Unfortunately after 20 minutes, in some chips, whole blood leaked into the plasma section at the edges of the membrane (Figure 22(d)). These figures show the sealing with PDMS bonding (Figure 22). This type of sealing was difficult for assembling the chip since a small opening between the top well and the sealing remained. Therefore, a sealing covering the whole chip except the inlets and outlet was preferred.

(a)	*(b)*	*(c)*	*(d)*
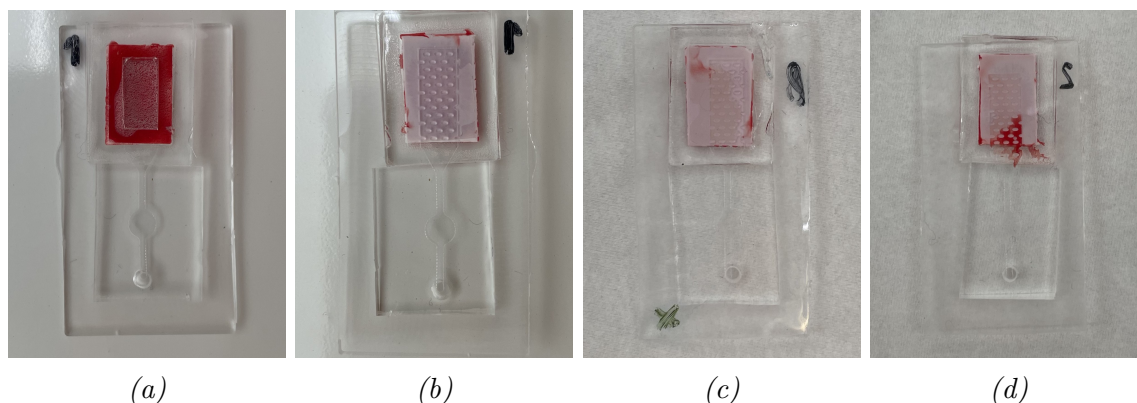
Figure 22: The top view (a) and the bottom view (b) of the assembled PDMS blood plasma separation chip at t=0, visibility of plasma obtained by the chip (c) and leakage of blood at the sides of the membrane (d).

Some plasma was visible in the collection reservoir. However, since the plasma did not flow into the channel and read-out reservoir, it could not be validated. It was hypothesized that the issue was due to the added volume being too little due to the membrane having a sponge-like functioning. Since 100 μL is already quite a large volume for a fingerprick blood sample, it was decided to make the design smaller instead of the volume larger. Different new, smaller designs were made to investigate whether more plasma could be wicked from the membrane (Appendix C.1). However, in the new designs, there was a 0% success rate in obtaining plasma. It is expected that this is due to fouling of the membrane. The blood volume recommendation of the manufacturer is 40-50 μL/cm^2 [53]. In the smaller designs, the membrane has an area of 0.48 cm^2 to which 100 μL blood was added. The initial design has a membrane area of 1.26 cm^2, so according to the manufacturer 50.4-63 μL blood is optimal.

One of the smaller designs was made with the possibility of pipetting Tris buffer into the blood plasma separation chip after obtaining plasma to flush the plasma from the collecting reservoir into the channel. Even though no plasma was obtained with the smaller design, it was tested whether pipetting buffer into the read-out reservoir. This was done successfully, and thus the original, larger design was made with the addition of an extra inlet to pipette the Tris buffer in. A downside is that the flow through the membrane is two-directional, so Tris buffer rises up in the blood inlet of the top well. Additionally, the exact ratio of the plasma dilution is difficult to measure this way.

Based on the results from the previous designs some small adjustments were made for

the last design. The opening in the sealing tape for the plasma to pass was reduced from 1.4x0.9 cm^2 to 1.2x0.7 cm^2 to prevent leakage of blood. Additionally, a small PDMS cap was created (1x0.5 cm^2) to reduce the rising of the Tris buffer through the membrane and help wick the plasma into the capillary pump reservoir. Two different final chips with an inlet for the Tris buffer were created: 0.3 mm height with adhesive tape as a sealing cover and 0.15 mm height with a PCR well plate sealing cover. For the 0.3 mm height design, 100% of the assembled chips obtained plasma; in 60% it also reached the read-out reservoir after adding the Tris buffer. For one chip without the possibility to add Tris buffer, pure plasma reached the read-out reservoir. The adhesive tape material was less suitable as sealing tape since it has stripes which makes the validation of the plasma more difficult under the microscope. The 0.15 mm height chips had easier fabrication as fewer bubbles in the PDMS were created when pouring. However, due to the height being so small the sealing tape more easily closed the read-out reservoir. The outcomes concerning plasma collection for the 0.15 mm chips were less successful. Plasma was obtained in 66.6% and the diluted plasma reached the reservoir in 33.3% of the devices. It was not possible to pipette the diluted plasma out of the chip, so no cell count could be performed.

Since the volume was presumably not the problem in the BPS, other possibilities for optimization were considered. The donor's first tube of blood is used, which can have different characteristics of congestion of blood. Since the plasma flow in the microfluidic device was tested beforehand, the congestion was most likely no problem.

3.2.1 Plasma validation

The obtained plasma had in terms of cell count a purity >99% in all investigated 0.3 mm height chips (Table 3). The cell count per milliliter was higher for the plasma samples obtained from the chips (1A-2B) compared to the control plasma samples. However, when assuming a cell count of 5 million per cubic millimeter [54], the percentages of blood cells still present in the plasma sample after separation are significantly lower than 1%. Additionally, the force needed to pipette the plasma out of the chip caused some blood to leak at the edges of the opening.

The assessment of plasma purity under the microscope was inconvenient with the use of adhesive tape as cover. The adhesive tape created stripes, which complicated the validation of the obtained plasma. The PCR tape as sealing shows a clearer image of the reservoir.

Table 3: *The cell count of the plasma obtained by the 0.3 mm height devices with Tris flush.*

Objective slide number	Cell count (/mL)	Percentage cells blood sample (%)
1A	$6.37*10^4$	0.001
1B	$3.85*10^5$	0.008
2A	$9.79*10^4$	0.002
2B	$1.43*10^5$	0.003
Control 1	$<5*10^4$	<0.001
Control 2	$<5*10^4$	<0.001

41
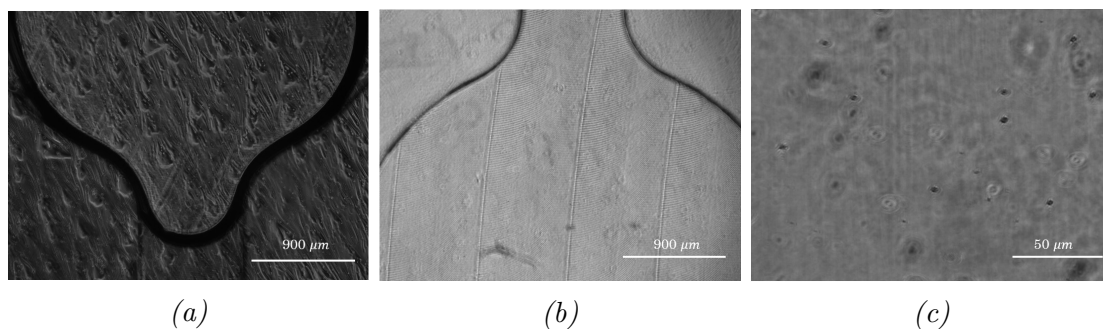
Figure 23: The images of the read-out reservoirs of the BPS devices with: 0.3 mm height and adhesive sealing tape showing stripes, scale bar = 900 μm (a), 0.15 mm height and PCR sealing, scale bar = 900 μm (b) and 0.15 mm height and PCR sealing, scale bar = 50 μm (c).

3.3   On-chip reagent storage

Figure 24 shows the results of the experiment performed with the eye lens to mimic the blister pouch. The blue food coloring in the read-out reservoir shows good prospects for the use of blister pouches for on-chip reagent storage. The eye lens demonstrated proof of concept, but the use of blister pouches with potentially different force requirements for opening necessitates additional validation in the final device. The eye lens showed proof of concept. The blister pouches are smaller and the required force to open them will be different. Therefore, additional validation of the use of blister pouches in the final device should be performed.
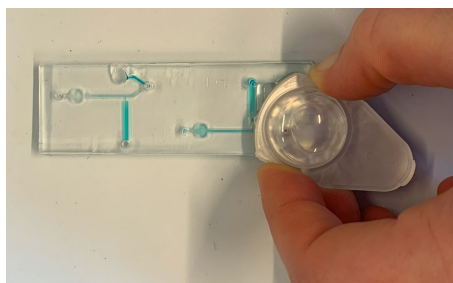
Figure 24: The results of the eye lens mimicking the blister pouch with blue food coloring in the trigger valve and after actuation blue being visible in the read-out reservoir.
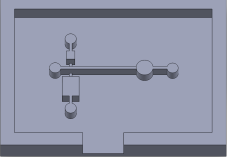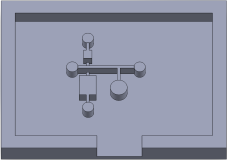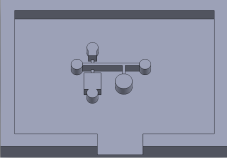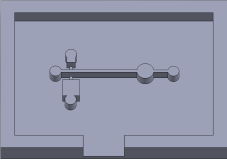
3.3.1   Two reagent chips

100% of the produced chips were suitable for experimental use. The design of the reservoirs aimed to accommodate volumes of 6 μL and 18 μL, mimicking the small plasma volume while enabling free thiol measurements. Additionally, the Tris buffer volume required for plasma dilution at a ratio of 1:4 was also considered. However, the hydrostatic pressure was too low for these volumes, so no meniscus was formed. Doubling the volumes led to possible meniscus formation in the designs. It was hypothesized that the activation volume added to the inlet could be very low. While testing the designs it

became clear that 20 μL was needed to add to be able to properly activate the trigger valves and possibly fill the read-out reservoir.

Three designs were tested on one day after storing the chips for a day after plasma bonding. The chip with a straight channel and inlet connected to the reservoir (Figure 8(d)) was tested a few hours after plasma bonding, which caused the liquids to flow immediately through the whole design after adding them to the reservoirs. It was hypothesized that the designs were still too hydrophilic, so the experiment was performed again. After storing the chips in the oven for 1 hour at 60 °C, the meniscus formation at the valves was possible. The images of the four designs with the blue and yellow food coloring in the reservoirs, and after actuation can be seen in Appendix P. The design with a straight channel and inlet connected to the reservoir (Figure 8(d)) had a success rate of 100% for the liquid reaching the reservoir. However, the success rate of the meniscus formation was not perfect (40%). It was expected that this was due to the hydrostatic pressure being too high. Compared to the smaller reservoir, the droplet of liquid on top of the inlet was a lot bigger for the larger reservoir. Therefore, for the mixing experiment, the addition of volume to the larger reservoir was reduced to 30 μL, while keeping the volume added to the smaller reservoir at 12 μL.

Table 4: The success rates and limitations of the different two reagent chip designs.

Chip Design	Design Characteristics	Success rate meniscus formation	Success rate reservoir filling	Limitations
	• Narrowing after inlet • Straight reservoir	100%	60%	• Difficulties pipetting • Not completely emptying the reservoir
	• Narrowing after inlet • Reservoir at 90°	40%	0%	• Read-out did not fill • Difficulties pipetting • Not completely emptying the reservoir
	• Inlet connected to reservoir • Reservoir at 90°	100%	0%	• Read-out did not fill • Not completely emptying the reservoir
	• Inlet connected to reservoir • Straight channel	40%	100%	• Not completely emptying reservoir

3.4 Enhanced mixing design

The herringbone and serpentine structures were created successfully. The micromill was limited in precisely creating the side wells to the serpentine. All the pictures are shown in Appendix C.4. The images of the experiment assessing the mixing efficiency of the different designs are shown in Appendix Q. The actuation creating laminar flow at the beginning of the channel showing a step function of the concentration over the cross-section was achieved successfully in some situations (Figure 25). However, the expected step function at the beginning of the channel was not as clear for all designed structures (Figure 26). Since the mean concentration over the cross-section of only three chips was taken, no images were excluded. The blue food dye and water did show laminar flow in most situations (Figure 25). The serpentine structure showed the clearest transformation from a step function at the beginning of the channel to a horizontal line at the end of the channel (Figure 26(c)). Compared to the straight channel, the line was more horizontal at the end of the channel indicating the mixing was more efficient. The herringbone structure shows a horizontal line, yet a very low concentration. The herringbone structure did not

have a positive increase in the mixing efficiency compared to the straight channel. This is due to the concentration at the end of the channel being lower than the expected two third of the initial concentration, and in most cases, the liquid did not reach the end of the channel. The herringbone structure was visible in the images and pixels of the structure instead of the empty channel are possibly selected for analysis, which could have affected the results. Due to the low average concentration at the end of the channel, this structure was rejected. The serpentine with side wells structure does show a similar correlation between the concentration and intensity as the serpentine without side wells. However, the average concentration is lower, and this structure was a bit larger than the others due to the side wells causing the liquid to not reach the reservoir. Based on this finding, this structure was excluded for further development.
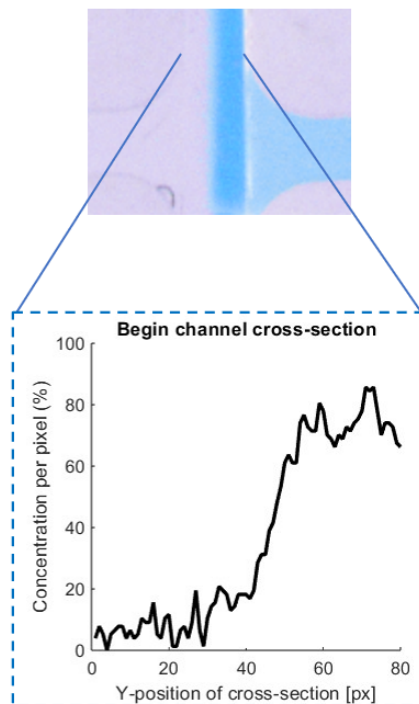
Figure 25: The obtained laminar flow in the channel and corresponding concentration over the cross-section.

The intensity plots over the cross-section show similar results, with a mirrored step function as a higher intensity is related to a lower concentration (Appendix R). The individual lines of the straight channel do not show one clear trend. In all designs, a decrease in concentration at the right side of the images is seen. This decrease could be due to the white reflection of the side of the channel. The intensity of the channel is related to the concentration, using equation 1. In general, it would have been better to create a calibration curve of the relationship between the concentration and the intensity [47].

(a) Straight channel

(b) Herringbone structure

(c) Serpentine structure

(d) Serpentine structure with side wells
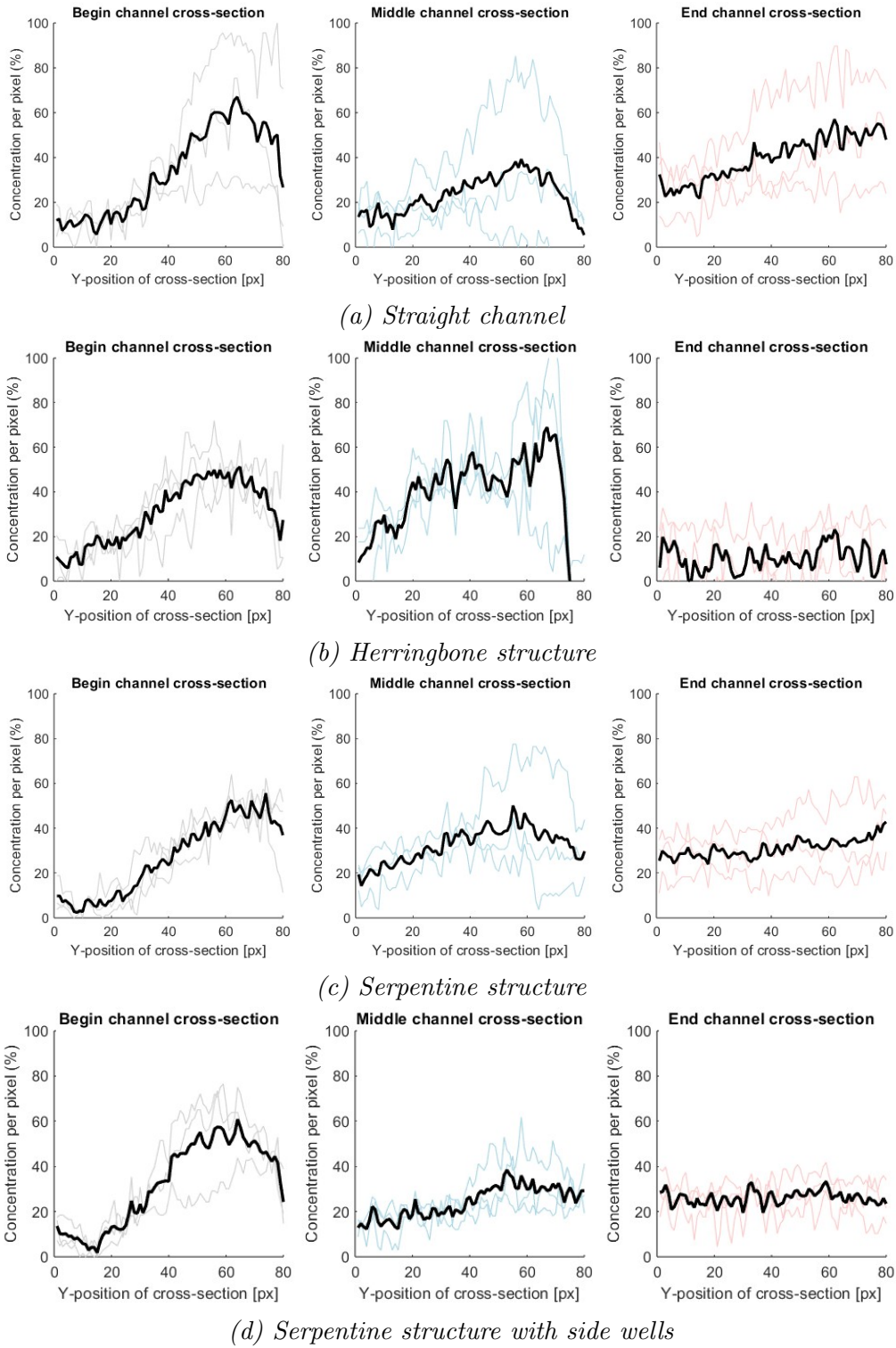
Figure 26: The concentrations (%) over the cross-section at the beginning, middle, and end of the channel for the straight channel (a), herringbone structure (b), serpentine structure (c), and serpentine structure with side wells (d).

The mixing efficiency over time also showed the lowest efficiency for the herringbone structure (Figure 27(b)). The mixing efficiency is increased for both the serpentine with

and without side wells compared to the straight channel. It is also clear from the graph of the serpentine structure mixing efficiency that the increase in mixing efficiency after 10 minutes is not as large (Figure 27(c)). Therefore, it could be concluded that the incubation time could be reduced due to the enhanced mixing design. Further research is needed to investigate whether similar results are obtained for plasma and Tris buffer since their diffusion rate is not exactly comparable with that of the food dye and water.
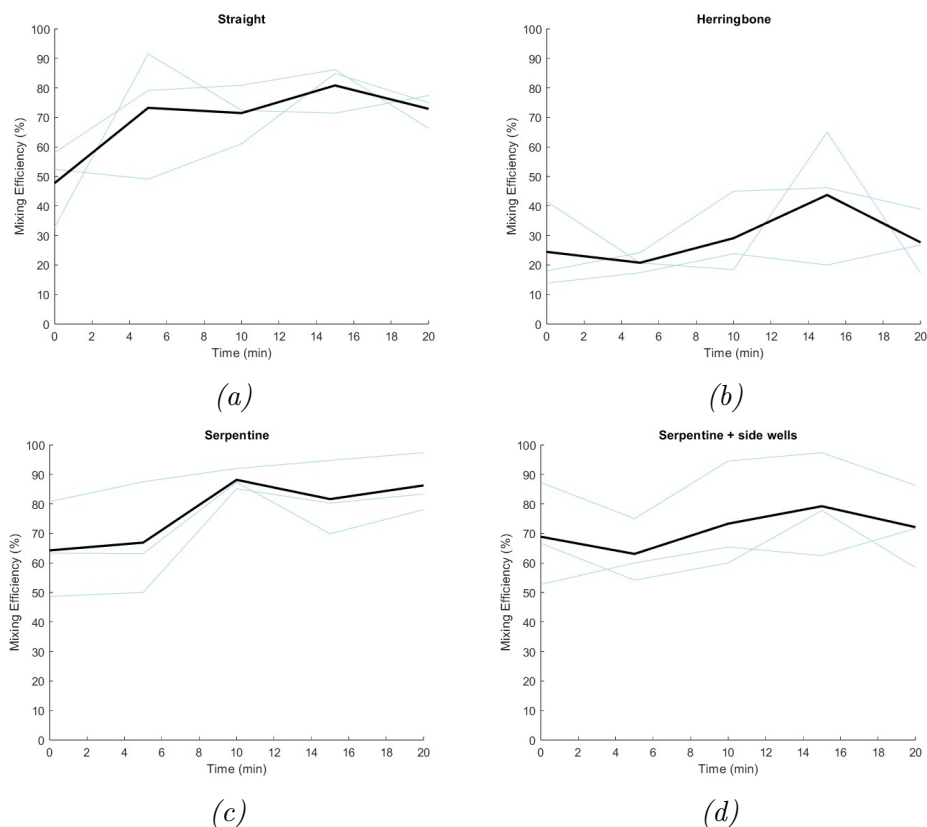
Figure 27: The mixing efficiency over the time for the straight channel (a), herringbone structure (b), serpentine structure (c), and serpentine structure with side wells (d).

3.5   Flow characterization two read-out design

The FITC pipetted into the side channel creates a clear meniscus shape at the trigger valve (Figure 28a). The grooves visible next to the channel are due to the micromilling and printed in the PDMS. This had no effect on the plasma binding of the device. The trigger valve was designed to have an angle of 90° between the side channel and main channel. Due to limitations in the cutting radius using micromilling for device fabrication the trigger valve has more rounded edges. Although, this had no effect on the functioning of the trigger valve. After the addition of water to the main channel, some FITC was sucked into the main channel (Figure 28b). However, it is also visible that not all the FITC was taken along by the water. The water-FITC mixture does reach the read-out reservoir for the design with the control and experimental read-out in one line (Figure 28c). Unfortunately, backflow of FITC into the control read-out reservoir was also seen.
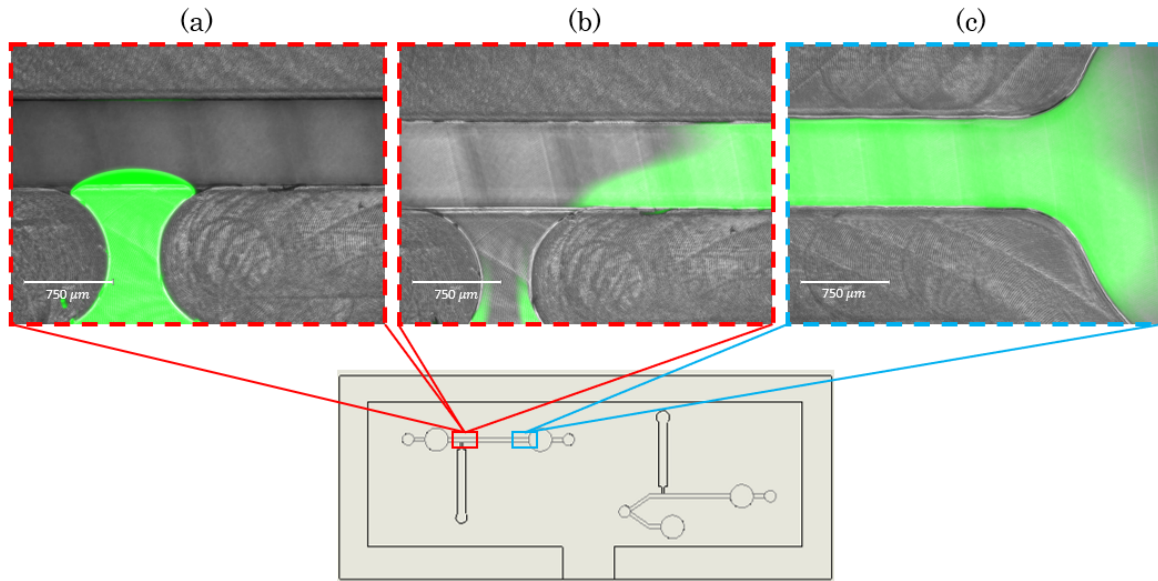
Figure 28: Fluorescence image of the trigger valve before addition of water (a), after addition of water (b), and of the read-out reservoir after addition of water (c).

3.6   Volume control

The results of the created mechanical valve were not sufficient as the size of the valve was too large making it not precise enough. A working microdispenser was not achieved since the designs were very sensitive to the differences in channel size. Additionally, a soft valve is not very robust since it starts leaking when hold at an angle.

Different designs of the PDMS Quake-valve were created to optimize the system for this specific purpose. It was possible to set pressure on the control layer. Physical differences can be seen when pressure is applied (Figure 29).
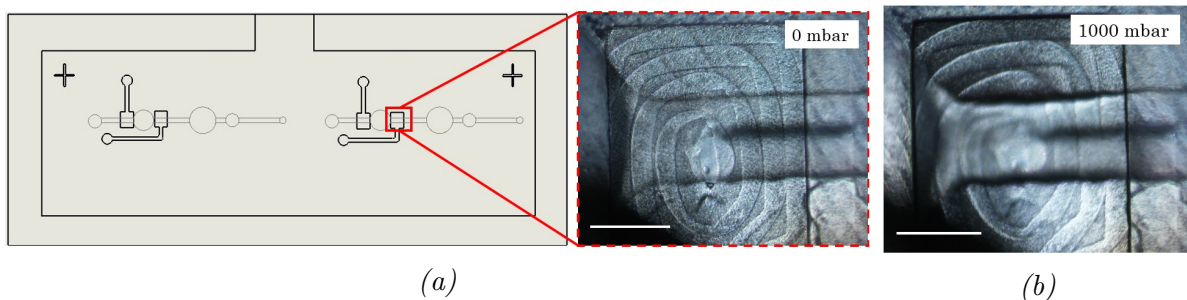
Figure 29: The pneumatic valve design without pressure applied to the control layer (a) and with 1 bar positive pressure applied (b). Scale bar = 700 μm

In Appendix S the measured values of the experiments are shown. The relationship between the applied pressure to the vial and obtained flow rate is linear (Figure 30). However, the obtained flow rate in the chip was relatively low. The back pressure in the chip could be high due to the channel size or the small outlet, causing the required

pressure by the pressure pump to be large as well. The calculations also show high resistance in the order of magnitude of $10^9 Pa \cdot \cdot m^{-3}$ (Appendix I).
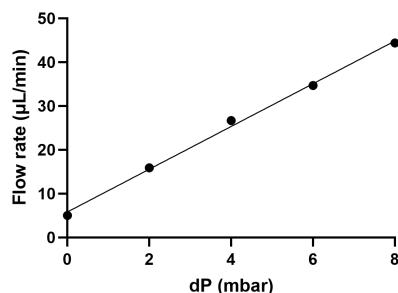
Figure 30: The relationship between the applied pressure and obtained flow rate in the device.

After filling the complete chip with blue food coloring the flow rate was set to zero and the pressure of the control layer was increased in order to close the valve (Figure 31). At the control layer pressure of 1600 mbar the valve was almost completely closed, judged by the blue food coloring being pushed out of the channel. By further increasing the pressure the connection tubing was automatically detached from the pressure pump due to the high pressure. For further characterization of the valve, a different set-up was used since the Nemesys syringe pump can be set to a certain flow rate independently of the force needed. This leads to the valve being pushed open despite the high pressure applied to the control layer. Therefore, a set-up with a flow rate sensor independent of the applied pressure was used for the next experiments.

(a) (b) (c) (d) (e)
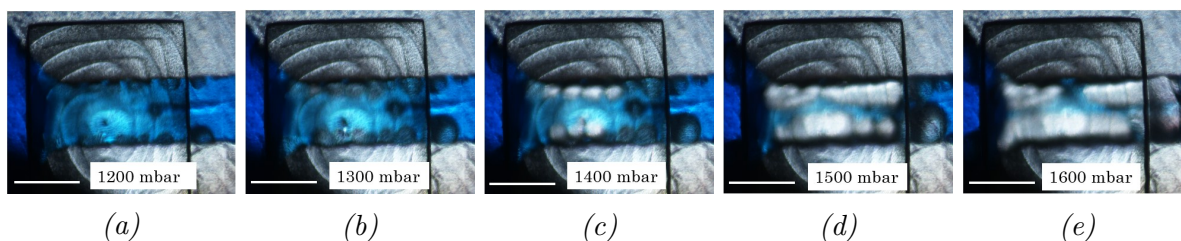
Figure 31: The pneumatic valve design with increasing positive pressure applied: 1200 mbar (a), 1300 mbar (b), 1400 mbar (c), 1500 mbar (d), and 1600 mbar (e). Scale bar = 700 μm

To validate the visually assessed closing of the valve, the flow rate was measured. The pressure of the control layer was set to 1500 mbar and the pressure difference between the inlet and outlet of the chip was increased slowly. For a pressure difference until 6 mbar, the valve remained closed. With further increase of the pressure difference, the flow rate increased. In the other experiment, the pressure applied to the pressure pump was constant and the pressure on the control layer was increased stepwise. With the flow rate being set to 30 mbar (approximately 137 μL/min) and increasing the pressure of the control layer, the flow rate decreased (Figure 32(b)). However, the decrease in flow rate was relatively little and it was not possible to close the valve completely while

maintaining the flow rate. In the developed device, no continuous flow rate will be present, so the designed Quake-valve could still be useful. The modest decrease observed could potentially be attributed to the relatively high initial pressure difference, which might impede the valve's closure process. It could be interesting to place the flow rate sensor behind the chip to see whether the flow rate could be stopped completely by the valve.
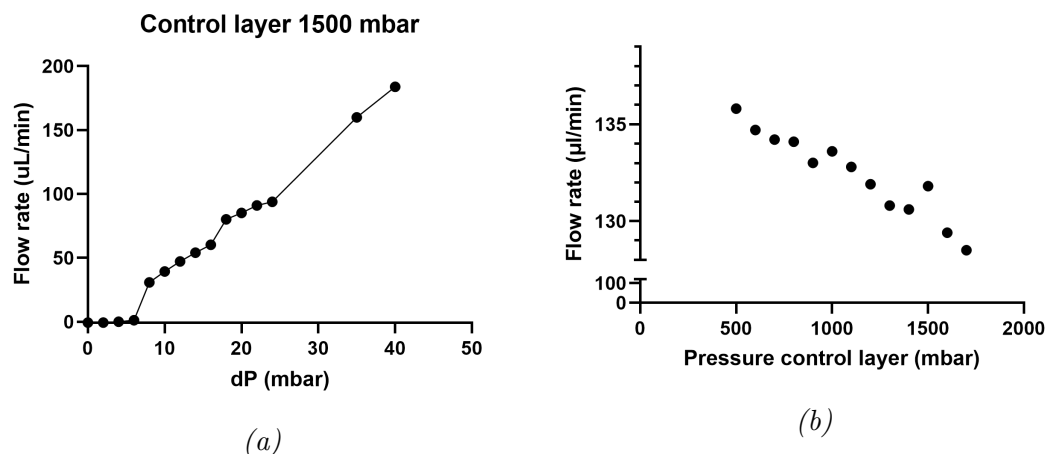
Figure 32: The measured flow rate with increasing the pressure difference in the channel and the control layer with a pressure of 1500 mbar (a) and the measured flow rate with increasing pressure on the control layer and the pressure difference set at 30 mbar (b).

3.7 Calibration curve L-Cysteine on-chip

A clear color change for the increasing L-Cysteine concentration of the standards is seen both in the well plate and on-chip (Figure 33). The relationship between the absorption and concentration L-Cysteine is linear for both the measurements in the 96-wells plate and on-chip (Figure 34(a)). The mean standard deviation of the measured standards is 0.76 for the 96-well plate and 9.96 for the chips. The small differences could be due to pipetting mistakes. Additionally, the diffusion length of DTNB was longer for the chips. Compared to the control measurement, the absorbance is lower for the measured chips. This is probably due to the difference in path length. The path length of the reservoirs in the chip is 2 mm, and the volume in the 96 wells plate is 110 mL, leading to a height of 3.44 mm. The resulting difference in absorbance could be due to the chip holder bottom not being completely transparent. Finally, the read-out chambers of the four higher L-Cysteine standard concentrations were not as precisely aligned in the chip holder as the lowest four, which could have affected the absorption measurements and increased the concentration standard deviation from the known concentrations.
Almost no differences are seen between the measured absorbance in the well plate and the theoretically calculated absorbance values (Figure 34(b)).

The calibration curves of the absorption of L-Cyteine solutions created on different days are also deviating. It was hypothesized that the difference in calibration curve was due to the degradation of the DTNB. However, the slope was larger for the calibration curve

created on the later time point. The different L-Cyteine solutions, which received the same DTNB solution on different days, show deviating results as well. Together with the UMCG, it was concluded that the differences in calibration curve were mostly due to the L-Cyteine solution as this was not properly stored. It is important that the DTNB is consistent in giving results. Otherwise the test results could not be interpreted from a standard calibration curve, and a new calibration curve should be obtained for each test, making it less suitable for POCT.

Figure 33: A picture of the calibration curve measurements in triplo on a wells plate (a) row A,B,C with increasing concentration colomn 1-8, and in microfluidic devices (b) with increasing concentration from top left to bottom right.
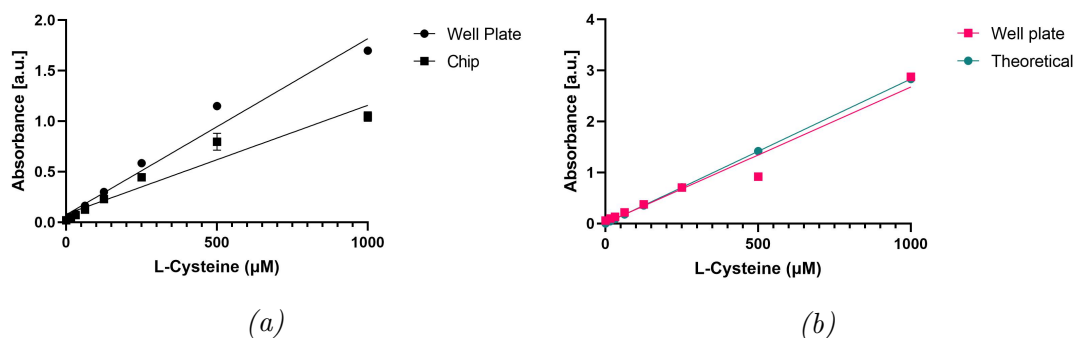
Figure 34: The calibration curve of the L-Cysteine standards measured in a 96-wells plate and on-chip (a) the well plate absorbance values compared to the theoretically calculated values (b).
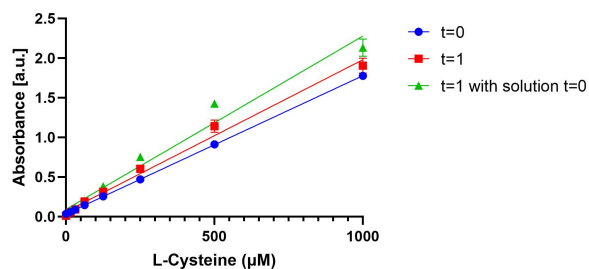
Figure 35: The calibration curve of the L-Cysteine standards measured in a 96-wells plate in three different conditions (two time points).

3.8 Lyophilization of DTNB ❄

The prepared standards showed a linear relationship between the concentration of L-Cysteine and measured absorption. The calculated concentration of the control samples (90 μL 1 mM L-Cysteine in Tris buffer + 20 μL DTNB in phosphate buffer) was 669.0 μM. The L-Cysteine samples added to the freeze-dried DTNB gave a concentration of 603.85 μM. The difference of the average concentrations of L-Cysteine samples determined with freeze-dried DTNB in Eppendorfs compared to the control is -9.7%. An intra-CV below 5% is preferred, yet 6.7% is still relatively low. The concentration of the L-Cysteine samples added to microfluidic devices with freeze-dried DTNB was 79.12 μM, which is significantly lower than that of the control. Additionally, the standard deviation and intra-CV are extremely high indicating very poor results. Excluding the samples from the microfluidic devices (tested on day 2) the L-Cysteine concentration is 229.82μM. Only one concentration of the L-Cysteine samples (645.32 μM) determined on the microfluidic device was within a reasonable range of the control and freeze-dried DTNB in Eppendorfs.
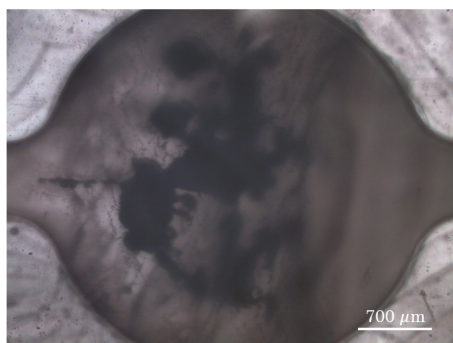
Figure 36: The read-out chamber of the microfluidic device with freeze-dried DTNB.

Type of sample	Concentration (μM)	SD (μM)	Intra-CV (%)
Control (well plate)	669.0	9.7	1.5
Eppendorf	603.9	40.7	6.7
Microfluidic device	79.1	197.4	249.4

The control samples showed different concentrations of L-Cysteine than the expected standard concentration L-Cysteine (1000 myM). Since the intra-CV was only 1.5% it

52

is assumed that a mistake was made weighing the L-Cysteine. Since the background measurements of the 1 mM standard were also used for the experimental measurements, it is also possible that these concentrations are aberrant due to this. So, the concentration of the L-Cysteine samples added to the freeze-dried DTNB in Eppendorfs is compared to the control samples. The -9.7% in concentration can be due to the lower volume in the well. The total volume was 90 μL instead of 110 μL since the 20μL phosphate buffer in which the DTNB was dissolved was evaporated. This alters the absorbance measurement's path length and thus the obtained absorption value. Another explanation could be that some of the freeze-dried DTNB particles did not adhere to the walls of the Eppendorf and were lost in the vacuum chamber.

The results of the determined concentration of the L-Cysteine samples in the microfluidic devices containing freeze-dried DTNB were deviating from the control values. Various explanations for the low measured concentration and high standard deviation are possible. A previously designed chip holder was used, in which movement of the glass slide in the holder and movement of the holder in the plate reader was possible. The plate reader therefore could have measured the PDMS walls instead of the reservoir. Additionally, the path length in the chips differs from the standard well height as well. It is also possible that the DTNB did not adhere to the PDMS or glass walls of the chip. Remarkable is that especially the results from the chips tested on the second day are deviating the most. The same solution of L-Cysteine is used, which had not properly been stored in the fridge. Making a fresh solution of L-Cysteine and DTNB could have led to a lower intra-CV. Another logical explanation would be that the change in the freezing method caused the differences in the results. Liquid nitrogen caused a very quick decrease in temperature while storing the chips in the -80 °C freezer overnight freezes the DTNB a lot slower. This could damage the DTNB and cause it to lose its function.

3.9 Excess of DTNB lyophilized on filter paper ❄

Adding different concentrations of DTNB to the same concentration L-Cysteine (0-1000 μM) does not influence the absorbance for the lower concentrations (Figure 37(a)). The absorbance shows a horizontal line for the L-Cysteine concentrations until 125 μM for the different added concentrations DTNB. For these concentrations L-Cysteine, the lowest tested concentration DTNB (0.24 mM) still gives the same absorbance value, so the lowest DTNB concentration before the possible reaction of thiols with formed mixed disulfides is not found. All the measured absorbance values can be found in Appendix T. The relevant physiological range (100-500 μM) shows a horizontal relationship after a DTNB concentration of 0.95 mM. Therefore, by adding an excessive amount of DTNB the reaction will always be favored towards to products. Based on this finding it was decided to lyophilize a surplus of DTNB on filter paper and add this to the chip. For 1000 μM L-Cysteine the absorbance further increases with increasing DTBB concentration. More research should be performed to find a more detailed window of concentrations for the DTNB saturation.

It was also investigated whether for the different added DTNB concentrations the calibration curve of the absorbance and L-Cysteine concentration remained unchanged. For DTNB concentrations of 1.9 mM and higher the calibration curve shows a linear relationship. Thus, the 1.9 mM DTNB added in the standard protocol of the UMCG is a

minimum value. An excess of DTNB does not largely influence the calibration curve, even though there are small differences. The calibration curves with a DTNB concentration lower than 1.9 mM are bent to the concentration axis, indicating a lack of DTNB added for sufficient chemical reaction with the free thiols.
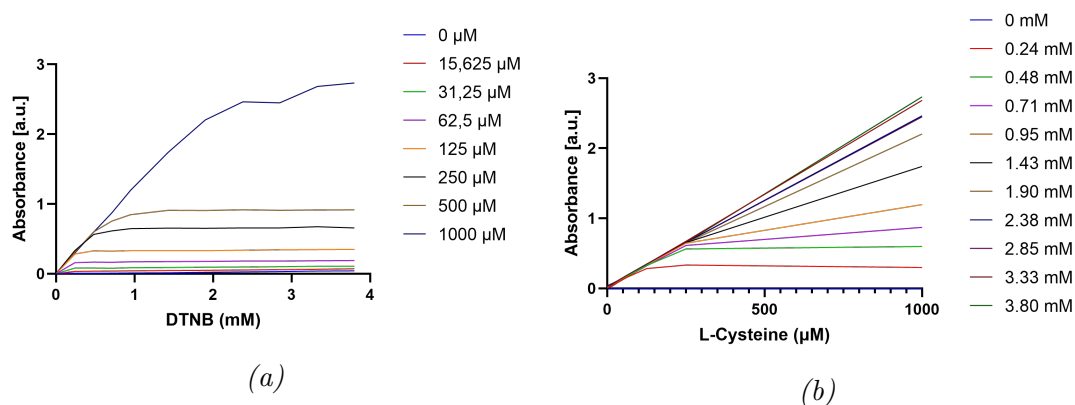
Figure 37: The measured absorbance for 0-1000 µM L-Cysteine for different concentrations (liquid) DTNB at 412 nm (background 630 nm) (a) and the corresponding calibration curves (b).

The chips with 8 read-out chambers containing 8 filter papers with lyophilized DTNB were assembled successfully. The calibration curve was made successfully with a similar design, without the addition of the filter paper. The calibration curve created based on the absorbance measurements from the chip seems to be linear until the concentration of 250 µM L-Cysteine (Figure 38(a)). For higher concentrations a plateau occurs, which could be due to a DTNB deficit. An excess of DTNB was added to the filter paper, yet some of the DTNB could have been lost during the lyophilization process. A larger piece of filter paper could be added to the chip or a higher concentration DTNB could be freeze-dried onto the filter paper. When a higher concentration DTNB was freeze-dried a larger absorbance value was measured for the higher concentrations L-Cysteine (Figure 38(b)). However, the absorbance values did also plateau. Since the plateau does not occur for the liquid-added DTNB (Figure 38(a)), the assumption of saturation due to lack of DTNB is most probable.

3.10   Validation of the calibration curves ✿

For the chips, the inter-CV is measured since three different chips are used to create the calibration curve in triplo. For the well plate, the intra-CV of the different wells within the well plate is determined. The well plate has the lowest accuracy (67.3%), but also the best precision (CV = 1.75 %). For the measurements on-chip the accuracy was higher, but there was more variation between the measurements. The inter-CV for the calibration curves obtained with the lyophilized DTNB was the highest (15.7%). Additionally, the on-chip measurements with lyophilized DTNB did not show a linear fit, and therefore the LOD and LLOQ are not determined. The LOD and LLOQ for the measurements with the well plate are 5.46 and 16.6 µM, respectively. The on-chip measurements of the calibration curve had a higher LOD and LLOQ of 36.2 and 109.6
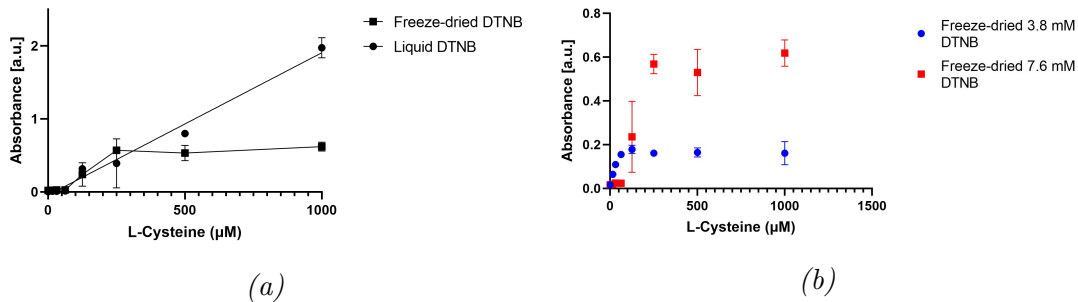
Figure 38: The calibration curves obtained with the microfluidic device with liquid and freeze-dried DTNB (a) and the calibration curves obtained with two different concentrations freeze-dried DTNB.

μM, respectively. However, the LLOQ of the on-chip measurements is only slightly above the lower physiological range limit.

	Accuracy	Precision	Sensitivity	
	Recovery(%)	CV (%)	LOD (μM)	LLOQ (μM)
Well plate	67.3	1.75	5.46	16.6
On-chip liquid DTNB	88.0	9.00	36.2	109.6
On-chip freeze-dried DNTB	68.0	15.7	x	x

Since the measurements on-chip with lyophilized DTNB did not show a linear fit, these were excluded from the analysis. Based on the provided results of the ANOVA test (Table 5), the p-value (Pr(>F)) is 0.158, which is greater than the typical significance level of 0.05. Therefore, the null hypothesis is not rejected, which suggests that there is no significant difference in absorbance measured with the well plate across different concentration levels. Moreover, the analysis revealed that the concentration levels did also not have a statistically significant effect on the absorbance measured with the chips ($F(1, 22) = 3.604$, p = 0.0708). However, there is no large difference between the p-value of 0.0708 and the significance level of 0.05. Therefore, further optimization of the on-chip measurements should be performed since a marginally significant difference is present.

When comparing the obtained calibration curves of the two different methods, a highly significant difference is found ($F(1, 22) = 487.3$, p < 2e-16). The null hypothesis is rejected and a substantial difference between the measured absorbance of the different methods across the concentrations of the calibration curve is found. The values were relatively normally distributed in the Q-Q plot and scattered across the identity line in the null residual plot (Appendix X.1). However, there is room for improvement.

Table 5: The results of the analysis of variance (ANOVA) test for the calibration curves data of both the well plate and chips with DF: degrees of freedom, SS: Sum of Squares, MS: Mean Squares, and α 0.05.

Source of variation	DF	SS	MS	F-value	P-value
Between methods (well vs chip)	1	17.801	17.801	487.3	<2e-16
Within well plate	1	1.647	1.6471	2.137	0.158
Between chips	1	1.410	1.4098	3.604	0.0708

3.11 Plasma measurements on-chip

The control values of larger studies of the UMCG measured at different moments in time had varying inter-CV values (Table 6). The measured values are shown in Appedix V. This means that the measurements are not very consistent. However, all inter-CV values are below 10% and therefore considered sufficient. If the variation between different tests is even lower, it is easier to create a device without a calibration curve on-chip.

Table 6: The intra-CV values of the control samples of an IBD cohort from the UMCG measured over 7 different days.

	Inter-CV (%)	
	Control sample 1	Control sample 2
Day 1	5.48	7.61
Day 2	3.30	2.88
Day 3	9.27	7.34
Day 4	5.92	7.28
Day 5	6.51	5.75
Day 6	8.77	6.02
Day 7	3.27	4.52

The free thiol concentration in plasma samples is also measured on-chip (Figure 39). The average free thiol concentration determined from the control well plate is 464.12 μM with an intra-CV value of 3.94%. The measured absorbance values of the plasma samples can be found in Appendix W. The concentration measured on-chip with liquid DTNB was 433.37 μM with an intra-CV value of 19.5%. The spread in calculated concentrations is a lot larger for the on-chip measurements. There were some air bubbles created in the microfluidic channels and read-out reservoirs, which caused the exclusion of 5 measurements. The on-chip concentration determination is solely based on three concentrations. There could be more uncertainties in the measurements due to pipetting problems. The free thiol concentration determined from the devices with lyophilized DTNB was a lot lower than for the liquid-DTNB. The lyophilization of the DTNB had been performed some weeks before. Even though the freeze-dried filter paper had been stored in a dry, dark place, the DTNB could have degraded. Another possibility is that the lyophilized particles did not stick to the paper. In that case, the microfluidic devices should be assembled immediately after freeze-drying.
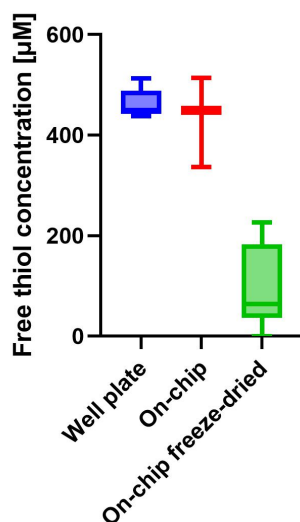
Figure 39: The measured free thiol concentration (μM) measured in a well plate, on-chip with liquid and freeze-dried DTNB.

3.11.1 Validation

When looking at the measured plasma concentrations by the two different methods, no significant difference was concluded (Table 7). The Welch Two Sample t-test gives a p-value of 0.6148, which is not close to the significance level of 0.05. The performed ANOVA also gave an F-value of 0.867 with a corresponding p-value of 0.376. The values were normally distributed and the Bland-Altman plot did not show outliers (Appendix X.2). Overall, based on the statistical analysis, we conclude that there is no significant difference in plasma concentrations determined with the two assays.

The significant difference in absorbance over the concentration between the different methods did not affect the determination of the concentration. The significant difference could be due to the difference in path length as the measured absorbance within the methods itself across the concentration did not show a significant difference. So, the absorbance measurements on-chip can sufficiently determine the free thiol concentration in plasma samples.

Table 7: The results of the analysis of variance (ANOVA) test for the free thiol concentration in the plasma samples measured with the well plate and chips with DF: degrees of freedom, SS: Sum of Squares, MS: Mean Squares, and α 0.05.

Source of variation	DF	SS	MS	F-value	P-value
Between methods (well vs chip)	1	2063	2063	0.867	0.376

3.12 Portable spectrophotometer

The results of the colorimetric analysis were not successful. The results and developed color strip can be found in Appendix Y.1. The colorimetric detection was considered not sensitive enough for the determination of free thiol concentrations in plasma due to many

uncertainties in the measurements. Additionally, the use of a smartphone application to measure the RGB values did also not give satisfying results (Appendix Y.2). Both methods are very sensitive to stray lighting and cannot measure the color changes accurately enough.

The measurements performed with the Mykee showed more consistent results. In initial measurements, the absorbance values of different concentrations of L-Cysteine measured with the Mykee did not show a linear relationship. For both the blue LED and the white LED the relationship did seem linear until 250 μM L-cysteine, thereafter it plateaus (Figure 40(a)(c)). The results of the other Mykees are shown in Appendix Y.3. At concentration 250 μM two wells (E and F) give a deviating absorbance. This is likely due to the air bubbles in these wells. Excluding these two measurements, the limit of linearity (LOL) is at 250 μL.

Stray radiation from the LED source can cause a negative deviation from the Lambert-Beer law leading to the plateau of the graph. Larger deviations can occur in the measurements with the Mykee since reflection is used for the measurements instead of transmittance as used in the plate reader. Using reflectance, the light of the LED can be reflected and detected by the sensor. For higher concentrations, the effects are bigger since more light would have been absorbed. The Lambert-Beer law also has some limitations above certain concentrations. However, the relationship did show a linear correlation when measured in the wells plate using the plate reader for the same concentrations. Therefore, the most likely reason for the deviation is the stray light of the light source. Since the Mykee has a sealed cabinet around the cartridge, minimal interference from other light could have occurred. Even though the relationship is not completely linear using the Mykee, the Mykees could still be used to measure the free thiol concentrations in the patient samples. It is important that the shape of the graph is constant, so unknown concentrations can be determined based on the absorbance of the sample.

A correction for the stray radiation was performed. The percentage of absorbance at the concentration of 1mM L-Cysteine was tested later by measuring the absorbance for higher concentrations of L-Cysteine (Figure 41). The absorbance seems to saturate after 2 mM. The average absorbance for 1000 μM is 84% from the average of the absorbance values of 2-6 mM. Therefore, 84% of the average measured absorbance at 1000 μM at wavelength 412 was subtracted from the absorbance values to correct for the stray radiation. This results in a more linear relationship between the concentration and absorbance (Figure 40(b)(d)). However, this also causes a wider distribution between the measurements. Table 8 shows the slope, offset and R^2-values of the calibration curves of the different wells in the Mykee using both the white LED and the blue LED. The linear fit for the calibration curves was sufficient (>0.96). The white LED showed more consistent results between the different sensors of the wells. The slope and offset differs between the different LEDs.
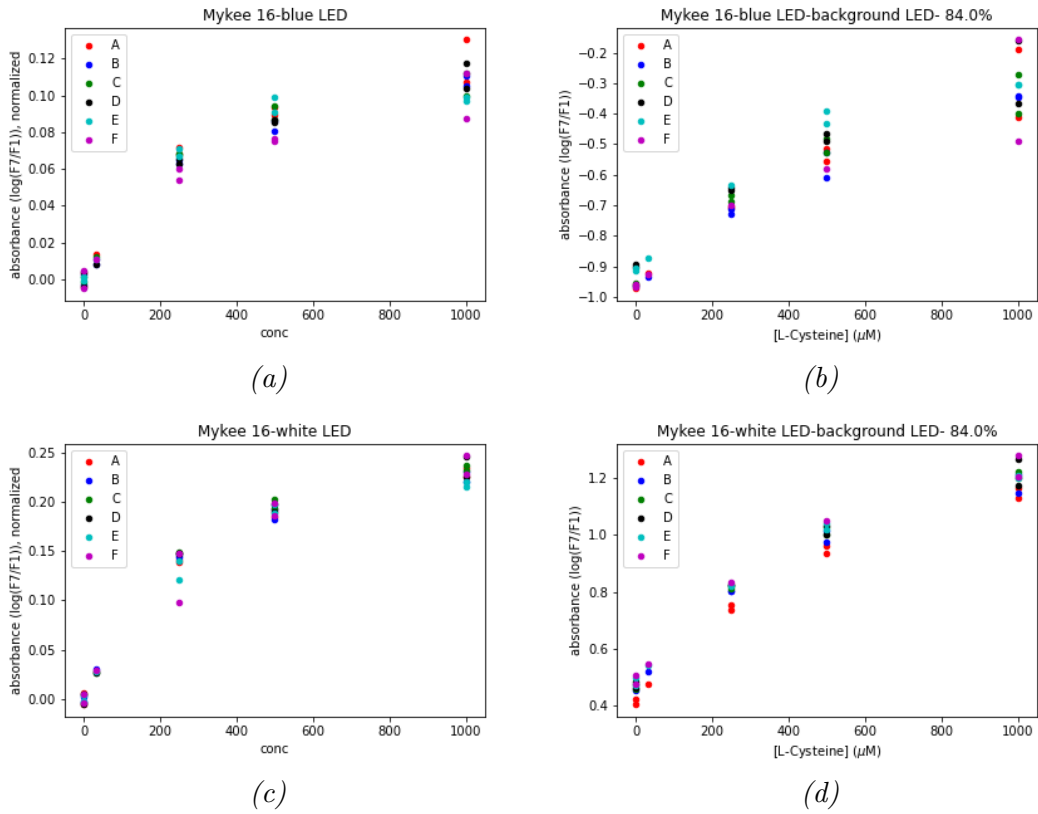
Figure 40: The calibration curve of the absorbance measured with the Mykee (number 16) using a blue LED with normalized values (a) and stray light correction (b) and using a white LED with normalized values (c) and stray light correction (d).
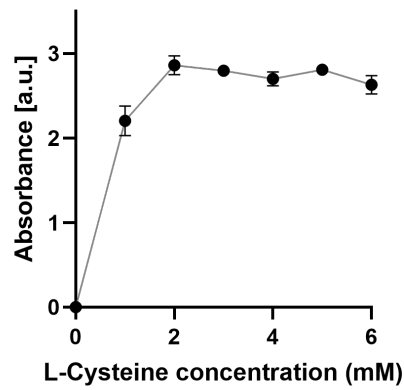
Figure 41: The investigation of the saturation of L-Cysteine by measuring the absorbance of L-Cysteine for higher concentrations.

Table 8: The slope, offset, and R^2 of the fitted plots of Mykee 16 with stray light correction (Figure 40(b)(d))

Mykee	Well	White LED			Blue LED		
		Slope * 10^{-4} (abs/μM)	Offset	R^2	Slope * 10^{-4} (abs/μM)	Offset	R^2
16	A	10.71	0.44	0.98	8.60	-0.95	0.98
	B	10.50	0.49	0.97	7.85	-0.95	0.96
	C	10.95	0.49	0.97	9.13	-0.94	0.98
	D	10.91	0.50	0.97	8.42	-0.88	0.99
	E	10.88	0.50	0.99	9.99	-0.91	1.00
	F	11.40	0.50	0.99	7.88	-0.95	0.97

The performance of the Mykee for measuring the free thiol concentration in plasma are compared to those measured with the plate reader. The slope, offset and R^2 of the created calibration curves are compared to each other and the calibration curve obtained with the Lambert-Beer law (Table 9). The slopes of the Mykee calibration curves are lower than the theoretically expected slope and the slopes of the calibration curves measured with the plate reader. Even though the reflectance has the same path length, the values could be deviating due to the different methods. Additionally, the offsets of the Mykee calibration curves are further from zero. Based on the R^2 values the Mykee calibration curves have a good linear fit: 0.98 for both the blue LED and the white LED. The regression line fits the experimental data of the calibration curve concentrations even better than the plate reader (0.98 and 0.96, for the Mykee and plate reader, respectively). So, even though the slope and offset are deviating from those measured with the plate reader, the calibration curves will be sufficient to calculate the free thiol concentrations. No difference in the R^2 value of the calibration curve fit was seen between the well plate and chip measured with the plate reader. The chip, with liquid DTNB, did have a smaller slope.

Table 9: The slope, offset, and R^2 of the calibration curved measured with the plate reader (well plate and chip) and Mykee (white and blue LED).

	Slope * 10^{-4} (abs/μM)	Offset (abs)	R^2
Theoretical	28.31	0.00	1
Well plate, plate reader	26.65	0.01	0.96
Chip, plate reader	19.52	-0.04665	0.96
Avg Mykee 16, white LED	10.89	0.49	0.98
Avg Mykee 16, blue LED	8.65	-0.93	0.98

3.13   Integration of the system

To enhance the integration process, it is advisable to further optimize each individual development step. In order to demonstrate the compatibility of the distinct steps within a monolithic device, initial measures are undertaken to move towards an integrated system.

There was plasma obtained from the whole blood sample in all cases. However, pipetting the Tris buffer into the inlet was a big challenge. Since the total channel length

was larger the force it took to pipette the Tris buffer into the device was larger. The serpentine mixer caused too long a distance to bridge for the diluted plasma. Therefore, it did not reach the freeze-dried DTNB and a color change of the plasma occurred. The read-out reservoir also had a height of 0.15 mm instead of the 2 mm used in the individual development steps for the absorbance measurements. It was already expected that the amount of obtained volume would cause limitations for the device. The blister pouch could improve the addition of the Tris buffer. In that case, the height of the read-out reservoir and control layer could be increased for the performed measurement. The integrated system was now designed to fit a microscopic glass slide and be able to measure the absorbance using the plate reader. If using the Mykee the reservoirs' height can be reduced to 1 mm since they use reflection. The control read-out with macrovalve is also not yet integrated into the device since the set-up is still too big at this moment. There are more POCT systems for the actuation of pneumatic valves [55].

After further optimization of the individual to-be-developed steps and achieving complete integration, clinical validation could be performed, in which the performance of the microfluidic device is compared to the current standard. The instruction video on the current integrated device can be found in Appendix Z.

4 Conclusion

The first steps are taken toward a sample-in-answer-out microfluidic device for POCT of free thiol levels in plasma. It was possible to determine the free thiol concentration in plasma samples on-chip using a path length of 2 mm. The intra-CV was 19.5% compared to the 3.94% of the currently used free thiol assay. A laminar flow and capillary pressures of -291 and -223 Pa was established in the devices, which is within the expected range. Additionally, the images of the mixing optimization experiment confirmed the laminar flow. The trigger valves with a height difference of 1500 μm were sufficient in blocking the flow. The obtained flow rate in the volume control experiments was between 10 and 137 μL/min, which is at the lower side of the expected range.

1. **Sample collection**
   This development step was not tested. However, from literature, it was concluded that the Microvette® would be a suitable option for precise sample collection.

2. **Blood plasma separation**
   A PDMS-based microfluidic device with a capillary pump and 0.3 mm height, covered with PCR tape, and the Vivid™ Plasma Separation Membrane GR can successfully obtain plasma in 100% if the cases. In 66.6% of the cases, plasma diluted with Tris buffer was able to flow through the microfluidic channels and had a plasma purity of >99%.

3. **On-chip reagent storage**
   A proof of concept for the use of blister pouches was performed, which showed good prospects. However, more research is needed. Additionally, reservoirs with a more negative burst pressure have a higher success rate regarding meniscus formation. It is concluded that the read-out reservoir of the two reagent chips could better be in line with the channel than at an angle.

4. **Optimizing the mixing process**
   It is concluded that a serpentine mixer without side wells optimizes the mixing efficiency the most over the length of the channel. Additionally, the highest mixing efficiency was already obtained after 10 minutes, so the incubation time could possibly be reduced.

5. **Two read-out design**
   Without the use of a valve, backflow from DTNB into the control read-out reservoir is seen. To prevent this backflow, and therefore enabling a two read-out design, implementation of the researched valves on the chip is needed.

6. **Volume control**
   The use of a pneumatically actuated Quake-valve shows the best prospects in terms of obtaining precise volumes in the microfluidic device compared to the other investigated valves. The valve could be used to prevent backflow, and to accurately measure the Tris buffer volume before addition to the plasma. However, the valve is currently consisting of a large set-up, which should be reduced for POCT.

7. **Lyophilization of DTNB** ❄

The lyophilization of DTNB on filter paper is possible. However, when integrating the freeze-dried DTNB on filter paper into the microfluidic device, the absorbance saturates after a concentration of 250 μM L-Cysteine, which is still in the physiological range of 100-500 μM free thiols. The free thiol concentration determination in plasma using the lyophilized DTNB instead of the liquid DTNB was not successful. It is found that the currently used ratio for the addition of DTNB to the diluted plasma sample is irrelevant. Providing the plasma sample with an excess DTNB of at least 1.9 mM is sufficient for the assay.

8. **Portable spectrophotometer** 📷

The developed Mykee spectrophotometer for POCT is suitable for the POC assessment of the free thiol concentration in plasma since the linearity of the calibration curve is sufficient ($R^2 = 0.98$).

No successful integration of the different development steps is performed. The specified practical requirements are mostly applicable to the integrated device. The different steps show good prospects for the development of a LoC for biomarker detection of oxidative stress in IBD patients. The device will need a lower sample volume, be rapid, portable, and possibly be fully automated. Not all established practical requirements are met. The calibration curve of the lyophilized DTNB did not show a linear relationship within the physiological range, but for liquid DTNB it did. The device does not yet have a monolithic approach. However, it is designed to be after optimization and integration of all steps. The LLOQ was 109.6 μM, which is above the set requirement of 50 μM. The specificity is not tested. The obtained plasma purity requirement was met since it was above 99%. The accuracy and precision of the calibration curve were 88% and 9.84%, respectively, while the requirements were $> 95\%$ and $< 5\%$. No control read-out was included in the integrated device yet. The test is not expected to exceed 30 minutes, but no tests were performed. The other practical requirements (10-18) are focused on the clinical setting and can therefore not yet be assessed.

5 Future outlook

5.1 Limitations of current research

This research has some limitations. First of all, the experiments are performed on a small scale in a controlled environment. It is recommended to repeat the experiments on a larger scale and for the final design to perform the experiment in the actual clinical setting. Due to the smaller scale, some experiments only showed a proof of concept. Further research is needed for both the blister pouches and the use of a Mykee for free thiol concentration determination.

Since all development steps are optimized individually, it is not known whether they will function while integrated. Especially the differences in optimal flow rate could cause problems in the integrated device. It might be beneficial to explore ways to optimize the development steps collectively, rather than individually. This approach could help ensure that the integrated device operates smoothly and efficiently. By considering the interactions and dependencies between different steps during the optimization process, researchers can work towards a more cohesive and compatible design.

Another limitation is due to the plate reader-compatible chip holder. The created chip holder for placing the chips in the plate reader influenced the absorbance values. A suggestion for future research would include optimizing the mill settings to prevent the melting of polystyrene. However, the on-chip absorbance measurements with liquid DTNB did show a linear relationship indicating that the influence was similar for all wells. This is confirmed by the low standard deviation.

Not all established practical requirements are investigated. For example, the specificity of the device was not measured. This should be investigated in the future since it is important that the assay can determine the analyte accurately, also in the presence of other materials. Especially in the case of lyophilized DTNB some impurities, other solvents, or degradation products may be present. In a clinical study with known IBD patients, the false positives and false negatives should be determined. A ROC curve could give a good overview of the sensitivity and specitivity, which could be used to compare the working of the microfluidic device to already existing methods for monitoring disease activity like calprotectin.

Another limitation is that the developed devices did not include a control read-out reservoir. This is important to validate the test, and this was also a requirement. In this thesis the focus was on the control read-out for background measurements, which could indicate deviating absorbance possible due to hemolytic or lipemic plasma samples. A positive control of the test should be included that can indicate whether the result is valid. Reasons for an invalid test could include insufficient sample volume or the chemical process of the color change by DTNB has not been initiated. The developed Quake-valve could introduce another reservoir for the positive control. However, the volume control experiments were performed only once. To increase the accuracy of the measurements multiple experiments should be performed. This would lead to better assessment of the Quake-valve for the use of volume control in the device.

Another limitation is that the values of the calibration curve of the absorbance measurements on-chip are not very consistent. The p-value was 0.07, which is relatively close to the significance value 0.05. Further optimization is needed for clinical use to prevent false conclusions. Another option is to create a calibration curve on-chip for each measurement. However, this will increase the complexity of the device and add more steps.

5.2 Optimization of current steps

The BPS membrane used in this study is a commercially available membrane. It is worth considering the exploration of the other types of the Pall Vivid™ Plasma Separation Membrane (GF and GX) to potentially increase the volume of plasma obtained [53]. Another possibility is developing a custom membrane specifically designed for this test, although this may incur higher costs, potentially compromising the low-cost requirement. Enhancing the capillary force within the BPS on-chip system could be a further improvement to promote better wicking of plasma from the membrane. While the added blood volume to the membrane has already been optimized, the inadequate plasma volume may also be attributed to the hydrophobic nature of the PDMS channel walls. Applying a hydrophilic coating like Pluronic F-127 could be beneficial, as it reduces the contact angle of the material. It has been observed that the hydrophilicity of the coating can persist for an extended duration when stored in a dark and vacuum environment [43]. In addition to coating the PDMS, it is also possible to apply a hydrophilic coating to the BPS membrane. Alternatively, the option of incorporating wetting agents or surfactants into the fingerprick blood sample can be considered, although this would introduce additional complexity to the test execution steps.
The validation of the plasma could be expanded. Next to the cell count and visual examination under the microscope, other tests could be performed to assess the purity and composition of the plasma. The HPLC profiles of the plasma obtained with the microfluidic device and with centrifugation could be compared. Additionally, the effect of cell lysis on the plasma purity could be investigated through quantification of nucleic acid levels using qPCR.

The two reagent designs were not further optimized. With further calculations on the geometries, the retention burst valves could completely empty the reservoirs. Retention burst valves emptying reservoirs in a specific order have been developed before. If this could be established, the volume control will also be easier as the volume of the reservoir could be used as an exact volume measure.
Due to time limitations, the enhanced mixing designs also have not undergone further optimization. Among the tested designs, the serpentine structure has shown the most promising results in terms of improving mixing efficiency. Enhancements could be made by increasing the size of turns or adding more bends to the serpentine structure. Other potential improvements include surface modifications and the introduction of obstacles or Dean vortices within the channel to enhance mixing performance [41].
Moreover, the designed serpentine structure has demonstrated an optimized mixing efficiency within a 10-minute timeframe for water and blue food dye. Further investigation can be conducted to evaluate the mixing performance of plasma and Tris buffer, and

assess whether they also mix rapidly. Additionally, in the integrated device, a serpentine structure introduced after the filter paper with lyophilized DTNB could be examined to determine if the incubation time of 20 minutes for the diluted plasma with DTNB is truly necessary or could be reduced.

The calibration curves obtained with lyophilized DTNB instead of liquid DTNB do not yet show a linear relationship. By increasing the DTNB concentration of the solution being lyophilized on filter paper the absorbance further increased. Immediate introduction of the filter paper into the microfluidic device could reduce detachment of the DTNB particles from the filter paper, which reduces the final concentration DTNB introduced into the device. It has been concluded that a DTNB concentration of 1.9 mM is minimal for an accurate color change reaction of DTNB with free thiols. The exact DTNB concentration on filter paper can be investigated through the addition of a 1000 μM L-Cysteine solution since the relationship between the absorbance and DTNB concentration is linear for the 1000 μM L-Cysteine concentration (LOL: 2 mM DNTB)

The cause of the saturation of the calibration curve was not investigated. Besides detachment of the DTNB particles, other explanations for saturation are residual structures of the solvents which may influence the absorbance or the influence of possible structural changes in DTNB due to the freeze-drying process affecting the colorigenic abilities of DTNB. Lyoprotectants, such as sugars or polyols, could be added to the DTNB solution before freeze-drying to enhance stability [56]. However, these lyoprotectants could in turn influence the absorbance measurements.

Finally, since the absorbance measurements and lyophilization was not performed on the same day, degradation of the DTNB could occur. The influence of the degradation of freeze-dried DTNB on the absorbance measurement should be investigated. To quantify the influence of the degradation the following equation could be used [57]:

$$Signal\% = \frac{\text{(Value at day x - Value blank sample)}}{\text{(Value at day 0} - \text{Value blank sample)}} \tag{6}$$

It is recommended to measure after 3 months, 6 months and 1 year to properly assess the degradation.

As mentioned before, only a proof of concept for the use of the Mykee for measuring the free thiol concentration in plasma is performed. The settings should be further optimized to reduce the spread between the different calibration curves. The height of the cartridge is only 1 mm instead of 2 mm since reflection is used. The differences in results of plasma samples between absorption and reflection should be assessed. The integration of the different steps into the Mykee cartridge is challenging. The freeze-dried DTNB on filter paper would be possible. However, storing liquids on the device is more difficult. A requirement is that the cartridge fits the Mykee inlet. It would be possible to create one microfluidic device for the blood plasma separation, addition of Tris buffer, and enhanced mixing, and another cartridge for the addition of freeze-dried DTNB and absorbance measurements. The diluted plasma sample could more easily be added to two different read-outs for the background and experimental measurements. The downside of this approach is that it contains more executive steps, making it more error prone. Additionally, the device will not meet the monolithic device requirement.

The differences and comparison of the different calibration curves created off-chip and on-chip should be further investigated. It should be prevented to create a calibration curve for every test since this complicates the test. Therefore, the calibration curve should be very consistent. It is recommended to graph the current assay with the concentration on the x-axis and the variation of the calibration lines on the y-axis and see where the variation is largest. If the variance is acceptable within the physiological range, then the microfluidic test is still clinically relevant. There are different implementation strategies that should be taken into account for the calibration curve. At first, regularly testing of control values should be performed to continuously verify the accuracy and precision of the assay. In the UMCG there are always two control samples included in each well plate of a study over time. Statistical analyses should be performed often to estabish whether there is a significant difference between the performed tests. Regular calibration and maintenance of the portable spectrophotometer could improve the stability of the calibration curve results. Evaluation and feedback of users can further improve the microfluidic device.

If the calibration curve of the assay is not consistent enough, it should not give a free thiol concentration as output. Another possibility will be to use the test with a certain threshold value. If the free thiol concentrations are reduced below a certain threshold value that has taken the variance into account, a hospital visit is recommended.

5.3   Further integration

An integrated device of the blood plasma separation, Tris buffer addition, enhanced mixing design, and freeze-drying of DTNB was created. However, no successful results were obtained. The other development steps were not included in the integrated design, so further integration and optimization of the integrated device should be performed. No control read-out reservoir was integrated into the device for judging the validity of the test. The pneumatic valve should be actuated POC before integration into the device. When the actuation would be possible using a screw [55] or air displacement, the backflow of DTNB to the control read-out reservoir could be prevented. For a sample-in-answer-out device, the collaboration with Micronit should be further investigated. The integration of all steps on the Mykee cartridge could lead to at-home absorbance measurements.

After complete integration of the different steps, the integrated device could be optimized for use in clinical practice. Before use in the clinical setting the accuracy, precision, sensitivity, and specificity should be assessed again.

PDMS and glass are transparent materials, which are advantageous during research to see what happens inside the chip. Failure of microfluidic valves, leakage and insufficient mixing can be more easily established. However, DTNB is a light-sensitive substance. Therefore, designing a plastic cover around the chip would protect DTNB from light. Additionally, PDMS is a soft material and the results from the test could be influenced if the user presses the PDMS. A cover would also protect the device from deformed microchannels.

PDMS is a commonly used material in the academic world, however, for mass produc-

tion in the pharmaceutic world it is considered relatively slow [58]. It could be investigated whether polymers, such as Norland Optical Adhesive or off stoichiometric thiolenes, which can be cured within seconds, would show the same promising results as LoC devices obtained with PDMS. Another advantage of using NOA is that, unlike PDMS, it retains it hydrophilic surface after UV curing. This could further improve the blood plasma separation.

In future research implementing other IBD biomarkers on the chip could be investigated for better monitoring disease activity and progression. Blood-based biomarker CRP would be a valuable addition. Another interesting addition to the device would be albumin. In many studies a correction in free thiol concentration for albumin is made [11]. This is due to albumin representing the highest percentage extracellular free thiols (75%). Additionally, albumin itself is clinically relevant in measuring oxidative stress since it's reduced levels is related to poorer nutritional status, patients with low-grade inflammation or infections.

5.4   Clinical validation and use

After complete integration, the next steps would be in the design and clinical validation of the end product. Wang and Kricka created a development pathway for new POCT devices based on a framework of The World Health Organization [59]. In their framework, the different steps from need assessment to implementation are shown (Figure 42). The POCT for free thiol detection in plasma is at the clinical sample testing step. Additionally, the supplemented sample testing phase is performed, but not yet finished as the above-mentioned optimization indicators could be assessed. After the implementation for adoption and uptake, the test could be used in practice. Figure 43 shows the care pathway of UC, which is similar to the CD care pathway. After further optimization of the microfluidic device for measuring oxidative stress, the test could be utilized in step three of the care pathway: stratification. The use of this test instead of endoscopy to monitor disease activity could reduce the costs and increase patient satisfaction. The economics analysis mentioned in the second step of the development pathway for POCT devices is not yet executed (Figure 42). An early Health Technology Assessment could give a clear image of the added value of this device.
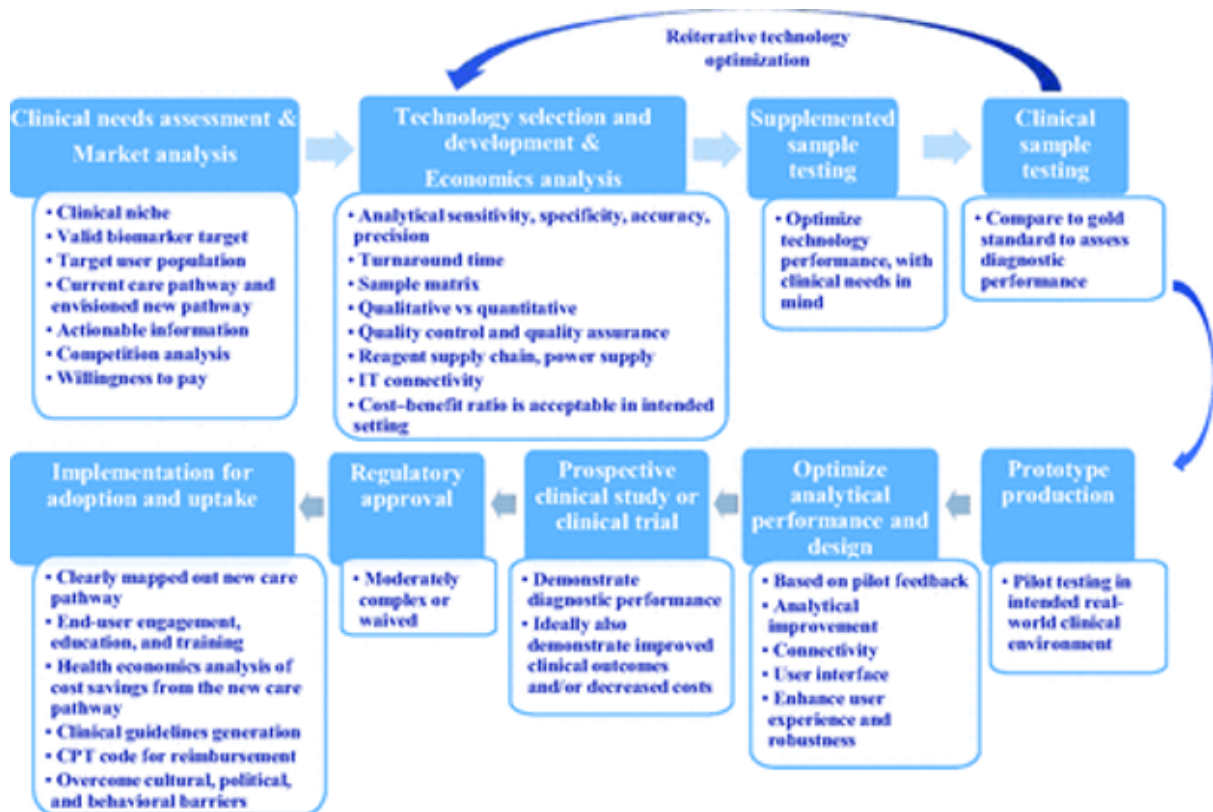
Figure 42: The development pathway for new POCT devices including all steps from need assessment to implementation (reprinted from [59]).
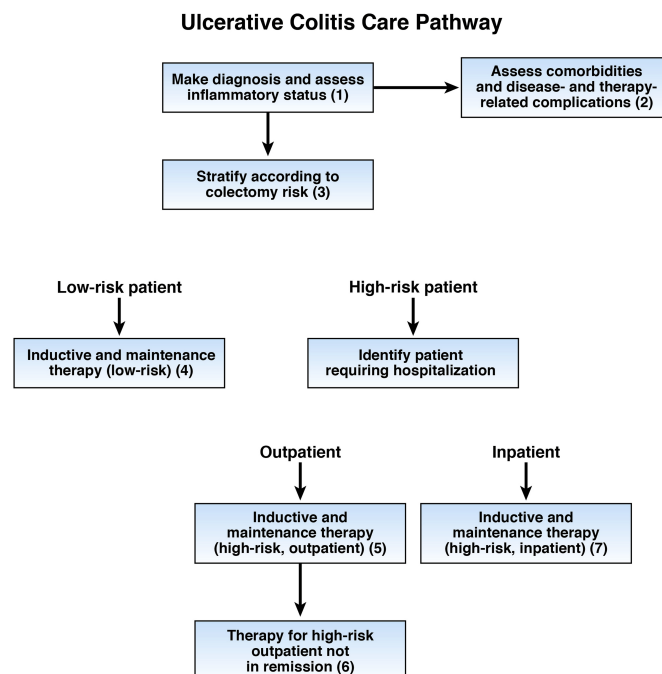
Figure 43: The care pathway for UC patients (reprinted from [60]).

Acknowledgements

References

1. Van Linschoten R, Leeuwen N van, Hazelzet JA, Woude CJ van der, Noord D van, and West RL. OP25 Prevalence of IBD in the Netherlands: development and validation of machine learning models for administrative data. Journal of Crohn's and Colitis 2023 Jan; 17:i34–i35. DOI: 10.1093/ecco-jcc/jjac190.0025

2. ISO 15189:2022 - Medical laboratories — Requirements for quality and competence. Available from: https://www.iso.org/standard/76677.html

3. Lee M and Chang EB. Inflammatory Bowel Diseases (IBD) and the Microbiome—Searching the Crime Scene for Clues. Gastroenterology 2021 Jan; 160:524–37. DOI: 10.1053/j.gastro.2020.09.056

4. Cosnes J, Gowerrousseau C, Seksik P, and Cortot A. Epidemiology and natural history of inflammatory bowel diseases. Gastroenterology 2011; 140:1785–94. DOI: 10.1053/j.gastro.2011.01.055

5. Flynn S and Eisenstein S. Inflammatory Bowel Disease Presentation and Diagnosis. 2019 Dec. DOI: 10.1016/j.suc.2019.08.001

6. De Groof EJ, Rossen NG, Van Rhijn BD, Karregat EP, Boonstra K, Hageman I, Bennebroek Evertsz F, Kingma PJ, Naber AH, Van Den Brande JH, Mallant-Hent RC, Mundt MW, D'Haens GR, and Ponsioen CY. Burden of disease and increasing prevalence of inflammatory bowel disease in a population-based cohort in the Netherlands. European Journal of Gastroenterology and Hepatology 2016 Sep; 28:1065–72. DOI: 10.1097/MEG.0000000000000660

7. Zhao M, Gönczi L, Lakatos PL, and Burisch J. The Burden of Inflammatory Bowel Disease in Europe in 2020. Journal of Crohn's and Colitis 2021 Sep; 15:1573–87. DOI: 10.1093/ecco-jcc/jjab029. Available from: https://doi.org/10.1093/ecco-jcc/jjab029

8. Ananthakrishnan AN, Bernstein CN, Iliopoulos D, Macpherson A, Neurath MF, Ali RA, Vavricka SR, and Fiocchi C. Environmental triggers in IBD: A review of progress and evidence. 2018 Jan. DOI: 10.1038/nrgastro.2017.136

9. Lopes EW, Chan SSM, Song M, Ludvigsson JF, Håkansson N, Lochhead P, Clark A, Burke KE, Ananthakrishnan AN, Cross AJ, Palli D, Bergmann MM, Richter JM, Chan AT, Olén O, Wolk A, and Khalili H. Lifestyle factors for the prevention of inflammatory bowel disease. Gut 2022 Dec :2022–328174. DOI: 10.1136/GUTJNL-2022-328174. Available from: https://gut.bmj.com/content/early/2022/11/28/gutjnl-2022-328174

10. Tontini GE, Vecchi M, Pastorelli L, Neurath MF, and Neumann H. Differential diagnosis in inflammatory bowel disease colitis: State of the art and future perspectives. World Journal of Gastroenterology 2015 Jan; 21:21–46. DOI: 10.3748/wjg.v21.i1.21

11. Bourgonje AR, Gabriëls RY, De Borst MH, Bulthuis ML, Faber KN, Van Goor H, and Dijkstra G. Serum free thiols are superior to fecal calprotectin in reflecting endoscopic disease activity in inflammatory bowel disease. Antioxidants 2019 Sep; 8. DOI: 10.3390/antiox8090351

12. Iskandar HN and Ciorba MA. Biomarkers in inflammatory bowel disease: Current practices and recent advances. 2012. DOI: 10.1016/j.trsl.2012.01.001

13. Lewis JD. The utility of biomarkers in the diagnosis and therapy of inflammatory bowel disease. Gastroenterology 2011; 140:1817–26. DOI: 10.1053/j.gastro.2010.11.058

14. Buisson A, Gonzalez F, Poullenot F, Nancey S, Sollellis E, Fumery M, Pariente B, Flamant M, Trang-Poisson C, Bonnaud G, Mathieu S, Thevenin A, Duruy M, Filippi J, L'Hopital F, Luneau F, Michalet V, Genès J, Achim A, Cruzille E, Bommelaer G, Laharie D, Peyrin-Biroulet L, Pereira B, Nachury M, Bouguen G, Dapoigny M, Goutorbe F, Duron C, Goutte M, Boschetti G, Flourié B, Danion P, Bourreille A, Dupas JL, and Hébuterne X. Comparative Acceptability and Perceived Clinical Utility of Monitoring Tools: A Nationwide Survey of Patients with Inflammatory Bowel Disease. Inflammatory Bowel Diseases 2017 Aug; 23:1425–33. DOI: 10.1097/MIB.0000000000001140. Available from: https://dx.doi.org/10.1097/MIB.0000000000001140

15. Colombel JF, D'Haens G, Lee WJ, Petersson J, and Panaccione R. Outcomes and Strategies to Support a Treat-to-target Approach in Inflammatory Bowel Disease: A Systematic Review. Journal of Crohn's and Colitis 2020 Feb; 14:254–66. DOI: 10.1093/ECCO-JCC/JJZ131. Available from: https://academic.oup.com/ecco-jcc/article/14/2/254/5548492

16. Poggi A, Benelli R, Venè R, Costa D, Ferrari N, Tosetti F, and Zocchi MR. Human gut-associated natural killer cells in health and disease. Frontiers in Immunology 2019; 10. DOI: 10.3389/FIMMU.2019.00961

17. Alemany-Cosme E, Sáez-González E, Moret I, Mateos B, Iborra M, Nos P, Sandoval J, and Beltrán B. antioxidants Oxidative Stress in the Pathogenesis of Crohn's Disease and the Interconnection with Immunological Response, Microbiota, External Environmental Factors, and Epigenetics. 2021. DOI: 10.3390/antiox. Available from: https://doi.org/10.3390/antiox10010064

18. Million M and Raoult D. Linking gut redox to human microbiome. Human Microbiome Journal 2018 Dec; 10:27–32. DOI: 10.1016/j.humic.2018.07.002

19. Bourgonje AR, Feelisch M, Faber KN, Pasch A, Dijkstra G, and Goor H van. Oxidative Stress and Redox-Modulating Therapeutics in Inflammatory Bowel Disease. 2020 Nov. DOI: 10.1016/j.molmed.2020.06.006

20. Bourgonje AR, Von Martels JZ, Bulthuis ML, Van Londen M, Faber KN, Dijkstra G, and Van Goor H. Crohn's disease in clinical remission is marked by systemic oxidative stress. Frontiers in Physiology 2019; 10. DOI: 10.3389/fphys.2019.00499

21. Luceri C, Bigagli E, Agostiniani S, Giudici F, Zambonin D, Scaringi S, Ficari F, Lodovici M, and Malentacchi C. Analysis of oxidative stress-related markers in Crohn's disease patients at surgery and correlations with clinical findings. Antioxidants 2019 Sep; 8. DOI: 10.3390/antiox8090378

22. Chen P, Zhou G, Lin J, Li L, Zeng Z, Chen M, and Zhang S. Serum Biomarkers for Inflammatory Bowel Disease. Frontiers in Medicine 2020 Apr; 7:123. DOI: `10.3389/FMED.2020.00123/BIBTEX`

23. Alghoul Z, Yang C, and Merlin D. The Current Status of Molecular Biomarkers for Inflammatory Bowel Disease. Biomedicines 2022, Vol. 10, Page 1492 2022 Jun; 10:1492. DOI: `10.3390/BIOMEDICINES10071492`. Available from: `https://www.mdpi.com/2227-9059/10/7/1492/htm%20https://www.mdpi.com/2227-9059/10/7/1492`

24. ILO; Unep; WHO; Ipcs. Biomarkers In Risk Assessment: Validity And Validation. Geneve, Switzerland: World Health Organization, 2001

25. Preiser JC. Oxidative Stress. Journal of Parenteral and Enteral Nutrition 2012 Mar; 36:147–54. DOI: `https://doi.org/10.1177/0148607111434963`. Available from: `https://doi.org/10.1177/0148607111434963`

26. Neubauer K, Kempinski R, Matusiewicz M, Bednarz-Misa I, and Krzystek-Korpacka M. Nonenzymatic Serum Antioxidant Capacity in IBD and Its Association with the Severity of Bowel Inflammation and Corticosteroids Treatment. Medicina 2019, Vol. 55, Page 88 2019 Apr; 55:88. DOI: `10.3390/MEDICINA55040088`. Available from: `https://www.mdpi.com/1648-9144/55/4/88/htm%20https://www.mdpi.com/1648-9144/55/4/88`

27. Van Deen WK, Skup M, Centeno A, Duran N, Lacey P, Jatulis D, Esrailian E, Van Oijen MG, Hommes DW, Hoekman D, Zeevenhooven J, D'haens G, and Benninga M. The effect of a coordinated care programme for inflammatory bowel diseases on health care utilisation P488 IBS-type symptoms in patients with quiescent inflammatory bowel disease are unrelated to ongoing inflammation. Available from: `https://academic.oup.com/ecco-jcc/article/10/suppl_1/S347/2482333`

28. Hueppe A, Langbrandtner J, and Raspe H. Inviting Patients with Inflammatory Bowel Disease to Active Involvement in Their Own Care: A Randomized Controlled Trial. Inflammatory Bowel Diseases 2014 Jun; 20:1057–69. DOI: `10.1097/MIB.0000000000000044`. Available from: `https://dx.doi.org/10.1097/MIB.0000000000000044`

29. Jong MJ de, Meulen-de Jong AE van der, Romberg-Camps MJ, Becx MC, Maljaars JP, Cilissen M, Bodegraven AA van, Mahmmod N, Markus T, Hameeteman WM, Dijkstra G, Masclee AA, Boonen A, Winkens B, Tubergen A van, Jonkers DM, and Pierik MJ. Telemedicine for management of inflammatory bowel disease (myIBDcoach): a pragmatic, multicentre, randomised controlled trial. The Lancet 2017 Sep; 390:959–68. DOI: `10.1016/S0140-6736(17)31327-2`. Available from: `http://www.thelancet.com/article/S0140673617313272/fulltext%20http://www.thelancet.com/article/S0140673617313272/abstract%20https://www.thelancet.com/journals/lancet/article/PIIS0140-6736(17)31327-2/abstract`

30. Sewell GW, Marks DJ, and Segal AW. The immunopathogenesis of Crohn's disease: a three-stage model. Current Opinion in Immunology 2009 Oct; 21:506–13. DOI: `10.1016/J.COI.2009.06.003`

31. Wilkens R, Novak KL, Maaser C, Panaccione R, and Kucharzik T. Relevance of monitoring transmural disease activity in patients with Crohn's disease: current status and future perspectives. Therapeutic Advances in Gastroenterology 2021 Apr; 14. DOI: `10.1177/17562848211006672/ASSET/IMAGES/LARGE/10.1177{\_}17562848211006672-FIG2.JPEG`. Available from: `https://journals.sagepub.com/doi/full/10.1177/17562848211006672`

32. Goodsall TM, Noy R, Nguyen TM, Costello SP, Jairath V, and Bryant RV. Systematic Review: Patient Perceptions of Monitoring Tools in Inflammatory Bowel Disease. Journal of the Canadian Association of Gastroenterology 2021 Apr; 4:e31–e41. DOI: `10.1093/JCAG/GWAA001`. Available from: `https://academic.oup.com/jcag/article/4/2/e31/5715171`

33. Paans W, Dieperink W, De Ruiter H, and Luttik ML. Point of Care Testing bij flebitis. TVZ - Verpleegkunde in praktijk en wetenschap 2021 131:3 2021 Jun; 131:32–3. DOI: `10.1007/S41184-021-0990-Z`. Available from: `https://link.springer.com/article/10.1007/s41184-021-0990-z`

34. Wilkens R, Dolinger M, Burisch J, and Maaser C. Point-of-Care Testing and Home Testing: Pragmatic Considerations for Widespread Incorporation of Stool Tests, Serum Tests, and Intestinal Ultrasound. Gastroenterology 2022 Apr; 162:1476–92. DOI: `10.1053/J.GASTRO.2021.10.052`

35. Hejl J, Theede K, Møllgren B, Madsen KV, Heidari A, Steig A á, and Fenger M. Point of care testing of fecal calprotectin as a substitute for routine laboratory analysis. Practical Laboratory Medicine 2018 Mar; 10:10–14. DOI: `10.1016/J.PLABM.2017.11.002`

36. Nasser Y, Labetoulle R, Harzallah I, Berger AE, Roblin X, and Paul S. Comparison of Point-of-Care and Classical Immunoassays for the Monitoring Infliximab and Antibodies Against Infliximab in IBD. Digestive Diseases and Sciences 2018 Oct; 63:2714–21. DOI: `10.1007/S10620-018-5144-Y/TABLES/5`. Available from: `https://link.springer.com/article/10.1007/s10620-018-5144-y`

37. Arshavsky-Graham S and Segal E. Lab-on-a-Chip Devices for Point-of-Care Medical Diagnostics. Advances in Biochemical Engineering/Biotechnology 2022; 179:247–65. DOI: `10.1007/10{\_}2020{\_}127/FIGURES/9`. Available from: `https://link.springer.com/chapter/10.1007/10_2020_127`

38. E.J. Hammink. Development of a microfluidic device for point of care testing of oxidative stress. PhD thesis. University of Twente, 2022. Available from: `https://purl.utwente.nl/essays/92154`

39. Schoots MH, Gordijn SJ, Scherjon SA, Goor H van, and Hillebrands JL. Oxidative stress in placental pathology. Placenta 2018 Sep; 69:153–61. DOI: `10.1016/J.PLACENTA.2018.03.003`

40. Wang S, Zhang X, Ma C, Yan S, Inglis D, and Feng S. A Review of Capillary Pressure Control Valves in Microfluidics. Biosensors 2021, Vol. 11, Page 405 2021 Oct; 11:405. DOI: `10.3390/BIOS11100405`. Available from: `https://www.mdpi.com/2079-6374/11/10/405/htm%20https://www.mdpi.com/2079-6374/11/10/405`

41. Li Z, Zhang B, Dang D, Yang X, Yang W, and Liang W. A review of microfluidic-based mixing methods. Sensors and Actuators A: Physical 2022 Sep; 344:113757. DOI: 10.1016/J.SNA.2022.113757

42. VERORDENING (EU) 2017/ 746 VAN HET EUROPEES PARLEMENT EN DE RAAD - van 5 april 2017 - betreffende medische hulpmiddelen voor in-vitrodiagnostiek en tot intrekking van Richtlijn 98/ 79/ EG en Besluit 2010/ 227/ EU van de Commissie. Publicatieblad van de Europese Unie

43. Moonen EJM. Design, fabrication and testing of a point-of-care microfluidic chip integration of on-chip blood separation and luminescence detection. PhD thesis. TU Eindhoven, 2019

44. Tomeh MA and Zhao X. Recent Advances in Microfluidics for the Preparation of Drug and Gene Delivery Systems. Molecular Pharmaceutics 2020 Dec; 17:4421–34. DOI: 10.1021/ACS.MOLPHARMACEUT.0C00913/ASSET/IMAGES/LARGE/MP0C00913{_}0005.JPEG. Available from: https://pubs.acs.org/doi/full/10.1021/acs.molpharmaceut.0c00913

45. Kwak TJ, Nam YG, Najera MA, Lee SW, Strickler JR, and Chang WJ. Convex Grooves in Staggered Herringbone Mixer Improve Mixing Efficiency of Laminar Flow in Microchannel. PLoS ONE 2016 Nov; 11. DOI: 10.1371/JOURNAL.PONE.0166068. Available from: /pmc/articles/PMC5096722/%20/pmc/articles/PMC5096722/?report=abstract%20https://www.ncbi.nlm.nih.gov/pmc/articles/PMC5096722/

46. Johnson TJ, Ross D, and Locascio LE. Rapid microfluidic mixing. Analytical Chemistry 2002 Jan; 74:45–51. DOI: 10.1021/AC010895D/ASSET/IMAGES/LARGE/AC010895DF00007.JPEG. Available from: https://pubs.acs.org/doi/full/10.1021/ac010895d

47. Bossink EGBM, Vollertsen AR, Loessberg-Zahl JT, Meer AD van der, Segerink LI, and Odijk M. Systematic characterization of cleanroom-free fabricated macrovalves, demonstrating pumps and mixers for automated fluid handling tuned for organ-on-chip applications. Microsystems & Nanoengineering 2022 May; 8:54. DOI: 10.1038/s41378-022-00378-y

48. Bayraktar T and Pidugu SB. Characterization of liquid flows in microfluidic systems. International Journal of Heat and Mass Transfer 2006 Mar; 49:815–24. DOI: 10.1016/J.IJHEATMASSTRANSFER.2005.11.007

49. 5,5'-Dithiobis(2-nitrobenzoic acid) — C14H8N2O8S2 - PubChem. Available from: https://pubchem.ncbi.nlm.nih.gov/compound/6254#section=Chemical-and-Physical-Properties

50. Fluorescein-5-isothiocyanate — C21H11NO5S - PubChem. Available from: https://pubchem.ncbi.nlm.nih.gov/compound/18730#section=Chemical-and-Physical-Properties

51. Al-Nimry SS and Khanfar MS. Validation of an RP-HPLC Method for the Determination of Asenapine Maleate in Dissolution Media and Application to Study In Vitro Release from Co-Crystals. Scientia Pharmaceutica 2021 Mar; 89:14. DOI: 10.3390/scipharm89010014

52. Research project: VIRAPOC. Available from: `https://www.micronit.com/get-inspired/stay-up-to-date/research-projects/virapoc`

53. Vivid™ Plasma Separation Membrane - Pall Shop. Available from: `https://shop.pall.com/us/en/medical/advanced-materials/diagnostics-2/zidgri78lls`

54. Dean L. Chapter 1, Blood and the cells it contains. 2005. Available from: `https://www.ncbi.nlm.nih.gov/books/NBK2263/`

55. Zheng Y, Dai W, and Wu H. A screw-actuated pneumatic valve for portable, disposable microfluidics. Lab on a Chip 2009 Feb; 9:469–72. DOI: 10.1039/B811526E. Available from: `https://pubs.rsc.org/en/content/articlelanding/2009/lc/b811526e`

56. Debulis K and Klibanov AM. Dramatic enhancement of enzymatic activity in organic solvents by lyoprotectants. Biotechnology and Bioengineering 1993 Mar; 41:566–71. DOI: 10.1002/BIT.260410509. Available from: `https://onlinelibrary.wiley.com/doi/full/10.1002/bit.260410509%20https://onlinelibrary.wiley.com/doi/abs/10.1002/bit.260410509%20https://onlinelibrary.wiley.com/doi/10.1002/bit.260410509`

57. Chen CA, Yeh WS, Tsai TT, Li YD, and Chen CF. Three-dimensional origami paper-based device for portable immunoassay applications. Lab on a Chip 2019 Feb; 19:598–607. DOI: 10.1039/C8LC01255E. Available from: `https://pubs.rsc.org/en/content/articlehtml/2019/lc/c8lc01255e`

58. Olanrewaju A, Beaugrand M, Yafia M, and Juncker D. Capillary microfluidics in microchannels: from microfluidic networks to capillaric circuits. Lab on a Chip 2018 Aug; 18:2323–47. DOI: 10.1039/C8LC00458G. Available from: `https://pubs.rsc.org/en/content/articlehtml/2018/lc/c8lc00458g%20https://pubs.rsc.org/en/content/articlelanding/2018/lc/c8lc00458g`

59. Wang P and Kricka LJ. Current and Emerging Trends in Point-of-Care Technology and Strategies for Clinical Validation and Implementation. Clinical Chemistry 2018 Oct; 64:1439–52. DOI: 10.1373/CLINCHEM.2018.287052. Available from: `https://dx.doi.org/10.1373/clinchem.2018.287052`

60. Dassopoulos T, Cohen RD, Scherl EJ, Schwartz RM, Kosinski L, and Regueiro MD. Ulcerative Colitis Care Pathway. Gastroenterology 2015 Jul; 149:238–45. DOI: 10.1053/j.gastro.2015.05.036. Available from: `http://www.gastrojournal.org/article/S0016508515007301/abstract`

61. Whitesides GM. The origins and the future of microfluidics. Nature 2006 Jul; 442:368–73. DOI: 10.1038/nature05058

62. Preetam S, Nahak BK, Patra S, Toncu DC, Park S, Syväjärvi M, Orive G, and Tiwari A. Emergence of microfluidics for next generation biomedical devices. Biosensors and Bioelectronics: X 2022 May; 10:100106. DOI: 10.1016/J.BIOSX.2022.100106

63. Cheng S, Chen W, and Zhang P. Developing advanced polymer films based on microfluidic laminar flow. Giant 2022 Mar; 9:100091. DOI: 10.1016/J.GIANT.2022.100091

64. Guo W, Hansson J, and Wijngaart W van der. Capillary pumping independent of the liquid surface energy and viscosity. Microsystems & Nanoengineering 2018 4:1 2018 Mar; 4:1–7. DOI: `10.1038/s41378-018-0002-9`. Available from: `https://www.nature.com/articles/s41378-018-0002-9`

65. Zimmermann M, Schmid H, Hunziker P, and Delamarche E. Capillary pumps for autonomous capillary systems. Lab on a Chip 2006 Dec; 7:119–25. DOI: `10.1039/B609813D`. Available from: `https://pubs.rsc.org/en/content/articlehtml/2007/lc/b609813d`

66. Iakovlev AP, Erofeev AS, and Gorelkin PV. Novel Pumping Methods for Microfluidic Devices: A Comprehensive Review. Biosensors 2022, Vol. 12, Page 956 2022 Nov; 12:956. DOI: `10.3390/BIOS12110956`. Available from: `https://www.mdpi.com/2079-6374/12/11/956/htm%20https://www.mdpi.com/2079-6374/12/11/956`

67. Park J, Han DH, and Park JK. Towards practical sample preparation in point-of-care testing: user-friendly microfluidic devices. Lab on a Chip 2020 Mar; 20:1191–203. DOI: `10.1039/D0LC00047G`. Available from: `https://pubs.rsc.org/en/content/articlehtml/2020/lc/d0lc00047g`

68. Zhang X, Xia K, and Ji A. A portable plug-and-play syringe pump using passive valves for microfluidic applications. Sensors and Actuators B: Chemical 2020 Feb; 304:127331. DOI: `10.1016/J.SNB.2019.127331`

69. Nguyen NT, Hejazian M, Ooi CH, and Kashaninejad N. Recent Advances and Future Perspectives on Microfluidic Liquid Handling. Micromachines 2017, Vol. 8, Page 186 2017 Jun; 8:186. DOI: `10.3390/MI8060186`. Available from: `https://www.mdpi.com/2072-666X/8/6/186/htm%20https://www.mdpi.com/2072-666X/8/6/186`

70. Mielczarek WS, Obaje EA, Bachmann TT, and Kersaudy-Kerhoas M. Microfluidic blood plasma separation for medical diagnostics: Is it worth it? Lab on a Chip 2016; 16:3441–8. DOI: `10.1039/c6lc00833j`

71. Wang Y, Nunna BB, Talukder N, Etienne EE, and Lee ES. Blood plasma self-separation technologies during the self-driven flow in microfluidic platforms. 2021 Jul. DOI: `10.3390/bioengineering8070094`

72. Mateen SA and Bhole KS. A review on microfluidic devices for separation of blood constituents. IOP Conference Series: Materials Science and Engineering 2020 Mar; 810:012024. DOI: `10.1088/1757-899X/810/1/012024`. Available from: `https://iopscience.iop.org/article/10.1088/1757-899X/810/1/012024`

73. Kuan DH, Wu CC, Su WY, and Huang NT. A Microfluidic Device for Simultaneous Extraction of Plasma, Red Blood Cells, and On-Chip White Blood Cell Trapping. Scientific Reports 2018 8:1 2018 Oct; 8:1–9. DOI: `10.1038/s41598-018-33738-8`. Available from: `https://www.nature.com/articles/s41598-018-33738-8`

74. Rafeie M, Zhang J, Asadnia M, Li W, and Warkiani ME. Multiplexing slanted spiral microchannels for ultra-fast blood plasma separation. Lab on a Chip 2016 Jul; 16:2791–802. DOI: `10.1039/C6LC00713A`. Available from: `https://pubs.rsc.org/en/content/articlehtml/2016/lc/c6lc00713a`

75. Tripathi S, Varun Kumar YV, Prabhakar A, Joshi SS, and Agrawal A. Passive blood plasma separation at the microscale: a review of design principles and microdevices. Journal of Micromechanics and Microengineering 2015 Jul; 25:083001. DOI: 10.1088/0960-1317/25/8/083001. Available from: https://iopscience.iop.org/article/10.1088/0960-1317/25/8/083001

76. Hatami A and Saadatmand M. Extremely Precise Blood–Plasma Separation from Whole Blood on a Centrifugal Microfluidic Disk (Lab-on-a-Disk) Using Separator Gel. Diagnostics 2022, Vol. 12, Page 2873 2022 Nov; 12:2873. DOI: 10.3390/DIAGNOSTICS12112873. Available from: https://www.mdpi.com/2075-4418/12/11/2873/htm%20https://www.mdpi.com/2075-4418/12/11/2873

77. Liu C, Mauk M, Gross R, Bushman FD, Edelstein PH, Collman RG, and Bau HH. Membrane-based, sedimentation-assisted plasma separator for point-of-care applications. Analytical chemistry 2013 Nov; 85:10463. DOI: 10.1021/AC402459H. Available from: https://www.ncbi.nlm.nih.gov/pmc/articles/PMC3897712/

78. Membrane Chips - microfluidic ChipShop. Available from: https://www.microfluidic-chipshop.com/catalogue/microfluidic-chips/polymer-chips/membrane-chips/

79. Mauk MG, Song J, Liu C, and Bau HH. Simple Approaches to Minimally-Instrumented, Microfluidic-Based Point-of-Care Nucleic Acid Amplification Tests. Biosensors 2018, Vol. 8, Page 17 2018 Feb; 8:17. DOI: 10.3390/BIOS8010017. Available from: https://www.mdpi.com/2079-6374/8/1/17/htm%20https://www.mdpi.com/2079-6374/8/1/17

80. Liu C, Liao SC, Song J, Mauk MG, Li X, Wu G, Ge D, Greenberg RM, Yang S, and Bau HH. A high-efficiency superhydrophobic plasma separator. Lab on a Chip 2016 Jan; 16:553–60. DOI: 10.1039/C5LC01235J. Available from: https://pubs.rsc.org/en/content/articlehtml/2016/lc/c5lc01235j%20https://pubs.rsc.org/en/content/articlelanding/2016/lc/c5lc01235j

81. Zhang H, Chen Z, Dai J, Zhang W, Jiang Y, and Zhou A. A low-cost mobile platform for whole blood glucose monitoring using colorimetric method. Microchemical Journal 2021 Mar; 162:105814. DOI: 10.1016/J.MICROC.2020.105814

82. Caratelli V, Ciampaglia A, Guiducci J, Sancesario G, Moscone D, and Arduini F. Precision medicine in Alzheimer's disease: An origami paper-based electrochemical device for cholinesterase inhibitors. Biosensors and Bioelectronics 2020 Oct; 165:112411. DOI: 10.1016/J.BIOS.2020.112411

83. Minivette® POCT - Sarstedt - PDF Catalogs — Technical Documentation. Available from: https://pdf.medicalexpo.com/pdf/sarstedt/minivette-poct/69921-152650.html

84. Hoffmann J, Mark D, Lutz S, Zengerle R, and Von Stetten F. Pre- storage of liquid reagents in glass ampoules for DNA extraction on a fully integrated lab-on-a-chip cartridge. Lab on a Chip 2010 May; 10:1480–4. DOI: 10.1039/B926139G. Available from: https://pubs.rsc.org/en/content/articlehtml/2010/lc/b926139g

85. Deng J and Jiang X. PROGRESS REPORT 1800625 (1 of 16) Advances in Reagents Storage and Release in Self-Contained Point-of-Care Devices. 2019. DOI: `10.1002/admt.201800625`. Available from: `https://onlinelibrary.wiley.com/doi/10.1002/admt.201800625`

86. Van Oordt T, Barb Y, Smetana J, Zengerle R, and Von Stetten F. Miniature stick-packaging – an industrial technology for pre-storage and release of reagents in lab-on-a-chip systems. Lab on a Chip 2013 Jul; 13:2888–92. DOI: `10.1039/C3LC50404B`. Available from: `https://pubs.rsc.org/en/content/articlehtml/2013/lc/c3lc50404b`

87. Smith S, Sewart R, Becker H, Roux P, and Land K. Blister pouches for effective reagent storage on microfluidic chips for blood cell counting. Microfluidics and Nanofluidics 2016 Dec; 20:1–14. DOI: `10.1007/S10404-016-1830-2/FIGURES/15`. Available from: `https://link.springer.com/article/10.1007/s10404-016-1830-2`

88. Kawasaki H, Shimanouchi T, and Kimura Y. Recent Development of Optimization of Lyophilization Process. Journal of Chemistry 2019; 2019. DOI: `10.1155/2019/9502856`

89. Ghosh S, Aggarwal K, Vinitha TU, Nguyen T, Han J, and Ahn CH. A new microchannel capillary flow assay (MCFA) platform with lyophilized chemiluminescence reagents for a smartphone-based POCT detecting malaria. Microsystems and Nanoengineering 2020 Dec; 6. DOI: `10.1038/S41378-019-0108-8`. Available from: `https://www.researchgate.net/publication/338838316_A_new_microchannel_capillary_flow_assay_MCFA_platform_with_lyophilized_chemiluminescence_reagents_for_a_smartphone-based_POCT_detecting_malaria`

90. Ghosh S and Ahn CH. Lyophilization of chemiluminescent substrate reagents for high-sensitive microchannel-based lateral flow assay (MLFA) in point-of-care (POC) diagnostic system. Analyst 2019 Mar; 144:2109–19. DOI: `10.1039/C8AN01899E`. Available from: `https://pubs.rsc.org/en/content/articlehtml/2019/an/c8an01899e`

91. Tonooka T. Microfluidic device with an integrated freeze-dried cell-free protein synthesis system for small-volume biosensing. Micromachines 2021 Jan; 12:1–10. DOI: `10.3390/MI12010027`

92. 5,5'-DITHIO-BIS(2-NITROBENZOIC ACID) Product Number D8130

93. Olanrewaju AO, Robillard A, Dagher M, and Juncker D. Autonomous microfluidic capillaric circuits replicated from 3D-printed molds. Lab on a Chip 2016 Sep; 16:3804–14. DOI: `10.1039/C6LC00764C`. Available from: `https://pubs.rsc.org/en/content/articlelanding/2016/lc/c6lc00764c`

94. Cai Z, Xiang J, and Wang W. A pinch-valve for centrifugal microfluidic platforms and its application in sequential valving operation and plasma extraction. Sensors and Actuators B: Chemical 2015 Dec; 221:257–64. DOI: `10.1016/j.snb.2015.06.034`

95. Hitzbleck M, Avrain L, Smekens V, Lovchik RD, Mertens P, and Delamarche E. Capillary soft valves for microfluidics. Lab on a Chip 2012; 12:1972. DOI: 10.1039/c2lc00015f. Available from: http://xlink.rsc.org/?DOI=c2lc00015f

96. Du W, Li L, Nichols KP, and Ismagilov RF. SlipChip. Lab on a Chip 2009; 9:2286. DOI: 10.1039/b908978k

97. Venzac B, Liu Y, Ferrante I, Vargas P, Yamada A, Courson R, Verhulsel M, Malaquin L, Viovy JL, and Descroix S. Sliding walls: a new paradigm for fluidic actuation and protocol implementation in microfluidics. Microsystems & Nanoengineering 2020 Apr; 6:18. DOI: 10.1038/s41378-019-0125-7

98. Liu R, Bonanno J, Yang J, Lenigk R, and Grodzinski P. Single-use, thermally actuated paraffin valves for microfluidic applications. Sensors and Actuators B: Chemical 2004 Mar; 98:328–36. DOI: 10.1016/j.snb.2003.09.037

99. Puntambekar A, Choi JW, Ahn CH, Kim S, and Makhijani V. Fixed-volume metering microdispenser module. Lab on a Chip 2002 Nov; 2:213–8. DOI: 10.1039/B206934B. Available from: https://pubs.rsc.org/en/content/articlehtml/2002/lc/b206934b

100. Nishat S, Jafry AT, Martinez AW, and Awan FR. Paper-based microfluidics: Simplified fabrication and assay methods. Sensors and Actuators B: Chemical 2021 Jun; 336:129681. DOI: 10.1016/j.snb.2021.129681

101. Salter C, Langhus DL, and Kauffman GB. Chemistry for Everyone The Chemistry of Swimming Pool Maintenance W Products of Chemistry edited by. Journal of Chemical Education 2007; 84:49. Available from: www.JCE.DivCHED.org

102. Mogera U, Guo H, Namkoong M, Rahman MS, Nguyen T, and Tian L. Wearable plasmonic paper-based microfluidics for continuous sweat analysis. Science Advances 2022 Mar; 8:1736. DOI: 10.1126/SCIADV.ABN1736/SUPPL{_}FILE/SCIADV.ABN1736{_}SM.PDF. Available from: https://www.science.org/doi/10.1126/sciadv.abn1736

103. Liu D, Liu Z, Feng S, Gao Z, Chen R, Cai G, and Bian S. Wearable Microfluidic Sweat Chip for Detection of Sweat Glucose and pH in Long-Distance Running Exercise. Biosensors 2023 Feb; 13:157. DOI: 10.3390/BIOS13020157/S1. Available from: https://www.mdpi.com/2079-6374/13/2/157/htm

104. Xiao G, He J, Chen X, Qiao Y, Wang F, Xia Q, Yu L, and Lu Z. A wearable, cotton thread/paper-based microfluidic device coupled with smartphone for sweat glucose sensing. Cellulose 2019 Apr; 26:4553–62. DOI: 10.1007/S10570-019-02396-Y/TABLES/1. Available from: https://link.springer.com/article/10.1007/s10570-019-02396-y

105. Park C, Kim HR, Kim SK, Jeong IK, Pyun JC, and Park S. Three-Dimensional Paper-Based Microfluidic Analytical Devices Integrated with a Plasma Separation Membrane for the Detection of Biomarkers in Whole Blood. ACS Applied Materials and Interfaces 2019 Oct; 11:36428–34. DOI: 10.1021/ACSAMI.9B13644/ASSET/IMAGES/LARGE/AM9B13644{_}0005.JPEG. Available from: https://pubs.acs.org/doi/full/10.1021/acsami.9b13644

106. Cho JH, Gao Y, Ryu J, and Choi S. Portable, Disposable, Paper-Based Microbial Fuel Cell Sensor Utilizing Freeze-Dried Bacteria for in Situ Water Quality Monitoring. ACS Omega 2020 Jun; 5:13940–7. DOI: 10.1021/ACSOMEGA.0C01333/ASSET/IMAGES/LARGE/AO0C01333{_}0006.JPEG. Available from: https://pubs.acs.org/doi/full/10.1021/acsomega.0c01333

107. Van Loon JC. General Principles. *Analytical Atomic Absorption Spectroscopy*. Ed. by Van Loon JC. Elsevier, 1980 :1–76. DOI: 10.1016/B978-0-12-714050-6.50006-1. Available from: https://linkinghub.elsevier.com/retrieve/pii/B9780127140506500061

108. Öztürk K. Development and in-vitro characterization of l-cysteine loaded alginate beads for oral delivery. 2022. DOI: 10.29228/jrp.119. Available from: https://dx.doi.org/10.29228/jrp.119

109. Yanagisawa N, Mahmud S, and Dutta D. Absorbance Detection in Multireflection Microfluidic Channels Using a Commercial Microplate Reader System. Analytical Chemistry 2020 Oct; 92:13050–7. DOI: 10.1021/acs.analchem.0c01961. Available from: https://pubs.acs.org/doi/10.1021/acs.analchem.0c01961

110. Ortiz U and Cuesta O. Light-Actuated Microfluidics. PhD thesis. Universitat Politècnica de Catalunya, 2017

111. DTNB (Ellman's Reagent) (5,5-dithio-bis-(2-nitrobenzoic acid). Available from: https://www.thermofisher.com/order/catalog/product/22582

112. Nelson GL, Lines AM, Bello JM, and Bryan SA. Online monitoring of solutions within microfluidic chips: simultaneous raman and uv-vis absorption spectroscopies. ACS Sensors 2019 Sep; 4:2288–95. DOI: 10.1021/ACSSENSORS.9B00736. Available from: https://pubs.acs.org/doi/full/10.1021/acssensors.9b00736

113. Guo X, Zheng F, Li C, Yang X, Li N, Liu S, Wei J, Qiu X, and He Q. A portable sensor for in-situ measurement of ammonia based on near-infrared laser absorption spectroscopy. Optics and Lasers in Engineering 2019 Apr; 115:243–8. DOI: 10.1016/J.OPTLASENG.2018.12.005

114. Huang S and Fair RB. Quantitative measurements of inorganic analytes on a digital microfluidics platform. SN Applied Sciences 2019 Dec; 1:1–14. DOI: 10.1007/S42452-019-1693-8/FIGURES/21. Available from: https://link.springer.com/article/10.1007/s42452-019-1693-8

115. Jung DG, Jung D, and Kong SH. A Lab-on-a-Chip-Based Non-Invasive Optical Sensor for Measuring Glucose in Saliva. Sensors 2017, Vol. 17, Page 2607 2017 Nov; 17:2607. DOI: 10.3390/S17112607. Available from: https://www.mdpi.com/1424-8220/17/11/2607/htm

116. Zainal Alam MNH, Jaya Kumar J, John Whyte D, Doeven EH, and Kouzani A. A portable sensor for cell optical density measurement in microfluidic chips. Measurement and Control 2018 Sep; 51:213–22. DOI: 10.1177/0020294018783440. Available from: http://journals.sagepub.com/doi/10.1177/0020294018783440

117. Gu Y, Jiao L, Cao F, Liu X, Zhou Y, Yang C, Gao Z, Zhang M, Lin P, Han Y, and Dong D. A Real-Time Detection Method of Hg2+ in Drinking Water via Portable Biosensor: Using a Smartphone as a Low-Cost Micro-Spectrometer to Read the Colorimetric Signals. Biosensors 2022 Nov; 12:1017. DOI: 10.3390/BIOS12111017/S1. Available from: https://www.mdpi.com/2079-6374/12/11/1017

118. O'Toole M and Diamond D. Absorbance Based Light Emitting Diode Optical Sensors and Sensing Devices. Sensors (Basel, Switzerland) 2008 Apr; 8:2453. DOI: 10.3390/S8042453. Available from: https://www.ncbi.nlm.nih.gov/pmc/articles/PMC3673425/

119. Chen JM, Huang PC, and Lin MG. Analysis and experiment of capillary valves for microfluidics on a rotating disk. Microfluidics and Nanofluidics 2008 May; 4:427–37. DOI: 10.1007/S10404-007-0196-X/FIGURES/10. Available from: https://link.springer.com/article/10.1007/s10404-007-0196-x

120. Oosterbroek R. Modelling, design and realization of microfluidic components. PhD thesis. Enschede: University of Twente, 1999 Nov :58–9. Available from: https://research.utwente.nl/en/publications/modelling-design-and-realization-of-microfluidic-components

A Theory

Microfluidics is the technology of manipulation of fluids having a volume in the order of magnitude 10^{-9} to 10^{-18} liters [61]. Microfluidic devices have several applications among which separation and detection are the most common. High sensitivity and resolution are challenging, yet there is a large technology push. The main advantages of microfluidic devices are the low costs and rapid read-out. The fundamentals of microfluidics have shown new capabilities for biological and chemical analyses. There has been increasing interest in microfluidics over the past years [62]. This line of research is of high value in the biomedical engineering field since the potential of lab-on-a-chip applications is a lot higher than for conventional techniques. Examples of different applications are in the direction of diagnostics, single-cell analysis, or organ-on-chip devices for disease mimicking.

In this chapter, theories relevant to the development of microfluidic devices are discussed, including capillary flow, -pressure, microfluidic valves, mixing techniques, and capillary pumps.

A.1 Capillary flow

Flow can be categorized into two types; laminar and turbulent flow [44, 63]. If fluids flow parallel in a forward direction without currents in other or the opposite direction, it is called laminar flow. In laminar flow mixing of fluids is solely dependent on diffusion, while turbulent flow enhances the mixing process due to irregular fluctuations.

Besides the different types of flow, the flow rate is also a crucial aspect of microfluidics. The Navier-Stokes equation can be used for the determination of the flow rate for fluids assuming a steady, laminar flow[58]:

$$Q = \frac{h^3 w \Delta P}{12 \eta L} \cdot \left[1 - \sum_{n,odd}^{\infty} \frac{1}{n^5} \frac{192}{\pi^5} tanh(n\pi \frac{w}{2h}) \right] \tag{7}$$

where h and w are the channel's height and width, ΔP is the capillary pressure difference over the channel, L is the characteristic length, and η is the dynamic viscosity of the fluid.

A.1.1 Reynolds number

The Reynolds number is a dimensionless measure for the turbulence of the fluid caused by viscous and inertial forces [44, 63]:

$$Re = \frac{\rho u L}{\mu} \tag{8}$$

where ρ is the fluid density, u the velocity, L the characteristic length the fluid travels, μ the dynamic viscosity. For L, the hydraulic diameter of the channel is used: $D_h = \frac{4A}{P_{wet}}$ with A the cross-sectional area and P_{wet} the wetted perimeter.

The Reynolds number can distinguish flows between laminar and turbulent flows, as for laminar flows $Re < 2000$ [63]. Turbulent flows occur when the Reynolds number is higher or when alternative microstructure designs such as the herringbone structure are present, which is discussed later. Since in microfluidics the dimensions of the channels are very small, there is (mainly) laminar flow.

A.2 Capillary pressure

Capillary pressure is the pressure difference between two immiscible fluids or gases, which can be both the driving force and the opposing force [58]. Capillary pressure is related to the surface tension and geometry of the channel. In capillary tubes, the capillary pressure is responsible for the vertical rising of the liquid.

Capillary pumps use capillary pressure to transport fluids [64]. They wick the fluids and rely on capillary action. They use the later-explained adhesive and cohesive forces to transport the fluid [65].

Microvalves are used to control the liquid flow in microfluidic devices [40]. It is a low-cost and relatively reliable system for flow control. The actuation of the valve can be either active or passive. Active actuation is possible by the usage of an external source such as electrostatic, electromagnetic, pneumatic, hydraulic or photothermal energy sources. This type of actuation is suited for devices with an external liquid pressure control or pumping of the liquid. However, the needed external energy source limits the miniaturization of the microfluidic device and could affect the liquid or device material. Passive actuation overcomes these limitations and has been shown to further improve microfluidic devices. Passive actuation is solely dependent on the Laplace pressure difference [40, 58]. The Young-Laplace equation (9) describes the relationship between the capillary pressure and the channel geometry, contact angle, and surface tension.

$$P = -\gamma \left[\frac{cos\theta_t + cos\theta_b}{h} + \frac{cos\theta_l + cos\theta_r}{w} \right] \tag{9}$$

The equation shows the relation for rectangular microchannels, where P is the capillary pressure, γ the surface tension, h and w the height and width of the channel and $cos\theta_{t,b,l,r}$ the liquid's top, bottom, left and right wall contact angles (Figure 1(a)). The liquid flow and capillary pressure can be changed by altering the dimensions of the channel.

The surface tension is the perpendicular tension between the two sides of the liquid surface [40]. The cohesion between liquid molecules is greater than the adhesion between liquid and air, therefore the liquid surface acts like an elastic membrane.

The contact angle shows the relation between the liquid and the solid surface (Figure 1(b)). The contact angle is dependent on the surface tension and the characteristics of the solid material. Negative pressure prevents liquid from flowing out of the channel due to the concave liquid-air meniscus [58]. This negative pressure is caused by a wettable surface (contact angle < 90°). If the contact angle is > 90°, the pressure is positive and the liquid will flow. Contact angles between a surface and a droplet of water < 90° are considered hydrophilic surfaces, and larger surfaces with greater contact angles are hydrophobic. A stable contact angle < 60° is preferred to create a high yield [58]. Common hydrophilic materials which can form hydrogen bonds with the liquid are aluminum, glass, and other metals and minerals [40]. Hydrophobic materials used in microfluidics are paraffin, Teflon, and/or polymers such as PDMS and PMMA.
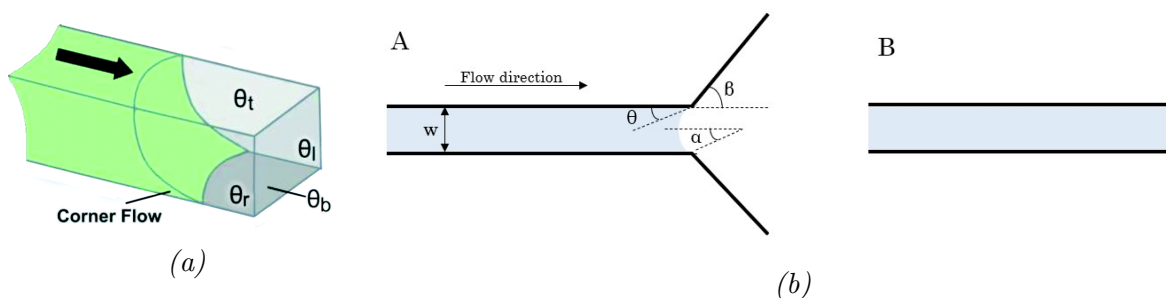
Figure A.1: A schematic image of the principle of flow in a rectangular channel with hydrophilic bottom and hydrophobic top (a), reprinted from [63], and a schematic image of the contact angle before (A) and after (B) reaching the expansion with α the meniscus curvature, β the expansion angle, θ the contact angle, and w the width of the channel (b).

When modifying the surface of the material, the hydrophobic or hydrophilic characteristics can be altered to the preferred characteristics for the microfluidic design. The most widely used materials for microfluidics are PDMS and glass [40]. PDMS is a material with several advantages for microfluidics, such as non-toxicity, light permeability, chemical inertness and stability, plasticity, and easy production. Untreated PDMS is hydrophobic with a contact angle of 113.5°. Due to the surface instability of PDMS, surface modification is difficult and the modification will always be reversed, called hydrophobic recovery. The most common surface treatment of PDMS is plasma treatment [40]. Ionized oxygen with reduced electrons and positive and negative ions is used to expose the hydrophilic functional groups of the PDMS surface. The surface energy, and thus the adhesion of the PDMS surface is increased. The hydrophilic properties will be lost in minutes due to the bonding of the functional groups with hydrophobic polymer chains. The hydrophobic recovery can be delayed by keeping the PDMS in water or using solvent extraction [40].

A.2.1 Types of microfluidic valves

Microfluidic valves are components of microfluidic devices, which control flow and liquid transport. Olanrewaju et al. reviewed different types of microfluidic valves: stop valves, trigger valves, soft valves, retention valves, burst valves, and delay valves [58]. Stop valves stop, sometimes temporarily, the flow of the liquid. This can either be done by changing the hydrophilic or hydrophobic properties of the channel or by a sudden change in geometry to create a concave liquid-air meniscus. For hydrophilic materials, an abrupt expansion of the channel creates a stop valve, and for hydrophobic materials an abrupt shrinkage. The biggest advantage of stop valves is the simple fabrication. For short durations, the stop valves have high reliability, but with increasing duration, the reliability decreases. Additionally, for low contact angles, there is a chance of creating air bubbles in the channel and an external source is needed to overcome the flow stop.

To avoid the latter problem, the flow stop can be created at an intersection with another channel [58]. This is called a trigger valve. When the liquid flowing through the second channel reaches the intersection point the liquid from the trigger valve will start flowing again. When the first liquid reaches the trigger valve the flow is blocked due to

the increase of Laplace pressure caused by the abrupt change in cross-section dimension. However, when the second liquid reaches the intersection point where the trigger valve is located a new liquid concave meniscus is created not strong enough to block the liquid flow. Trigger valves with a Y-shaped junction can stop flow for 15 minutes, while orthogonal intersection trigger valves, named two-level trigger valves, can block flow for up to 30 minutes [40, 58].

Another type of valve is the soft valve, in which the capillary pressure is decreased by manual actuation [58]. PDMS is a soft material, so when pressing on the cover with a sharp tip, the channel height is reduced and the flow restarts. The actuation by the user adds an additional step to the process, yet can be advantageous due to specific flow control.

Besides filling microchannels, microfluidic valves can also be used at the end of channels [58]. When a valve is placed before a capillary pump, the so-called retention valves allow the consecutive release of liquids. Thereby, they prevent complete drainage, the introduction of air, and vaporizing of liquids in the channels. The cross-section of the valve needs to be smaller than the dimensions of the capillary pump for the pressure to be higher and prevent liquid flow. The Young-Laplace equation (equation 9) can be used to calculate the pressure for which a burst valve bursts open. So, by creating a retention burst valve channel with specific geometry, reservoirs can be drained in a specific order. With the presence of a capillary pump, the burst pressure is limited as the pump needs to create a higher negative pressure.

Lastly, it can be desired to delay the release of one or multiple liquids for precise delivery times [58]. These delay valves can be based on porous matrices or dissolvable materials like sucrose. In the case of dissolvable materials, accumulation in the channel and interference with the assay should be prevented. An example of delay valve usage is to ensure a certain incubation time.

A.2.2 Types of capillary pumps

The generation of flow to transfer reagents through the capillaries of a microfluidic device remains a challenge [66]. In the capillary systems of microfluidic devices the flow can be regulated using a capillary pump. There are both active and passive capillary pumps, with both their advantages and disadvantages. As described before the flow is dependent on the Reynolds number, density, viscosity, and velocity gradient. The surface properties of the channel also affect the flow.

The main advantage of active capillary pumps is that they are highly efficient and create higher flow rates [66]. Passive capillary pumps are easier to fabricate and better to use in POCT, yet have lower flow rates.

In passive capillary pumps, the microfluidic design is created with dimensions from 15-250 μm to obtain a certain capillary pressure [65]. In other words, capillary pumps have a large influence on the hydraulic performance of the device. Zimmermann et al. designed various passive capillary pumps [65]. Firstly, a channel with supporting posts to prevent the PDMS structure to collapse. Moreover, they made a channel that is split into multiple smaller parallel channels to create a higher pressure. However, the flow resistance can increase significantly with increasing channel length. Lastly, to reduce the flow resistance, microstructures like hexagons can be patterned in the microchannel.

This alternative is suitable for pumping larger volumes at a constant flow rate. In passive capillary pumps solely based on capillary action it can be difficult to control the flow rate [66].

Pumps often capture air inside the device, which could affect the outcomes of the LOC device [67]. Currently, microfluidic pumps are often used in immunoassays. Additionally, capillary pumps are widely used to facilitate the mixing process of multiple reagents on chip. Vacuum-driven pumps such as degassed PDMS pumps are a great example. They rely on the gas-permeable characteristics of PDMS. To prevent pressure drop due to dissolving air into the PDMS, the outside could be coated with non-permeable materials like epoxy or glass. In blood plasma separation gravitation is usually used as force, sometimes in combination with a vacuum-driven pump for compartmentalization of the plasma. The downside of using vacuum-driven capillary pumps is that it requires vacuum storage, which complicates the manufacturing process [66].

Active capillary pumps can be based on pressure, centrifugal force, electrokinetic- or acoustic-driven methods [66]. Pressure-based active pumps can be hand or finger-operated [67]. Hand-operated devices include the usage of a syringe or pipette to create a pressure in the channels. Compared to the syringe, the pipette can more precisely insert certain volumes. Finger actuation includes pressing a button with a finger to create pressure. An elastomer chamber can be deformed by pressing on it. Electrokinetic-driven pumps are highly effective and accurate, yet have difficult fabrication [66]. It is a popular non-pressure driven capillary pump method, which relies on a charged electrode creating flow at the electrode-electrolyte surface. In acoustic-driven pumps sound waves are used for the control of fluid in microfluidic devices. Complex structures are needed to obtain a controlled flow rate using acoustic methods.

Syringe pumps are commonly used in laboratories, together with pressure pumps or peristaltic pumps [68]. However, these commercial pumps are not best suited for POCT as they are relatively expensive and bulky equipment. Still, precise flow control is of high importance in microfluidics due to the small volumes. Zhang et al. developed a portable syringe pump for POCT [68]. The pump is spring actuated and provides a constant flow rate.

For POCT, active capillary pumps are less convenient due to the complex systems. To obtain the desired sample-in-answer-out microfluidic device the required flow rate should be generated inside the device without external materials [67].

A.3 Microfluidic mixing techniques

Microfluidic-based mixing is the process of uniformly mixing two liquids in a LoC device [41]. It is one of the most commonly used processes in the microfluidic industry. In microfluidic devices, the mixing and reaction time of reactants can tremendously be reduced to only several seconds. To improve the reliability and efficiency of microfluidic mixing techniques, new methods have been investigated to optimize the performance, minimize the costs and maximize practicality. There are two categories of microfluidic mixers: active and passive mixing techniques.

Active mixing techniques aim to increase the contact area [41]. There are four types of active microfluidic mixers; based on a magnetic, acoustic, electric, or thermal field. A magnetic field can establish mixing by magnets generating a direct or alternating current. This current influences the flow and enhances mixing in a proven efficient manner. Newer studies introduced magnetic microbeads, cilia, or bars in the microfluidic device to improve the mixing process. A different way to disturb the flow of the fluid is via acoustic waves. It creates a strong vortex at sharp edges in a channel only requiring a low power input. This makes the method suitable for temperature-sensitive reagents or samples. The smaller the angle of the edges implemented in the channel, the better the mixing performance. This method is especially useful for fluids with a low Reynolds number. For fluids that are not temperature sensitive, a thermal field can be created to increase mixing via the obtained temperature gradient. An electric field can create electroosmotic vortices, which affect the laminar flow of the fluid. This method is relatively easy to fabricate. An electrolyte solution comes in contact with a solid wall, which will be hydrolyzed and attract ions from the fluid.

Next to active mixing techniques, there are also passive mixing techniques that do not require external energy [41]. They are solely based on hydrodynamics and therefore widely used. Passive mixing techniques create vortices to disturb the laminar flow of the fluid based on the geometric structure of the device. Their structures can either be specially designed or obstacle based. If the cross-sectional area of the microfluidic channel is altered, the flow is disturbed. The earliest design for passive mixing is the T-shaped mixer, in which two fluids come together via two inlets directly across from each other [44]. A variation on this microfluidic mixer is the Y-shaped channel, where the angle between the two inlets is less than 90° (Figure 2(a)). The diffusion rate is relatively slow using these mixing techniques due to the low Reynolds number caused by the flow being mainly laminar flow [41, 44]. By increasing the flow rate and further developing the geometrical design of the microfluidic mixers, the mixing efficiency was higher.

Another commonly known passive mixer is the serpentine structure [41]. It is a curved channel, which creates a difference in pressure between the inlet and outlet. It was concluded that the focal length of the x-axis is more important for better mixing than the foci of the y-axis, meaning that a longer channel works better than wider curves (Figure 2(b)). It was found that adding side wells to the serpentine structure enhances turbulent flow, and further increases the mixing performance (Figure 2(c)). Other known structures are zigzag or square-wave channels. Round cavities at the side of a straight channel

are another way to disrupt the cross-sectional area of the channel. These round cavities are combined with a T-shaped channel where two liquids are introduced in the two ends simultaneously, obtaining an efficient mixing process within seconds. For extremely small volumes the use of droplet-based mixing has been extensively investigated. With the use of round cavities, new vortices are introduced, improving the mixing by the structure of the channel.

Next to altering the shape of the channel itself, obstacles can be placed inside the channel [41]. Obstacles can introduce a different flow, enhancing the mixing process. Sharp corners are considered the most efficient obstacles. Obstacles can be placed symmetrically and asymmetrically over the channel. It is shown that asymmetrical structures can transport more fluid and are therefore more efficient, especially for fluids with a high Reynolds number. By introducing obstacles in a serpentine structure, different passive micromixing techniques can be combined.

The staggered herringbone mixer is a microchannel with an innovative design [44]. The bottom of the channel consists of a pattern of repeated grooves (Figure 2(d)). These grooves can cause a chaotic flow, for optimizing the mixing. The benefits of this design are that the path length can be reduced and it is suitable for Reynolds numbers in the range of 0-100 Re. Kwak et al. compared the results of positive and negative grooves of the staggered herringbone [45]. Positive grooves arise from the bottom of the channel while negative grooves are dug into the bottom (Figure 2(d),a). The mixing efficiency was better for the positive grooves as only two cycles were needed compared to four or five for the negative grooves. The effects of the forward and reverse patterns were also compared. Forward flow does give a better mixing efficiency compared to the negative flow.

For the staggered herringbone, adding mixing chambers next to the channel is explored [44]. This led to the design of the toroidal mixer structure. In this design the mixing was further optimized by extra vortices and centrifugal forces created by the mixing chambers, making the mixing process even more rapid. The toroidal structure allows for larger-scale production, which is useful in for example the pharmaceutical industry. Additionally Nguyen et al. reviewed more complex geometries to further increase the mixing efficiency is the above mentioned structures did not meet the requirements [69]. To obtain a higher chaotic advection, more complex geometries of the microchannel are created in these cases.

In conclusion, in passive micromixing techniques a vortex is created by altering the cross-sectional area of the channel and in active mixing methods an external energy field creates vortices for optimizing mixing. In general, active mixers are easier to make and more efficient while passive mixers are smaller, cheaper and do not have an impact on the sample [41].
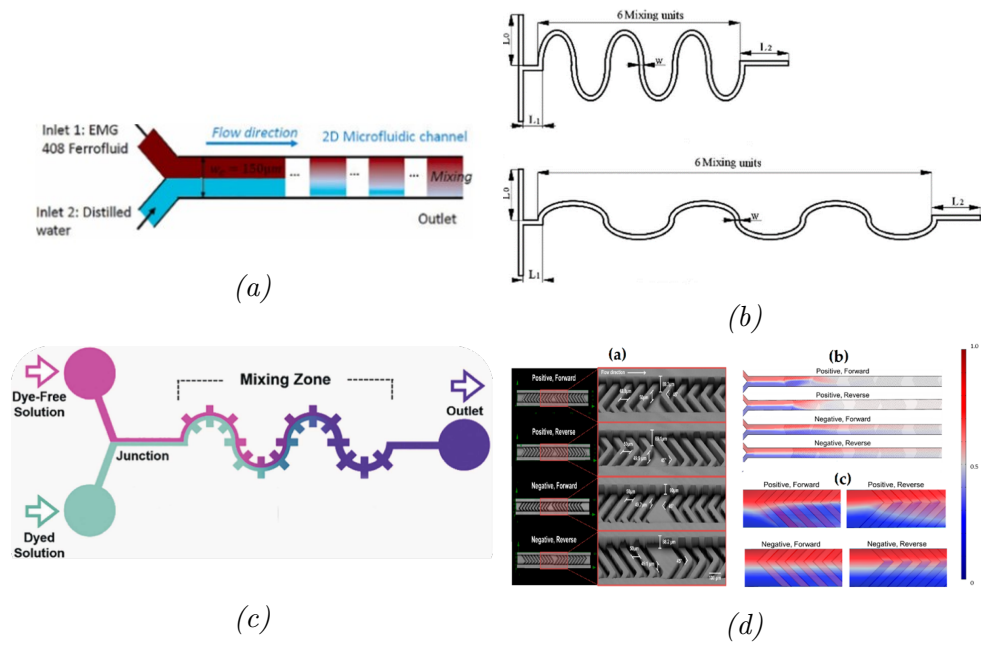
Figure A.2: The different passive microfluidic mixers: Y-mixer (a), serpentine mixer (b), serpentine mixer with side wells (c), and herringbone mixer (d) (reprinted from [41],[41],[41],[69])

B   Literature Research

Next to the theory on microfluidics, there is an extent number of already existing microfluidic devices for all kinds of purposes. In this chapter, different studies of LoC devices are investigated. Firstly, different blood plasma separation methods and examples are explored. Afterward, we looked into the possibilities to storage reagents on-chip and the different methods to keep the precise sample volumes of the reagents and samples. Paper-based microfluidics are investigated for their suitability of free thiol concentration determination in plasma samples. Lastly, the theory of absorbance spectroscopy and its application in the detection of free thiols is analysed.

B.1   Blood plasma separation methods

Microscale blood plasma separation (BPS) in LoC devices remains a challenge [70]. Current microfluidic devices with plasma samples as input often rely on bench-top centrifugation, which adds a step to the process making it more time-consuming. For POCT devices it is preferred to have complete functioning integrated in one chip. The presence of blood cells can influence the detection of the targeted biomarker. Therefore, blood plasma separation on-chip is preferred. Other challenges that can arise are due to the small sample size. In microfluidic devices the sample volume is limited due to the size of the LoC and the comfort of the patient [71]. The limited volume generates additional problems, such as limited flow rate and low Reynolds number of the blood flow. Other challenges in LoC blood plasma separation are clogging of the device and the throughput and purity of the plasma.

There are different methods for plasma separation. The first distinction is between active and passive separation methods. Active methods require an external force (magnetic-, acoustic- or dielectrophoretic force) to determine the direction of the blood cells and separate the plasma [72]. For passive methods the technique relies on capillary flow within microchannels, which does not require an external force. Due to fabrication ease and the 'self-separation', which make the device portable and user-friendly, passive blood plasma separation methods are preferred over active methods [71].

Passive separation techniques are based on sedimentation, microfiltration or hydrodynamic effects [70, 71, 72]. Of these techniques, sedimentation is the oldest and most straightforward [71]. Its principle is based on the differences in density between the blood cells and plasma, with the density of plasma being 70 kg/m^3 and 20-60 kg/m^3 lower than the density of red blood cells (RBCs) and white blood cells (WBCs), respectively [71]. The biggest limitation is the low sedimentation velocity, especially for larger volumes. For fingerprick blood volumes the sedimentation technique is commonly used. Additionally, this technique is often used in combination with microfiltration.

Blood plasma microfiltration can be categorized into four categories; weir filtration, dead-end filtration, cross-flow filtration and membrane filtration (Figure B.1A)[71]. In weir filtration obstacles in the microchannel prevent the blood cells from passing, only allowing blood plasma to flow through the narrow channel (Figure B.1A1). Both dead-end

filtration and cross-flow filtration consist of a row of pillars with narrow spacing between them, blocking access of the blood cells through the channels (Figure B.1A2,3). The difference between both methods is the flow direction, in dead-end filtration, the blood flow is in the same direction as the pillars, whereas the blood flow in cross-flow filtration is perpendicular to the pillars. The advantage of cross-flow filtration is that there is a smaller chance of clogging the pillar spaces. The last microfiltration technique uses a membrane with pores (Figure B.1A4). This technique allows for more flexibility in pore size, but complexifies the production of the device.

Separation due to hydrodynamics is based on the forces on the blood created by the capillaries. This can be explained by the bifurcation law, also called Zweifach-Fung effect [71, 73]. A red blood cell entering the bifurcation ridge will flow into the higher flow rate daughter branch due to the pressure difference and shear forces that work on the RBC (Figure B.1B)[71]. As little RBCs will flow into the lower flow rate daughter branch, it could be used to separate plasma. By creating a main channel with a larger width and smaller perpendicular placed bifurcation channels, the RBC will stay in the main channel and plasma will skim into the side channels. This principle can also be utilized to separate both RBCs and WBCs. Kuan et al. optimized the system by placing the bifurcation channels at an angle of 60 degrees and managed to separate the cells and plasma in under 20 minutes [73]. The advantage of using hydrodynamics as a separation technique is that is allows for relatively simple designs [72]. The lower accuracy of the method is a disadvantage.

Another principle of hydrodynamics is the Dean vortex flow. In a spriral microchannel a centrifugal force will be created on the flow of the fluid, which will be higher at the outside of the curvature (Figure B.1C)[71]. The pressure difference will cause a secondary flow from the outer wall to the inside wall of the curvature. The viscosity of the fluid can also create a secondary flow since the center flow of the fluid experiences a higher centrifugal force than near the outside walls, causing a secondary flow from the center to the outer wall of the microchannel. These two secondary flows together are called the Dean vortex flow. This principle can cause the RBCs to flow to the outer wall, thereby separating the plasma. A study shows that using a trapezoidal cross-section having a higher wall at the inside of the curvature, causes enhancement of the Dean vortex flow and traps the RBCs and WBCs at the outside [74] (Figure B.1C,left). In all hydrodynamic techniques the created forces are highly dependent on the radius of the channel and the flow rate [75].

The viscosity of the blood has an influence on the BPS. Differences in individuals' blood viscosity are due to their sex, health condition and diet [71]. A higher blood viscosity it related a the higher concentration hematocrit and lower temperature of the blood. The blood temperature will decrease ex vivo in the microfluidic device. Therefore it might be necessary for a functional microfluidic blood plasma separation device to dilute the blood to reduce its viscosity. For example, a study showed that for low hematocrit concentrations (0.5-1%) the separated plasma had a 100% purity. This purity decreased with increasing hematocrit concentrations. According to Kuan et al. separated plasma has two requirements [73]. Firstly, a minimum plasma dilution factor as this could lead to background interference when measuring the biomarker. Secondly, a low hemolysis effect since this will lead to plasma contamination.

B.1.1 On-chip or off-chip BPS

According to Mielczarek et al. on-chip blood plasma separation should be prevented as there are too many uncertainties in the LoC developments regarding the separation process [70]. If possible, they recommend to use whole blood samples. The uncertainties in separation arise from the requirement to dilute the sample in most cases, which leads to inconsistencies in the measurements. Additionally, complex designs and time consuming systems cause extra costs. Currently, blood plasma separation in tests and as sample preparation for LoC devices is obtained using a centrifuge. The benefits of using a centrifuge over the on-chip separation techniques are the high obtained yield, purity and reproducibility of the machine. In general, it is a very well established separation technique. Mielczarek et al. do list limitations of the centrifuge regarding its use for POCT [70]. Centrifuges are bulky and expensive machines, which are designed for batch processing. In the article they name the advantages of microfluidic devices over centrifuging, which mainly are the low-costs, portability, standardization and integration in continuous flow of the device. Overall the limitations of on-chip BPS are lack of reproducibility due to varying effects and efficiencies, and the low obtained yield. In more detail the advantages and disadvantages per blood plasma separation technique can be found in Table 10.

A microfluidic centrifugal disk, combines the advantages of centrifuging and microfluidic devices. The devices are also known as lab on a disk (LoaD). They are also based on the hydrodynamic effect and have high potential for clinical application [76]. The rotational force causes the plasma to separate from the blood due to the same principle as in larger centrifugal machines (Figure B.1D). Different designs are developed and currently, they can achieve a plasma purity of >99% and the plasma can be transferred into a different chamber on the device [76]. The downside of centrifugal disks is that still an external rotating platform is needed for the blood plasma separation. Additionally, looking at all the steps that need to be integrated for the free thiol assay on-chip, a LoaD is not preferred.

Next to centrifuging, there are other microfluidic off-chip devices. For example, a small off-chip cartridge design based on sedimentation, with superhydrophobic walls and a membrane in the middle is used for blood plasma separation of relatively big volumes (200 μL) [77]. 1-8 mL whole blood is introduced in the device and the separation process takes approximately 10 minutes, whereafter the plasma can be pipetted out of the device (Figure B.1E). Another example exists of a superhydrophobic device which increases the contact angle of the blood sample, increases the blood clotting time and reduces hemolysis. The membrane in the middle of the superhydrophobic material is pushed on top of the sample to obtain the plasma (Figure B.1F). Additionally, there are commercially available BPS devices (Figure B.1G) [78]. Using one of these devices or using sedimentation would be an option. However, the plasma then should be manually added to the buffer and pipetted into the chip.

Table 10: The advantages and disadvantages of the different passive blood plasma separation.

	Advantages	Disadvantages
Centrifuge	High yield and purity	Time-consuming Large samples Bulky equipment Expensive
Sedimentation	Portable Small sample volume Very low-cost	Time-consuming Low yield
Microfiltration	Portable Small sample volume Low-cost	Chance of clogging Low flow rate
Hydrodynamic effect	Portable High-throughput Continuous output	Large sample volume Low yield Sensitive to flow rate

Based on the literature, there is chosen to start the testing phase using an off-chip blood plasma technique; the centrifuge. This will make the microfluidic device usable for POCT performed by specialists. When focusing on patient use of the device, blood plasma separation on chip is preferred. Based on the listed advantages and disadvantages of the passive blood plasma separation techniques on chip (Table 10), the membrane microfiltration is most convenient. Even though it adds an extra fabrication step, it is expected to be most robust since hydrodynamics is especially dependent on the flow rate. For LoaD devices, or other hydrodynamic based devices, the patient would need external machinery to establish the rotating force, which makes it less attractive for the purpose of at home measuring.

A suitable membrane is the Pall Vivid™ Plasma Separation Membrane [53]. It is a highly efficient membrane of approximately 330 μm thick, which is widely used in the industry [53, 77, 79, 80, 81]. It is appropriate for microfluidic devices and has a plasma separation time below 2 minutes. It is a highly hydrophilic, asymmetric polysulfone matrix, which captures the whole blood cellular components (Figure B.2). There are three different types of membranes differing in pore size, and based on the preferred input sample volume, the most suitable membrane can be selected. Important characteristics are that the abundant proteins can pass through the filter and the prevention of cell lysis. Liu et al. used the Vivid™ membrane more than once and received sufficient plasma purity (Figure B.1E,F) [77, 80]. Besides, more recent studies show the suitable use of this membrane [81, 82].

B.1.2 Sample collection

According to the UMCG both plasma and serum samples give similar results for the free thiol assay. For POCT, the Minivette® can be utilized for exact sample collection [83]. Firstly, a fingerprick needs to be performed to obtain the blood drops. There are also

home kits available for this. After the patient washed their hands and cleaned them with an alcohol wipe, the lancet can be pressed into the finger. After wiping the first drop of blood, the whole blood sample can be collected using the Minivette®. To use the device, the tip is hold against the blood drop from the fingerprick and the air hole at the piston should be open. When the blood reaches the filter and no air bubbles are visible the collection is completed. The Minivette® is available for volumes of 10, 20, 50, 100 and 200 μL. The blood sample can be released from the device by slightly pressing the piston. It can accurately dispense the blood samples without spillage, which makes it suitable for usage by patients. The device is neutrally available or with a EDTA or heparin coating.
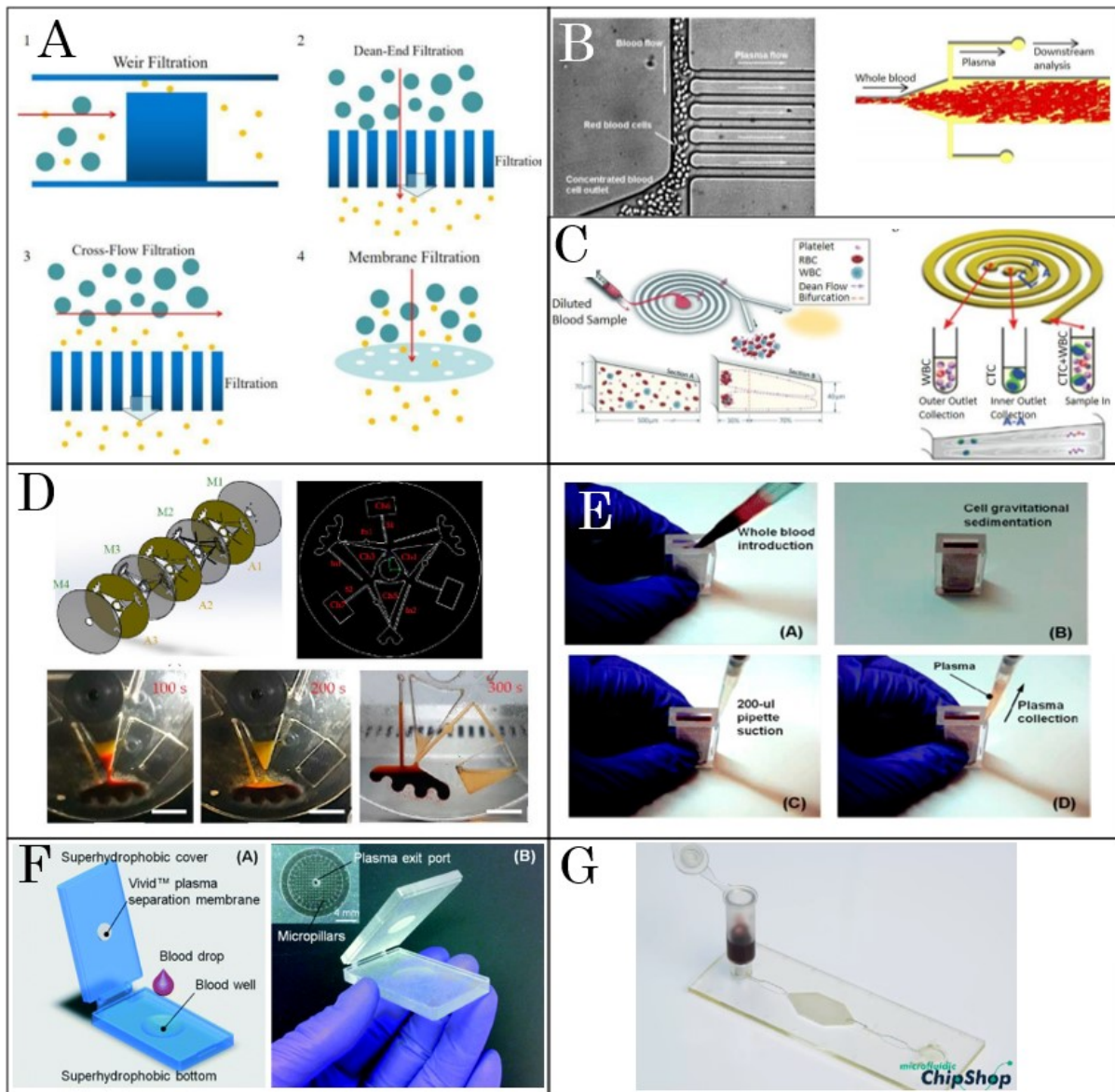
Figure B.1: A schematic image of the different filtration techniques (a), a schematic image of the Zweifach-Fung effect (b), a schematic image of the Dean vortex principle (c), an image of BPS on a LoaD (d), an example of a membrane-based BPS (e), an example of a membrane-based BPS (f), a commercially available membrane-based BPS system (g). (a-g reprinted from [71],[71],[71],[76],[77],[80],[78]).
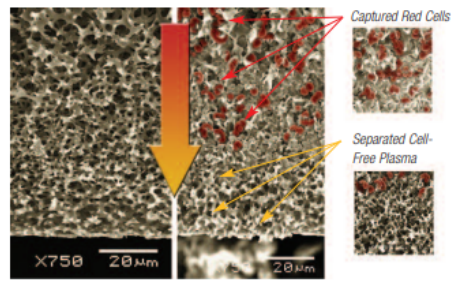
Figure B.2: Pall's asymmetric Vivid^{TM} Plasma Separation Membrane capturing RBCs and allowing the passing through of plasma (reprinted from [53]).

B.2   On-chip reagent storage

Compared to conventional diagnosis or monitoring techniques, microfluidic devices are smaller, require fewer steps and these steps do not always need to be performed by specialists [84, 85]. This makes microfluidic devices easier and more convenient. It remains one of the biggest challenges for LoC devices to store liquid reagents on-chip [84]. An ideal situation would be self-containing microfluidic devices, in which all reagents for the detection are integrated. This would make the devices more patient-friendly, and better suitable for POCT without needing medical specialists [85, 86]. Different techniques for on-chip reagent storage have already been investigated, yet there is no universal integration method considered [85]. In this chapter the use of three manually activated methods for on-chip liquid storage are discussed.

Firstly, the use of glass ampoules has been explored. Glass ampoules containing reagents are placed inside a cartridge [84]. The reagent can be released on demand by firmly pressing the flexible cartridge until the glass ampoule breaks (Figure B.3A). The usage of glass has several advantages, such as the inert and airtight properties of the material. This allows for long-term storage and prevention of cross-contamination of reagents. They suggest storing liquids in glass ampoules together with lyophilized reagents on the same chip.

Stick-packaging is another method for on-chip reagent storage, which is already widely used in food and drug packaging [86]. Oordt et al. miniaturized the method for LoC usage and created stick packages for volumes of 80-500 μL (Figure B.3B). The packaging can burst to release the liquid when pressures of 20-140 kPa are applied. They showed a reagent loss of < 0.5%. In addition to bursting the reagents, they created a more reliable releasing method using trigger valves. LoC devices need to prevent leakages and therefore be shock-resistant, as leakage of reagents will influence the results of the test. As trigger valves are sensitive to vibrations and shocks, they can be sealed using paraffin. The paraffin wax melts at 65° [85], and can be melted using a laser, heater or Peltier element. This method is called phase transition valves, and even though it is a simple method, additional energy sources are not preferred [86].

A similar method to the stick-packages, also used for packaging in the pharmaceutical industry, are blister pouches (Figure B.3C)[87]. This method has proven to protect the reagent from UV exposure and increase the shelf-life of the device. Due to these advantages and the simple nature of the packaging method, it is already widely used. Smith et al. further investigated a possible mechanical actuation system for controlled fluid release [87]. Their developments ensured precise volume control, which was successfully used in blood cell count experiments.

Besides these methods, Deng and Jiang reviewed different other storage methods for liquids [85]. For DNA detection, the reagents are stored in the microcapillaries of the device. Others investigated a vacuum syringe for storage of liquids and in centrifugal microfluidic disks the liquid is stored in reservoirs as there is no easy leaking. A thermoplastic elastomer membrane can be used to separate a reagent from the sample or other reagents until heated. Lastly, they showed the use of a PDMS sponge which contains

reagents and are released when pressure is applied. They emphasized on that liquid storage is difficult due to the storage conditions of some reagents. Due to the complexity of these reviewed examples [85], there is focused on the relatively simple manually actuated on-chip reagent options. The advantages and disadvantages of the glass ampoules, stick packages, and blister pouches can be found in Table 11.

Table 11: The advantages and disadvantages of the different on-chip liquid storage methods.

	Actuation method	Advantages	Disadvantages
Glass ampoules	Mechanical actuation	Inert Airtight	Larger volumes Chance of glass splinters
Stick-packaging	Mechanical actuation	Miniaturized UV protection Low reagent loss	Difficulty sealing
Blister pouches	Mechanical actuation	Miniaturized UV protection Low reagent loss Clear fluid direction	More expensive
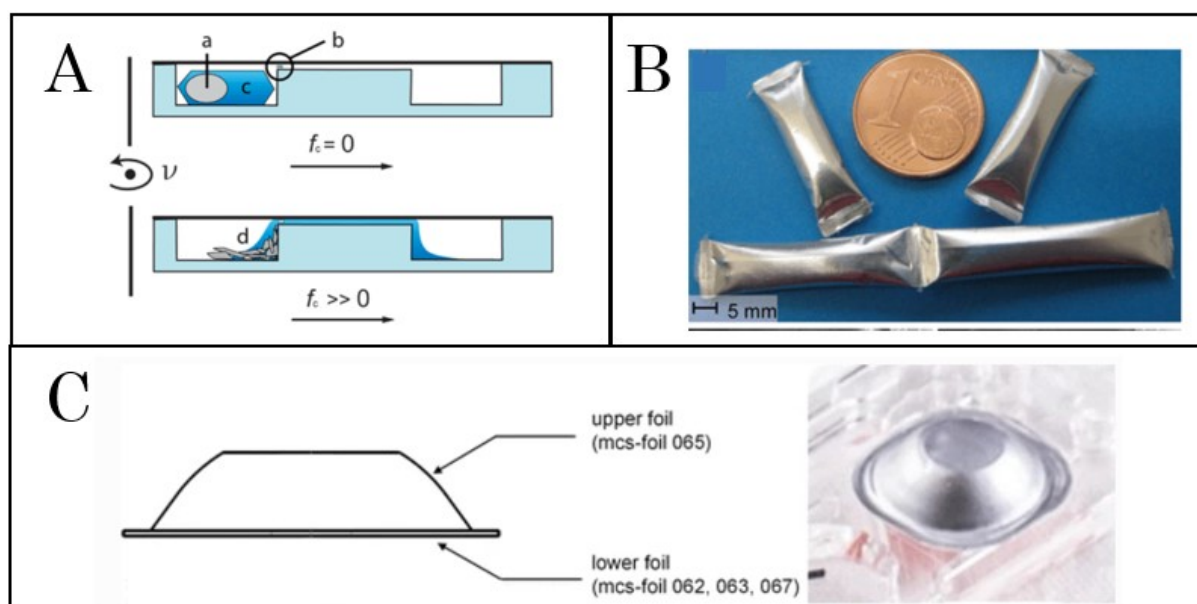
Figure B.3: An overview of the literature research on on-chip reagent storage with glass ampoules (a), stick packaging (b), and blister pouches (c). (a-c reprinted from [84],[86],[87]).

Lyophilizing liquid reagents is another option for easily storing them on-chip[85]. This procedure, also known as freeze-drying, uses a vacuum and low temperatures to remove the water from the reagent. In the pharmaceutical industry, lyophilization is an effective and long-established process [88]. If the lyophilization process is not fully optimized it can

be time-consuming and costly. The process consists of three steps; the freezing step, the primary drying step, and the secondary drying step (Figure B.4). In the freezing phase, the temperature is significantly dropped to transform the water in the substance into ice, which can take several hours. The pressure in the liquid's chamber or microfluidic channel is lowered below the equilibrium vapor pressure of ice during the primary drying step. This step is also called the sublimation step since the temperature is increased to obtain a heat transfer from the surface to the product. This causes sublimation of the ice, and the vapor will be collected in a condenser. The secondary drying step is to remove water that did not freeze during the freezing step. In this step adsorption of remaining water captured in solute components takes place. This step can also take several hours and determines the quality of the created freeze-dried product.

Deng and Jiang name several examples of lyophilization in microfluidics [85]. For example, the creation of a patterned scaffold, storing freeze-dried components in paraffin or lyophilizing substrates on glass fibers to activate a chemiluminescence reaction. The lyophilization method is a well-known method for the on-chip storage of reagents. It is commonly used for polymerases, primers, and dyes [79]. LAMP reactants can be freeze-dried and stored for over one year. Storing lyophilized reagents in paraffin is a method to better secure the lyophilized reagent [85]. However, the stored reagent has to be temperature resistant.

According to Ghosh et al., lyophilization facilitates the ideal sample-in-answer-out chip as no user intervention is needed [89]. In their design, they created a lyophilization chamber of a volume of 30 μl with capillary channels above and under the chamber. The narrow capillaries prevent the fluid from flowing back. The lyophilization is obtained by first pre-freezing the liquids using liquid nitrogen for 5 minutes, and afterwards freezing at -54°C and 0.010 mbar for 24 hours [90].

Tonooka showed another example of freeze-drying a liquid in a microfluidic device [91]. The microfluidic device was first placed In a vacuum chamber for 20 minutes, whereafter the liquid was pipetted in the inlet. When the chambers of the device were completely filled, 200 μl air was injected into the channel in 0.8 seconds. In this method, there was also chosen to pre-freeze the liquid at -80 °C for 30 minutes, and afterward, it was freeze-dried at -20 °C for 3 hours at -10mTorr. The freezing conditions were dependent on the vacuum pump. Dried particles were visible under the microscope after the lyophilization process.

Table 12: The advantages and disadvantages of lyophilizing reagents.

	Advantages	Disadvantages
Lyophilization of reagents	Long-term stability	Adds fabrication step
	Easy transportation	Complex method
	No reagent preparation	More expensive
	Sample-in-answer-out prospects	Loss of activity some reagents

For the dilution of the plasma, lyophilization is not possible, but for the DTNB storage it has potential. Even though it adds to the complexity of the fabrication, it has many advantages for on-chip storage of reagents (Table 12). DTNB is bought as a lyophilized

powder and manually dissolved in a phosphate buffer. Additionally, DTNB reacts at room temperature and is not known to be temperature sensitive [92].
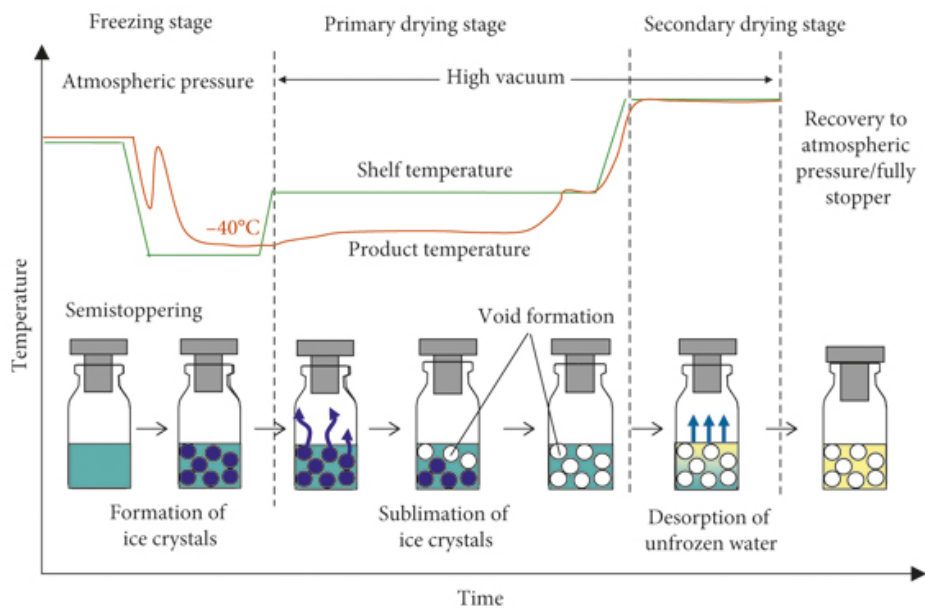

Figure B.4: Schematic visualization of lyophilization process: the freezing step, the primary drying step, and the secondary drying step (reprinted from [88]).

B.3 Volumes control

For the detection of the free thiols in plasma, it is essential that the 1:4 plasma to Tris buffer ratio and 1:4.5 DTNB to diluted plasma ratio are very precise. It is challenging to measure these sample volumes on-chip accurately. The absorption and background absorption will be measured from the diluted plasma sample, before and after DTNB addition. It is important to find a balance between obtaining turbulent flow for mixing enhancement and keeping the laminar flow to prevent backflow. Backflow or diffusion of DTNB into the control read-out chamber should be prevented. Additionally, if using trigger valves, they should empty the reservoirs completely to obtain the right ratios. In this chapter different methods to allow for precise sample volumes are discussed. Since many different methods have been researched, a selection of interesting options for the application of the free thiol assay is discussed and compared.

Possibly, retention burst valves will be more suited than trigger valves in this device since these can be emptied completely. Retention burst valves can sequentially release liquid from reservoirs, based on the geometry characteristics. Differences in height and width cause differences in capillary pressure. The design of Olanrewaju et al. can autonomously deliver eight different liquids in order and in under 7 minutes [93]. The principle is based on the burst pressure of reservoirs which will burst when activation liquid is pipetted into the inlet channel, leading to drainage of the reservoir (Figure B.5A). The advantage is that different liquids can be added to the sample in a specific order.

Besides looking into retention burst valves, other valves could also play a role in obtaining the exact ratios needed in the development of the design. All different types of valves are extensively investigated for their use in precise volume regulation in microfluidic devices [94]. Mechanical valves show excellent prospects for volume regulation [94]. Mechanical actuation valves could be used to add a partition between the absorption and background absorption sample after the addition of DTNB, which could help the prevention of backflow. Additionally, mechanically actuated valves could be used to empty reservoirs.

One example of a mechanically actuated valve is developed by Hitzbleck et al. [95]. Their design, named a capillary soft valve, is based on the principle of a capillary barrier at the inlet of a reservoir. This capillary barrier is a cross-section expansion and can be decreased by pressing on top of the valve with a pencil or tweezers (Figure B.5B). They claim that valves play a large role in the timing of reactions, for example in their successfully performed nucleic acid probe hybridization on-chip. These mechanically actuated valves have several advantages since they do not need external bulky equipment for actuation, or incorporation of other structures during fabrication. They do require one side of the device made of a soft material like PDMS and appropriate surface chemistry.

Pin-type valves are also mechanically activated and have several advantages; "simple structure, robust operation, low dead volume and leakage, and non-contact with the sample" [94]. This type of valve has different actuation mechanisms. Cai et al. developed a pinch-valve for centrifugal disks [94]. In their design, they use a spring plunger, which presses against a channel separated by a membrane. In the initial state the valve

is closed, and by creating a centrifugal force by spinning the actuation disk the valve can be opened (Figure B.5C). The actuation disk is connected to a flyball governor. The burst frequency to open the valve is 910 rpm. The valve is opened since the flyball governor lowers the actuation disk and pulls the spring plunger away from the membrane.

The SlipChip is a known example in which controlled sample volumes are used for multiplexed experiments [96]. The SlipChip is also based on mechanical actuation and exists of two PDMS microwell plates. The bottom plate consists of an array of wells containing the reagents. A top plate contains wells for the sample complementary to the bottom-plate wells. A fluidic path is created between the top en bottom plate when assembled, which can be used to load the sample. To activate the experiment the top plate is slid over the bottom plate, which allows the sample and reagent to mix (Figure B.5D). To quote Venzac et al.: "Highly parallelised fluidic operations can be performed with a simple mechanical motion, but the variety of operations permitted is limited, and the tight seal between the plates requires a thin lubricating layer of oil [97]."

Due to these limitations Venzac et al. developed another mechanical actuation method: sliding walls [97]. This method physically places a partition in the channel, which could be used for the prevention of backflow or diffusion. For the fabrication of sliding walls, they use soft-lithography for the fabrication of PDMS molds. A rigid structure functioning as a wall is slid into the PDMS guiding channel (Figure B.5E). This guiding channel is perpendicular to the flow channel and blocks liquid flowing through the channel. This method can be manually actuated, so does not need bulky equipment for actuation, which makes it smaller, simpler and cheaper. Additionally, in this paper, they mention that manually driven mechanical actuation methods are beneficial for non-specialists.

Liu et al. developed a thermally actuated valve with paraffin as actuation material. They tested their chip for use of a DNA polymerase chain reaction (PCR) [98]. The analyte could be isolated successfully during the reaction. In the article, they explain different designs with paraffin incorporated; a 'close-open' valve, an 'open-close-open' valve and a 'T-valve'. All designs can be used for different purposes. In all designs, a bulk of paraffin is placed in a heating zone (Peltier element or resistive heater). By heating the device to 90 °C the birthday candles melt as the melting temperature is 70°C. After heating, pressure from the upstream channel section moves the paraffin downstream (Figure B.5F). When removed from the hot plate, the paraffin solidifies.

Another option is to use a pneumatically activated design. Puntambekar et al. developed a microdispenser that allowed for loading small volumes into a chip with high accuracy and repeatability [99]. Their design consists of a reservoir which size determines the volume with two passive valves at each sides of the reservoir. Between the valve at the side of the inlet and the reservoir an air inlet placed, much smaller than the width of the channel. When air flows into the inlet with a higher pressure than the resistance of the passive valve at the other side of the reservoir, a split in the liquid channel is created, causing the reservoir to be drained. In Figure B.5G the process of the precise volume drainage is shown.

Quake-valves are another pneumatically operated method. Quake-style valves are

commonly used PDMS valves, which are normally open. They consist of two layers with perpendicular microchannels. Bossink et al. developed quake-style PDMS macrovalves for larger geometry chips, in their case for the accommodation of cell cultures in an organ-on-chip [47]. They use molds obtained via micromilling en created closing channels with a maximum size of 700x1000 μm. A flow layer and control layer were created from PDMS, which are aligned on top of each other (Figure B.5H). They used consecutive macrovalves to mimic a peristaltic pump motion, which increased the mixing of two liquids.

Zheng et al. developed another Quake-valve, which does not make use of an external pressure source [55]. In their design, they designed the control layer on top of the flow channel layer. They use screws to pneumatically activate the valve. The control layer is filled with water and sealed with a thin PDMS layer. By manually rotating the screw, pressure to close the valve is obtained. They used a top-down Quake-valve, while Bossink et al. used the bottom-up principle [47, 55]). In Figure B.5I a visualization of the opening and closing of the valve is shown. All valves are open in the top images, and the second valve is closed in the bottom images. The PDMS membrane between the two layers pushes onto the flow layer preventing liquid to flow through [55]. Quake-valves with the control layer connected to a pressure regulator need bulky and expensive hardware that applies continuous pressure. The advantages of this valve are its simplicity and easy fabrication. Additionally, it does create dead volume. However, the downsides are that the valve is relatively slow to operate and it is not electronically controlled. In the article, they do mention the possibilities of controlling the valve electronically using a braille display.

Table 13: The advantages and disadvantages of the precise sample volume methods.

|	Actuation method	Advantages	Disadvantages
Retention burst valve	Passive valve	No external machinery Specific order drainage	Very flow rate dependent Error prone
Pencil valve	Mechanical actuation	Easy to actuate	Not the most precise volume Single use valve
Pin valve	Mechanical actuation	Reusable	External force needed
SlipChip	Mechanical actuation	Easy to use	Single-use Limited usability options
Sliding walls	Mechanical actuation	Reusable Simple, low-cost materials	Difficult fabrication Chance of leaking
Paraffin valve	Thermal actuation	Complete sealing analyte	Extra fabrication step Heating element needed
Microdispenser	Pneumatic actuation	Very accurate volumes Nothing touching sample Reusable	Highly sensitive Error prone
PDMS macrovalve	Pneumatic actuation	Easy fabrication (micromilling) Reusable	Extra fabrication step Larger volumes
Screw Quake-valve	Mechanical + Pneumatic	Reusable Easy actuation	Extra fabrication step Slow
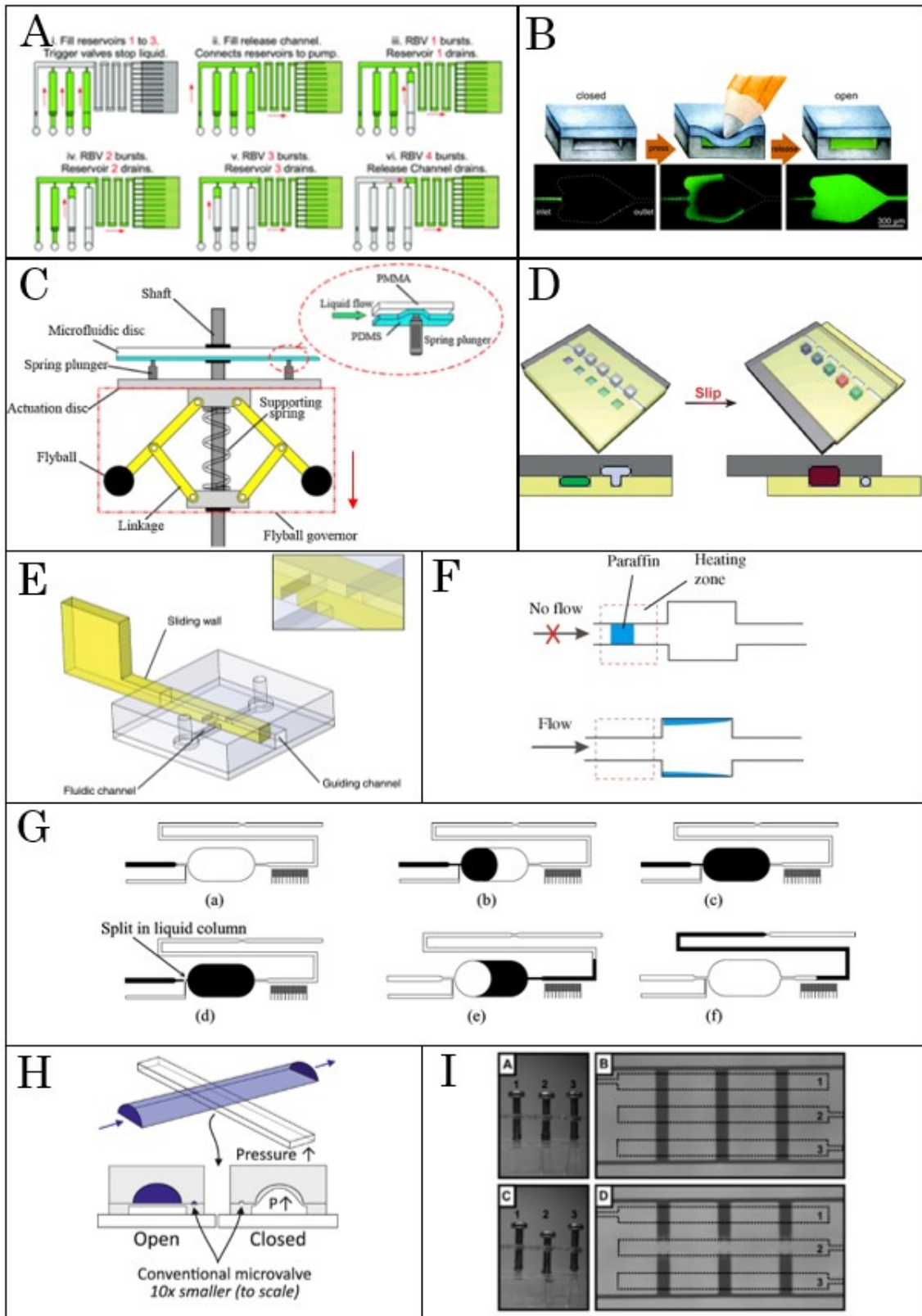
Figure B.5: An overview of the literature research on valves to maintain precise samples volumes: Retention burst valves (a), Pencil valve (b), Pin valve (c), SlipChip (d), Sliding walls (e), Paraffin valve (f), an air-based microdispenser (g), PDMS macro Quake-valve (h) and a screw-driven quake-valve (I) (reprinted from [93],[95],[94],[96],[97],[98],[99],[47],[55])

B.4 Paper-based microfluidics

Paper-based microfluidics is another branch of microfluidics, characterized by the devices made of paper or other porous membranes [100]. The driving force in paper-based microfluidics is also capillary action. Instead of channels created through micromilling or lithography, channels are patterned in the paper. There are many different methods to pattern these channels, including plotting, printing, masking and stamping. The most commonly known fabrication method is cutting. This is a very simple method, without the need for much external equipment or any chemicals. Another popular method is wax printing. In this method, a hot plate or wax printer is used to pattern wax on the paper creating hydrophobic walls of the channels.

Microfluidic paper-based analytical devices (μPADs) are more widely investigated due to their simplicity [100]. The readily available materials and simple fabrication, together with the low price and no need for external pumps, make them perfect for POCT. One example that has been frequently in the news in the past few years is the COVID-19 μPAD. This μPAD is a lateral-flow assay, which has the same principle as a home pregnancy test (Figure B.6A). In lateral-flow assays, multiple layers of porous membranes are stacked. On a sample pad, the sample is placed which is wicked through the device. The device includes a test line that forms a colored band when a certain analyte is present in the sample. The downside of lateral-flow assays is that they only allow for qualitative answers. Besides lateral-flow assays, dipsticks are other conventional μPADs. Dipsticks contain dried reagents and are dipped into a liquid sample, which can allow a certain color change (Figure B.6B). The advantage is that this method can provide some information on the concentration of the analyte in the sample based on its color shade or intensity. However, this usually has low specificity and a poor limit of detection. Commonly known examples are the pH color strips and the chloride strips to measure the total chloride concentration in pools [101]. If the test strip is placed in the liquid it will give a color change indicating the pH or chloride concentration. These types of tests are provided with a series of color references to be able to determine the right pH or concentration. The tests are excellent for a first indication, yet lack a good sensitivity.

Next to the named examples μPADs have many more possible detection examples, such as: "viral hepatitis, HIV/AIDS, dengue, tuberculosis, typhoid, malaria, and non-communicable diseases (e.g. diabetes, obesity, hypertension, cardiovascular disorders, and cancer)" [100]. For the development of a lab-on-a-chip for free thiol detection literature research is performed on paper-based microfluidics with colorimetric analyses, paper-based blood plasma separation, and freeze-drying on paper.

A newly developed paper-based microfluidic sensor is a patch for sweat secretion analysis [102]. Sweat is a body fluid that can be used for sensing physical activity and health monitoring. From sweat, different analytes such as ions, hormones, and drugs can be measured. Mogera et al. created a sweat sensor with an inlet reservoir connected to a chromatography paper channel containing gold nanorods (Figure B.6C) [102]. It can real-time measure analyte concentrations, and sweat loss and rate. The measurements are performed using surface-enhanced Raman spectroscopy (SERS). They protect the skin during SERS measurements by implementing black carbon blocks in the sensor. A layer of double-sided tape is placed on the skin on which the carbon blocks, the paper

channel, plasmonic sensors and PDMS top layer are placed. This construction makes the sensor flexible, thin, stretchable, and possible to easily remove without irritation to the skin. Some of the relevant advantages they list for this study are cost-effectiveness, easy disposal, no need for an external pump or force, absorbency for sample and reagent storage, and no risk of bubbles due to air permeability. Additionally, they state that the serpentine structure in paper-based microfluidics is also beneficial for mixing purposes. With their sensor, they measure the uric acid concentration of healthy individuals. They quantified a concentration of 28 μM from a sample volume of 13 μl.

Another paper-based sweat sensor, which measures pH and the glucose concentration of long-distance runners, is developed by Liu et al. [103]. It is an instant colorimetric and non-invasive sensor. Sweat is collected in a reservoir and flows through Triton X-100 modified hydrophilic channels to the paper on which the color reaction takes place (Figure B.6D). Glucose oxidase is used for the color reaction of glucose and commercial pH test paper was used for the pH measurements. They use a smartphone to take pictures of the sensor and quantify the glucose and pH values. Colorimetric detection in sweat analysis is more suitable than other methods since it's simple and easy to read out results. In all performed tests, the paper-based sensor was saturated due to the limited sample volume needed. The developed chip can detect relatively low glucose concentrations from sweat in the range of 0.05 mM to 0.40 mM, and a pH in the range of 4.0 to 6.5. To obtain these values they determined the RGB-values using Color Analysis software. The higher the glucose concentration, the darker blue the sample colors, and the lower the R-value in the software. A higher pH gives a darker yellow/greenish color and the B-value increases accordingly.

Xiao et al. developed another paper-based μPAD for the colorimetric detection of sweat glucose [104]. They sequentially add chitosan, glucose oxidase, horseradish peroxide and 3,3',5,5'-tetramethylbenzidine (TMB) on filter paper for the development of the glucose sensor. A difference is that they use hydrophilic cotton thread is used as microfluidic channel, which is sewed to a wearable fabric for sweat collection (Figure B.6E). In their experiments, they also use a smartphone for the RGB-values determination. They used the Color Grab application software. To prevent light interference they did the analysis in a dark box and used the smartphone's LED as the only light source. A linear calibration curve for the decreasing R-value with increasing glucose concentration could be obtained from the μ-PADs for artificial glucose concentrations 0-1500 μM. However, as also seen in the glucose sensor from Liu et al. in the practical application of the sensor the range of measurements with a linear relationship was decreased to 0.05-0.25 mM with a detection limit of 0.035 mM. Therefore, colorimetric detection can be useful, yet it is dependent on the physiological range of the analyte of interest and the linear detection range.

Park et al. developed a paper-based LoC for biomarker detection in whole blood [105]. They combined their μPAD with a commercial blood plasma separation membrane (Figure B.6F). They used the Pall Vivid$^{\text{TM}}$ Plasma Separation Membrane type GR. In their μPAD they attached the membrane to the filter paper using adhesive tape. The challenge in designing such a microfluidic device lies in the fabrication of the chip since the alignment and bonding need to be very precise to prevent leakage. They used 3D printing

to print reservoirs for sample collection on the membrane and detection reservoirs on the filter paper. The RBCs were filtered and plasma was obtained. In the detection zone, they dried a reagent mixture in an incubator at 37 °C for 10 min, causing a color reaction with its substrate. They state their µPAD is useable for POCT and the detection of several biomarkers from whole blood. They were able to measure clinically relevant glucose concentrations in diabetes patients with a limit of detection of 0.3 mM. Other biomarkers they could detect were cholesterol and triglycerides.

The lyophilization of reagents on filter paper in paper-based microfluidic devices has been widely investigated [106]. As mentioned before is freeze-drying commonly used for the preservation and long-term storage of biological samples and reagents. Cho et al. freeze-dried bacterial cells on sensors for monitoring water quality [106]. They used lyophilization as a storage method since the cell's activity and viability could be maintained longer, and the transport is easier (Figure B.6G). For measurements, water is dropped on the sensor with freeze-dried bacteria, rehydrating the bacteria and resulting in current outputs.

Chen et al. freeze-dried antibodies on their origami-paper-based µ-PAD (Figure B.6H) [57]. They found out that lyophilization of the antibodies increased the stability and reproducibility of the assay due to extended storage possibilities. Additionally, it allowed for high user-friendliness and possible automation of the complete assay, which has high prospects for the desired sample-in-answer-out principle. They developed their device to detect protein A in human synovial fluid, which is related to the *Staphylococcus aureus* infection. They used a CMC-EDC/NHS surface modification to create a signal amplification. After adding 3 µL analyte to the inlet reservoir, it was slit onto the detection area with the freeze-dried antibodies. After washing with PBS to transport the antibodies to the inlet reservoir and wash away non-specific bindings, the part was slit back for visual analysis of the color change after the addition of TMB. The whole process can be performed in under 7 minutes. Due to the addition of different liquids, it is not completely automated, yet still very suitable for POCT. The device has a limit of detection of 0.01 ng/mL.

Table 14: The advantages and disadvantages of paper-based microfluidics.

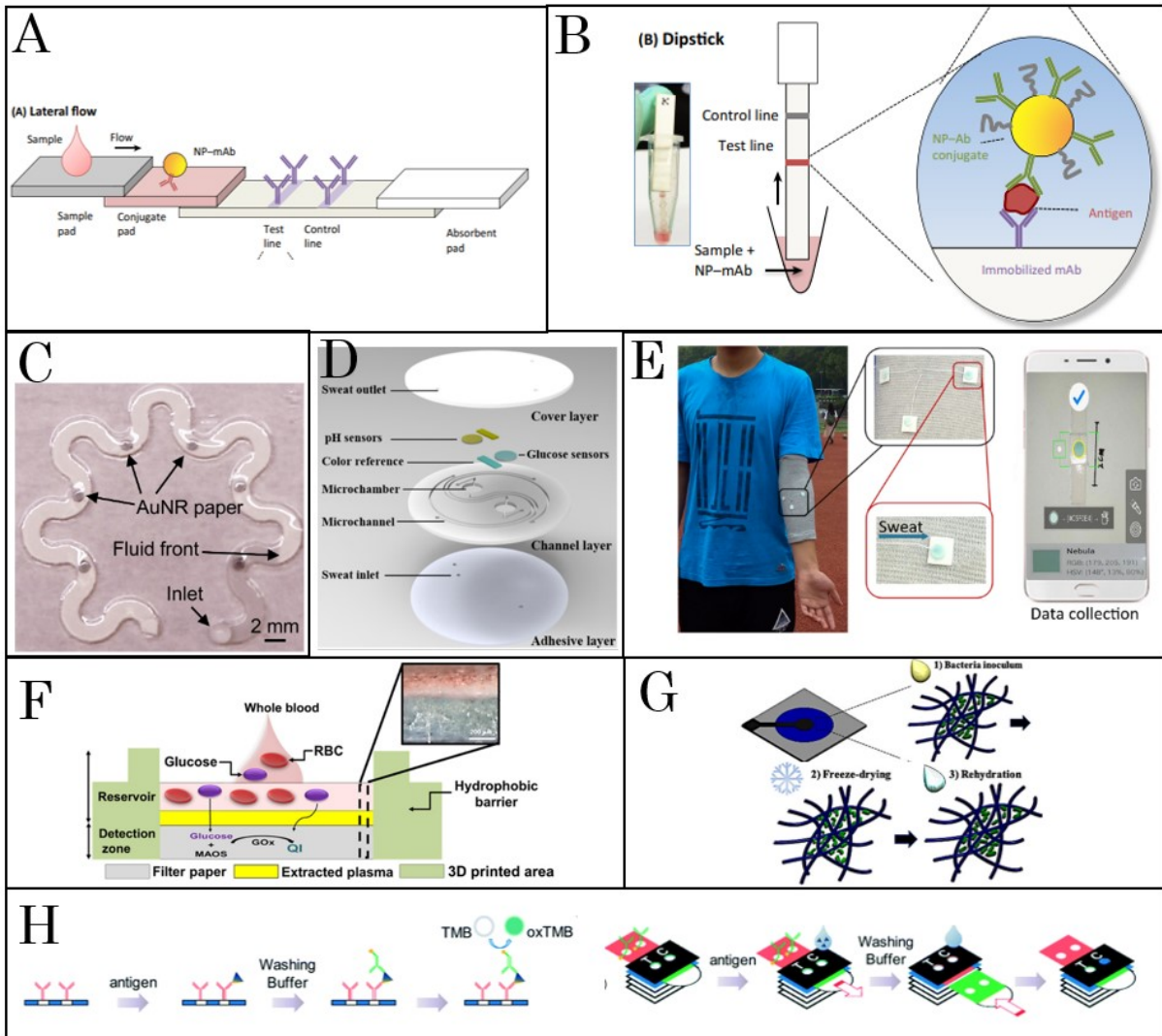|	Advantages	Disadvantages
Paper-based microfluidics	Easy fabrication	Limitations in complexity
	Cost-effective	Single-use product
	Easy transportation	Sample evaporation
	Long-term stability	Possible degradation with chemical reaction
	High capillary action	Only colorimetric analysis

Figure B.6: An overview of the literature research on paper-based microfluidics: lateral-flow assay (a), dipstick assay (b), sweat glucose sensors (c,d,e), blood plasma separation (f), freeze-dried bacteria (g), freeze-dried antibodies (h). (a-g reprinted from [100],[100],[102],[103],[104],[105],[106],[57]).

B.5 Absorbance spectroscopy

For the detection of free thiols in the plasma absorbance spectroscopy will be used. Absorbance spectrophotometry is an important technique for measuring and analyzing elements [107]. The advantage of using absorbance as a detection technique is that it is relatively simple and cheap. Additionally, this technique is currently used in the lab of the UMCG in combination with DTNB (Ellman's reagent). Absorption is the quantity of light absorbed by the investigated sample, and the electronic transition can be expressed in terms of wavelength [107]. For the detection of biomarkers, absorbance is often used due to its relation to concentration. According to the Lambert-Beer law, for transparent solutions, the absorption of each layer is equal due to the irrelevance of the light intensity. Therefore, the absorbed light is linearly related to the number of absorbing species. The Lambert-Beer law can be described as a function of the absorbance (A) dependent on the molar absorption coefficient (a), path length (b), and concentration (c), as described in equation J. Additionally, the absorbance is related to both the intensity of the incidence- and output light.

$$A = log_{10}(I_0/I) = abc \tag{10}$$
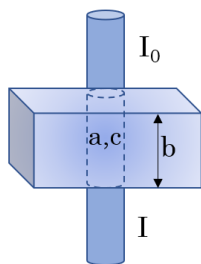
Figure B.7: The relation between the absorbance (A) of a sample and the absorption coefficient (a), path length (b), concentration (c), incidence light (I_0), and output light (I).

The absorption is the difference in absorbed incidence and output light ($log_{10}(I_0) - log_{10}(I)$) (Figure B.7). The relationship between the absorbance and concentration can only be assumed linear if a and b remain constant. A calibration curve can be created by measuring the absorbance for different sample concentrations [107]. Thereafter, based on the measured absorbance, the concentration can be obtained from the linear calibration curve. A common phenomenon for calibration curves is that they bend to the concentration axis for the higher concentrations. A recently constructed calibration curve of L-cysteine can be found in Figure B.8. The calibration curve is not very stable across several experiments, according to the UMCG. The stability of the calibration curve is crucial since it will be used to determine concentrations based on the measured absorbance of the plasma free thiols in the microfluidic device samples. The process of creating a calibration curve on-chip for every measurement will be time-consuming and difficult to implement on-chip.

Figure B.8: The calibration curve of L-cysteine showing the absorbance values for L-cysteine concentrations between 0.25-1.5 mM (reprinted from [108]).

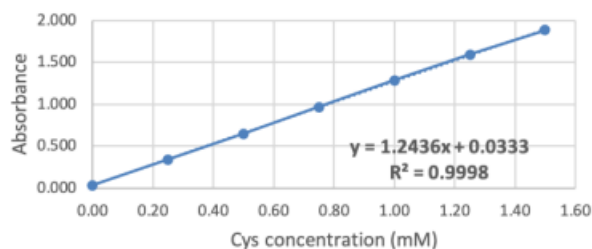### B.5.1   Limitations absorbance measurements

There are different kinds of interference that can occur when using absorbance [107]. For example, the absorption profile overlaps with that of another substance in the solution. Therefore, even though the emission lines are usually very narrow, plasma is used as an input sample instead of whole blood. Other interferences could be caused by light scattering of the light source, viscosity, surface tension, or limitations due to ionization.

There are additional limitations for using absorbance spectroscopy for measuring biomarkers in microfluidic devices. Firstly, the optical path length compared to in a cuvette or wells plate is much smaller [109]. From equation 1 follows, that a smaller optical path leads to lower absorbance. Another problem is that microfluidic devices do not have the same sensitivity as commercially available instruments [109, 110]. There has been a lot of research on improving the signal-to-noise ratio in LoC devices to improve sensitivity. The challenge of using absorption as a detection technique is on one side minimizing the size of the device, and on the other hand, assure a low limit of detection (LoD) and high sensitivity.

B.5.2   Chemical reaction

DTNB, also called Ellman's reagent is a chemical solution with the chemical name 5,5'-dithio-bis-[2-nitrobenzoic acid] [111]. The substance is reactive towards sulfhydryl groups (-SH) of for example cysteine and other free thiols. Together it yields the detectable product 2-nitro-5-thiobenzoic acid (TNB) and a disulfide (Figure B.9). The maximum absorption of TNB is at the wavelength of 412 nm. The reaction rate is dependent on pH, pKa and possible steric- or electrostatic hindrance. However, between a pH of 7.6 and 8.6, it is stable. DTNB is used for the detection of free thiols as TNB is a yellow-colored species, which is in the visible range. Additionally, TNB has a high molar absorption coefficient (a = 14150 $M^{-1}cm^{-1}$ at 412 nm).
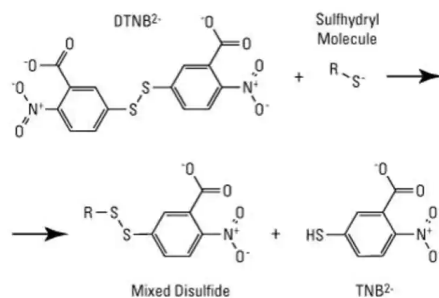
Figure B.9: DTNB reaction with free thiols to form colored TNB and a disulfide (reprinted from [111]).

B.5.3 Portable spectrophotometer

A portable read-out device for the absorbance measurements would utilize better POCT. According to Gilbert et al. portable absorbance measurement devices would utilize the full advantage of the small size and organization of the LoC devices [112]. In their study, they successfully developed a small device measuring concentrations of components of interest by UV-vis and micro-Raman spectroscopy using a laser.

A portable laser sensor for measuring ammonia concentrations is created by Guo et al. [113]. It is a validated device based on infrared spectroscopy, which has very small dimensions. A clear linear relationship between the absorbance and ammonium concentrations was obtained. Their developments are ideal for POCT due to the robustness, size, response rate and high sensitivity of the device.

Another study investigated the use of a LED light source in combination with a photodetector as a low-cost portable absorbance measure device [110]. They received higher detection of concentration using their device compared to the standard plate reader, but still concluded their results were satisfactory.

More studies utilized a LED and photodiode for portable absorbance measurements [114, 115, 116]. Huang and Fair created a microfluidic device that measured sulfate concentrations in droplets [114]. They used a silicon oil medium, which was unstable, causing uncertainties if the light path was perpendicular to the chip. The horizontal light path gave comparable results as the commercial plate reader regarding the limit of detection and variability.

To replace invasive glucose measurements, Jung et al. created a LoC device measuring glucose concentrations from saliva samples with absorption utilizing a LED [115]. They used a reflective surface placed at an angle of 45° to increase the optical path length, creating an increased sensitivity. The results obtained from the blue-colored saliva samples were slightly different from the UV-Vis measured concentrations, but the analytical performance was similar.

Alam et al. created a portable absorbance device, which can be connected to a smartphone application for at-home analysis [116]. Their optical density sensor also consisted of a LED, optical fibers, and a detection photodiode (Figure B.10). An electric circuit controls the light signaling and includes a Bluetooth transceiver that sends the information to the smartphone. The system also measures a reference value from the LoC and both absorbance values can be read and interpreted at home using the developed smartphone application.

Another portable absorbance device with a connection to an application was created by Gu et al. [117]. Their portable sensor detects gold nanoparticles and Hg^{2+} ions, and had a limit of detection of 0.14μM and 1.2 nM, respectively. They used a smartphone camera as a spectrometer, and together with a halogen beam and optical accessories, they established the colorimetric detection of the particles. The results could be sent to a smartphone application.

LEDs have been used for medical non-invasive diagnosis and monitoring purposes for a long time [118]. LEDs only emit light at one single wavelength, which is useful in absorbance measurements as the element of interest usually has a maximum absorption at a certain wavelength. Additionally, it minimizes the absorption of other substances. Other advantages of using LEDs are the small sizes, long lifetime, lower costs, high efficiency and brightness, and the broad availability of the wavelengths in the spectral range. Their use is also widely investigated in microfluidics due to the fast response rate.
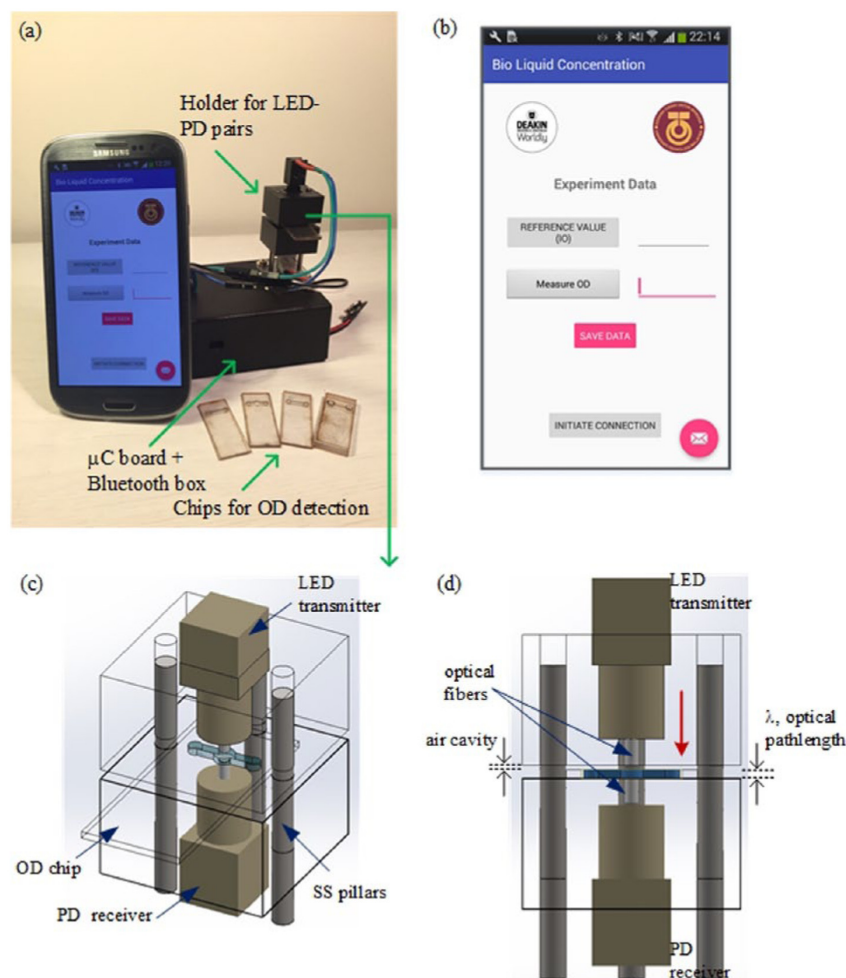

Figure B.10: An example of a portable spectrophotometer using a LED, optical fibers, and a photodiode for detection, and the connection to a smartphone for easy and fast result read-out (reprinted from [116]).

C   Walkthrough of the chip designs

C.1   Blood plasma separation

The initial design adapted from the design of Emma Moonen [43] consists of a capillary pump and a read-out reservoir (Figure C.1). A membrane is clamped between the capillary pump and a top well to drop the blood sample in with adhesive tape. 100 μL blood was pipetted in the top well. In 55.6% of the cases, plasma was obtained in the capillary pump reservoir. However, none was seen in the read-out reservoir. The limitations of the device were thought to be:

- The volume was not enough due to the sponge-like functioning of the membrane.

- The capillary action was not strong enough.

- The device was too hydrophobic.
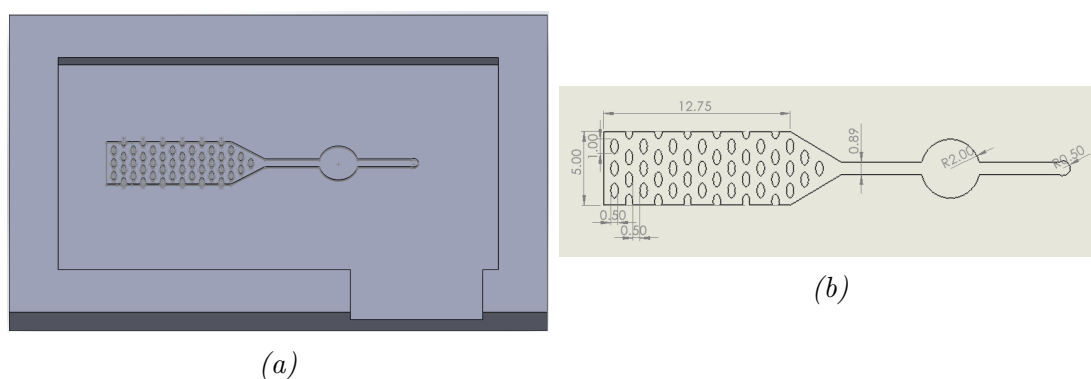
Figure C.1: The first BPS design in Solidworks (a) and the technical drawing with top view (b).

To begin with, the first hypothesis was investigated. The used blood volume (100 μL) was already quite large for a fingerprick blood sample. Therefore, instead of increasing the sample volume, the device size was decreased (Figures C.2 and C.3). Two different smaller devices were tested (n=5), but no plasma was obtained in any of the chips.
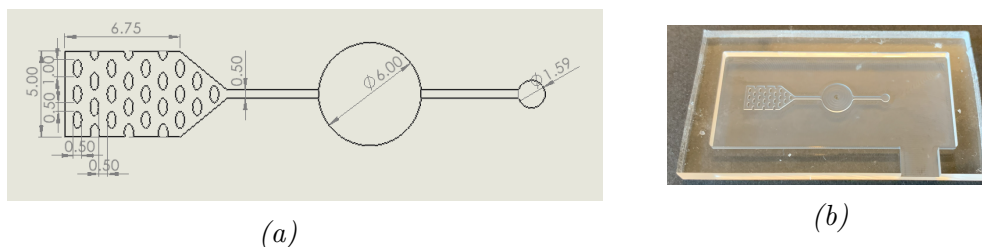
Figure C.2: The technical drawing of the smaller BPS design with top view (a) and the created PMMA mold (b).
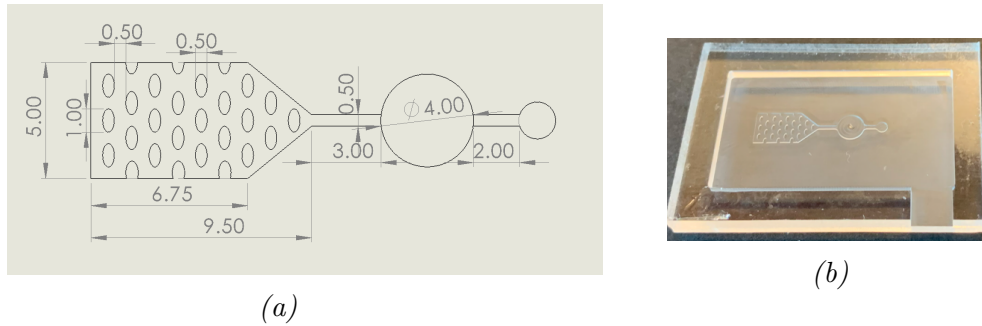
Figure C.3: The technical drawing of the smallest BPS design with top view (a) and the created PMMA mold (b).

Another design reduced in size was created (Figure C.4). Additionally, another inlet was added. The purpose of this inlet was to pipette Tris buffer into the capillary pump to flush the obtained plasma further into the channel. Even though no plasma was obtained (n=5), still the functioning of the Tris buffer flushing was investigated. The limitations were:

- Difficulties pipetting due to low capillary pressure.

- The membrane is two-directional so some of the pipetted Tris buffer flows into the top well.

- No exact ratio of the Tris buffer and obtained plasma is known.
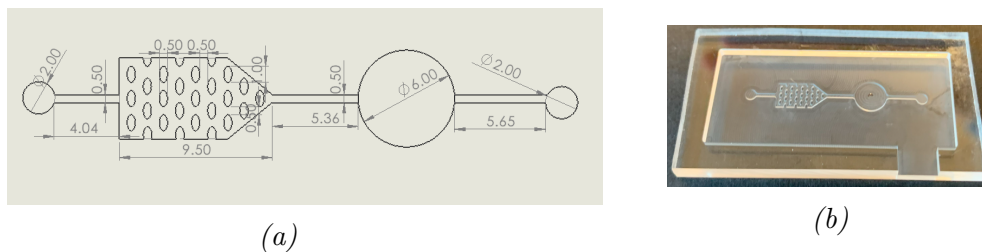
Figure C.4: The technical drawing with top view of the smaller BPS design with Tris buffer flush through (a) and the created PMMA mold (b).

Even though the flushing of the Tris buffer has some limitations it was integrated into the initial design (Figure C.5). Other changes that were made were the reduced size of the hole of the sealing to prevent leakage. And the use of a cap on the top well pushes the blood sample onto the membrane and prevents the flow of the Tris buffer into the top well. Additionally, two different heights were tested: 0.3 and 0.15 mm. It was expected to increase the capillary action with the lower height. However, the 0.3 mm height had a 100% success rate in obtaining plasma while the 0.15 mm height only obtained plasma in 66.6% of the chips. Additionally, the plasma reached the read-out reservoir after pipetting the Tris buffer in 60% and 33.3% of the cases for the 0.3 mm and 0.15 mm height, respectively. Whether the pipetting of the Tris buffer also increased the wicking of the plasma from the membrane was hard to assess.

(a)

(b)
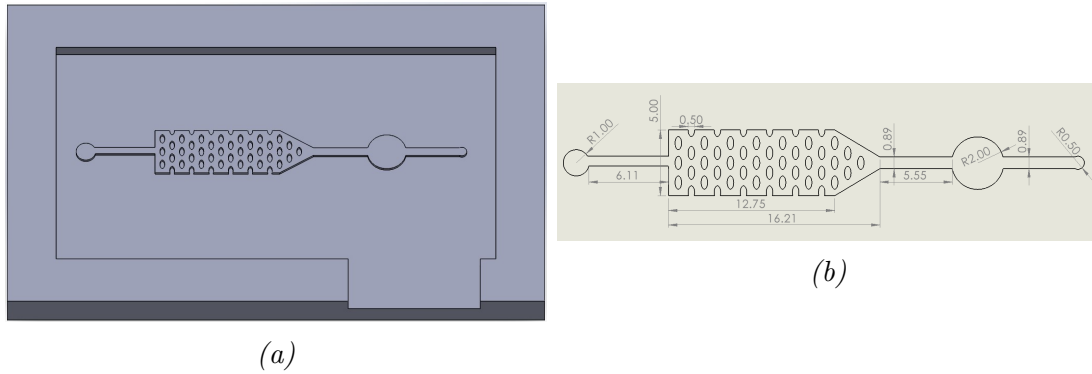
Figure C.5: The final design with Tris buffer flush through in Solidworks (a) and the technical drawing with top view (b).

C.2 Two read-outs design
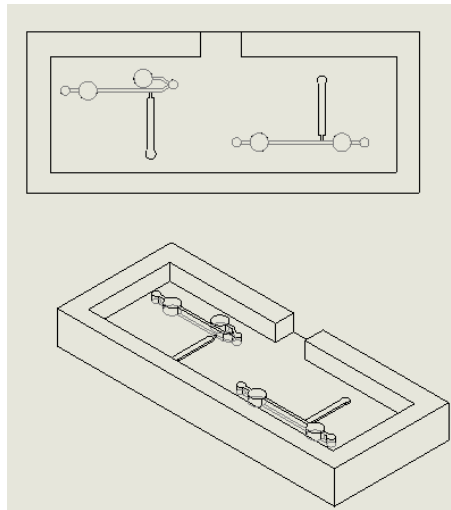
Figure C.6: Technical drawing of the two read-outs design with the control read-out at a junction (left) and the control read-out in a straight channel before the trigger valve (right)

There were two different designs for the chip with two read-outs; one for the reference measurement without DTNB and one experimental read-out for after the addition of DTNB (Figure F.3). The chip design contains one reservoir, which was for the storage of DTNB, and in the inlet, the diluted plasma should be pipetted. This chip was tested with FITC for DTNB due to the similar chemical characteristics and water for the diluted plasma. The trigger valve in this design worked really well and the meniscus formation of the fluid in the reservoir was relatively easy. The trigger valve did not completely have 90° angles due to the micromilling (Figure C.7(a)), yet it still allowed for the meniscus formation. However, there were also some limitations:

- To be able to create the meniscus of the reservoir fluid at the trigger valve the volume of the liquid had to be much larger than the designed volume to exactly fit

the reservoir. This causes high hydrostatic pressure, which enabled the meniscus formation. However, the precise ratio of the DTNB and diluted plasma was more difficult to determine.

- The design asked for continuous pipetting in the inlet to keep pulling the DTNB out of the reservoir and the design worked best with filter paper added to the outlet.

- The emptying of the trigger valve was very dependent on the pipetting speed.

- In the design with the junction after the inlet for the two read-outs, the fluid only flowed in one direction. This could be due to the edges of the junction to the read-out reservoir in one of the designs not being shartp, but more rounded (Figure C.7(b)).

- Due to diffusion there was also a fluorescent signal visible in the control read-out of the straight channel design. So, the DTNB would most likely also diffuses into the control read-out, which negatively affects the experiment.

(a)   (b)
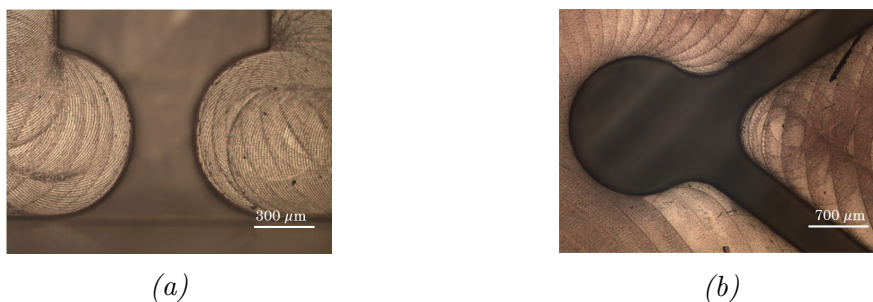
Figure C.7: The trigger valve under the microscope (a) and the junction for the control read-out in the left design (b).

C.3 Two reagent chip designs

Due to the limitations of the two read-outs design, it was decided to make the larger reservoir, the reservoir of the diluted plasma, the control read-out. The four designs visible in Figure C.8 are the chip designs for the diluted plasma and DTNB mixture. The goal was to actuate both the two reagents in the reservoirs with a small actuation volume and lead them to the experimental read-out. These designs are tested on their ability to form a meniscus at the trigger valves and the liquid reaching the reservoir.
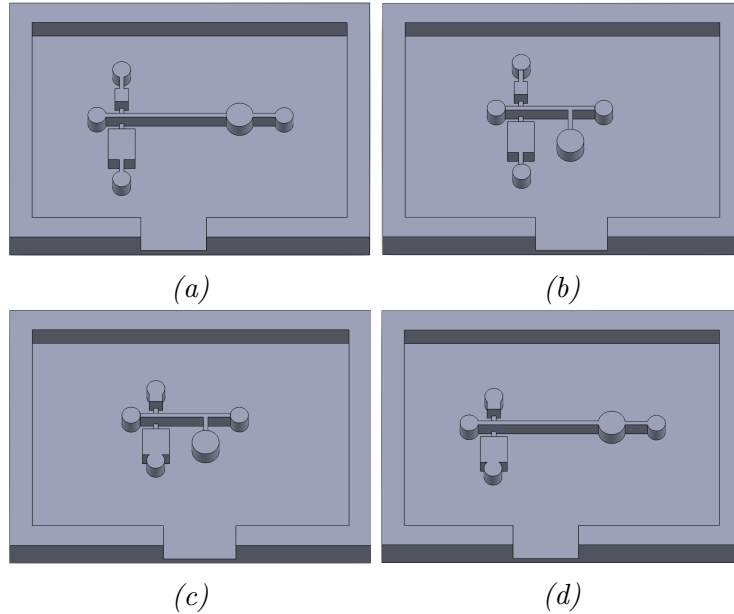
Figure C.8: The four different designs for two reagents on-chip with differences in width after inlet: narrowing after the inlet (a+b) vs. inlet connected to channel (c+d), and differences in channel direction: straight (a+d) vs. at 90° (b+c)

Yellow and blue food dye was used for testing the design. If no mixing occurred before actuation and green food coloring reached the read-out reservoir, the whole test was performed successfully. However, the limitations of these designs included:

- Pipetting the liquid into the trigger valve reservoir was challenging. The trigger valves were very sensitive to the flow rate, so pipetting should be done at low speed.

- The read-out reservoirs at an angle did not fill.

- The trigger valve reservoirs were not emptied completely, which led to unknown ratios of the added food dyes.

C.4 Enhanced mixing designs

To enhance the mixing of the plasma and Tris buffer, different structures are tested: a herringbone structure, and a serpentine structure without and with side wells (Figure C.9). The herringbone structure is a positive structure. It has four sets of grooves: the first two with a forward flow direction and the last two with a reverse flow direction (Figure C.10(a)). The grooves have an angle of 90° and are created successfully using the mill (Figure C.10(b)). The serpentine structure without side wells was created without problems. On the other hand, the serpentine structure with side wells did have some problems. The side wells had a width of only 0.2 mm with five side wells in a turn (Figure C.11(a)). These structures were too small to mill, resulting in a wider channel with wave-like walls (Figure C.11(b)). This wider channel also influenced the results of the experiments as no liquid reached the read-out reservoir in the chips with this design. No further improvements on the enhanced mixing designs are made.
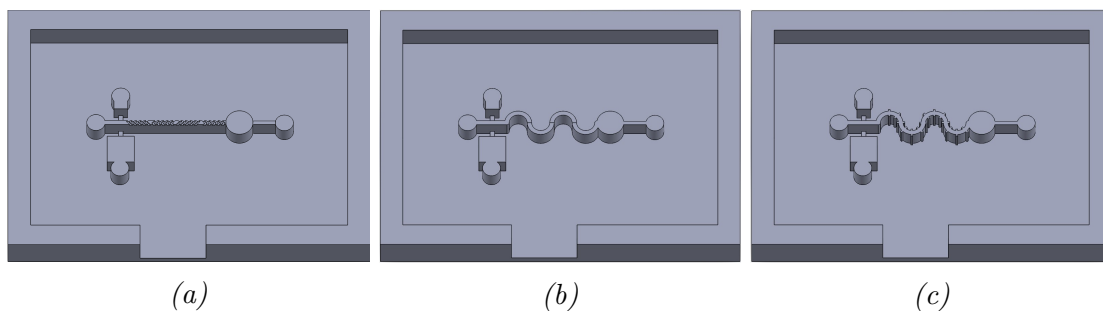
Figure C.9: The three different designs for enhancing the mixing process: a herringbone structure (a), a serpentine structure (b), and a serpentine structure with side wells (c).
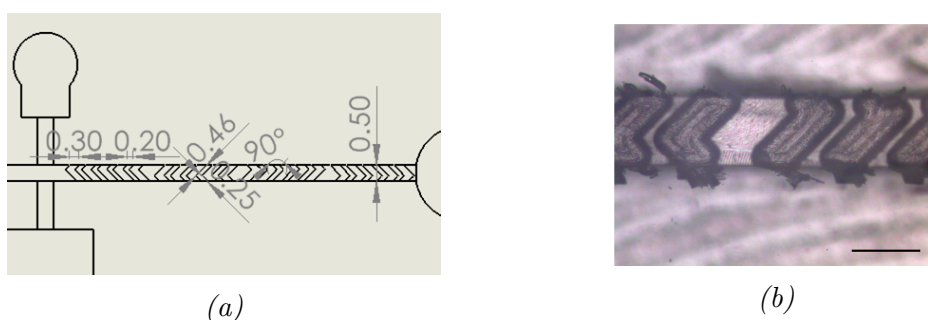
Figure C.10: The herringbone mixing structure: a technical drawing with top view (a) and under the microscope with magnification 40x (b) scale bar = 500 μm.

Figure C.11: The serpentine mixing structure with side wells: a technical drawing with top view (a) and under the microscope with magnification 40x (b) scalebar = 500 μm.

C.5 Volume control designs

C.5.1 Microdispenser

Since it is important in the protocol that the plasma sample and Tris buffer are mixed in the exact ratio of 1:4, it is of interest to create a design in which the volumes of the used reagents can be fixed. Based on the fixed volume design of Puntambekar et

al. a SolidWorks design was made [99] (Figure C.12). This design aimed to enable a fixed volume measurement of the reagents on the chip. It consists of an air channel with smaller A needle was attached to the inlet of the smaller channel. Food dye was pipetted into the inlet until the reservoir was filled. Afterward, air was pressed into the small channel inlet via a syringe attached to the needle. It was hypothesized that this would create a gap in front of the reservoir allowing the fixed volume of the reservoir to flow further. Unfortunately, in this design, the food dye flowed beyond the reservoir before the air-driven pressure was applied. Additionally, food dye flowed into the smaller channel intended for the air.

(a)

(b)
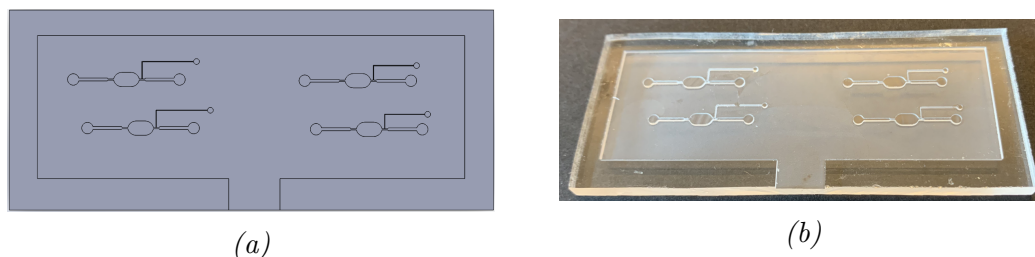
Figure C.12: The first microdispenser design in Solidworks (a) and the created PMMA mold (b).

(a)

(b)
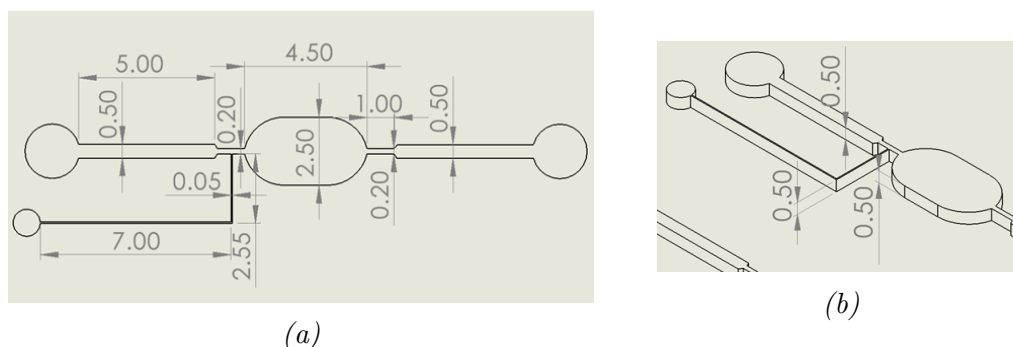
Figure C.13: The technical drawing of the first microdispenser design with top view (a) and on an angle to see the different heights (b).

Another design was made to overcome the encountered challenges (Figure C.14). The first alterations that were made, were the dimensions of the channels. The difference in width of the small channel for the air and the main channel for food dye was increased (Figure C.14, shown in blue). The shape of the reservoir was changed from oval to rectangular. This was to increase the expansion angle from the channel to the reservoir and vice versa. A larger change in angle more easily stops the flow of the liquid. Additionally, the size of the reservoir was increased by increasing the height. Still, the same problems as before were seen.

- No flow stoppage at the outlet of the reservoir.

- Flow of the food dye into the air channel.
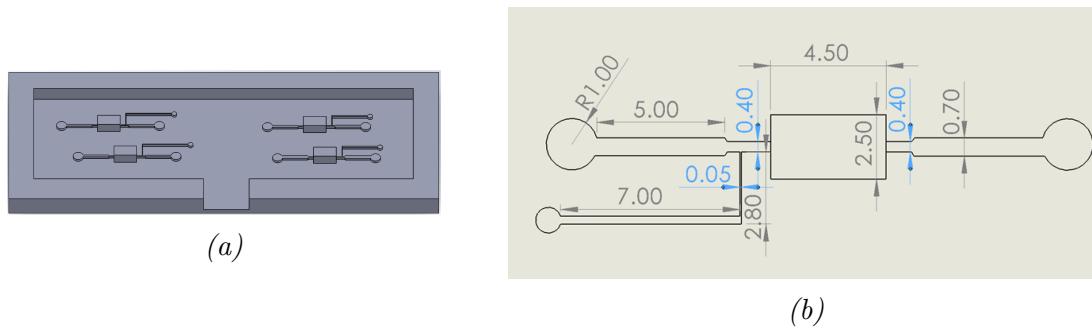
Figure C.14: The design of the improved microdispenser in Solidworks (a) and the technical drawing (b).
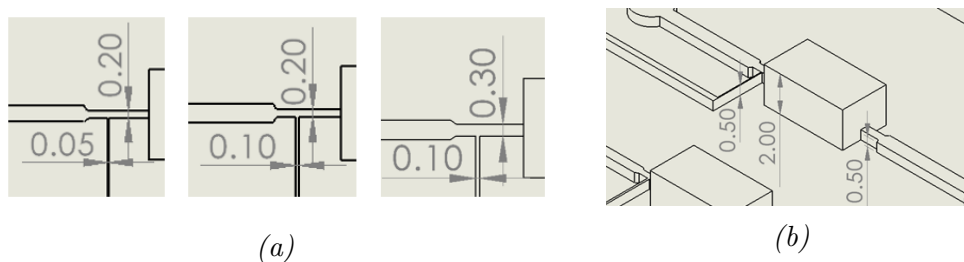
Figure C.15: The technical drawing of the improved microdispenser with the different air channel and flow channel width combinations (a) and on an angle to see the different heights (b).

In the new design, the height of the channel at the side of the inlet and the reservoir was 500 μm and the channel after the reservoir was 2000 μm high. This was to stop the fluid flow at the reservoir, which succeeded with this design. Even though food dye flowed into the smaller air channel, it was still possible to create a gap by applying air-driven pressure via the syringe. However, due to the height difference, the pressure was not high enough to continue the liquid flow of the liquid in the reservoir. It was discovered that pressing on the inlet side of the reservoir did allow the liquid to flow to the read-out reservoir. Therefore, there was chosen to not continue this idea of creating a fixed volume.
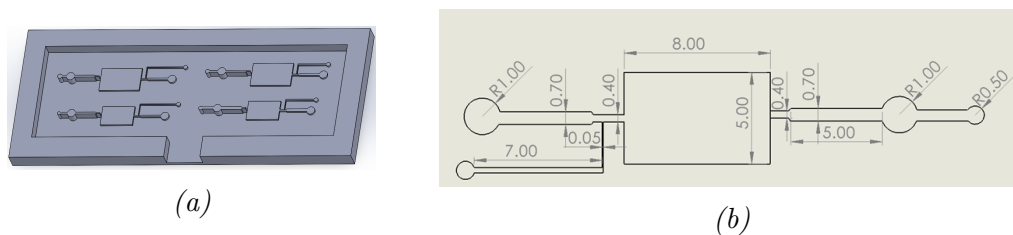
Figure C.16: The design of the further improved microdispenser in Solidworks (a) and the technical drawing (b).
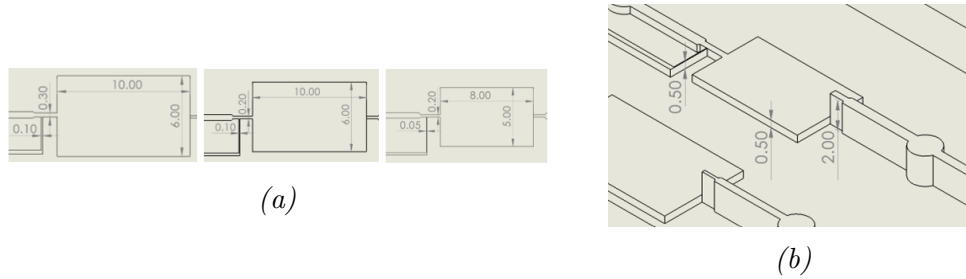
Figure C.17: The technical drawing of the further improved microdispenser with the different air channel and flow channel width combinations and different reservoir sizes (a) and on an angle to see the different heights (b).

C.5.2 Mechanical actuated valves

Based on the conclusions of the microdispenser chips, it was decided to create a PDMS soft valve. The design is adapted from Hitzbleck et al. [95] (Figure C.18). The larger rectangular reservoir fits 22.5 mm^3 liquid (Figure 19(a)). The stop valve at the end of the reservoir stopped the liquid flow due to the height difference of 1500 μm (Figure 19(b)). After pressing on the stop valve, the liquid flowed further into the channel due to the sudden expansion of the geometry. The arrow-shaped design reduced the liquid from flowing back into the reservoir significantly. The functioning of the trigger valve was investigated by pipetting blue food dye in the trigger valve and performing the experiment of the valve with water. Blue coloring was seen in the channel while pressing on the stop valve. Therefore, it was concluded that the trigger valve worked. The main limitations were:

- While pressing on the soft valve the liquid flowed further into the channel, but once removing the pressure the liquid flowed back.

- The design was very gravity sensitive since all liquid flowed back into the original reservoir after holding the device with the outlet pointing to the ceiling.
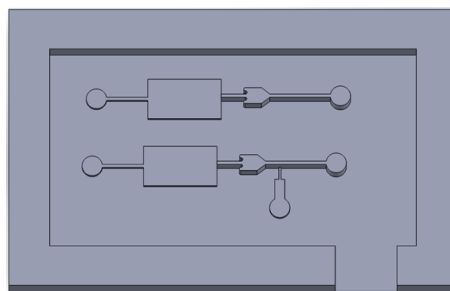
Figure C.18: The Solidworks design of the soft valve adapted from []
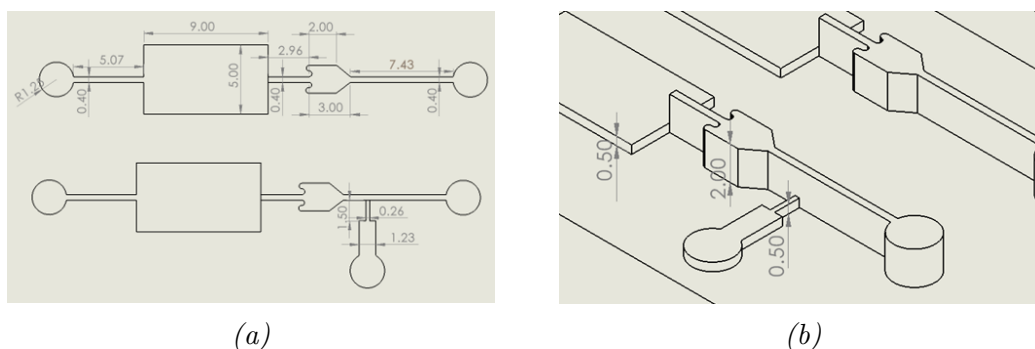
Figure C.19: The technical drawings of the created soft valve with top view (a) and on an angle to see the different heights (b).

Due to the limitations of the soft valve, a mechanically actuated valve with prevention of backflow was desired. A valve, with similar characteristics to a G-clamp, was made from plastic. The microfluidic chip can be placed between a bottom and plastic pillar pressing on the top of the channel. The valve is mechanically actuated by turning the round lid clockwise as the pillar moves down simultaneously. The flow layer of the Quake-valve design is used for testing this valve (Figure 23(a)). The measurement reservoir is the most left reservoir, which could contain a volume of 14.9 μL. The clamp successfully prevents the flow from flowing through the channel further (Figure 20(a)). Additionally, after moving the clamp to before the reservoir, the food dye was successfully pushed out of the channel without backflow (Figure 20(b)). If the clamp is set in place and the pressure is not removed from the clamp, it will sufficiently bring the liquid to the read-out reservoir. The limitations of this valve were:

- The size of the clamp is very large, which causes the volume to be not very precise. A smaller clamp will be needed to accurately measure the volumes.

- Actuation is relatively slow since it is manually performed by turning the lid.

- Pipetting the food dye into the device was very difficult since the clamp closed the channel and there was no air vent.
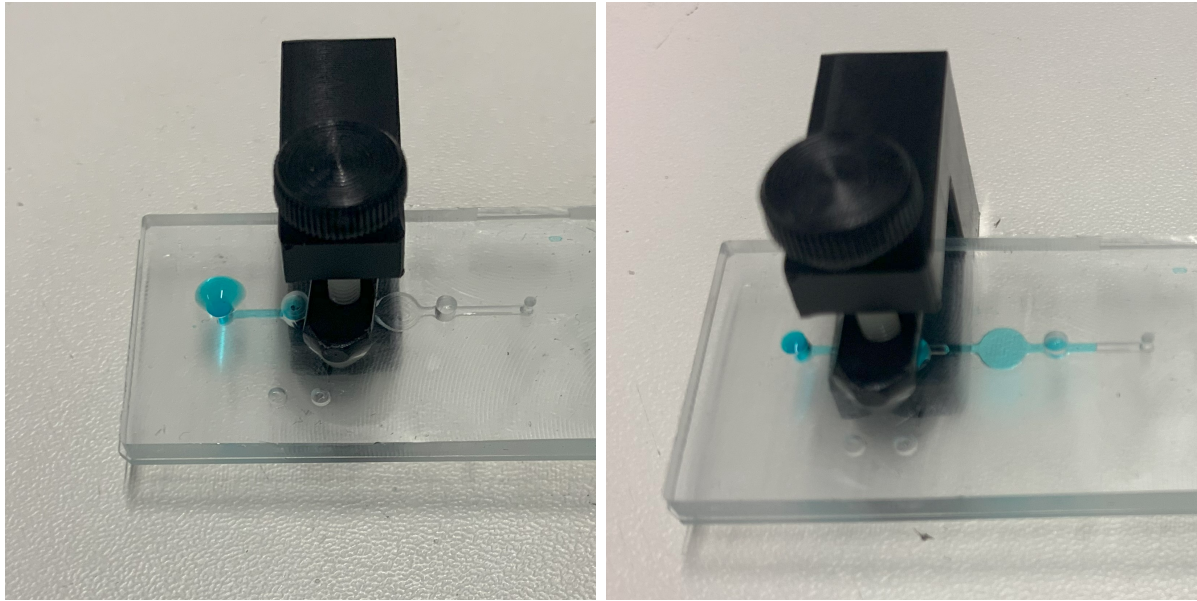
(a)   (b)

Figure C.20: The mechanically actuated G-clamp valve with prevention of flowing past the measurement reservoir (a) and pushing the liquid out of the measurement reservoir (b)

C.5.3 Quake-valves

In the literature review, Quake-valves were also analyzed for their use in volume control. A Quake-valve design that could be obtained through micromilling was adapted from Bossink et al. [47]. The design is a two layer PDMS design with a flow layer and control layer (Figure C.21). It has a bottom-up principle, meaning that the control layer is below the flow layer, closing the channel by pushing the channel from underneath. The chip has the size of a microscopic glass slide with two different flow channels on it. The flow channel has a measurement reservoir that is enclosed by two pneumatically activated valves. The principle is explained in Figure C.22

Figure C.21: The first design of the Quake-valve in Solidworks with the control layer in black lines and the flow layer in gray lines.
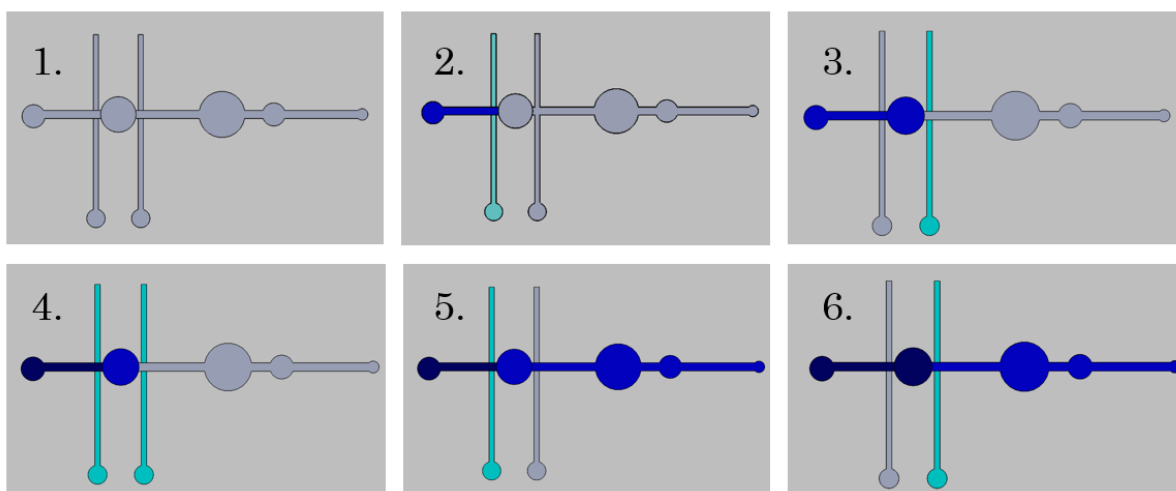
Figure C.22: The volume control principle of the Quake-valve with gray mimicking air, turquoise mimicking air, blue mimicking the blue food dye, and dark blue residual blue food dye after closing the valves. The steps include: 1. valves open, no liquid, 2. the first valve closed, food dye pipetted in, 3. first valve open and second valve closed, dye flowing in measurement reservoir, 4. both valves closed, exact volume in measurement reservoir, 5. second valve open and first valve close, liquid pushed out of the reservoir, 6. second valve closed, preventing backflow of liquid

The measurement reservoir fits a volume of 14.9 μL. The measurement reservoir also functions as a control read-out reservoir and has a height of 2 mm. The right reservoir is the read-out reservoir and also has a height of 2 mm. The middle reservoir was to fit the filter paper with freeze-dried DTNB for the integration of different development steps. Besides the read-out reservoirs, the channel height was 0.5 mm. The width of the valves of the control layer was 0.45 mm. Unfortunately, this design did not give the desired results. The limitations were:

- The Quake-valves could not completely close the flow layer channels.

- The closing of the first valve and opening of the second valve did not generate a large enough force to push the food dye out of the channel.

- Since the valves could not close the flow channel properly there was backflow from the read-out reservoir to the control read-out reservoir.
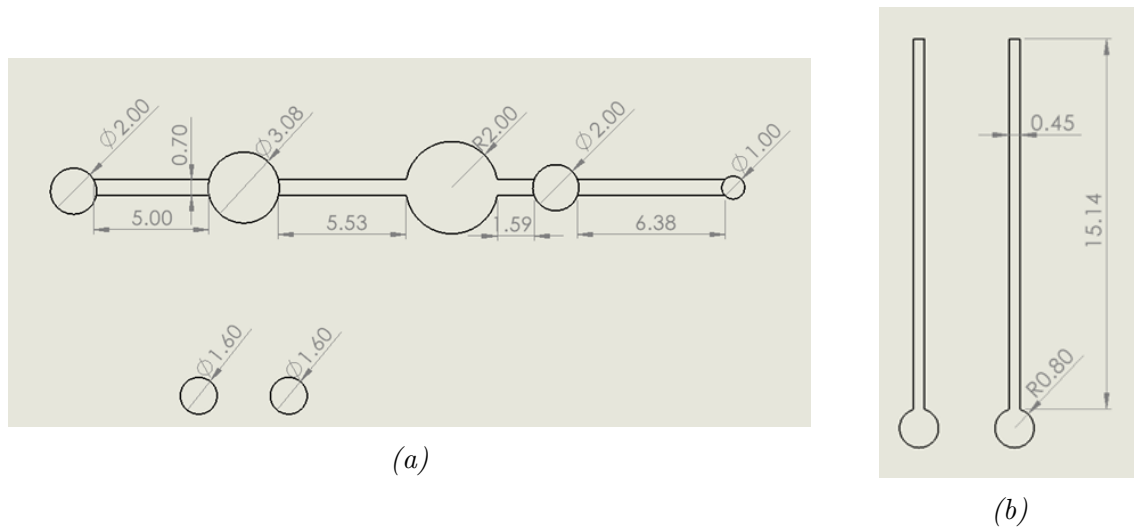
Figure C.23: The technical drawings of the first Quake-valve design with top view of the flow layer (a) and control layer (b).

Based on the listed limitations changes in the design were made (Figure C.24). A small channel was added to the measurement reservoir through which air could be pumped to help push the liquid out of the reservoir (Figure 25(a)). The small channel needed to be closed during filling of the measurement reservoir (Figure C.22, step 3). The valve before the measurement reservoir needs to be closed while using the liquid out to make sure to push the liquid towards the outlet and not the inlet (Figure C.22, step 5). To enable this, the second valve is made at 90° to close the small channel and main flow channel after the measurement reservoir simultaneously. Additionally, the width of the control layer was increased twice: first to 0.55 mm (Figure 25(b)) and afterward to 1.95 mm (Figure 25(c)). The flow layer channel was only closed with a width of 1.95 mm without a flow rate. The last change in the flow layer design was to reduce the inlet size to 1 mm, so the small capillary tubing fit better.
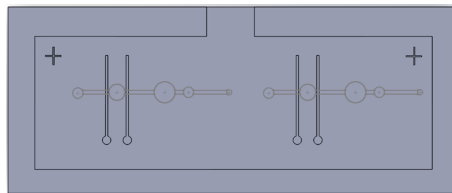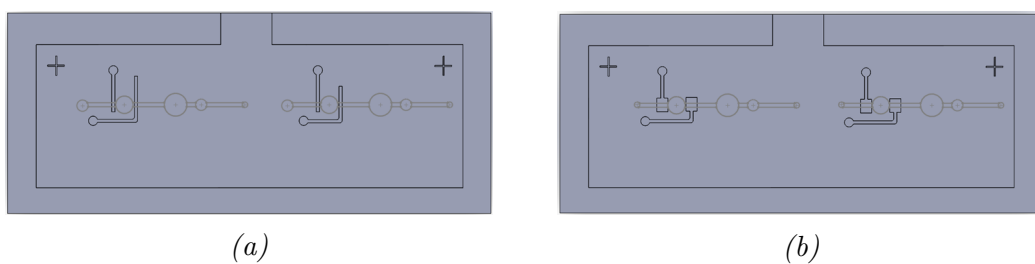

Figure C.24: The second (a) and last (b) designs of the Quake-valve in Solidworks with the control layer in black lines and the flow layer in gray lines.

Figure C.25: *The technical drawings with top view of the second Quake-valve design flow layer (a) and second (b) and last (c) control layer designs.*

C.6 Calibration curve designs

It was desired to fit the read-out reservoirs of the 8 concentrations of the calibration curve on one chip to investigate the linearity of absorbance concentration relation on-chip (Figure **??**). The 8 reservoirs were designed so they match the 384 well plate locations when the chip is placed in the plate reader holder. The distance between the reservoirs is 4.5 mm, the same distance as between the wells in a 384 well plate (Figure 26(b)).

Figure C.26: *The calibration curve design in Solidworks (a) and the zoomed-in technical drawing with top view (b).*

The design of Figure C.26 works perfectly for measuring the absorbance of the calibration on-chip. However, it was needed to punch a 1 mm air vent in the read-out reservoir, which could have influenced the absorbance when not punched carefully at the side. This design was not suitable for testing with the freeze-dried DTNB on filter paper. To be able to place the freeze-dried filter paper in the device an extra reservoir is introduced (Figure 27(a)). A 3.5 mm puncher is used to punch the circles out of the filter paper with freeze-dried DTNB. The 8 filter paper circles are manually placed into the device before plasma bonding. The dimensions between the reservoir are kept the same (Figure 27(b)).

126

Figure C.27: The calibration curve design with filter paper reservoir in Solidworks (a) and the zoomed-in technical drawing with top view (b).

C.7 Integrated device

The larger BPS device with Tris buffer flush through (Figure 5(b)) was combined with the serpentine mixing structure (Figure 9(b)), the reservoir for the filter paper and the read-out reservoir. For the dimension of between the filter paper and read-out reservoir the dimensions of Figure 26(b) were used. The dimensions of the other structures were kept the same (Figure C.28). Due to the large device, the height was set to 0.15, which will have an influence on the absorbance values due to the Lambert-Beer law (equation J).
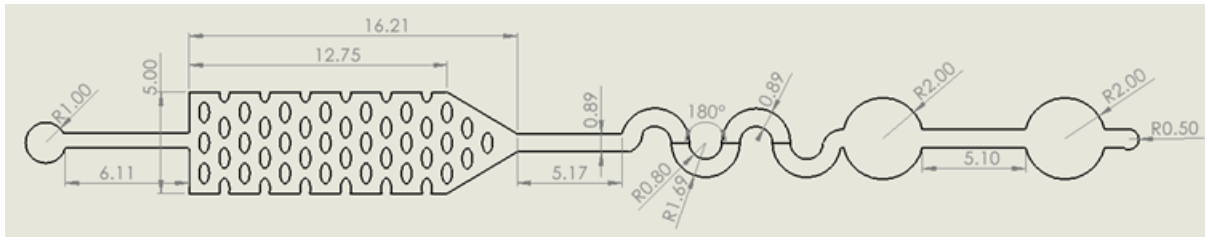
Figure C.28: The technical drawing of the integrated device with top view.

D   HSM settings
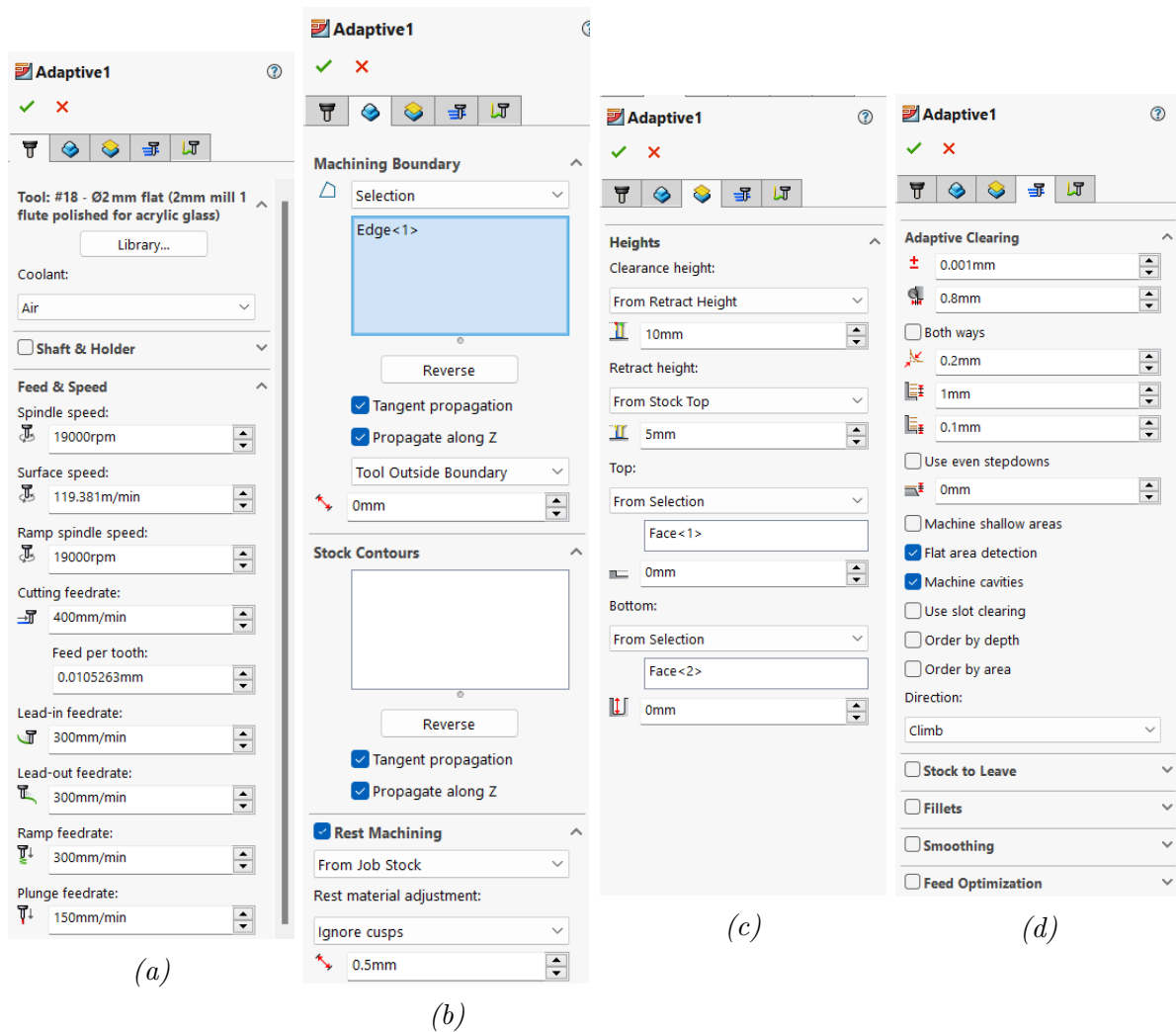
Figure D.1: *The settings of the HSM add-on in Solidworks for creating the .simple file for micromilling.*

E   Free thiol ELISA method used at the UMCG

At the UMCG the following materials are used for the free thiol ELISA; L-Cystein (Sigma Aldrich), 0.1 M Tris (pH = 8.2, Merck), EDTA (Serva), DTNB (Sigma Aldrich), K_2HPO_4 (Merck) and KH_2PO_4 (Merck). At the UMCG the colorimetric detection of free thiol groups is performed in different samples; serum, plasma and urine. First, the standards are prepared by preparing fresh 10 mM L-Cystein for the calibration curve. For serum and plasma samples 15.625 to 1000 μM final concentration is adhered to, and for urine 1.953 to 125 μM final concentration. For the sample preparation, all samples are centrifuged for 10 minutes at 10000 rpm at 4 °C. Urine samples are undiluted, and serum and plasma samples are diluted 1:4 with the 0.1M Tris buffer (75 μl sample and 225 μl buffer). 90 μl sample is pipetted in triplicates into a 96 wells plate (Costar), and the background absorption and reference are measured at 412 nm and 630 nm, respectively (CLARIOstar plus microplate reader, BMG Labtech). Then, 20 μl 1.9 mM DTNB in 0.1 M phosphate buffer (pH = 7) is added to the sample. The mixture is incubated in the dark for 10 minutes, and placed on a plate shaker at 15 rpm. When removed from the plate shaker the sample is incubated for another 20-60 minutes in the dark at room temperature. Afterward, the absorption and reference are measured at 412 nm and 630 nm, respectively. The background absorption is subtracted from the DTNB absorption, and the sample concentrations are calculated using the L-Cystein standard solution calibration curve.

F   Calculations two reagent chips

Several calculations are done for the two reagent designs. The width and height of the channel are 0.5 mm and 2 mm, respectively. The width of the trigger valve is 0.5 mm, and the height 0.5 mm.
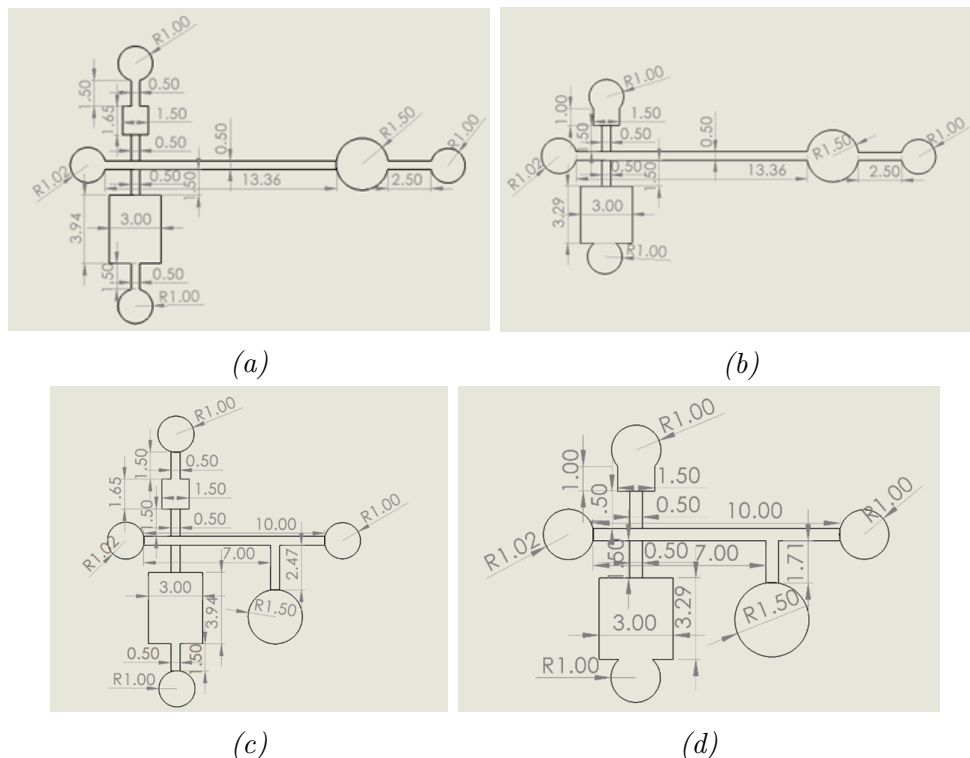
Figure F.1: The technical drawing of the four different designs for two reagents on-chip.

F.1   Pressure barrier trigger valve

The pressure barrier (ΔP) which is created by a sudden expansion can be explained by the following equation [119]:

$$\Delta P = \frac{2\gamma}{w} \left[\left(-\frac{w}{h} \right) cos\theta_c + \left(\frac{cos\theta_c - \frac{\alpha_w sin\beta}{sin\alpha_w}}{-cos\beta + \frac{sin\beta}{sin\alpha_w} \left(\frac{\alpha_w}{sin\alpha_w} - cos\alpha_w \right)} \right) \right] \tag{11}$$

where, γ is the surface tension (N/m), w the width (m), h the height (m), θ_c the contact angle (rad), β the expansion angle (rad) and α_w the meniscus curvature. Using the surface tension of water at 25 °C, 72 mN/m, and the contact angle between the liquid and plasma-treated PDMS, 31°, the following value of the pressure barrier is calculated:

$$\Delta P = \frac{2 \cdot 72 \cdot 10^{-3}}{0.7 \cdot 10^{-3}} \left[\left(-\frac{0.7 \cdot 10^{-3}}{2 \cdot 10^{-3}} \right) cos31 \cdot \frac{\pi}{180} + \right.$$

$$\left. \left(\frac{cos(31 \cdot \frac{\pi}{180}) - \frac{31 \cdot \frac{\pi}{180} sin(90 \cdot \frac{\pi}{180})}{sin(31 \cdot \frac{\pi}{180})}}{-cos(90 \cdot \frac{\pi}{180}) + \frac{sin(90 \cdot \frac{\pi}{180})}{sin(31 \cdot \frac{\pi}{180})} \left(\frac{31 \cdot \frac{\pi}{180}}{sin(31 \cdot \frac{\pi}{180})} - cos(31 \cdot \frac{\pi}{180}) \right)} \right) \right)$$

$$\Delta P = -168 Pa$$

F.2 Retention Burst Valves

The microfluidic structure including the trigger valves and retention burst valves can be seen as a capillary circuit [93]. Using this structure the retention burst pressure and hydraulic resistance in the channels can be calculated.
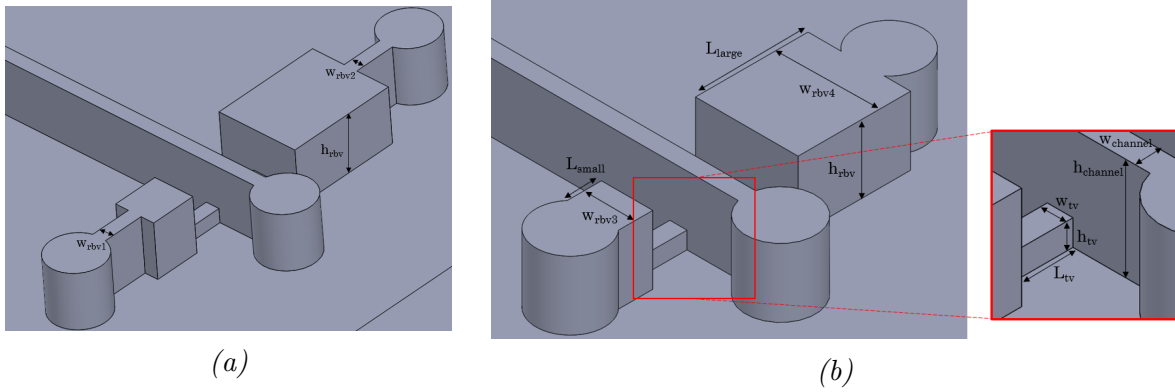
Figure F.2: *The dimensions of the retention burst valves of the chip with narrowing after inlet (a) and without narrowing (b) including magnification of the trigger valve.*
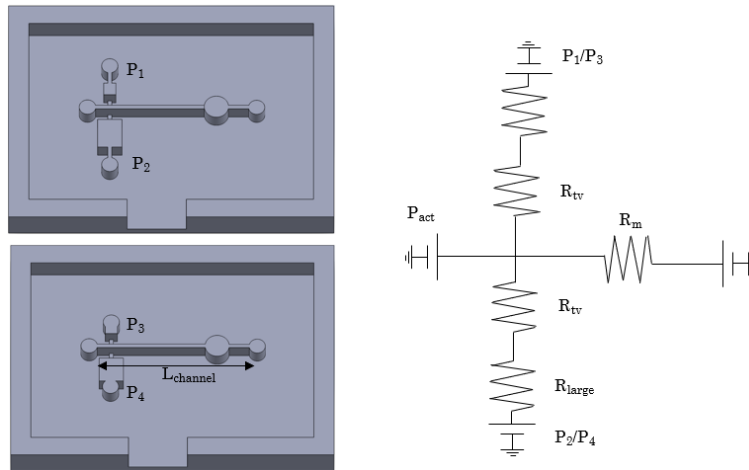
Figure F.3: *The schematic overview of the capillaric circuit.*

The retention burst pressure can be calculated with the same equation as for the capillary pressure (the Young-Laplace equation):

$$P = -\gamma \left(\frac{cos\theta_t + cos\theta_b}{h} \cdot \frac{cos\theta_r + cos\theta_l}{w} \right) \tag{12}$$

The hydraulic resistance of a channel with a rectangular cross-section is given by:

$$R = \frac{12\eta L}{[1 - 0.63(h/w)]} \frac{1}{(h^3 w)} \tag{13}$$

All abbreviations with descriptions, used values and calculated values for the retention burst pressures and flow resistances can be found in Table 15.

Using Ohm's law and Kirchhoff's law the pressure needed for drainage of the reservoirs can be calculated:

$$P_J = \frac{P_i \cdot R_M + P_c \cdot (R_{RV} + R_i)}{(R_M + R_{RV} + R_i)} \tag{14}$$

Table 15: All the abbreviations and descriptions including values of the retention burst valve calculations.

Abbreviation	Description	Value
γ	Surface tension	72 mN/m
θ_t	The top contact angle	31°
θ_b	The bottom contact angle	68.5°
θ_l	The left contact angle	31°
θ_r	The right contact angle	31°
$w_{channel}$	Width of the main channel	0.5 mm
$h_{channel}$	Height of the main channel	2 mm
$L_{channel}$	Length of the main channel	18.84 mm
P_{act}	Capillary pressure of the actuation	-291 Pa
w_{rbv1}	Width of RBV1	0.5 mm
w_{rbv2}	Width of RBV2	0.5 mm
w_{rbv3}	Width of RBV3	1.5 mm
w_{rbv4}	Width of RBV4	3 mm
h_{rbv}	Height of all RBVs	2 mm
P_1	Burst pressure of branche 1	-291 Pa
P_2	Burst pressure of branche 2	-291 Pa
P_3	Burst pressure of branche 3	-126 Pa
P_4	Burst pressure of branche 4	-85 Pa
η	The viscosity	$1\ mPa \cdot s$
w_{tv}	Width of the trigger valve	0.5 mm
h_{tv}	Height of the trigger valve	0.5 mm
L_{tv}	Length of the trigger valve	1.5 mm
L_{small}	Length of the small reservoir	1 mm
L_{large}	Length of the large reservoir	3.29 mm
R_M	Flow resistance of the main channel	$6.71 \cdot 10^7$ Pa $\cdot sm^{-3}$
R_{tv}	Flow resistance of the trigger valve	$7.78 \cdot 10^8$ Pa $\cdot s \cdot m^{-3}$
R_{small}	Flow resistance of the small reservoir	$9.09 \cdot 10^6$ Pa $\cdot s \cdot m^{-3}$
R_{large}	Flow resistance of the large reservoir	$6.67 \cdot 10^6$ Pa $\cdot s \cdot m^{-3}$

G   Matlab script mixing analysis

G.1   Concentration over the cross-section

```matlab
clc , clear , close all

ChannelPic1 = imread('Normal -1.ome.tif');
ChannelPic2 = imread('Normal -2.ome.tif');
ChannelPic3 = imread('Normal -3.ome.tif');

Channel_Width = 80;

N=Channel_Width;

[x1, y1, Values] = impixel(ChannelPic1);

for i = 1:Channel_Width
    x1Begin(i) = x1(1);
    y1Begin(i) = y1(1) + i - 1;
end

for i = 1:Channel_Width
    x1Middle(i) = x1(2);
    y1Middle(i) = y1(2)  + i - 1;
end

for i = 1:Channel_Width
    x1End(i) = x1(3);
    y1End(i) = y1(3)  + i - 1;
end

[x2, y2, Values] = impixel(ChannelPic2);

for i = 1:Channel_Width
    x2Begin(i) = x2(1);
    y2Begin(i) = y2(1) + i - 1;
end

for i = 1:Channel_Width
    x2Middle(i) = x2(2);
    y2Middle(i) = y2(2)  + i - 1;
end

for i = 1:Channel_Width
    x2End(i) = x2(3);
    y2End(i) = y2(3)  + i - 1;
```

```matlab
43  end
44
45  [x3, y3, Values] = impixel(ChannelPic3);
46
47  for i = 1:Channel_Width
48      x3Begin(i) = x3(1);
49      y3Begin(i) = y3(1) + i - 1;
50  end
51
52  for i = 1:Channel_Width
53      x3Middle(i) = x3(2);
54      y3Middle(i) = y3(2)  + i - 1;
55  end
56
57  for i = 1:Channel_Width
58      x3End(i) = x3(3);
59      y3End(i) = y3(3)  + i - 1;
60  end
61
62  figure, imshow(ChannelPic1)
63  hold on
64  plot(x1Begin, y1Begin);
65  plot(x1Middle, y1Middle);
66  plot(x1End, y1End);
67
68  figure, imshow(ChannelPic2)
69  hold on
70  plot(x2Begin, y2Begin);
71  plot(x2Middle, y2Middle);
72  plot(x2End, y2End);
73
74  figure, imshow(ChannelPic3)
75  hold on
76  plot(x3Begin, y3Begin);
77  plot(x3Middle, y3Middle);
78  plot(x3End, y3End);
79
80  grayChannelPic1 = rgb2gray(ChannelPic1);
81  grayChannelPic2 = rgb2gray(ChannelPic2);
82  grayChannelPic3 = rgb2gray(ChannelPic3);
83
84  Values_Begin1 = impixel(grayChannelPic1,x1Begin,y1Begin);
85  Values_Middle1 = impixel(grayChannelPic1,x1Middle,y1Middle);
86  Values_End1 = impixel(grayChannelPic1,x1End,y1End);
87
88  Values_Begin2 = impixel(grayChannelPic2,x2Begin,y2Begin);
```

```matlab
Values_Middle2 = impixel(grayChannelPic2,x2Middle,y2Middle);
Values_End2 = impixel(grayChannelPic2,x2End,y2End);

Values_Begin3 = impixel(grayChannelPic3,x3Begin,y3Begin);
Values_Middle3 = impixel(grayChannelPic3,x3Middle,y3Middle);
Values_End3 = impixel(grayChannelPic3,x3End,y3End);

[c0_1] = impixel(grayChannelPic1);
[c_max1] = max(Values_Begin1);
[c0_2] = impixel(grayChannelPic2);
[c_max2] = max(Values_Begin2);
[c0_3] = impixel(grayChannelPic3);
[c_max3] = max(Values_Begin3);



Channel_WidthN = [1:Channel_Width];

%% Normalized values concentration
NormV_Begin1 = 1-(Values_Begin1 - c0_1(1))./(c_max1(1)-c0_1
    (1));
Norm_c0_1 = 1;
Norm_c_avg1 = 2/3*Norm_c0_1;

NormV_Begin2 = 1-(Values_Begin2 - c0_2(1))./(c_max2(1)-c0_2
    (1));
Norm_c0_2 = 1;
Norm_c_avg2 = 2/3*Norm_c0_2;

NormV_Begin3 = 1-(Values_Begin3 - c0_3(1))./(c_max3(1)-c0_3
    (1));
Norm_c0_3 = 1;
Norm_c_avg3 = 2/3*Norm_c0_3;

NormV_Middle1 = 1-(Values_Middle1 - c0_1(1))./(c_max1(1)-c0_1
    (1));
NormV_Middle2 = 1-(Values_Middle2 - c0_2(1))./(c_max2(1)-c0_2
    (1));
NormV_Middle3 = 1-(Values_Middle3 - c0_3(1))./(c_max3(1)-c0_3
    (1));

NormV_End1 = 1-(Values_End1 - c0_1(1))./(c_max1(1)-c0_1(1));
NormV_End2 = 1-(Values_End2 - c0_2(1))./(c_max2(1)-c0_2(1));
NormV_End3 = 1-(Values_End3 - c0_3(1))./(c_max3(1)-c0_3(1));


```

```matlab
%% Mixing efficiency
%Begin
for i = 1:Channel_Width
    c_m1 = NormV_Begin1(i,1);
    mixing_effStep1_Begin(i) = 100* (1-((sqrt((c_m1-
        Norm_c_avg1).^2))/(sqrt((Norm_c0_1-Norm_c_avg1).^2))))
        ;
end

for i = 1:Channel_Width
    c_m2 = NormV_Begin2(i,1);
    mixing_effStep2_Begin(i) = 100* (1-((sqrt((c_m2-
        Norm_c_avg2).^2))/(sqrt((Norm_c0_2-Norm_c_avg2).^2))))
        ;
end

for i = 1:Channel_Width
    c_m3 = NormV_Begin3(i,1);
    mixing_effStep3_Begin(i) = 100* (1-((sqrt((c_m3-
        Norm_c_avg3).^2))/(sqrt((Norm_c0_3-Norm_c_avg3).^2))))
        ;
end
%Middle
for i = 1:Channel_Width
    c_m1_Middle = NormV_Middle1(i,1);
    mixing_effStep1_Middle(i) = 100* (1-((sqrt((c_m1_Middle-
        Norm_c_avg1).^2))/(sqrt((Norm_c0_1-Norm_c_avg1).^2))))
        ;
end

for i = 1:Channel_Width
    c_m2_Middle = NormV_Middle2(i,1);
    mixing_effStep2_Middle(i) = 100* (1-((sqrt((c_m2_Middle-
        Norm_c_avg2).^2))/(sqrt((Norm_c0_2-Norm_c_avg2).^2))))
        ;
end

for i = 1:Channel_Width
    c_m3_Middle = NormV_Middle3(i,1);
    mixing_effStep3_Middle(i) = 100* (1-((sqrt((c_m3_Middle-
        Norm_c_avg3).^2))/(sqrt((Norm_c0_3-Norm_c_avg3).^2))))
        ;
end
%End
for i = 1:Channel_Width
    c_m1_End = NormV_End1(i,1);
```

```matlab
        mixing_effStep1_End(i) = 100* (1-((sqrt((c_m1_End-
            Norm_c_avg1).^2))/(sqrt((Norm_c0_1-Norm_c_avg1).^2))))
            ;
end

for i = 1:Channel_Width
    c_m2_End = NormV_End2(i,1);
    mixing_effStep2_End(i) = 100* (1-((sqrt((c_m2_End-
        Norm_c_avg2).^2))/(sqrt((Norm_c0_2-Norm_c_avg2).^2))))
        ;
end

for i = 1:Channel_Width
    c_m3_End = NormV_End3(i,1);
    mixing_effStep3_End(i) = 100* (1-((sqrt((c_m3_End-
        Norm_c_avg3).^2))/(sqrt((Norm_c0_3-Norm_c_avg3).^2))))
        ;
end
%% Mean values

for i = 1:80
  MeanBegin_norm(i) = 100*(NormV_Begin1(i) + NormV_Begin2(i)
      + NormV_Begin3(i))/3;
end

for i = 1:80
  MeanMiddle_norm(i) = 100*(NormV_Middle1(i) + NormV_Middle2(
      i) + NormV_Middle3(i))/3;
end

for i = 1:80
  MeanEnd_norm(i) = 100*(NormV_End1(i) + NormV_End2(i) +
      NormV_End3(i))/3;
end

%% Plots concentration
figure
subplot(1,3,1)
hold on
plot(Channel_WidthN, NormV_Begin1(:,1)*100,'Color',"#D3D3D3",
    'LineWidth',0.7)
plot(Channel_WidthN,NormV_Begin2(:,1)*100,'Color',"#D3D3D3",'
    LineWidth',0.7)
plot(Channel_WidthN, NormV_Begin3(:,1)*100,'Color',"#D3D3D3",
    'LineWidth',0.7)
plot(Channel_WidthN,MeanBegin_norm,"Black",'LineWidth',2)
```

```matlab
197  hold off
198  title('Begin channel cross-section')
199  xlabel('Y-position of cross-section [px]')
200  ylim([0 100])
201  ylabel('Concentration per pixel (%)')
202
203  subplot(1,3,2)
204  hold on
205  plot(Channel_WidthN, NormV_Middle1(:,1)*100,'Color',"#ADD8E6
         ",'LineWidth',0.7)
206  plot(Channel_WidthN, NormV_Middle2(:,1)*100,'Color',"#ADD8E6
         ",'LineWidth',0.7)
207  plot(Channel_WidthN,  NormV_Middle3(:,1)*100,'Color',"#ADD8E6
         ",'LineWidth',0.7)
208  plot(Channel_WidthN,MeanMiddle_norm,"Black",'LineWidth',2)
209  hold off
210  title('Middle channel cross-section')
211  xlabel('Y-position of cross-section [px]')
212  ylim([0 100])
213  ylabel('Concentration per pixel (%)')
214
215  subplot(1,3,3)
216  hold on
217  plot(Channel_WidthN,  NormV_End1(:,1)*100,'Color',"#FFCCCB",'
         LineWidth',0.7)
218  plot(Channel_WidthN, NormV_End2(:,1)*100,'Color',"#FFCCCB",'
         LineWidth',0.7)
219  plot(Channel_WidthN,  NormV_End3(:,1)*100,'Color',"#FFCCCB",'
         LineWidth',0.7)
220  plot(Channel_WidthN,MeanEnd_norm,"Black",'LineWidth',2)
221  hold off
222  title('End channel cross-section')
223  xlabel('Y-position of cross-section [px]')
224  ylim([0 100])
225  ylabel('Concentration per pixel (%)')
226
227  %% Stap Functie
228  % Nullen = zeros(40);
229  % Honderden = ones(40)*100;
230  %
231  % Stap = [Nullen Honderden];
232  % xStap = [1:80];
233  %
234  % close all
235  %
236  % plot(xStap, Stap,'LineWidth',2)
```

```
237  % ylim([-5 110]);
238  % xlabel('Y-position of cross-section [px]')
239  % ylabel('Concentration per pixel (%)')
240  %hold on
241  %plot(xStap, mixing_effStep)
242
243  %figure
244  %plot(xStap,Values_Begin1(:,1))
```

G.2 Intensity over the cross-section

```
 1  clc, clear, close all
 2
 3  ChannelPic1 = imread('Wells-2.ome.tif');
 4  ChannelPic2 = imread('Wells-3.ome.tif');
 5  ChannelPic3 = imread('Wells-4.ome.tif');
 6
 7  Channel_Width = 80;
 8
 9  N=1;
10  %c_0=?;  % unmixed concentration = in reservoir
11  %c_m=?;  % concentration along channel = selected from
        picture
12  %c_avg=? % average concentration = 2/3*c_0
13  %mixing_efficiency=(1-((sqrt(1/N*(c_m-c_avg)^2))/(sqrt(1/N*(
        c_0-c_avg)^2))));
14
15  [x1, y1, Values] = impixel(ChannelPic1);
16
17  for i = 1:Channel_Width
18      x1Begin(i) = x1(1);
19      y1Begin(i) = y1(1) + i - 1;
20  end
21
22  for i = 1:Channel_Width
23      x1Middle(i) = x1(2);
24      y1Middle(i) = y1(2)  + i - 1;
25  end
26
27  for i = 1:Channel_Width
28      x1End(i) = x1(3);
29      y1End(i) = y1(3)  + i - 1;
30  end
31
32  [x2, y2, Values] = impixel(ChannelPic2);
```

```matlab
for i = 1:Channel_Width
    x2Begin(i) = x2(1);
    y2Begin(i) = y2(1) + i - 1;
end

for i = 1:Channel_Width
    x2Middle(i) = x2(2);
    y2Middle(i) = y2(2)  + i - 1;
end

for i = 1:Channel_Width
    x2End(i) = x2(3);
    y2End(i) = y2(3)  + i - 1;
end

[x3, y3, Values] = impixel(ChannelPic3);

for i = 1:Channel_Width
    x3Begin(i) = x3(1);
    y3Begin(i) = y3(1) + i - 1;
end

for i = 1:Channel_Width
    x3Middle(i) = x3(2);
    y3Middle(i) = y3(2)  + i - 1;
end

for i = 1:Channel_Width
    x3End(i) = x3(3);
    y3End(i) = y3(3)  + i - 1;
end

figure, imshow(ChannelPic1)
hold on
plot(x1Begin, y1Begin);
plot(x1Middle, y1Middle);
plot(x1End, y1End);

figure, imshow(ChannelPic2)
hold on
plot(x2Begin, y2Begin);
plot(x2Middle, y2Middle);
plot(x2End, y2End);

figure, imshow(ChannelPic3)
```

```matlab
hold on
plot(x3Begin, y3Begin);
plot(x3Middle, y3Middle);
plot(x3End, y3End);

grayChannelPic1 = rgb2gray(ChannelPic1);
grayChannelPic2 = rgb2gray(ChannelPic2);
grayChannelPic3 = rgb2gray(ChannelPic3);

Values_Begin1 = impixel(grayChannelPic1,x1Begin,y1Begin);
Values_Middle1 = impixel(grayChannelPic1,x1Middle,y1Middle);
Values_End1 = impixel(grayChannelPic1,x1End,y1End);

Values_Begin2 = impixel(grayChannelPic2,x2Begin,y2Begin);
Values_Middle2 = impixel(grayChannelPic2,x2Middle,y2Middle);
Values_End2 = impixel(grayChannelPic2,x2End,y2End);

Values_Begin3 = impixel(grayChannelPic3,x3Begin,y3Begin);
Values_Middle3 = impixel(grayChannelPic3,x3Middle,y3Middle);
Values_End3 = impixel(grayChannelPic3,x3End,y3End);

[c0_1] = impixel(grayChannelPic1);
[c0_2] = impixel(grayChannelPic2);
[c0_3] = impixel(grayChannelPic3);

c_avg1 = c0_1*2/3;
c_avg2 = c0_2*2/3;
c_avg3 = c0_3*2/3;


for i = 1:80
  MeanBegin(i) = (Values_Begin1(i) + Values_Begin2(i) +
      Values_Begin3(i))/3;
end

for i = 1:80
  MeanMiddle(i) = (Values_Middle1(i) + Values_Middle2(i) +
      Values_Middle3(i))/3;
end

for i = 1:80
  MeanEnd(i) = (Values_End1(i) + Values_End2(i) + Values_End3
      (i))/3;
end

Channel_WidthN = [1:Channel_Width];
```

```matlab
NormV_Begin1 = (Values_Begin1 -149)./(213-149);
Norm_c0_1 = (c0_1(1) - 149)/(213-149);
Norm_c_avg1 = (c_avg1(1) - 149)/(213-149);


for i = 1:Channel_Width
    c_m = NormV_Begin1(i,1);
    mixing_eff(i) = (1-((sqrt(1/N*(c_m-Norm_c_avg1)^2))/(sqrt
        (1/N*(Norm_c0_1-Norm_c_avg1)^2)))));
    mixing_eff2(i) = 1 - (c_m - Norm_c_avg1)/(Norm_c0_1 -
        Norm_c_avg1);
end


figure
subplot(1,3,1)
hold on
plot(Channel_WidthN, Values_Begin1(:,1),'Color',"#D3D3D3",'
    LineWidth',0.7)
plot(Channel_WidthN, Values_Begin2(:,1),'Color',"#D3D3D3",'
    LineWidth',0.7)
plot(Channel_WidthN, Values_Begin3(:,1),'Color',"#D3D3D3",'
    LineWidth',0.7)
plot(Channel_WidthN,MeanBegin,"Black",'LineWidth',2)
hold off
title('Begin channel cross-section')
xlabel('Y-position of cross-section [px]')
ylim([150 250])
ylabel('Intensity')

subplot(1,3,2)
hold on
plot(Channel_WidthN, Values_Middle1(:,1),'Color',"#ADD8E6",'
    LineWidth',0.7)
plot(Channel_WidthN, Values_Middle2(:,1),'Color',"#ADD8E6",'
    LineWidth',0.7)
plot(Channel_WidthN, Values_Middle3(:,1),'Color',"#ADD8E6",'
    LineWidth',0.7)
plot(Channel_WidthN,MeanMiddle,"Black",'LineWidth',2)
hold off
title('Middle channel cross-section')
xlabel('Y-position of cross-section [px]')
ylim([150 250])
ylabel('Intensity')
```

```
160
161  subplot(1,3,3)
162  hold on
163  plot(Channel_WidthN, Values_End1(:,1),'Color',"#FFCCCB",'
        LineWidth',0.7)
164  plot(Channel_WidthN, Values_End2(:,1),'Color',"#FFCCCB",'
        LineWidth',0.7)
165  plot(Channel_WidthN, Values_End3(:,1),'Color',"#FFCCCB",'
        LineWidth',0.7)
166  plot(Channel_WidthN,MeanEnd,"Black",'LineWidth',2)
167  hold off
168  title('End channel cross-section')
169  xlabel('Y-position of cross-section [px]')
170  ylim([150 250])
171  ylabel('Intensity')
```

G.3 Mixing efficiency over time

```
1   clc, clear, close all
2
3   ChannelPic1 = imread('Normal-1 0min.png');
4   ChannelPic2 = imread('Normal-1 5min.png');
5   ChannelPic3 = imread('Normal-1 10min.png');
6   ChannelPic4 = imread('Normal-1 15min.png');
7   ChannelPic5 = imread('Normal-1 20min.png');
8
9   ChannelPic1_2 = imread('Normal-2 0 min.png');
10  ChannelPic2_2 = imread('Normal-2 5min.png');
11  ChannelPic3_2 = imread('Normal-2 10min.png');
12  ChannelPic4_2 = imread('Normal-2 15min.png');
13  ChannelPic5_2 = imread('Normal-2 20min.png');
14
15  ChannelPic1_3 = imread('Normal-3 0min.png');
16  ChannelPic2_3 = imread('Normal-3 5min.png');
17  ChannelPic3_3 = imread('Normal-3 10min.png');
18  ChannelPic4_3 = imread('Normal-3 15min.png');
19  ChannelPic5_3 = imread('Normal-3 20min.png');
20
21
22  Channel_Width = 80;
23
24  N=Channel_Width;
25
26  %% Values collection
27
```

```matlab
[x1, y1, Values] = impixel(ChannelPic1);
%1
for i = 1:Channel_Width
    x1(i) = x1(1);
    y1(i) = y1(1) + i - 1;
end

[x2, y2, Values] = impixel(ChannelPic2);

for i = 1:Channel_Width
    x2(i) = x2(1);
    y2(i) = y2(1) + i - 1;
end

[x3, y3, Values] = impixel(ChannelPic3);

for i = 1:Channel_Width
    x3(i) = x3(1);
    y3(i) = y3(1) + i - 1;
end

[x4, y4, Values] = impixel(ChannelPic4);

for i = 1:Channel_Width
    x4(i) = x4(1);
    y4(i) = y4(1) + i - 1;
end

[x5, y5, Values] = impixel(ChannelPic5);

for i = 1:Channel_Width
    x5(i) = x5(1);
    y5(i) = y5(1) + i - 1;
end
%2
[x1_2, y1_2, Values] = impixel(ChannelPic1_2);

for i = 1:Channel_Width
    x1_2(i) = x1_2(1);
    y1_2(i) = y1_2(1) + i - 1;
end

[x2_2, y2_2, Values] = impixel(ChannelPic2_2);

for i = 1:Channel_Width
    x2_2(i) = x2_2(1);
```

```matlab
        y2_2(i) = y2_2(1) + i - 1;
end

[x3_2, y3_2, Values] = impixel(ChannelPic3_2);

for i = 1:Channel_Width
    x3_2(i) = x3_2(1);
    y3_2(i) = y3_2(1) + i - 1;
end

[x4_2, y4_2, Values] = impixel(ChannelPic4_2);

for i = 1:Channel_Width
    x4_2(i) = x4_2(1);
    y4_2(i) = y4_2(1) + i - 1;
end

[x5_2, y5_2, Values] = impixel(ChannelPic5_2);

for i = 1:Channel_Width
    x5_2(i) = x5_2(1);
    y5_2(i) = y5_2(1) + i - 1;
end
%3
[x1_3, y1_3, Values] = impixel(ChannelPic1_3);

for i = 1:Channel_Width
    x1_3(i) = x1_3(1);
    y1_3(i) = y1_3(1) + i - 1;
end

[x2_3, y2_3, Values] = impixel(ChannelPic2_3);

for i = 1:Channel_Width
    x2_3(i) = x2_3(1);
    y2_3(i) = y2_3(1) + i - 1;
end

[x3_3, y3_3, Values] = impixel(ChannelPic3_3);

for i = 1:Channel_Width
    x3_3(i) = x3_3(1);
    y3_3(i) = y3_3(1) + i - 1;
end

[x4_3, y4_3, Values] = impixel(ChannelPic4_3);
```

```matlab
120
121  for i = 1:Channel_Width
122      x4_3(i) = x4_3(1);
123      y4_3(i) = y4_3(1) + i - 1;
124  end
125
126  [x5_3, y5_3, Values] = impixel(ChannelPic5_3);
127
128  for i = 1:Channel_Width
129      x5_3(i) = x5_3(1);
130      y5_3(i) = y5_3(1) + i - 1;
131  end
132  %% Gray values
133  grayChannelPic1 = rgb2gray(ChannelPic1);
134  grayChannelPic2 = rgb2gray(ChannelPic2);
135  grayChannelPic3 = rgb2gray(ChannelPic3);
136  grayChannelPic4 = rgb2gray(ChannelPic4);
137  grayChannelPic5 = rgb2gray(ChannelPic5);
138
139  grayChannelPic1_2 = rgb2gray(ChannelPic1_2);
140  grayChannelPic2_2 = rgb2gray(ChannelPic2_2);
141  grayChannelPic3_2 = rgb2gray(ChannelPic3_2);
142  grayChannelPic4_2 = rgb2gray(ChannelPic4_2);
143  grayChannelPic5_2 = rgb2gray(ChannelPic5_2);
144
145  grayChannelPic1_3 = rgb2gray(ChannelPic1_3);
146  grayChannelPic2_3 = rgb2gray(ChannelPic2_3);
147  grayChannelPic3_3 = rgb2gray(ChannelPic3_3);
148  grayChannelPic4_3 = rgb2gray(ChannelPic4_3);
149  grayChannelPic5_3 = rgb2gray(ChannelPic5_3);
150
151
152  Values_1 = impixel(grayChannelPic1,x1,y1);
153  Values_2 = impixel(grayChannelPic2,x2,y2);
154  Values_3 = impixel(grayChannelPic3,x3,y3);
155  Values_4 = impixel(grayChannelPic4,x4,y4);
156  Values_5 = impixel(grayChannelPic5,x5,y5);
157
158  Values_1_2 = impixel(grayChannelPic1_2,x1_2,y1_2);
159  Values_2_2 = impixel(grayChannelPic2_2,x2_2,y2_2);
160  Values_3_2 = impixel(grayChannelPic3_2,x3_2,y3_2);
161  Values_4_2 = impixel(grayChannelPic4_2,x4_2,y4_2);
162  Values_5_2 = impixel(grayChannelPic5_2,x5_2,y5_2);
163
164  Values_1_3 = impixel(grayChannelPic1_3,x1_3,y1_3);
165  Values_2_3 = impixel(grayChannelPic2_3,x2_3,y2_3);
```

```matlab
166  Values_3_3 = impixel(grayChannelPic3_3,x3_3,y3_3);
167  Values_4_3 = impixel(grayChannelPic4_3,x4_3,y4_3);
168  Values_5_3 = impixel(grayChannelPic5_3,x5_3,y5_3);
169
170  %% Normalization of values
171  [c0_1] = impixel(grayChannelPic1);
172  [c_max1] = max(Values_1);
173  [c0_2] = impixel(grayChannelPic2);
174  [c_max2] = max(Values_2);
175  [c0_3] = impixel(grayChannelPic3);
176  [c_max3] = max(Values_3);
177  [c0_4] = impixel(grayChannelPic4);
178  [c_max4] = max(Values_4);
179  [c0_5] = impixel(grayChannelPic5);
180  [c_max5] = max(Values_5);
181
182  [c0_1_2] = impixel(grayChannelPic1_2);
183  [c_max1_2] = max(Values_1_2);
184  [c0_2_2] = impixel(grayChannelPic2_2);
185  [c_max2_2] = max(Values_2_2);
186  [c0_3_2] = impixel(grayChannelPic3_2);
187  [c_max3_2] = max(Values_3_2);
188  [c0_4_2] = impixel(grayChannelPic4_2);
189  [c_max4_2] = max(Values_4_2);
190  [c0_5_2] = impixel(grayChannelPic5_2);
191  [c_max5_2] = max(Values_5_2);
192
193  [c0_1_3] = impixel(grayChannelPic1_3);
194  [c_max1_3] = max(Values_1_3);
195  [c0_2_3] = impixel(grayChannelPic2_3);
196  [c_max2_3] = max(Values_2_3);
197  [c0_3_3] = impixel(grayChannelPic3_3);
198  [c_max3_3] = max(Values_3_3);
199  [c0_4_3] = impixel(grayChannelPic4_3);
200  [c_max4_3] = max(Values_4_3);
201  [c0_5_3] = impixel(grayChannelPic5_3);
202  [c_max5_3] = max(Values_5_3);
203
204
205  NormV_1 = (Values_1 - c0_1(1))./(c_max1(1)-c0_1(1));
206  Norm_c0_1 = 1;
207  Norm_c_avg1 = 2/3*Norm_c0_1;
208  NormV_2 = (Values_2 - c0_2(1))./(c_max2(1)-c0_2(1));
209  Norm_c0_2 = 1;
210  Norm_c_avg2 = 2/3*Norm_c0_2;
211  NormV_3 = (Values_3 - c0_3(1))./(c_max3(1)-c0_3(1));
```

148

```
212  Norm_c0_3 = 1;
213  Norm_c_avg3 = 2/3*Norm_c0_3;
214  NormV_4 = (Values_4 - c0_4(1))./(c_max4(1)-c0_4(1));
215  Norm_c0_4 = 1;
216  Norm_c_avg4 = 2/3*Norm_c0_4;
217  NormV_5 = (Values_5 - c0_5(1))./(c_max5(1)-c0_5(1));
218  Norm_c0_5 = 1;
219  Norm_c_avg5 = 2/3*Norm_c0_5;
220
221  NormV_1_2 = (Values_1_2 - c0_1_2(1))./(c_max1_2(1)-c0_1_2(1))
         ;
222  Norm_c0_1_2 = 1;
223  Norm_c_avg1_2 = 2/3*Norm_c0_1_2;
224  NormV_2_2 = (Values_2_2 - c0_2_2(1))./(c_max2_2(1)-c0_2_2(1))
         ;
225  Norm_c0_2_2 = 1;
226  Norm_c_avg2_2 = 2/3*Norm_c0_2_2;
227  NormV_3_2 = (Values_3_2 - c0_3_2(1))./(c_max3_2(1)-c0_3_2(1))
         ;
228  Norm_c0_3_2 = 1;
229  Norm_c_avg3_2 = 2/3*Norm_c0_3_2;
230  NormV_4_2 = (Values_4_2 - c0_4_2(1))./(c_max4_2(1)-c0_4_2(1))
         ;
231  Norm_c0_4_2 = 1;
232  Norm_c_avg4_2 = 2/3*Norm_c0_4_2;
233  NormV_5_2 = (Values_5_2 - c0_5_2(1))./(c_max5_2(1)-c0_5_2(1))
         ;
234  Norm_c0_5_2 = 1;
235  Norm_c_avg5_2 = 2/3*Norm_c0_5_2;
236
237  NormV_1_3 = (Values_1_3 - c0_1_3(1))./(c_max1_3(1)-c0_1_3(1))
         ;
238  Norm_c0_1_3 = 1;
239  Norm_c_avg1_3 = 2/3*Norm_c0_1_3;
240  NormV_2_3 = (Values_2_3 - c0_2_3(1))./(c_max2_3(1)-c0_2_3(1))
         ;
241  Norm_c0_2_3 = 1;
242  Norm_c_avg2_3 = 2/3*Norm_c0_2_3;
243  NormV_3_3 = (Values_3_3 - c0_3_3(1))./(c_max3_3(1)-c0_3_3(1))
         ;
244  Norm_c0_3_3 = 1;
245  Norm_c_avg3_3 = 2/3*Norm_c0_3_3;
246  NormV_4_3 = (Values_4_3 - c0_4_3(1))./(c_max4_3(1)-c0_4_3(1))
         ;
247  Norm_c0_4_3 = 1;
248  Norm_c_avg4_3 = 2/3*Norm_c0_4_3;
```

```matlab
NormV_5_3 = (Values_5_3 - c0_5_3(1))./(c_max5_3(1)-c0_5_3(1))
    ;
Norm_c0_5_3 = 1;
Norm_c_avg5_3 = 2/3*Norm_c0_5_3;
%% Calculation mixing efficiency
%1
for i = 1:Channel_Width
    c_m1 = NormV_1(i,1);
    mixing_effStep1(i) = 100* (1-((sqrt((c_m1-Norm_c_avg1)
        .^2))/(sqrt((Norm_c0_1-Norm_c_avg1).^2))));
end

 for i = 1:Channel_Width
    c_m2 = NormV_2(i,1);
    mixing_effStep2(i) = 100* (1-((sqrt((c_m2-Norm_c_avg2)
        .^2))/(sqrt((Norm_c0_2-Norm_c_avg2).^2))));
 end

  for i = 1:Channel_Width
    c_m3 = NormV_3(i,1);
    mixing_effStep3(i) = 100* (1-((sqrt((c_m3-Norm_c_avg3)
        .^2))/(sqrt((Norm_c0_3-Norm_c_avg3).^2))));
  end

   for i = 1:Channel_Width
    c_m4 = NormV_4(i,1);
    mixing_effStep4(i) = 100* (1-((sqrt((c_m4-Norm_c_avg4)
        .^2))/(sqrt((Norm_c0_4-Norm_c_avg4).^2))));
   end

    for i = 1:Channel_Width
    c_m5 = NormV_5(i,1);
    mixing_effStep5(i) = 100* (1-((sqrt((c_m5-Norm_c_avg5)
        .^2))/(sqrt((Norm_c0_5-Norm_c_avg5).^2))));
    end
%2
for i = 1:Channel_Width
    c_m1_2 = NormV_1_2(i,1);
    mixing_effStep1_2(i) = 100* (1-((sqrt((c_m1_2-
        Norm_c_avg1_2).^2))/(sqrt((Norm_c0_1_2-Norm_c_avg1_2)
        .^2))));
end

 for i = 1:Channel_Width
    c_m2_2 = NormV_2_2(i,1);
```

```matlab
    mixing_effStep2_2(i) = 100* (1-((sqrt((c_m2_2-
        Norm_c_avg2_2).^2))/(sqrt((Norm_c0_2_2-Norm_c_avg2_2)
        .^2))));
  end

  for i = 1: Channel_Width
    c_m3_2 = NormV_3_2(i,1);
    mixing_effStep3_2(i) = 100* (1-((sqrt((c_m3_2-
        Norm_c_avg3_2).^2))/(sqrt((Norm_c0_3_2-Norm_c_avg3_2)
        .^2))));
  end

  for i = 1: Channel_Width
   c_m4_2 = NormV_4_2(i,1);
   mixing_effStep4_2(i) = 100* (1-((sqrt((c_m4_2-
        Norm_c_avg4_2).^2))/(sqrt((Norm_c0_4_2-Norm_c_avg4_2)
        .^2))));
    end

    for i = 1: Channel_Width
    c_m5_2 = NormV_5_2(i,1);
    mixing_effStep5_2(i) = 100* (1-((sqrt((c_m5_2-
        Norm_c_avg5_2).^2))/(sqrt((Norm_c0_5_2-Norm_c_avg5_2)
        .^2))));
      end
%3
for i = 1: Channel_Width
    c_m1_3 = NormV_1_3(i,1);
    mixing_effStep1_3(i) = 100* (1-((sqrt((c_m1_3-
        Norm_c_avg1_3).^2))/(sqrt((Norm_c0_1_3-Norm_c_avg1_3)
        .^2))));
end

 for i = 1: Channel_Width
    c_m2_3 = NormV_2_3(i,1);
    mixing_effStep2_3(i) = 100* (1-((sqrt((c_m2_3-
        Norm_c_avg2_3).^2))/(sqrt((Norm_c0_2_3-Norm_c_avg2_3)
        .^2))));
  end

  for i = 1: Channel_Width
    c_m3_3 = NormV_3_3(i,1);
    mixing_effStep3_3(i) = 100* (1-((sqrt((c_m3_3-
        Norm_c_avg3_3).^2))/(sqrt((Norm_c0_3_3-Norm_c_avg3_3)
        .^2))));
   end
```

```matlab
318
319     for i = 1:Channel_Width
320      c_m4_3 = NormV_4_3(i,1);
321      mixing_effStep4_3(i) = 100* (1-((sqrt((c_m4_3-
            Norm_c_avg4_3).^2))/(sqrt((Norm_c0_4_3-Norm_c_avg4_3)
            .^2))));
322     end
323
324     for i = 1:Channel_Width
325      c_m5_3 = NormV_5_3(i,1);
326      mixing_effStep5_3(i) = 100* (1-((sqrt((c_m5_3-
            Norm_c_avg5_3).^2))/(sqrt((Norm_c0_5_3-Norm_c_avg5_3)
            .^2))));
327     end
328 %% Mean
329 mean1 = mean(mixing_effStep1);
330 mean2 = mean(mixing_effStep2);
331 mean3 = mean(mixing_effStep3);
332 mean4 = mean(mixing_effStep4);
333 mean5 = mean(mixing_effStep5);
334
335 mean1_2 = mean(mixing_effStep1_2);
336 mean2_2 = mean(mixing_effStep2_2);
337 mean3_2 = mean(mixing_effStep3_2);
338 mean4_2 = mean(mixing_effStep4_2);
339 mean5_2 = mean(mixing_effStep5_2);
340
341 mean1_3 = mean(mixing_effStep1_3);
342 mean2_3 = mean(mixing_effStep2_3);
343 mean3_3 = mean(mixing_effStep3_3);
344 mean4_3 = mean(mixing_effStep4_3);
345 mean5_3 = mean(mixing_effStep5_3);
346
347 mean_tot1 = (mean1+mean1_2+mean1_3)/3;
348 mean_tot2 = (mean2+mean2_2+mean2_3)/3;
349 mean_tot3 = (mean3+mean3_2+mean3_3)/3;
350 mean_tot4 = (mean4+mean4_2+mean4_3)/3;
351 mean_tot5 = (mean5+mean5_2+mean5_3)/3;
352 %% Plot
353   xTime = [0 5 10 15 20] ;
354   yTime_mean = [mean1 mean2 mean3 mean4 mean5];
355  yTime_2_mean = [mean1_2 mean2_2 mean3_2 mean4_2 mean5_2];
356   yTime_3_mean = [mean1_3 mean2_3 mean3_3 mean4_3 mean5_3];
357   yTime_tot_mean = [mean_tot1 mean_tot2 mean_tot3 mean_tot4
          mean_tot5];
358
```

```matlab
359  yTime = [mixing_effStep1(1) mixing_effStep2(1)
         mixing_effStep3(1) mixing_effStep4(1) mixing_effStep5(1)];
360  yTime_2 = [mixing_effStep1_2(1) mixing_effStep2_2(1)
         mixing_effStep3_2(1) mixing_effStep4_2(1)
         mixing_effStep5_2(1)];
361  yTime_3 = [mixing_effStep1_3(1) mixing_effStep2_3(1)
         mixing_effStep3_3(1) mixing_effStep4_3(1)
         mixing_effStep5_3(1)];
362  yTime_avg = [(mixing_effStep1(1)+mixing_effStep1_2(1)+
         mixing_effStep1_3(1))/3 (mixing_effStep2(1)+
         mixing_effStep2_2(1)+mixing_effStep2_3(1))/3 (
         mixing_effStep3(1)+mixing_effStep3_2(1)+mixing_effStep3_3
         (1))/3 (mixing_effStep4(1)+mixing_effStep4_2(1)+
         mixing_effStep4_3(1))/3 (mixing_effStep5(1)+
         mixing_effStep5_2(1)+mixing_effStep5_3(1))/3];
363
364  figure
365  hold on
366  plot(xTime,yTime_mean,'Color',"#FFCCCB",'LineWidth',0.7)
367  plot(xTime,yTime_2_mean,'Color',"#FFCCCB",'LineWidth',0.7)
368  plot(xTime,yTime_3_mean,'Color',"#FFCCCB",'LineWidth',0.7)
369  plot(xTime,yTime_tot_mean,"Black",'LineWidth',2)
370  hold off
371  title('Herringbone')
372  xlabel('Time (min)')
373  ylim([0 100])
374  ylabel('Mixing Efficiency (%)')
375
376  figure
377  hold on
378  plot(xTime,yTime,'Color',"#ADD8E6",'LineWidth',0.7)
379  plot(xTime,yTime_2,'Color',"#ADD8E6",'LineWidth',0.7)
380  plot(xTime,yTime_3,'Color',"#ADD8E6",'LineWidth',0.7)
381  plot(xTime,yTime_avg,"Black",'LineWidth',2)
382  hold off
383  title('Straight')
384  xlabel('Time (min)')
385  ylim([0 100])
386  ylabel('Mixing Efficiency (%)')
```

153

H Calculations two read-out design

Several calculations are done for the two read-out design. The width and height of the channel are 0.7 mm and 2 mm, respectively. The width of the trigger valve is 0.4 mm, and the height 0.5 mm.
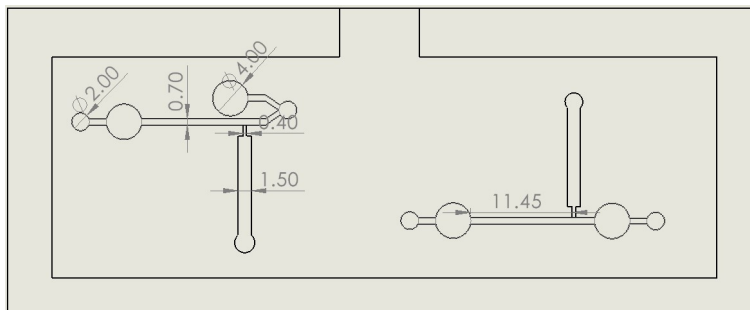
Figure H.1: The dimensions of the two read-out design.

H.1 Diffusion in the chip

For sphere-shaped proteins, the minimal radius of the particles can be determined by:

$$R_{min} = 0.066M^{1/3} \tag{15}$$

With the molecular mass (M) in Dalton and the minimal radius (R_min) in nm. For DTNB the R_min is:

$$R_{min} = 0.066 \cdot 395.972^{1/3} = 0.48nm$$

The Stokes-Einstein equation can be used to estimate the Diffusion constant of DTNB:

$$D = \frac{kT}{6\pi\mu r} \tag{16}$$

where k is Boltzmann's constant, T is the absolute temperature, r is the particle radius, and μ is the fluid viscosity.

$$D = \frac{1.380649 \cdot 10^{-23} \cdot 273}{6\pi \cdot 10^{-3} \cdot 0.48 \cdot 10^{-9}} = 417\mu^2/s$$

The time it takes to mix the liquids, t_{mix} (s), depends on the length, L (m), and diffusion coefficient, D (m^2/s) (equation 17). As the diffusion constant of DTNB is constant, the mixing time can be reduced by decreasing the path length to the minimum length for sufficient mixing.

$$t_{mix} = \frac{L^2}{2D} \tag{17}$$

With the L from the two read-outs design (2 mm) the t_{mix} is:

$$t_{mix} = \frac{(2 \cdot 10^{-3})^2}{2 \cdot 4.17 \cdot 10^{-10}} = 4801s$$

In conclusion, using the two read-outs design the time it takes to mix DTNB and water is 1.33 hours.

H.2   Reynolds number

The Reynolds number decreases with increasing pipetting time (Figure H.2).
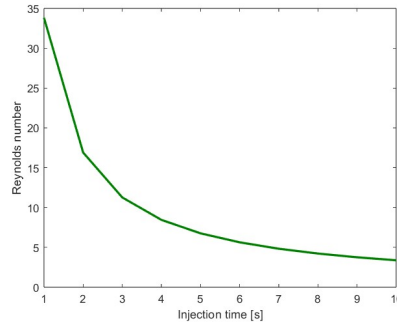
Figure H.2: Reynolds number for different pipetting times.

H.3   Hydrostatic pressure

In this microfluidic device the pressure-driven flow is generated by hydrostatic pressure, which creates a constant pressure difference:

$$\Delta P = \rho \cdot g \cdot h \tag{18}$$

where ρ is the solution density (kg/m^3), g the acceleration due to gravity (m/s^2) and h the height difference between the solution in the vessel and the microfluidic device (m).

$$\Delta P = 10^3 \cdot 9.81 \cdot 2 \cdot 10^{-3} = 19.62 Pa$$

H.4   Capillary Pressure

In a straight channel, capillary pressure is calculated with:

$$\Delta P = 2\gamma \left(\frac{1}{w} + \frac{1}{h} \right) cos\theta_c \tag{19}$$

$$\Delta P = 2 \cdot 72 \cdot 10^{-3} \left(\frac{1}{0.7 \cdot 10^{-3}} + \frac{1}{2 \cdot 10^{-3}} \right) cos(31 \cdot \frac{\pi}{180})$$

$$\Delta P = 238 Pa$$

The capillary pressure can be calculated with the Young-Laplace equation:

$$P = -\gamma \left(\frac{cos\theta_t + cos\theta_b}{h} \cdot \frac{cos\theta_r + cos\theta_l}{w} \right) \tag{20}$$

$$P = -222.8 Pa$$

I Calculations volume control design

The flow layer of the Quake-valve design has four different channels, separated by reservoirs (Figure I.1). The channels have a height of 0.5 mm, the middle reservoir for placing the filter paper also has a height of 0.5 mm, and the control and experimental read-out reservoirs (left and right) have a height of 2 mm.
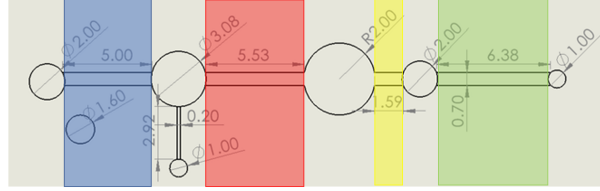
Figure I.1: The technical drawing with dimensions of the Quake-valve's flow layer with the four channel parts indicated with colors, from left to right: blue, red, yellow, green.

I.1 Hydraulic resistance

The resistance of the flow in the channels is calculated. Table 16 shows an overview of the length, widht, and height of the channels indicated in Figure I.1.

Table 16: All the abbreviations and descriptions of the four channels indicated with different colors (Figure I.1).

Color	Abbreviation	Description	Value
Blue	L_1	Length blue channel	5 mm
	w_1	Width blue channel	0.7 mm
	h_1	Height blue channel	0.5 mm
Red	L_2	Length red channel	5.53 mm
	w_2	Width red channel	0.7 mm
	h_2	Height red channel	0.5 mm
Yellow	L_3	Length yellow channel	1.59 mm
	w_3	Width yellow channel	0.7 mm
	h_3	Height yellow channel	0.5 mm
Green	L_4	Length green channel	6.38 mm
	w_4	Width green channel	0.7 mm
	h_4	Height green channel	0.5 mm

Two different equations are used for the calculations of the hydraulic resistance:

$$R = \frac{12\eta L}{[1 - 0.63(h/w)]} \frac{1}{(h^3 w)} [58, 93] \tag{21}$$

$$R = \frac{4\mu L}{ab^3} \left[\frac{16}{3} - 3.36\frac{b}{a}\left(1 - \frac{b^4}{12a^4}\right) \right]^{-1} [120] \tag{22}$$

$$2a = w$$

$$2b = h$$

Both equations calculate the resistance based on the velocity profile over the cross-section. The resistance indicates the difficulty with which a fluid can flow through a particular channel. Both equations are an approximation for a rectangular channel [58, 93, 120]. μ and η are used to indicated the dynamic viscosity and the value for water is assumed $(0.89 \cdot 10^{-3} Pa \cdot s)$ For the blue channel the example calculations are:

$$R = \frac{12 \cdot 0.89 \cdot 10^{-3} \cdot 5 \cdot 10^{-3}}{[1 - 0.63(0.5 \cdot 10^{-3}/0.7 \cdot 10^{-3})]} \cdot \frac{1}{((0.5 \cdot 10^{-3})^3 \cdot 0.7 \cdot 10^{-3})}$$
$$R = 1.11 \cdot 10^9 Pa \cdot s \cdot m^{-3}$$

$$R = \frac{4 \cdot 0.89 \cdot 10^{-3} \cdot 5 \cdot 10^{-3}}{0.35 \cdot 10^{-3} \cdot (0.25 \cdot 10^{-3})^3} \cdot \left[\frac{16}{3} - 3.36 \frac{0.25 \cdot 10^{-3}}{0.35 \cdot 10^{-3}} \cdot \left(1 - \frac{(0.25 \cdot 10^{-3})^4}{12 \cdot (0.35 \cdot 10^{-3})^4} \right) \right]^{-1}$$

$$R = 1.09 \cdot 10^9 Pa \cdot s \cdot m^{-3}$$

The calculated hydraulic resistance of all channels are listed in Table 17, for both equations. It is seen that with increasing channel length the resistance increases as well. The resistance values calculated with equation 21 are slightly higher than the values calculated with equation 22, but they are in the same order of magnitude with minimal differences between the values.

Table 17: *The hydraulic resistance for each channel of the flow layer design of the Quake-valve calculated with equation 21 and equation 22.*

Channel	R $[\cdot 10^9 Pa \cdot s \cdot m^{-3}]$(equation 21)	R $[\cdot 10^9 Pa \cdot s \cdot m^{-3}]$(equation 22)
Blue	1.11	1.09
Red	1.23	1.21
Yellow	0.35	0.35
Green	1.42	1.39

J Calculations theoretical absorbance values

The Lambert-Beer law (equation J) for the determination of the theoretical absorbance values.

$$A = log_{10}(I_0/I) = abc$$

The relation between the absorbance (A) of a sample and the absorption coefficient (a), path length (b), and concentration (c) is linear. The absorption coefficient for DTNB is 14,150 / $M \cdot cm$, the path length of the reservoirs is 2 mm, and the concentrations of the standards are used (0, 15.625, 31.25, 62.5, 125, 250, 500, 1000 μM). The calculated absorbance values are shown in Table 18 and Figure J.1.

Table 18: The calculated absorbance values for the standards' concentrations.

Concentration (uM)	Absorbance [a.u.]
0	0.00
15.625	0.04
31.25	0.09
62.5	0.18
125	0.35
250	0.71
500	1.42
1000	2.83
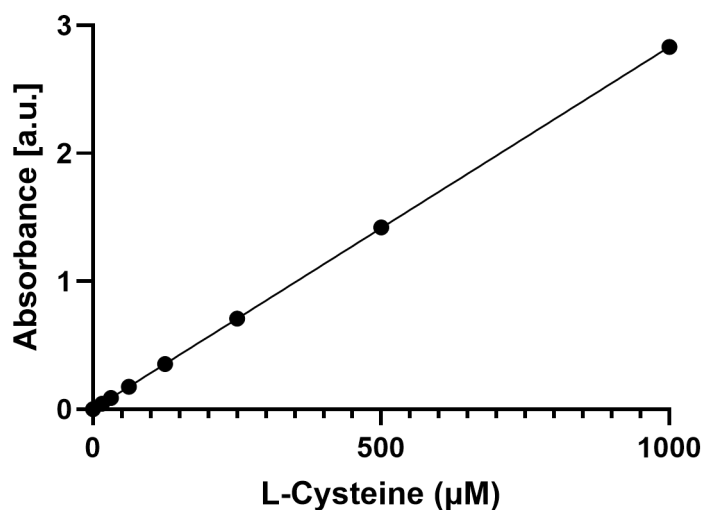
Figure J.1: The theoretically calculated calibration curve.

K   Protocol lyophilization

Control:

- Pipette 20 μL 1.9 mM DTNB in phosphate buffer (0.1 M, pH 7) in an Eppendorf.

- Freeze the DTNB in the Eppendorf by putting the Eppendorf in liquid nitrogen with the lid open.

- Place the Eppendorfs in the standard and put them in the vacuum chamber.

- Put a filter in the lid of the vacuum chamber.

- Place aluminum foil over the chamber to protect the DTNB from light.

- Open the vacuum tap.

- Run main drying of the Eppendorfs overnight at -55 degrees Celsius, with pressure set to 1 mbar.

- Carefully remove the vacuum to prevent the freeze-dried particles from moving through the vacuum chamber.

- If the particles move easily, the Eppendorfs could be closed with a hole poked into the lid before placing in the vacuum chamber.

Microfluidic chip:

- Pipette 20 μL 1.9 mM DTNB in phosphate buffer (0.1 M, pH 7) in the microfluidic chip inlet.

- Place them in a petri dish and stack them, so none of the inlets are covered.

- Freeze overnight in a freezer at -80 degrees Celsius.

- After freezing the chips stick together, so the inlets need to be checked before freezing.

- Place the chips on top of the Eppendorf standard and put them in the vacuum chamber.

- Put a filter in the lid of the vacuum chamber.

- Place aluminum foil over the chamber to protect the DTNB from light.

- Open the vacuum tap.

- Run main drying of the microfluidic chips overnight at -55 degrees Celsius, with pressure set to 1 mbar.

- Carefully remove the vacuum to prevent the freeze-dried particles from moving through the vacuum chamber.

K.1 Absorption measurement of lyophilization experiment

Control:

- Pipette 90 μL 10 mM L-Cystein 1:4 diluted with 0.1M pH 8.2 Tris buffer in the Eppendorfs

- Resuspend and also wash the walls of the Eppendorfs

- Incubate for 20 minutes in the dark at room temperature

- Pipette the 90 μL from the Eppendorfs into a 96 wells plate

- Pipette 90 μL 10 mM L-Cystein 1:4 diluted with 0.1M pH 8.2 Tris buffer without DTNB as negative control in the wells plate and pipette 20 μL 1.9 mM DTNB in phosphate buffer (0.1 M, pH 7) as positive control

- Pipette 90 μL 10 mM L-Cystein 1:4 diluted with 0.1M pH 8.2 Tris buffer in the wells and add 20 μL 1.9 mM DTNB in phosphate buffer (0.1 M, pH 7)

- Place the wells plate in the plate reader (SpectraMax ID3)

- Set the wavelengths to 412 and 630 nm.

- Measure the absorption

Microfluidic chip:

- Pipette 90 μL 10 mM L-Cystein 1:4 diluted with 0.1M pH 8.2 Tris buffer in the inlet

- Incubate for 20 minutes in the dark at room temperature

- Place the chip in the PMMA plate reader mold.

- Place the plate reader mold with the chip in the plate reader (SpectraMax ID3)

- Set the wavelengths to 412 and 630 nm.

- Measure the absorption with settings for a 96 wells plate and 384 wells plate

L Statistical analysis calibration curves and plasma samples using R-studio

L.1 R-script statistical analysis

```
#Master Thesis R-script
#Kim Eline de Jager


rm(list = ls())


#########################
#t-test plasma sample concentration
Plasma_conc <- c(112.3808007,
                 128.4526208,
                 84.1940524,
                 113.3624589,
                 128.3601673,
                 122.8713152,
                 120.204197,
                 111.8163034,
                 109.535724,
                 111.7389956,
                 110.3474556)


Plasma_conc_x_4 <- 4*Plasma_conc


Type <- c("Chip","Chip","Chip","Well","Well","Well","Well","Well","Well","W


t.test(Plasma_conc_x_4~Type)
aov_plasma <- aov(Plasma_conc_x_4~Type)
summary(aov_plasma)
plot(aov_plasma,1)
plot(aov_plasma,2)
# Extract the residuals
aov_residuals <- residuals(object = aov_plasma )
summary(aov_residuals)
# Run Shapiro-Wilk test
shapiro.test(x = aov_residuals )


#########################
#Bland-Altman plot
chip_plasma <- 4*c(112.3808007,
            128.4526208,
            84.19405241, NA, NA, NA, NA, NA)
well_plasma <- 4*c(113.3624589,
            128.3601673,
```

```
              122.8713152 ,
              120.204197 ,
              111.8163034 ,
              109.535724 ,
              111.7389956 ,
              110.3474556)


# Calculate differences and averages
diff <- (chip_plasma - well_plasma)
avg <- (chip_plasma + well_plasma) / 2

# Create Bland-Altman plot
plot(avg, diff, xlim = c(400, 550), ylim = c(-160, 10), xlab = "Average", y
abline(h = 0, col = "red", lty = 2)  # Add horizontal line at zero




####################################
#ANOVA calibration curves

# Concentration levels
Concentration <- c(0, 15.625, 31.250, 62.5, 125, 250, 500, 1000)

# Method 1 measurements (triplicates)
Well <- c(0.058,
                       0.0977 ,
                       0.1323 ,
                       0.2154 ,
                       0.375 ,
                       0.6842 ,
                       0.9279 ,
                       2.865 ,
                  0.056 ,
                 0.0968 ,
                 0.1345 ,
                 0.2196 ,
                 0.3735 ,
                 0.7114 ,
                 0.9205 ,
                 2.8777 ,
                  0.0579 ,
                 0.0973 ,
                 0.1328 ,
                 0.2158 ,
                 0.3782 ,
```

```
                    0.7149,
                    0.9051,
                    2.8777)




# Method 2 measurements (triplicates)
Chip <- c(0.0018,
          0.0098,
          0.0184,
          0.026,
          0.3061,
          0.0006,
          0.7521,
          1.8502,
            -0.0012,
              0.0019,
              0.0013,
              0.0048,
              0.3153,
              0.574,
              0.8174,
              1.9481,
              0.0007,
              0.0074,
              0.0046,
              0.0046,
              0.3186,
              0.5928,
              0.8222,
              2.1222)

# Create a data frame
data <- data.frame(Concentration = rep(Concentration, each = 3),
                   Method1 = Well,
                   Method2 = Chip)




# Perform the one-way ANOVA
result_compared <- aov(Method1 ~ Method2, data = data)

# Print the ANOVA table
summary(result_compared)
plot(result_compared,1)
plot(result_compared,2)
```

```r
# Extract the residuals
aov_residuals <- residuals(object = result_compared )
# Run Shapiro-Wilk test
shapiro.test(x = aov_residuals )

# Perform the one-way ANOVA
result_well <- aov(Method1 ~ Concentration , data = data)

# Print the ANOVA table
summary(result_well)

# Perform the one-way ANOVA
result_chip <- aov(Method2 ~ Concentration , data = data)

# Print the ANOVA table
summary(result_chip)
```

M Methods Mykee

M.1 Mykee settings

```
  {
 "version": "ProtoB",
 "A": {
   "heating": [],
   "acquisition": [
     {
       "startTime": 0,
       "duration": 300,
       "interval": 12,
       "collect": {
         "CHANNEL_F1_415": true,
         "CHANNEL_F2_445": true,
         "CHANNEL_F6_590": true,
         "CHANNEL_F7_630": true,
         "CHANNEL_F8_680": true
       },
       "warmupTime": 30,
       "integrationTime": 255,
       "gain": 4,
       "ledIntensities": {
         "0": 200
       }
     },
     {
       "startTime": 1,
       "duration": 300,
       "interval": 12,
       "collect": {
         "CHANNEL_F1_415": true,
         "CHANNEL_F2_445": true,
         "CHANNEL_F6_590": true,
         "CHANNEL_F7_630": true,
         "CHANNEL_F8_680": true
       },
       "warmupTime": 30,
       "integrationTime": 255,
       "gain": 4,
       "ledIntensities": {
         "1": 128
       }
     }
   ]
 },
 "B": {
   "heating": [],
   "acquisition": [
     {
       "startTime": 2,
       "duration": 300,
       "interval": 12,
       "collect": {
```

```
          "CHANNEL_F1_415": true,
          "CHANNEL_F2_445": true,
          "CHANNEL_F6_590": true,
          "CHANNEL_F7_630": true,
          "CHANNEL_F8_680": true
        },
        "warmupTime": 30,
        "integrationTime": 255,
        "gain": 4,
        "ledIntensities": {
          "0": 200
        }
      },
      {
        "startTime": 3,
        "duration": 300,
        "interval": 12,
        "collect": {
          "CHANNEL_F1_415": true,
          "CHANNEL_F2_445": true,
          "CHANNEL_F6_590": true,
          "CHANNEL_F7_630": true,
          "CHANNEL_F8_680": true
        },
        "warmupTime": 30,
        "integrationTime": 255,
        "gain": 4,
        "ledIntensities": {
          "1": 100
        }
      }
    ]
  },
  "C": {
    "heating": [],
    "acquisition": [
      {
        "startTime": 4,
        "duration": 300,
        "interval": 12,
        "collect": {
          "CHANNEL_F1_415": true,
          "CHANNEL_F2_445": true,
          "CHANNEL_F6_590": true,
          "CHANNEL_F7_630": true,
          "CHANNEL_F8_680": true
        },
        "warmupTime": 30,
        "integrationTime": 255,
        "gain": 4,
        "ledIntensities": {
          "0": 200
        }
      },
      {
```

166

```json
        "startTime": 5,
        "duration": 300,
        "interval": 12,
        "collect": {
          "CHANNEL_F1_415": true,
          "CHANNEL_F2_445": true,
          "CHANNEL_F6_590": true,
          "CHANNEL_F7_630": true,
          "CHANNEL_F8_680": true
        },
        "warmupTime": 30,
        "integrationTime": 255,
        "gain": 4,
        "ledIntensities": {
          "1": 128
        }
      }
    ]
  },
  "D": {
    "heating": [],
    "acquisition": [
      {
        "startTime": 6,
        "duration": 300,
        "interval": 12,
        "collect": {
          "CHANNEL_F1_415": true,
          "CHANNEL_F2_445": true,
          "CHANNEL_F6_590": true,
          "CHANNEL_F7_630": true,
          "CHANNEL_F8_680": true
        },
        "warmupTime": 30,
        "integrationTime": 255,
        "gain": 4,
        "ledIntensities": {
          "0": 200
        }
      },
      {
        "startTime": 7,
        "duration": 300,
        "interval": 12,
        "collect": {
          "CHANNEL_F1_415": true,
          "CHANNEL_F2_445": true,
          "CHANNEL_F6_590": true,
          "CHANNEL_F7_630": true,
          "CHANNEL_F8_680": true
        },
        "warmupTime": 30,
        "integrationTime": 255,
        "gain": 4,
        "ledIntensities": {
```

```
          "1": 128
        }
      }
    ]
  },
  "E": {
    "heating": [],
    "acquisition": [
      {
        "startTime": 8,
        "duration": 300,
        "interval": 12,
        "collect": {
          "CHANNEL_F1_415": true,
          "CHANNEL_F2_445": true,
          "CHANNEL_F6_590": true,
          "CHANNEL_F7_630": true,
          "CHANNEL_F8_680": true
        },
        "warmupTime": 30,
        "integrationTime": 255,
        "gain": 4,
        "ledIntensities": {
          "0": 200
        }
      },
      {
        "startTime": 9,
        "duration": 300,
        "interval": 12,
        "collect": {
          "CHANNEL_F1_415": true,
          "CHANNEL_F2_445": true,
          "CHANNEL_F6_590": true,
          "CHANNEL_F7_630": true,
          "CHANNEL_F8_680": true
        },
        "warmupTime": 30,
        "integrationTime": 255,
        "gain": 4,
        "ledIntensities": {
          "1": 128
        }
      }
    ]
  },
  "F": {
    "heating": [],
    "acquisition": [
      {
        "startTime": 10,
        "duration": 300,
        "interval": 12,
        "collect": {
          "CHANNEL_F1_415": true,
```

```json
          "CHANNEL_F2_445": true,
          "CHANNEL_F6_590": true,
          "CHANNEL_F7_630": true,
          "CHANNEL_F8_680": true
        },
        "warmupTime": 30,
        "integrationTime": 255,
        "gain": 4,
        "ledIntensities": {
          "0": 200
        }
      },
      {
        "startTime": 11,
        "duration": 300,
        "interval": 12,
        "collect": {
          "CHANNEL_F1_415": true,
          "CHANNEL_F2_445": true,
          "CHANNEL_F6_590": true,
          "CHANNEL_F7_630": true,
          "CHANNEL_F8_680": true
        },
        "warmupTime": 30,
        "integrationTime": 255,
        "gain": 4,
        "ledIntensities": {
          "1": 128
        }
      }
    ]
  }
}
```

M.2 Python script for Mykee data analysis

```python
    import pandas as pd #import relevant library
import matplotlib.pyplot as plt
import zipfile
import math
import numpy as np


lj = pd.read_excel('logbook.xlsx', usecols = "A:H", nrows = 28)
lj['identifier'] = np.nan
# lj['difference_white']= np.nan
# lj['difference_blue']= np.nan
lj[['A','B','C', 'D', 'E','F']] = np.nan #raw data difference F1&F7
lj[['Aabs','Babs','Cabs', 'Dabs', 'Eabs','Fabs']] = np.nan #absorbance
lj[['An','Bn','Cn', 'Dn', 'En','Fn']] = np.nan #normalized absorbance
lj[['bg_Aabs', 'bg_Babs', 'bg_Cabs', 'bg_Dabs', 'bg_Eabs', 'bg_Fabs']]
                                = np.nan #absorbance after
                                background subtraction (background
                                = signal at conc=1000)
```

```python
lj[['w_A','w_B','w_C', 'w_D', 'w_E','w_F']] = np.nan #raw data
                                      difference F1&F7
lj[['w_Aabs','w_Babs','w_Cabs', 'w_Dabs', 'w_Eabs','w_Fabs']] = np.nan
                                      #absorbance
lj[['w_An','w_Bn','w_Cn', 'w_Dn', 'w_En','w_Fn']] = np.nan #normalized
                                      absorbance
lj[['w_bg_Aabs', 'w_bg_Babs', 'w_bg_Cabs', 'w_bg_Dabs', 'w_bg_Eabs', '
                                      w_bg_Fabs']] = np.nan #absorbance
                                      after background subtraction (
                                      background = signal at conc=1000)
def importdata_F1F7(folder):

    z = zipfile.ZipFile(folder)
    Aw = pd.read_csv(z.open(z.infolist()[0].filename), sep=';', header=
                                      6)
    Ab = pd.read_csv(z.open(z.infolist()[1].filename), sep=';', header=
                                      6)
    Bw = pd.read_csv(z.open(z.infolist()[2].filename), sep=';', header=
                                      6)
    Bb = pd.read_csv(z.open(z.infolist()[3].filename), sep=';', header=
                                      6)
    Cw = pd.read_csv(z.open(z.infolist()[4].filename), sep=';', header=
                                      6)
    Cb = pd.read_csv(z.open(z.infolist()[5].filename), sep=';', header=
                                      6)
    Dw = pd.read_csv(z.open(z.infolist()[6].filename), sep=';', header=
                                      6)
    Db = pd.read_csv(z.open(z.infolist()[7].filename), sep=';', header=
                                      6)
    Ew = pd.read_csv(z.open(z.infolist()[8].filename), sep=';', header=
                                      6)
    Eb = pd.read_csv(z.open(z.infolist()[9].filename), sep=';', header=
                                      6)
    Fw = pd.read_csv(z.open(z.infolist()[10].filename), sep=';', header
                                      =6)
    Fb = pd.read_csv(z.open(z.infolist()[11].filename), sep=';', header
                                      =6)

    Ab['Timestamp'] = Aw['Timestamp']
    Bw['Timestamp'] = Aw['Timestamp']
    Bb['Timestamp'] = Aw['Timestamp']
    Cw['Timestamp'] = Aw['Timestamp']
    Cb['Timestamp'] = Aw['Timestamp']
    Dw['Timestamp'] = Aw['Timestamp']
    Db['Timestamp'] = Aw['Timestamp']
    Ew['Timestamp'] = Aw['Timestamp']
    Eb['Timestamp'] = Aw['Timestamp']
    Fw['Timestamp'] = Aw['Timestamp']
    Fb['Timestamp'] = Aw['Timestamp']


    F17 = Aw.filter(['Timestamp'])
    F17['Aw1'] = Aw['CHANNEL_F1_415']
    F17['Bw1'] = Bw['CHANNEL_F1_415']
    F17['Cw1'] = Cw['CHANNEL_F1_415']
```

```python
    F17['Dw1'] = Dw['CHANNEL_F1_415']
    F17['Ew1'] = Ew['CHANNEL_F1_415']
    F17['Fw1'] = Fw['CHANNEL_F1_415']


    F17['Aw7'] = Aw['CHANNEL_F7_630']
    F17['Bw7'] = Bw['CHANNEL_F7_630']
    F17['Cw7'] = Cw['CHANNEL_F7_630']
    F17['Dw7'] = Dw['CHANNEL_F7_630']
    F17['Ew7'] = Ew['CHANNEL_F7_630']
    F17['Fw7'] = Fw['CHANNEL_F7_630']


    F17['Ab1'] = Ab['CHANNEL_F1_415']
    F17['Bb1'] = Bb['CHANNEL_F1_415']
    F17['Cb1'] = Cb['CHANNEL_F1_415']
    F17['Db1'] = Db['CHANNEL_F1_415']
    F17['Eb1'] = Eb['CHANNEL_F1_415']
    F17['Fb1'] = Fb['CHANNEL_F1_415']


    F17['Ab7'] = Ab['CHANNEL_F7_630']
    F17['Bb7'] = Bb['CHANNEL_F7_630']
    F17['Cb7'] = Cb['CHANNEL_F7_630']
    F17['Db7'] = Db['CHANNEL_F7_630']
    F17['Eb7'] = Eb['CHANNEL_F7_630']
    F17['Fb7'] = Fb['CHANNEL_F7_630']

    Fdifb = Aw.filter(['Timestamp'])
    Fbrd  = Aw.filter(['Timestamp'])
    Fdifw = Aw.filter(['Timestamp'])
    Fwrd  = Aw.filter(['Timestamp'])

    # Fdifw = Aw.filter(['Timestamp'])
    # Difference raw data
    Fbrd['A'] =    F17['Ab1']-F17['Ab7']
    Fbrd['B'] =    F17['Bb1']-F17['Bb7']
    Fbrd['C'] =    F17['Cb1']-F17['Cb7']
    Fbrd['D'] =    F17['Db1']-F17['Db7']
    Fbrd['E'] =    F17['Eb1']-F17['Eb7']
    Fbrd['F'] =    F17['Fb1']-F17['Fb7']

# absorbance-way of calculating
    Fdifb['A'] =    np.log10(F17['Ab7']/F17['Ab1'])
    Fdifb['B'] =    np.log10(F17['Bb7']/F17['Bb1'])
    Fdifb['C'] =    np.log10(F17['Cb7']/F17['Cb1'])
    Fdifb['D'] =    np.log10(F17['Db7']/F17['Db1'])
    Fdifb['E'] =    np.log10(F17['Eb7']/F17['Eb1'])
    Fdifb['F'] =    np.log10(F17['Fb7']/F17['Fb1'])

    # Difference raw data--white
    Fwrd['w_A'] =    F17['Aw1']-F17['Aw7']
    Fwrd['w_B'] =    F17['Bw1']-F17['Bw7']
    Fwrd['w_C'] =    F17['Cw1']-F17['Cw7']
    Fwrd['w_D'] =    F17['Dw1']-F17['Dw7']
    Fwrd['w_E'] =    F17['Ew1']-F17['Ew7']
    Fwrd['w_F'] =    F17['Fw1']-F17['Fw7']
```

```python
# absorbance-way of calculating -- white
    Fdifw['A'] =     np.log10(F17['Aw7']/F17['Aw1'])
    Fdifw['B'] =     np.log10(F17['Bw7']/F17['Bw1'])
    Fdifw['C'] =     np.log10(F17['Cw7']/F17['Cw1'])
    Fdifw['D'] =     np.log10(F17['Dw7']/F17['Dw1'])
    Fdifw['E'] =     np.log10(F17['Ew7']/F17['Ew1'])
    Fdifw['F'] =     np.log10(F17['Fw7']/F17['Fw1'])


    Fmb= Fbrd.mean()
    Fmb.drop('Timestamp', inplace=True)

    Fmw= Fwrd.mean()
    Fmw.drop('Timestamp', inplace=True)


    return F17, Fdifb, Fmb, Fdifw, Fmw

# remove wells with air bubbles:
toremove = {'bg1':'B', '500 uM 2': 'F', '250 uM 1': 'EF', '31 uM1': 'CD
                                    '}

for correctiefactor in [0.9, 0.84]:
    print(correctiefactor)

    dfs = {}
    for index, row in lj.iterrows():
        ident =  str(row['Run'])+' '+row['sample']+' '+str(row['Mykee']
                                        )
        lj.loc[index, 'identifier'] = ident
        dfs[ident] = importdata_F1F7(row['zip'])
        data = dfs[ident][1].mean()
        data.rename({'A': 'Aabs', 'B': 'Babs', 'C':'Cabs', 'D':'Dabs',
                                        'E':'Eabs', 'F':'Fabs'},
                                        inplace=True)
        lj.loc[index, ['Aabs','Babs','Cabs', 'Dabs', 'Eabs','Fabs']] =
                                        data
        lj.loc[index, ['A','B','C', 'D', 'E','F']] = dfs[ident][2]

        data_2 = dfs[ident][3].mean()
        data_2.rename({'A': 'w_Aabs', 'B': 'w_Babs', 'C':'w_Cabs', 'D':
                                        'w_Dabs', 'E':'w_Eabs', 'F'
                                        :'w_Fabs'}, inplace=True)
        lj.loc[index, ['w_Aabs','w_Babs','w_Cabs', 'w_Dabs', 'w_Eabs','
                                        w_Fabs']] = data_2
        lj.loc[index, ['w_A','w_B','w_C', 'w_D', 'w_E','w_F']] = dfs[
                                        ident][4]

        if row['sample'] in toremove.keys():
            for w in toremove[row['sample']]:
                lj.loc[index, 'w_'+w+'abs'] = np.nan
                lj.loc[index, 'w_'+w] = np.nan
                lj.loc[index, w+'abs'] = np.nan
                lj.loc[index, w] = np.nan

    Mykees = [6,16,12]
```

```
for M in Mykees:
    ax = lj[lj['Mykee']==M].plot.scatter(x='conc', y =  'A', title
                                          = 'Mykee '+ str(M)+'-blue
                                          LED', color='r', label = 'A
                                          ')
    lj[lj['Mykee']==M].plot.scatter(x='conc', y =  'B', ax = ax,
                                          color='b', label = 'B')
    lj[lj['Mykee']==M].plot.scatter(x='conc', y =  'C', ax = ax,
                                          color='g', label = 'C')
    lj[lj['Mykee']==M].plot.scatter(x='conc', y =  'D', ax = ax,
                                          color='k', label = 'D')
    lj[lj['Mykee']==M].plot.scatter(x='conc', y =  'E', ax = ax,
                                          color='c', label = 'E')
    lj[lj['Mykee']==M].plot.scatter(x='conc', y =  'F', ax = ax,
                                          color='m', label = 'F')

    ax.set_ylabel('F1-F7')
    ax.set_xlabel('[L-Cysteine] ($\mu$M)')
    ax.get_figure().savefig('./plots/Mykee '+str(M)+' blue LED - F1
                                          -F7')


cor = {}
for M in Mykees:
    cor[M] = lj[(lj['Mykee']==M)&(lj['conc']==0)][['Aabs', 'Babs',
                                          'Cabs', 'Dabs', 'Eabs', '
                                          Fabs']].mean()

for index, row in lj.iterrows():
    n = row[['Aabs', 'Babs', 'Cabs', 'Dabs', 'Eabs', 'Fabs']]-cor[
                                          row['Mykee']]
    n.rename({'Aabs': 'An', 'Babs': 'Bn', 'Cabs':'Cn', 'Dabs':'Dn',
                                          'Eabs':'En', 'Fabs':'Fn'},
                                          inplace=True)
    lj.loc[index, ['An', 'Bn', 'Cn', 'Dn', 'En', 'Fn']]=n


for M in Mykees:
    ax = lj[lj['Mykee']==M].plot.scatter(x='conc', y =  'An', title
                                          = 'Mykee '+ str(M)+'-blue
                                          LED', color='r', label = 'A
                                          ')
    lj[lj['Mykee']==M].plot.scatter(x='conc', y =  'Bn', ax = ax,
                                          color='b', label = 'B')
    lj[lj['Mykee']==M].plot.scatter(x='conc', y =  'Cn', ax = ax,
                                          color='g', label = 'C')
    lj[lj['Mykee']==M].plot.scatter(x='conc', y =  'Dn', ax = ax,
                                          color='k', label = 'D')
    lj[lj['Mykee']==M].plot.scatter(x='conc', y =  'En', ax = ax,
                                          color='c', label = 'E')
    lj[lj['Mykee']==M].plot.scatter(x='conc', y =  'Fn', ax = ax,
                                          color='m', label = 'F')

    ax.set_ylabel('absorbance (log(F7/F1)), normalized')
```

```python
        ax.set_xlabel('[L-Cysteine] ($\mu$M)')
        ax.get_figure().savefig('./plots/Mykee '+str(M)+' blue LED -
                                        absorbance -normalized')


    for M in Mykees:
        ax = lj[lj['Mykee']==M].plot.scatter(x='conc', y = 'Aabs',
                                        title = 'Mykee '+ str(M)+'-
                                        blue LED', color='r', label
                                        = 'A')
        lj[lj['Mykee']==M].plot.scatter(x='conc', y = 'Babs', ax = ax,
                                        color='b', label = 'B')
        lj[lj['Mykee']==M].plot.scatter(x='conc', y = 'Cabs', ax = ax,
                                        color='g', label = 'C')
        lj[lj['Mykee']==M].plot.scatter(x='conc', y = 'Dabs', ax = ax,
                                        color='k', label = 'D')
        lj[lj['Mykee']==M].plot.scatter(x='conc', y = 'Eabs', ax = ax,
                                        color='c', label = 'E')
        lj[lj['Mykee']==M].plot.scatter(x='conc', y = 'Fabs', ax = ax,
                                        color='m', label = 'F')

        ax.set_ylabel('absorbance (log(F7/F1))')
        ax.set_xlabel('[L-Cysteine] ($\mu$M)')
        ax.get_figure().savefig('./plots/Mykee '+str(M)+' blue LED -
                                        absorbance')

# suppose 84% of the signal at conc=1000 is background radiation from
                                        the LED. subtract this from all
                                        signals
    backgrounddata = {}
    background = {}
    for M in Mykees:
        backgrounddata[M]={}
        for ident in lj[(lj['Mykee']==M)&(lj['conc']==1000)]['
                                        identifier']:
            backgrounddata[M][ident]=dfs[ident][0].mean()
        background_frame = pd.DataFrame(backgrounddata[M])
        background[M] = background_frame.mean(axis = 1)
        # background[M] = background_frame[background_frame.columns[0]]


    for index, row in lj.iterrows():
        # data = dfs[row['identifier']][0].mean()
        data = dfs[row['identifier']][0]
        # data['Aw1':'Fw1']-=background[row['Mykee']]['Aw1':'Fw1']
        # data['Ab1':'Fb1']-=background[row['Mykee']]['Ab1':'Fb1']
        data[['Aw1','Bw1', 'Cw1', 'Dw1', 'Ew1','Fw1']]-=correctiefactor
                                        *background[row['Mykee']][[
                                        'Aw1','Bw1', 'Cw1', 'Dw1',
                                        'Ew1','Fw1']]
        data[['Ab1','Bb1', 'Cb1', 'Db1', 'Eb1', 'Fb1']]-=
                                        correctiefactor*background[
                                        row['Mykee']][['Ab1','Bb1',
                                        'Cb1', 'Db1', 'Eb1', 'Fb1'
                                        ]]
```

```python
        if row['sample'] in toremove.keys():
            for w in toremove[row['sample']]:
                data[ w+'w1'] = np.nan
                data[ w+'b1'] = np.nan


    bgc_abs = []
    w_bgc_abs = []
    for well in range(6):
        w_bgc_abs.append(np.log10((data[data.columns[well+7]]/data[
                                        data.columns[well+1]]))
                                        .mean())
        bgc_abs.append(np.log10((data[data.columns[well+19]]/data[
                                        data.columns[well+13]])
                                        ).mean())
    lj.loc[index, ['w_bg_Aabs', 'w_bg_Babs', 'w_bg_Cabs', '
                                        w_bg_Dabs', 'w_bg_Eabs', '
                                        w_bg_Fabs']]=w_bgc_abs
    lj.loc[index, ['bg_Aabs', 'bg_Babs', 'bg_Cabs', 'bg_Dabs', '
                                        bg_Eabs', 'bg_Fabs']]=
                                        bgc_abs
    # n = row[['Aabs', 'Babs', 'Cabs', 'Dabs', 'Eabs', 'Fabs']]-cor
                                        [row['Mykee']]
    # n.rename({'Aabs': 'An', 'Babs': 'Bn', 'Cabs':'Cn', 'Dabs':'Dn
                                        ', 'Eabs':'En', 'Fabs':'Fn'
                                        }, inplace=True)
    # lj.loc[index, ['bg_Aabs', 'bg_Babs', 'bg_Cabs', 'bg_Dabs', '
                                        bg_Eabs', 'bg_Fabs']]=n


for M in Mykees:
    ax = lj[lj['Mykee']==M].plot.scatter(x='conc', y = 'bg_Aabs',
                                        title = 'Mykee '+ str(M)+'-
                                        blue LED-background LED- '
                                        + str(100*correctiefactor)+
                                        '%', color='r', label = 'A'
                                        )
    lj[lj['Mykee']==M].plot.scatter(x='conc', y = 'bg_Babs', ax =
                                        ax, color='b', label = 'B')
    lj[lj['Mykee']==M].plot.scatter(x='conc', y = 'bg_Cabs', ax =
                                        ax, color='g', label = 'C')
    lj[lj['Mykee']==M].plot.scatter(x='conc', y = 'bg_Dabs', ax =
                                        ax, color='k', label = 'D')
    lj[lj['Mykee']==M].plot.scatter(x='conc', y = 'bg_Eabs', ax =
                                        ax, color='c', label = 'E')
    lj[lj['Mykee']==M].plot.scatter(x='conc', y = 'bg_Fabs', ax =
                                        ax, color='m', label = 'F')

    ax.set_ylabel('absorbance (log(F7/F1))')
    ax.set_xlabel('[L-Cysteine] ($\mu$M)')
    ax.get_figure().savefig('./plots/Mykee '+str(M)+' blue LED -
                                        absorbance-background LED -
                                        ' + str(round(100*
                                        correctiefactor))+'%')
```

```python
for M in Mykees:
    ax = lj[lj['Mykee']==M].plot.scatter(x='conc', y =  'An', title
                                          = 'Mykee '+ str(M), color=
                                          'r', label = 'A')
    lj[lj['Mykee']==M].plot.scatter(x='conc', y =  'Bn', ax = ax,
                                     color='b', label = 'B')
    lj[lj['Mykee']==M].plot.scatter(x='conc', y =  'Cn', ax = ax,
                                     color='g', label = 'C')
    lj[lj['Mykee']==M].plot.scatter(x='conc', y =  'Dn', ax = ax,
                                     color='k', label = 'D')
    lj[lj['Mykee']==M].plot.scatter(x='conc', y =  'En', ax = ax,
                                     color='c', label = 'E')
    lj[lj['Mykee']==M].plot.scatter(x='conc', y =  'Fn', ax = ax,
                                     color='m', label = 'F')
    ax.set_yscale('log')
    ax.set_ylim([0.001,1])
    ax.set_ylabel('F1-F7, normalized')
    ax.set_xlabel('[L-Cysteine] ($\mu$M)')
    # ax.get_figure().savefig('./plots/'+d)


    # Repeat for white LED data
for M in Mykees:
    ax = lj[lj['Mykee']==M].plot.scatter(x='conc', y =  'w_A',
                                          title = 'Mykee '+ str(M)+'-
                                          white LED', color='r',
                                          label = 'A')
    lj[lj['Mykee']==M].plot.scatter(x='conc', y =  'w_B', ax = ax,
                                     color='b', label = 'B')
    lj[lj['Mykee']==M].plot.scatter(x='conc', y =  'w_C', ax = ax,
                                     color='g', label = 'C')
    lj[lj['Mykee']==M].plot.scatter(x='conc', y =  'w_D', ax = ax,
                                     color='k', label = 'D')
    lj[lj['Mykee']==M].plot.scatter(x='conc', y =  'w_E', ax = ax,
                                     color='c', label = 'E')
    lj[lj['Mykee']==M].plot.scatter(x='conc', y =  'w_F', ax = ax,
                                     color='m', label = 'F')

    ax.set_ylabel('F1-F7')
    ax.set_xlabel('[L-Cysteine] ($\mu$M)')
    ax.get_figure().savefig('./plots/Mykee '+str(M)+' white LED -
                            F1-F7')


cor = {}
for M in Mykees:
    cor[M] = lj[(lj['Mykee']==M)&(lj['conc']==0)][['w_Aabs', '
                                     w_Babs', 'w_Cabs', 'w_Dabs'
                                     , 'w_Eabs', 'w_Fabs']].mean
                                     ()

for index, row in lj.iterrows():
```

```python
    n = row[['w_Aabs', 'w_Babs', 'w_Cabs', 'w_Dabs', 'w_Eabs', '
                        w_Fabs']]-cor[row['Mykee']]
    n.rename({'w_Aabs': 'w_An', 'w_Babs': 'w_Bn', 'w_Cabs':'w_Cn',
                        'w_Dabs':'w_Dn', 'w_Eabs':'
                        w_En', 'w_Fabs':'w_Fn'},
                        inplace=True)
    lj.loc[index, ['w_An', 'w_Bn', 'w_Cn', 'w_Dn', 'w_En', 'w_Fn']]
                        =n


for M in Mykees:
    ax = lj[lj['Mykee']==M].plot.scatter(x='conc', y = 'w_An',
                                title = 'Mykee '+ str(M)+'-
                                white LED', color='r',
                                label = 'A')
    lj[lj['Mykee']==M].plot.scatter(x='conc', y = 'w_Bn', ax = ax,
                                color='b', label = 'B')
    lj[lj['Mykee']==M].plot.scatter(x='conc', y = 'w_Cn', ax = ax,
                                color='g', label = 'C')
    lj[lj['Mykee']==M].plot.scatter(x='conc', y = 'w_Dn', ax = ax,
                                color='k', label = 'D')
    lj[lj['Mykee']==M].plot.scatter(x='conc', y = 'w_En', ax = ax,
                                color='c', label = 'E')
    lj[lj['Mykee']==M].plot.scatter(x='conc', y = 'w_Fn', ax = ax,
                                color='m', label = 'F')

    ax.set_ylabel('absorbance (log(F7/F1)), normalized')
    ax.set_xlabel('[L-Cysteine] ($\mu$M)')
    ax.get_figure().savefig('./plots/Mykee '+str(M)+' white LED -
                                absorbance-normalized')

for M in Mykees:
    ax = lj[lj['Mykee']==M].plot.scatter(x='conc', y = 'w_Aabs',
                                title = 'Mykee '+ str(M)+'-
                                white LED', color='r',
                                label = 'A')
    lj[lj['Mykee']==M].plot.scatter(x='conc', y = 'w_Babs', ax =
                                ax, color='b', label = 'B')
    lj[lj['Mykee']==M].plot.scatter(x='conc', y = 'w_Cabs', ax =
                                ax, color='g', label = 'C')
    lj[lj['Mykee']==M].plot.scatter(x='conc', y = 'w_Dabs', ax =
                                ax, color='k', label = 'D')
    lj[lj['Mykee']==M].plot.scatter(x='conc', y = 'w_Eabs', ax =
                                ax, color='c', label = 'E')
    lj[lj['Mykee']==M].plot.scatter(x='conc', y = 'w_Fabs', ax =
                                ax, color='m', label = 'F')

    ax.set_ylabel('absorbance (log(F7/F1))')
    ax.set_xlabel('[L-Cysteine] ($\mu$M)')
    ax.get_figure().savefig('./plots/Mykee '+str(M)+' white LED -
                                absorbance')

for M in Mykees:
    ax = lj[lj['Mykee']==M].plot.scatter(x='conc', y = 'w_bg_Aabs'
                                , title = 'Mykee '+ str(M)+
```

```python
                                                    '-white LED -background LED -
                                                    ' + str (100*
                                                    correctiefactor )+'\%',
                                                    color='r', label = 'A')
    lj[lj['Mykee']==M].plot.scatter(x='conc', y =  'w_bg_Babs', ax
                                    = ax, color='b', label = 'B
                                    ')
    lj[lj['Mykee']==M].plot.scatter(x='conc', y =  'w_bg_Cabs', ax
                                    = ax, color='g', label = 'C
                                    ')
    lj[lj['Mykee']==M].plot.scatter(x='conc', y =  'w_bg_Dabs', ax
                                    = ax, color='k', label = 'D
                                    ')
    lj[lj['Mykee']==M].plot.scatter(x='conc', y =  'w_bg_Eabs', ax
                                    = ax, color='c', label = 'E
                                    ')
    lj[lj['Mykee']==M].plot.scatter(x='conc', y =  'w_bg_Fabs', ax
                                    = ax, color='m', label = 'F
                                    ')

    ax.set_ylabel('absorbance (log(F7/F1))')
    ax.set_xlabel('[L-Cysteine] ($\mu$M)')
    ax.get_figure().savefig('./plots/Mykee '+str(M)+' white LED -
                                    absorbance -background LED -
                                    ' + str(round(100*
                                    correctiefactor))+'\%')


# data from measurements with open reader in white tent
offset = {'A': [2657.100000, 1686.726667, 2172.426667, 1405.433333,
                                    2736.940000, 1659.706667],
'B': [2717.640000, 1660.940000, 2312.653333, 1473.213333, 2668.
                                    853333, 1634.506667],
'C': [2529.298013, 1623.566667, 2409.410596, 1524.273333, 2704.
                                    854305, 1671.613333],
'D': [2577.060000, 1646.846667, 2376.926667, 1552.653333, 2708.
                                    926667, 1650.113333],
'E': [2604.946667, 1699.264901, 2433.120000, 1569.560000, 2796.
                                    506667, 1690.386667],
'F': [2610.589404, 1657.940000, 2481.253333, 1593.080000, 2742.
                                    653333, 1651.806667]}

caldata = pd.DataFrame.from_dict(offset, orient='index')
caldata.columns = ['M06_1', 'M06_7', 'M12_1', 'M12_7', 'M16_1', '
                                    M16_7']

abs_caldata = pd.DataFrame()
abs_caldata['Mykee 6']=caldata['M06_7']/caldata['M06_1']
abs_caldata['Mykee 12']=caldata['M12_7']/caldata['M12_1']
abs_caldata['Mykee 16']=caldata['M16_7']/caldata['M16_1']

with pd.ExcelWriter("data.xlsx") as writer: lj.to_excel(writer)

wells = ['A', 'B', 'C', 'D', 'E', 'F']
```

```
    fitw = {}
    fitb = {}
    rsqw = {}
    rsqb = {}
    fitfrsb = {}
    fitfrsw = {}



for M in Mykees:
    x = lj[(lj['Mykee']==M) & (lj['conc']<1000)]['conc']
    fitb[M]={}
    fitw[M]={}
    rsqw[M]={}
    rsqb[M]={}

    for w in wells:
        y_b =  lj[(lj['Mykee']==M) & (lj['conc']<1000)]['bg_'+w+'
                                            abs']
        y_w =  lj[(lj['Mykee']==M) & (lj['conc']<1000)]['w_bg_'+w+'
                                            abs']
        idx_b = np.isfinite(y_b)
        idx_w = np.isfinite(y_w)
        fitb[M][w] = np.polyfit(x[idx_b], y_b[idx_b], 1)
        fitw[M][w] = np.polyfit(x[idx_w], y_w[idx_w], 1)
        rsqw[M][w] = np.append(fitw[M][w],np.corrcoef(x[idx_w], y_w
                                            [idx_w])[0,1]**2)
        rsqb[M][w] = np.append(fitb[M][w],np.corrcoef(x[idx_b], y_b
                                            [idx_b])[0,1]**2)
    fitfrsb[M] = pd.DataFrame.from_dict(rsqb[M]).T
    fitfrsb[M].columns=['slope',  'offset', 'Rsquared']
    fitfrsw[M] = pd.DataFrame.from_dict(rsqw[M]).T
    fitfrsw[M].columns=['slope',  'offset', 'Rsquared']
```

N   Data plate reader-compatible chip holder

The 384 well plate absorbance (at 412 nm)															
0.04	0.04	0.04	0.05	0.04	0.04	0.04	0.04	0.04	0.04	0.04	0.05	0.04	0.04	0.04	0.04
0.04	0.04	0.04	0.04	0.04	0.04	0.04	0.04	0.04	0.04	0.04	0.05	0.04	0.04	0.04	0.04
0.04	0.04	0.04	0.05	0.04	0.04	0.04	0.04	0.04	0.04	0.04	0.04	0.04	0.04	0.04	0.04
0.04	0.04	0.04	0.04	0.04	0.04	0.04	0.04	0.04	0.04	0.04	0.04	0.04	0.04	0.04	0.04
0.04	0.04	0.04	0.05	0.04	0.04	0.04	0.04	0.04	0.04	0.04	0.04	0.04	0.04	0.04	0.04
0.04	0.04	0.04	0.05	0.04	0.04	0.04	0.04	0.05	0.04	0.04	0.04	0.04	0.04	0.04	0.04
Plate reader-compatible chip holder absorbance (measured at 412 nm)															
0.59	0.54	0.31	0.26	0.22	0.18	0.21	0.22	0.25	0.24	0.25	0.25	0.25	0.26	0.32	0.50
0.35	0.15	0.10	0.10	0.12	0.11	0.11	0.12	0.15	0.12	0.12	0.14	0.13	0.16	0.11	0.24
0.23	0.13	0.09	0.11	0.10	0.09	0.10	0.13	0.09	0.12	0.10	0.10	0.13	0.11	0.11	0.20
0.26	0.11	0.09	0.11	0.10	0.10	0.11	0.11	0.10	0.10	0.09	0.11	0.13	0.12	0.11	0.22
0.33	0.13	0.09	0.10	0.08	0.11	0.10	0.11	0.09	0.09	0.09	0.13	0.15	0.12	0.13	0.15
0.56	0.45	0.38	0.35	0.24	0.22	0.18	0.18	0.20	0.18	0.17	0.16	0.18	0.19	0.28	0.41
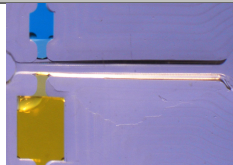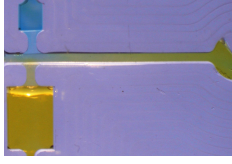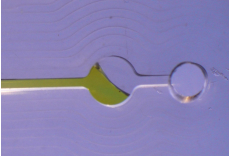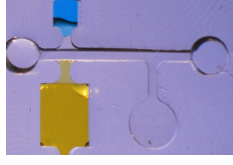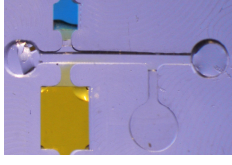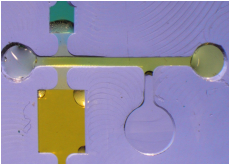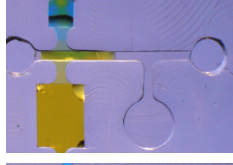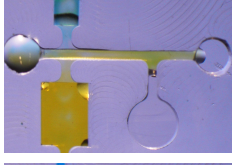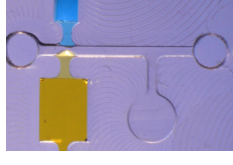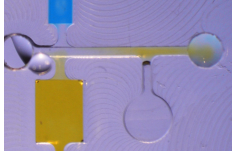
O Calcification buffer video
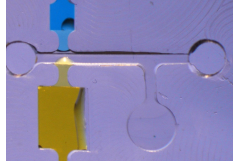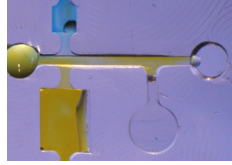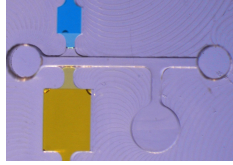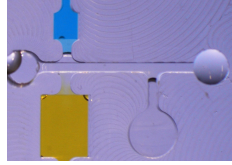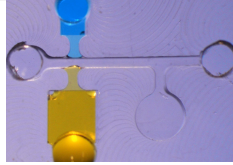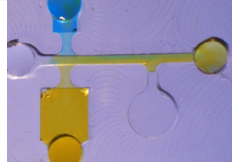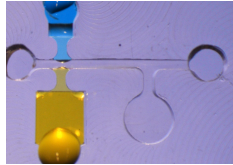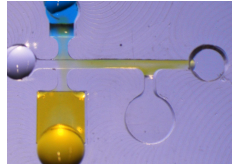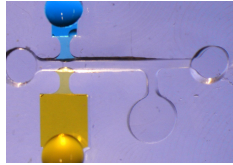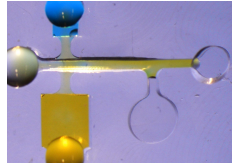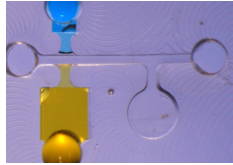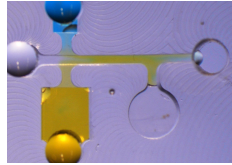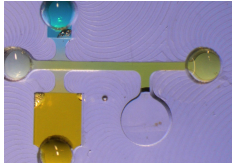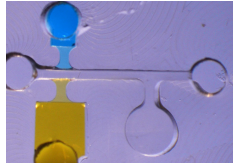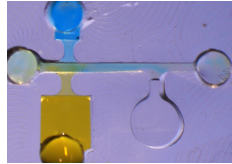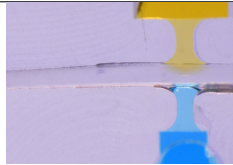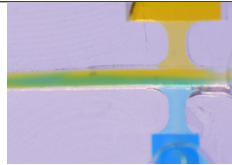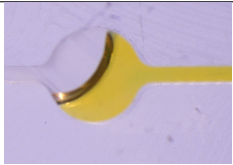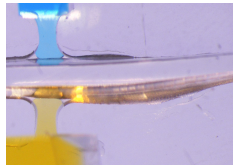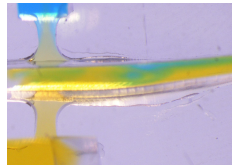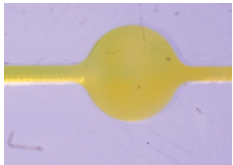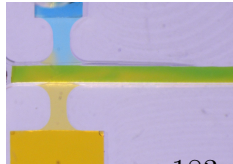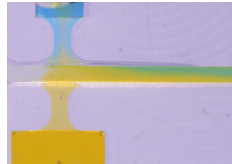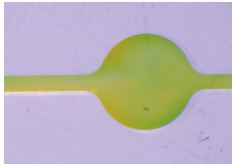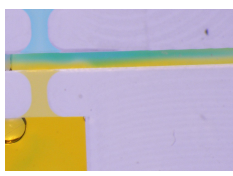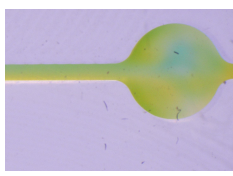
Figure O.1: The QR code to the video of the plasma sample with EDTA anti-coagulant and calcification buffer flowing through the channels of a Loc.

P Images chip success rate

Table 19: The images of the success rate experiment of the two read reagent chips.

Chip Characteristics	Number	Before activation	After activation	Reservoir
• Narrowing after inlet • Straight reservoir	1			
	2			
	3			
	4			
	5			
• Narrowing after inlet • Reservoir at 90°	1			
	2			
	3			

Chip Characteristics	Number	Before activation	After activation	Reservoir
	4			
	5			
• Inlet connected to reservoir • Reservoir at 90°	1			
	2			
	3			
	4			
	5			
• Inlet connected to reservoir • Straight channel	1			
	2			
	3			

Chip Characteristics	Number	Before activation	After activation	Reservoir
	4			
	5			

Q   Images mixing experiment

Table 20: The images of the mixing experiment over time.

Chip Characteristics	Number	t=0	t=5 min	t=10 min	15 min	t=20 min
Control: • Inlet connected to reservoir • Straight channel	1					
	2					
	3					
Herringbone Structure	1					
	2					
	3					
Serpentine Structure	1					
	2					
	3					
Serpentine Structure + Side Wells	1					
	2					
	3					

Q.1 Gifjes of the obtained pictures

Figure Q.1: The QR code to the video of the gifjes of the mixing experiment pictures over time.

R   Intensity plot different mixing designs
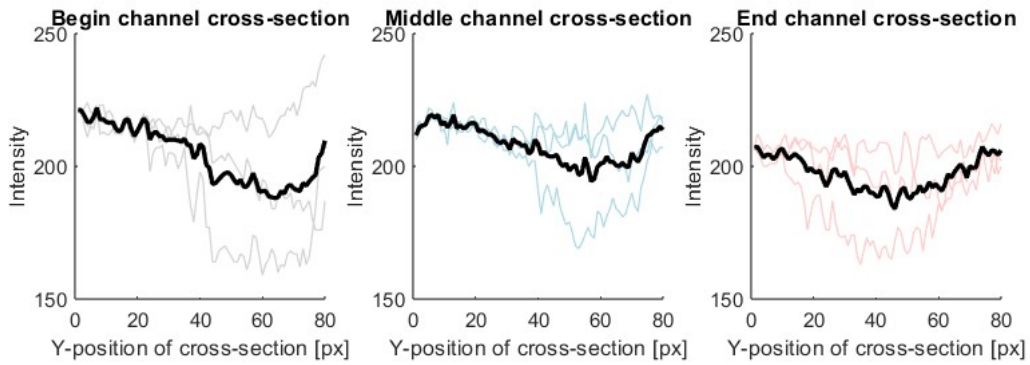
(a) Straight channel
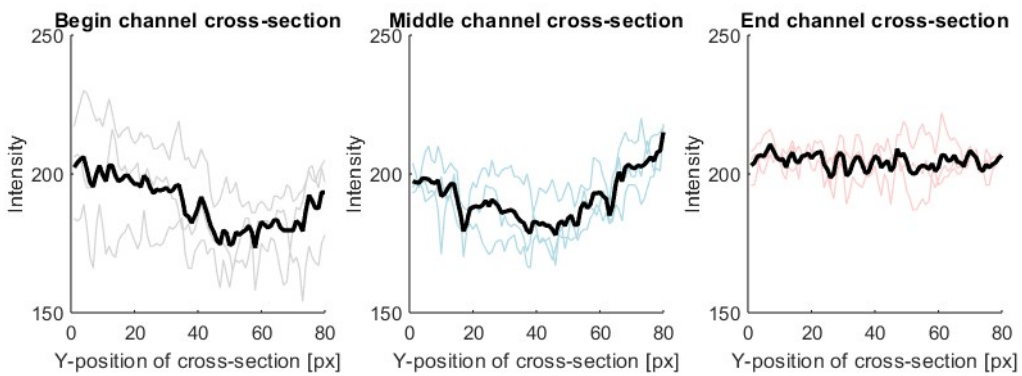
(b) Herringbone structure
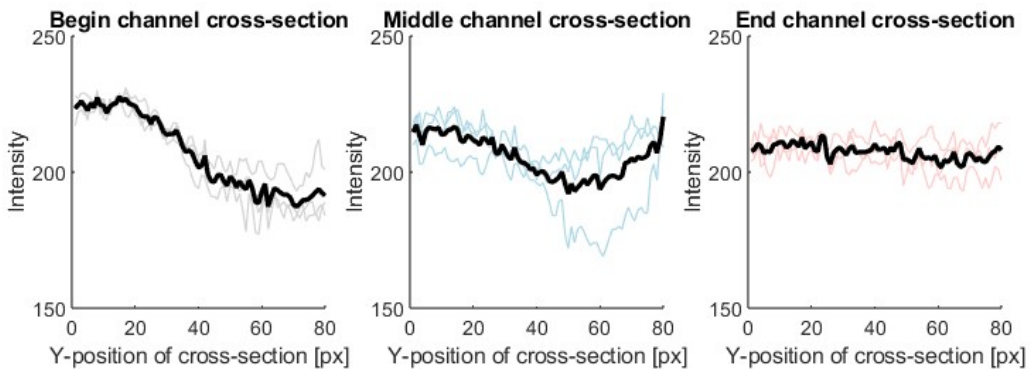
(c) Serpentine structure
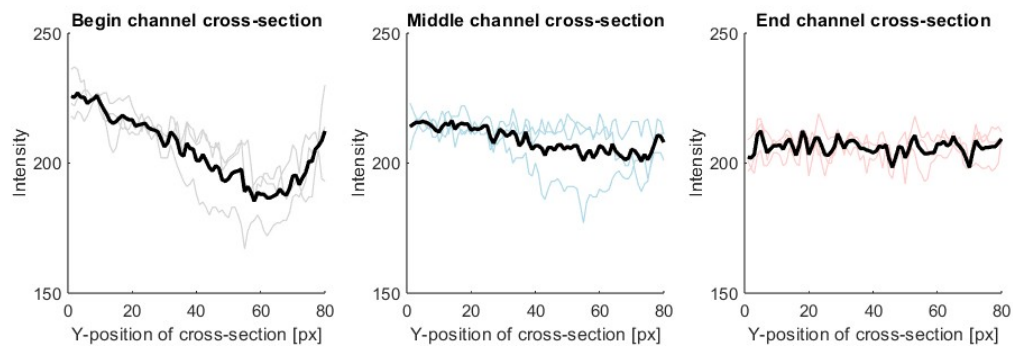
(d) Serpentine structure with side wells

Figure R.1: The intensity over the cross-section at the beginning, middle, and end of the channel for the straight channel (a), herringbone structure (b), serpentine structure (c), and serpentine structure with side wells (d).

S Data volume control experiments Quake-valve

Table 21: The measured flow rate for increasing pressure difference between the inlet and outlet with the control layer pressure set to 0 mbar

Pressure control layer 0 mbar	
dP (mbar)	flow rate (μl/min)
0	5
2	15.9
4	26.7
6	34.7
8	44.4

Table 22: The measured flow rate for increasing pressure difference (dP) between the inlet and outlet with the control layer pressure set to 1500 mbar

Pressure control layer 1500 mbar	
dP (mbar)	flow rate (μl/min)
0	-0.7
2	-0.7
4	0.1
6	1.2
8	30.9
10	39.4
12	47.3
14	54.1
16	60.2
18	80.2
20	85.1
22	91.1
24	93.9
35	160
40	183.8
40	183.8

Table 23: The measured flow rate for increasing pressure of the control layer with the dP set to 30 mbar (137 µl/min at 0 mbar for the control layer.)

dP 30 mbar (137 μl/min)	
pressure control layer (mbar)	**flow rate (μl/min)**
500	135.8
600	134.7
700	134.2
800	134.1
900	133
1000	133.6
1100	132.8
1200	131.9
1300	130.8
1400	130.6
1500	131.8
1600	129.4
1700	128.5

T   Data excess DTNB

Table 24: The layout of the 96 well plate for the excess of DTNB experiment with the L-Cysteine (L) concentrations in µM and the DTNB (D) concentrations in mM.

A	L-0 D-0	L-0 D-0.24	L-0 D-0.48	L-0 D-0.71	L-0 D-0.95	L-0 D-1.43	L-0 D-1.9	L-0 D-2.4	L-0 D-2.85	L-0 D-3.33	L-0 D-3.8	
B	L-15 D-0	L-15 D-0.24	L-15 D-0.48	L-15 D-0.71	L-15 D-0.95	L-15 D-1.43	L-15 D-1.9	L-15 D-2.4	L-15 D-2.85	L-15 D-3.33	L-15 D-3.8	
C	L-30 D-0	L-30 D-0.24	L-30 D-0.48	L-30 D-0.71	L-30 D-0.95	L-30 D-1.43	L-30 D-1.9	L-30 D-2.4	L-30 D-2.85	L-30 D-3.33	L-30 D-3.8	
D	L-60 D-0	L-60 D-0.24	L-60 D-0.48	L-60 D-0.71	L-60 D-0.95	L-60 D-1.43	L-60 D-1.9	L-60 D-2.4	L-60 D-2.85	L-60 D-3.33	L-60 D-3.8	
E	L-125 D-0	L-125 D-0.24	L-125 D-0.48	L-125 D-0.71	L-125 D-0.95	L-125 D-1.43	L-125 D-1.9	L-125 D-2.4	L-125 D-2.85	L-125 D-3.33	L-125 D-3.8	
F	L-250 D-0	L-250 D-0.24	L-250 D-0.48	L-250 D-0.71	L-250 D-0.95	L-250 D-1.43	L-250 D-1.9	L-250 D-2.4	L-250 D-2.85	L-250 D-3.33	L-250 D-3.8	
G	L-500 D-0	L-500 D-0.24	L-500 D-0.48	L-500 D-0.71	L-500 D-0.95	L-500 D-1.43	L-500 D-1.9	L-500 D-2.4	L-500 D-2.85	L-500 D-3.33	L-500 D-3.8	
H	L-1000 D-0	L-1000 D-0.24	L-1000 D-0.48	L-1000 D-0.71	L-1000 D-0.95	L-1000 D-1.43	L-1000 D-1.9	L-1000 D-2.4	L-1000 D-2.85	L-1000 D-3.33	L-1000 D-3.8	

Table 25: The absorbance of the excess DNTB experiment with the well plate layout from Table 24

	1	2	3	4	5	6	7	8	9	10	11	12
A	0	0.0033	0.006	0.0083	0.0115	0.0145	0.0219	0.0268	0.0321	0.0386	0.0417	
B	0	0.0347	0.0372	0.039	0.042	0.0464	0.0492	0.0548	0.0594	0.0649	0.0717	
C	-0.0006	0.0806	0.0819	0.0777	0.0851	0.0884	0.0931	0.0962	0.1011	0.1054	0.1068	
D	0.0007	0.1597	0.165	0.1634	0.1706	0.1725	0.1764	0.18	0.1821	0.1862	0.1881	
E	-0.0008	0.2849	0.3287	0.3242	0.3324	0.3324	0.3312	0.3367	0.3448	0.3452	0.3498	
F	0.0035	0.3344	0.5644	0.6125	0.6474	0.6535	0.6506	0.6573	0.6568	0.6737	0.6557	
G	-0.0002	0.3112	0.6004	0.7532	0.8466	0.9086	0.9062	0.9157	0.9088	0.913	0.9152	
H	0.0021	0.2979	0.599	0.8721	1.1957	1.7401	2.2027	2.4641	2.4496	2.6843	2.7341	

U Absorbance data calibration curves

Table 26: Absorbance values of the calibration curve in well plate with liquid DTNB

Sample concentration	Abs value 1	Abs value 1	Abs value 1	Mean (abs)	SD (abs)	CV(%)
0	0.058	0.056	0.0579	0.06	0.00	1.61
15.625	0.0977	0.0968	0.0973	0.10	0.00	0.38
31.25	0.1323	0.1345	0.1328	0.13	0.00	0.71
62.5	0.2154	0.2196	0.2158	0.22	0.00	0.87
125	0.375	0.3735	0.3782	0.38	0.00	0.52
250	0.6842	0.7114	0.7149	0.70	0.01	1.95
500	0.9279	0.9205	0.9051	0.92	0.01	1.03
1000	2.865	2.8777	2.8777	2.87	0.01	0.21

Table 27: Absorbance values of the calibration curve on-chip with liquid DTNB

Sample concentration	Abs value 1	Abs value 1	Abs value 1	Mean (abs)	SD (abs)	CV(%)
0	0.0018	-0.0012	0.0007	0.00	0.00	285.96
15.625	0.0098	0.0019	0.0074	0.01	0.00	51.94
31.25	0.0184	0.0013	0.0046	0.01	0.01	91.44
62.5	0.026*	0.0048	0.0046	0.00	0.00	2.13
125	0.3061	0.3153	0.3186	0.31	0.01	1.69
250	0.0006*	0.574	0.5928	0.58	0.01	1.61
500	0.7521	0.8174	0.8222	0.80	0.03	4.01
1000	1.8502	1.9481	2.1222	1.97	0.11	5.70

Table 28: Absorbance values of the calibration curve on-chip with freeze-dried DTNB

Sample concentration	Abs value 1	Abs value 1	Abs value 1	Mean (abs)	SD (abs)	CV(%)
0	0.0101	0.0281	0.0124	0.02	0.01	47.42
15.625	0.02	0.0175	0.0223	0.02	0.00	9.83
31.25	0.0195	0.0316	0.0213	0.02	0.01	22.09
62.5	0.0199	0.0324	0.0193	0.02	0.01	25.30
125	0.049	0.3349	0.3232	0.24	0.13	56.05
250	0.5723	0.6098	0.5222	0.57	0.04	6.32
500	0.4081	0.599	0.5822	0.53	0.09	16.29
1000	0.5998	0.5695	0.6856	0.62	0.05	7.95

V   Free thiol concentration control samples UMCG

Table 29: The free thiol concentrations of the control samples of the IBD cohort study in the UMCG

DAY 1	contr 1	22-Jun contr 2	DAY 2	contr 1	24-Jun contr 2	DAY 3	contr 1	1-Jul contr 2	DAY 4	contr 1	6-Jul contr 2
p	contr 1	contr 2	p	contr 1	contr 2	p	contr 1	contr 2	p	contr 1	contr 2
1	301.7	276.7	11	352.8	339.2	21	293.1	276.3	31	310.9	287.1
2	286.5	276.3	12	318.2	304.8	22	300.4	288.3	32	364.3	324.2
3	317.0	263.5	13	339.1	322.1	23	315.2	282.2	33	326.8	309.9
4	314.8	293.4	14	318.7	310.4	24	304.5	305.3	34	342.1	315.9
5	318.2	299.7	15	341.0	314.5	25	321.2	322.4	35	390.1	379.0
6	315.6	279.9	16	320.2	313.0	26	345.5	317.3	36	352.1	315.4
7	312.3	304.2	17	336.2	315.8	27	344.7	328.8	37	334.2	346.3
8	321.8	298.8	18	331.5	328.1	28	371.8	327.8	38	349.4	343.7
9	355.1	344.9	19	342.8	319.5	29	361.9	331.8	39	336.3	325.3
10	336.3	318.2	20	328.8	318.3	30	388.6	350.1	40	347.6	315.5
avg	317.9	295.6	avg	332.9	318.6	avg	334.7	313.0	avg	345.4	326.2
sd	17.4	22.5	sd	11.0	9.2	sd	31.0	23.0	sd	20.4	23.7

Table 30: The free thiol concentrations of the control samples of the IBD cohort study in the UMCG

DAY 5	contr 1	8-Jul contr 2	DAY 6	contr 1	13-Jul contr 2	DAY 7	contr 1	15-Jul contr 2
p	contr 1	contr 2	p	contr 1	contr 2	p	contr 1	contr 2
41	274.8	292.0	51	373.6	333.4	61	312.1	285.7
42	300.3	283.0	52	364.0	355.1	62	313.0	292.8
43	311.0	308.0	53	400.2	344.8	63	323.4	286.3
44	310.1	294.6	54	448.2	405.1	64	315.8	302.2
45	343.1	332.7	55	438.5	350.5	65	332.4	311.1
46	321.0	297.3	56	372.9	346.4	66	328.5	295.3
47	351.0	334.1	57	385.1	365.2	67	338.1	318.9
48	332.5	325.7	58	436.0	395.4	68	335.5	319.5
49	326.7	297.4	59	384.4	378.1	69	325.2	319.0
50	324.7	292.3	60	336.7	358.9	70	345.9	322.1
avg	319.5	305.7	avg	394.0	363.3	avg	327.0	305.3
sd	20.8	17.6	sd	34.6	21.9	sd	10.7	13.8

W   Plasma measurements on-chip

Table 31: The absorbance values for the plasma samples measured in the well plate,
and on-chip with liquid and freeze-dried DNTB

Plasma sample number	Well plate (abs)	Chip liquid DTNB (abs)	Chip Freeze-dried DTNB (abs)
1	0.4172	-0.0015	0.0352
2	0.456	0.0052	0.0032
3	0.4418	0.0059	0.0072
4	0.4349	0.0047	0.003
5	0.4132	0.2002	0.088
6	0.4073	0.2331	0.1249
7	0.413	0.1425	0.0999
8	0.4094	0.0153	-0.0936

X   Results statistical analysis

X.1   Figures calibration curves

```
                Df Sum Sq Mean Sq F value Pr(>F)
Concentration  1  1.647  1.6471   2.137  0.158
Residuals     22 16.958  0.7708
```

Figure X.1: The ANOVA results from R-studio on the calibration curves of the well
plate.

```
                Df Sum Sq Mean Sq F value Pr(>F)
Concentration  1  1.410  1.4098   3.604 0.0708 .
Residuals     22  8.605  0.3911
---
Signif. codes:  0 '***' 0.001 '**' 0.01 '*' 0.05 '.' 0.1 ' ' 1
```

Figure X.2: The ANOVA results from R-studio on the calibration curves of the well
chips.

```
                Df Sum Sq Mean Sq F value Pr(>F)
Concentration  1  1.647  1.6471   2.137  0.158
Residuals     22 16.958  0.7708
```

Figure X.3: The ANOVA results from R-studio on the difference in calibration
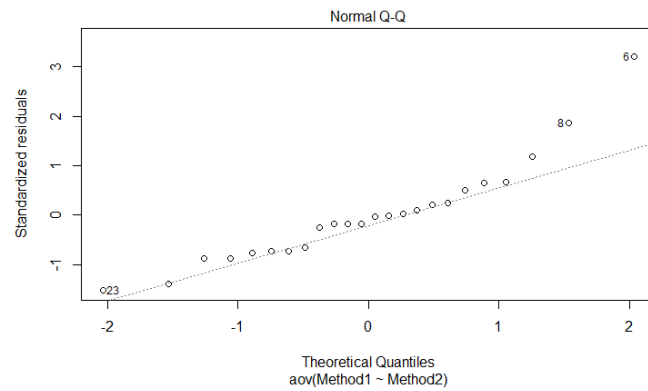curves between the well plate and chips.
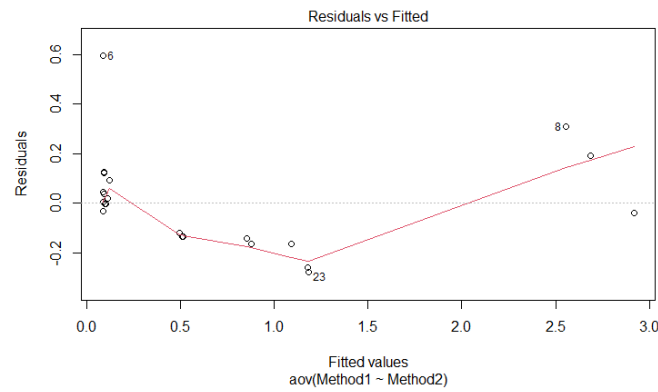
Figure X.4: The Q-Q plot of the calibration curves

Figure X.5: The null residual plot of the calibration curves.

X.2   Figures plasma samples

```
            Welch Two Sample t-test

data:  Plasma_conc_x_4 by Type
t = -0.58397, df = 2.1444, p-value = 0.6148
alternative hypothesis: true difference in means between group Chip and group Well is not equal to 0
95 percent confidence interval:
 -243.2938  181.7971
sample estimates:
mean in group Chip mean in group Well
        433.3700          464.1183
```

Figure X.6: The t-test results

	Df	Sum Sq	Mean Sq	F value	Pr(>F)
Type	1	2063	2063	0.867	0.376
Residuals	9	21406	2378		

Figure X.7: The ANOVA results from R-studio on the plasma samples.
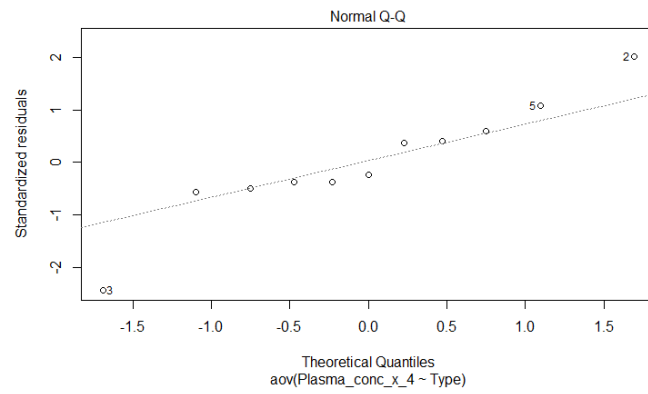
194

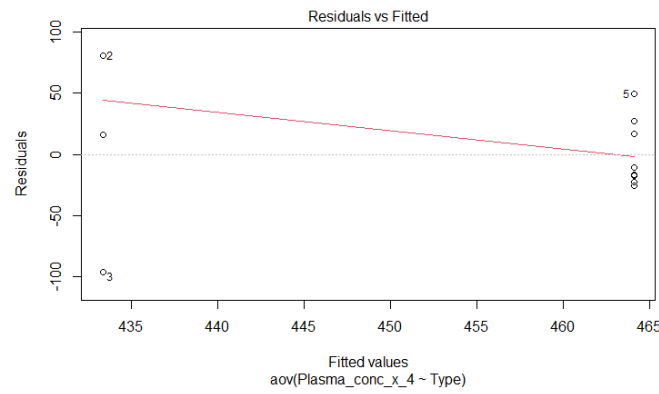*Figure X.8: The Q-Q plot of the plasma samples*

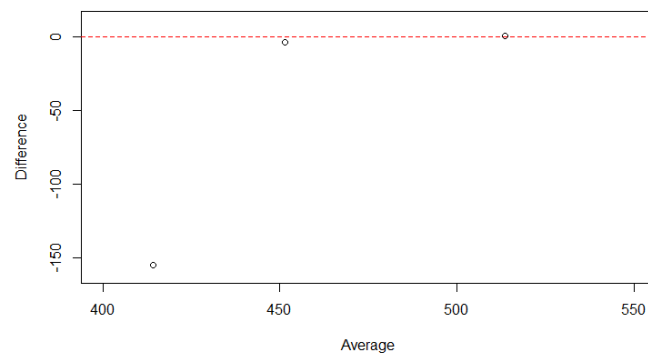*Figure X.9: The null residual plot of the plasma samples.*

Figure X.10: The Bland-Altman plot of the measured concentration of the plasma samples with the chip and well plate.

195

Y Colorimetric detection and portable spectrophotometer

Y.1 Making a color strip

The pictures taken with a microscope did not show any yellow coloring since the filter paper did not pass any light and the light source came from below. The pictures taken with the smartphone were very difficult to analyze since the lighting of the images had a large influence on the developed color strip (Figure Y.1 and Figure Y.2). Since the physiological range of the free thiol concentration is 100-500 μM, this method was not considered sensitive enough for making the distinction of having increased disease activity or not.

(a)

(b)

Figure Y.1: The picture taken with a smartphone with plastic background.

(a)

(b)

Figure Y.2: The picture taken with a smartphone with paper background.

Y.2 Using a smartphone application

The food coloring showed a clear increase in darkness with the increasing concentration (Figure 3(a)). Also, clearly visible using the light blue and dark blue backgrounds (Figure 3(b) and Figure 3(c)). However, the smartphone software was not suited to measure the RGB values of the different concentrations in the well plate. The values were constantly

staggering. This is possible due to the reflection of light on the walls of the well plate or stray radiation interfering with the measurements. It was expected that the B-value decreased with increasing yellow food coloring concentration as more light was expected to be absorbed. However, there was no clear relationship between the B-values and concentration, both when measured with the light blue background (Table 32) or the dark blue background (Table 33. Therefore, no measurements on the L-cysteine concentration are performed using this method.
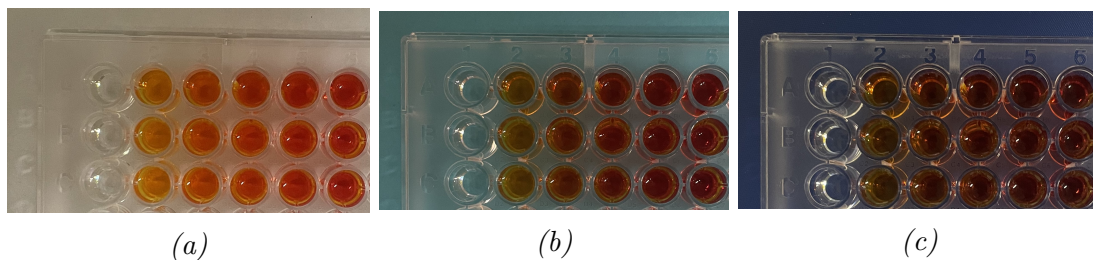

(a) (b) (c)

Figure Y.3: The food coloring concentrations in the well plate (0-100%) with white (a), light blue (b) and dark blue (c) background.

Table 32: The B-values of the triplo measurements using the light blue background

Concentration food coloring	B-value 1	B-value 2	B-value 3
0%	81	81	71
20%	128	153	81
40%	83	33	32
60%	205	205	48
80%	149	171	189
100%	116	94	147

Table 33: The B-values of the triplo measurements using the dark blue background

Concentration food coloring	B-value 1	B-value 2	B-value 3
0%	71	81	71
20%	186	171	171
40%	148	167	153
60%	48	81	102
80%	33	48	32
100%	207	153	2

Y.3 Mykee results

The results for the different Mykee's were similar, yet not identical (Figure 40, Figure Y.4 and Figure Y.5). This suggests that some differences in absorbance measurements are due to different sensors. Additionally, the slope, offset and R^2 values of the these Mykees are also calculated (Table 34 and Table 35).
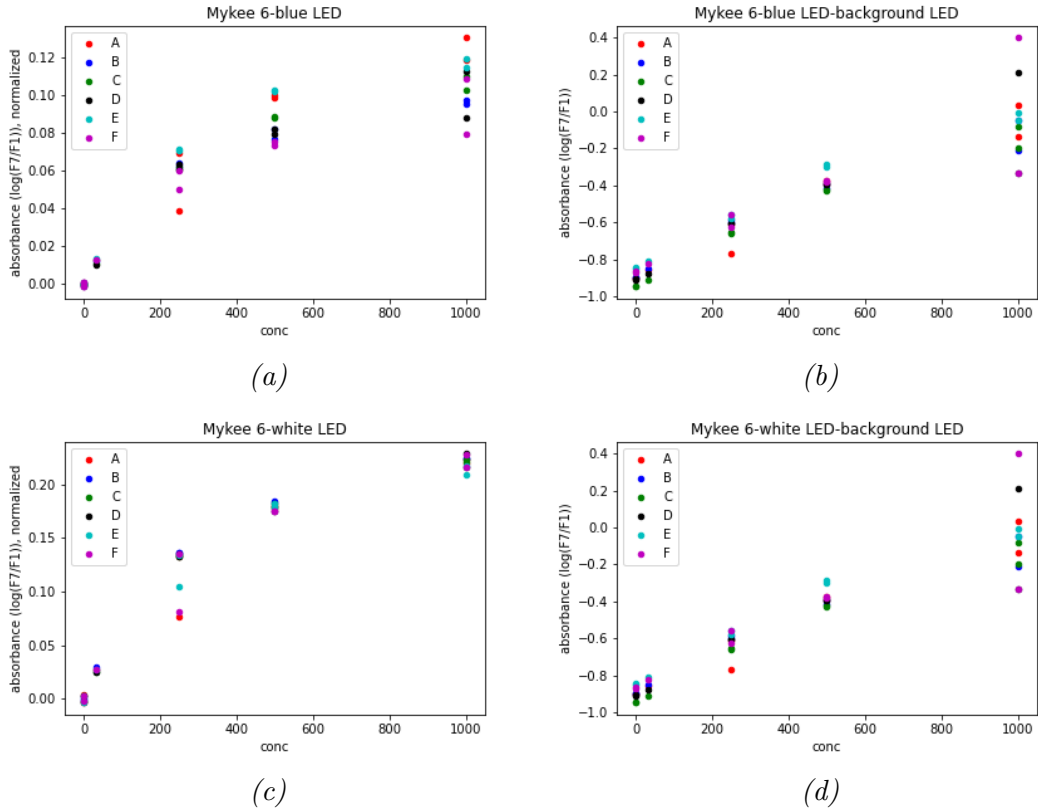
Figure Y.4: The calibration curve of the absorbance measured with the Mykee (number 6) using a blue LED with normalized values (a) and stray light correction (b) and using a white LED with normalized values (c) and stray light correction (d).

Table 34: The slope, offset, and R^2 of the fitted plots of Mykee 6 with stray light correction.

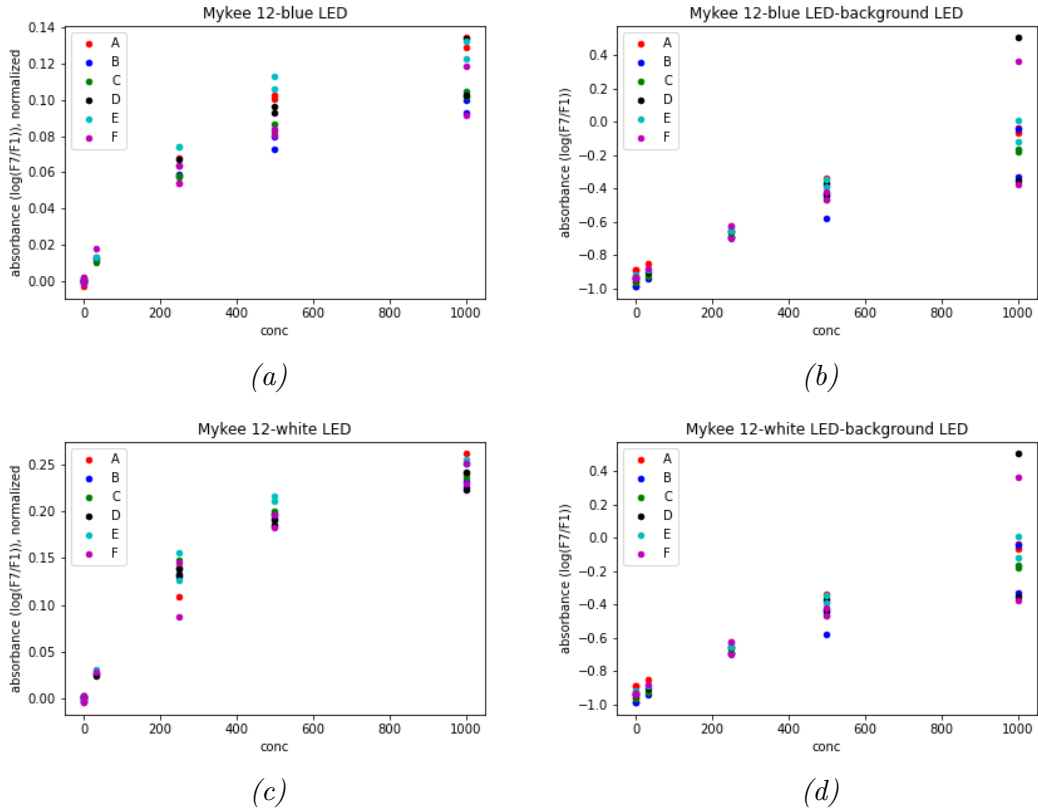| Mykee	Well	White LED			Blue LED		
		Slope * 10^{-4} (abs/μM)	Offset	R^2	Slope * 10^{-4} (abs/μM)	Offset	R^2
6	A	10.11	0.50	0.95	8.66	-0.93	0.95
	B	10.15	0.51	0.98	8.01	-0.90	0.97
	C	10.14	0.48	0.97	8.70	-0.96	0.99
	D	10.11	0.47	0.97	8.55	-0.93	0.98
	E	10.28	0.57	0.99	9.31	-0.87	1.00
	F	10.33	0.53	0.98	8.29	-0.89	0.98

(a)

(b)

(c)

(d)

Figure Y.5: The calibration curve of the absorbance measured with the Mykee (number 12) using a blue LED with normalized values (a) and stray light correction (b) and using a white LED with normalized values (c) and stray light correction (d).

Table 35: The slope, offset, and R^2 of the fitted plots of Mykee 12 with stray light correction.

Mykee	Well	White LED			Blue LED		
		Slope * 10^{-4} (abs/μM)	Offset	R^2	Slope * 10^{-4} (abs/μM)	Offset	R^2
12	A	10.58	0.55	0.99	8.82	-0.92	0.99
	B	10.38	0.46	0.99	7.74	-0.99	0.94
	C	10.89	0.45	0.98	8.66	-0.98	0.99
	D	10.68	0.49	0.98	9.06	-0.96	0.99
	E	11.24	0.45	0.99	9.44	-0.94	1.00
	F	11.10	0.45	0.99	8.21	-0.96	0.97

Z   Test instructions

Figure Z.1: The QR code to the instruction video on how to use the integrated device.